Measurement of the Higgs boson off-shell coupling to constrain the total width in the $H \to ZZ^{(*)} \to 4\ell$ channel and Level-1 Track muon isolation performance for the HL-LHC with the ATLAS detector

Sebastian Olivares

Doctor of Philosophy
The University of Edinburgh
October 2016

Abstract

Since the observation of a narrow mass resonance consistent with the Higgs boson by ATLAS and CMS collaborations in 2012, a number of important studies have been made in order to understand the properties of the newly discovered particle. The most fundamental precision measurements include the Higgs coupling to other particles and itself; properties that have a direct relation with the total decay width. The theoretical total width of the Standard Model (SM) Higgs boson is extremely small (4.2 MeV), making its direct measurement by the LHC experiments non feasible due to the finite experimental detector resolution. Recent publications have shown a novel way to set an indirect limit on the total Higgs boson width by using measurements of both off-shell and on-shell production. This thesis presents a determination of the off-shell Higgs boson coupling, and a further interpretation of the Higgs total width in the $H \to ZZ \to 4\ell$ channel ($\ell = e, \mu$). The results are based on pp collision data collected by the ATLAS experiment at the LHC, corresponding to an integrated luminosity of 20.3 fb^{-1} at a collision energy of $\sqrt{s} = 8$ TeV. Using the CLs statistical method and assuming the same higher-order QCD corrections applied for both signal and background processes, the observed 95% confidence level (CL) upper limit on the off-shell signal strength is 7.3 (with the yields normalized to the SM expectation). Similarly, the 95% CL upper limit on the Higgs total width is 24.7 MeV.

The LHC will undergo its last big upgrade in 2021, in preparation for the high-luminosity LHC Run (HL-LHC), with a luminosity increase of approximately a factor of 5 beyond its nominal design rate. Raising the muon transverse momentum threshold becomes a necessity in order to maintain a low online selection rate with the existing trigger system, at the cost of a reduced efficiency for the electroweak scale physics. An alternative to this approach is a proposed design of a first-level hardware trigger that uses tracking information. Being able to use tracking information at the first level of the ATLAS trigger in the implementation of a muon isolation algorithm offers an extra handle for

differentiating between signal and background. The second part of this thesis presents studies on the performance of tracking-based muon isolation designed for a first-level hardware trigger system. These studies demonstrate the improved trigger performance of the muon isolation algorithm when compared to an increase of the transverse momentum threshold of the muon candidates.

Lay summary

The Standard Model (SM) of particle physics describes the interactions between elementary particles for the three out of four known forces of nature: electromagnetism, weak, and strong force. The SM is constructed in terms of underlying principles that relates the interactions of elementary particles with the conservation of symmetries. The mathematically simplest way to ensure the conservation of these symmetries is by using exclusively massless fundamental particles. However, given that most of the fundamental particles have an experimentally measured non-zero mass, this explanation is unsatisfactory. Approximately 50 years ago a mechanism was proposed that explains the generation of mass through the non-conservation of one of these SM symmetries, by invoking a quantum field that permeates throughout the entire universe space. This prediction was tested and confirmed in 2012 by the collaborations of two independent experiments, ATLAS and CMS, at the Large Hadron Collider (LHC) in Geneva, Switzerland with the discovery of a particle associated with this field: the Higgs boson.

The LHC is a particle accelerator designed to accelerate protons to 7 TeV (energy equivalent to more than 80 kg of TNT), an order of magnitude higher than the previously most powerful accelerator, and smash them into each other. With a designed rate of 800 million collisions per second, it is an extremely harsh environment for the operation of the ATLAS and CMS detectors. The collaborations of these detectors use an online selection mechanism that ensures an intelligent filtering of potentially interesting events for permanent storage and offline analysis. This mechanism is called the Trigger. The selected stored information is used by several physics groups that analyse the data looking for a specific signal process, like the Higgs boson.

The Higgs boson is an unstable particle that decays almost instantaneously into other particles, which may decay further themselves. The experimental observation of the Higgs boson is therefore not achieved directly, but via the detection and reconstruction of the secondary particles, also known as the final state. The experimentally cleanest final states are the ones that can be reconstructed with photons, electrons or muons; however, the probability for the Higgs boson to decay into one of these clean states is small. For example, the production and further decay into one of the most distinguishable signatures, the $H \to ZZ^{(*)} \to 4\ell$ final state (where l is either a muon or an electron), occurs

roughly only once for every 10 trillion (10^{15}) proton-proton collisions.

After the experimental observation of the Higgs boson, a number of important studies have been made in order to understand the properties of the particle. The most fundamental measurement is the coupling to other particles and itself; a property that has a direct relation with the particles total decay width. The total width is defined as the particle's decay probability per time unit, corresponding to the reciprocal of its average decay lifetime. Unfortunately, the SM Higgs boson has a narrow total width, approximately 1,000 times smaller than the current detector resolution, making its direct measurement by the LHC experiments an unfeasible task. Instead, in this thesis I employ a novel indirect-measurement technique to set an exclusion limit on the total width by using non-resonant Higgs boson events.

The main part of this thesis comprises the measurement of the Higgs boson events above the on-shell mass peak with an indirect limit of the Higgs total width in the $H \to ZZ^{(*)} \to 4\ell$ channel. The measurement obtained with these results constitutes a dramatic improvement over previous direct measurements, constraining the Higgs total decay width to be smaller than 10 times the SM value hypothesis. The measurement precision can be further improved with the increase of the size of the data samples to be collected in the next years of the LHC operation.

There are three upgrade periods for the LHC accelerator, with the last one, the so-called high-luminosity LHC (HL-LHC) upgrade, scheduled for 2021. The proton collision rate is going to increase approximately by a factor of 5 beyond the design LHC operational point. This renders the implementation of additional selection algorithms in the trigger system mandatory. The baseline proposal is to restrict the muon selection by raising the kinematic threshold on its transverse momentum, effectively resulting in a signal efficiency loss below this threshold. An alternative proposal is an upgraded first-level hardware trigger that employs tracking information. In order to refine the separation between signal and background processes, one of the newly proposed selections is an algorithm that characterises muons by measuring how separated ("isolated") they are from the rest of the collision activity by employing tracking information. The muon isolation is quantified with the construction of a cone centred around the muon candidate, and by requiring that only the track of the muon candidate is contained within the cone and no other particle. In this thesis, I present studies that demonstrate that the incorporation of a tracking-based muon isolation algorithm at the trigger achieves a substantial improvement of the online signal selection compared to the baseline proposal, by keeping a highly controlled background event rate.

Declaration

I declare that this thesis was composed by myself, that the work contained herein is my own except where explicitly stated otherwise in the text, and that this work has not been submitted for any other degree or professional qualification except as specified.

Parts of this work have been published in [1].

(*Sebastian Olivares, October 2016*)

Dedicated to the memory of my mother

Letizia Pino

Acknowledgements

I would like to thanks the persons who became my second family during my period in Edinburgh: Francisca Garay, Juan Pablo Mira and Teo Mira.

I would like to acknowledge my advisor Christos Leonidopoulos for all the patience and support during these years. I would like to thanks my second advisor and close friend Yanyan Gao for being my mentor who even encourage me when I was lazy. I show great appreciation to my friend Alan Taylor for reading and improving my thesis. I am grateful for all the moments that I share with Tim Bristow and Paul Glaysher in Edinburgh and Geneva. I would like to thanks Adam Morris for his willingness during my PhD, as printing this thesis.

I would like to thanks my father Ruperto Olivares, brother Cristian Olivares, and sister Alejandra Olivares, for believe and support me with huge affection in all the decisions I took, especially during these last years. I would like to acknowledge the rest of my family: Amira Sarmiento, Alejandra Oviedo, Felipe Luengo, Carolina Oviedo, Pablo Beboto, Carolina Guerra, Pierre Touzet, and Matias Díaz, for all the love and devotion.

Finally, I would like to thanks the motive of my smiles, my faithful partner who has been by my side in all sweet and sour moments, my wife Claudia Oviedo. "*Y aunque no siempre he entendido mis culpas y mis fracasos, en cambio sé que en tus brazos el mundo tiene sentido*" (M. Benedetti).

This work was funded by CONICYT via the "Capital Humano Avanzado" scholarship.

Contents

Chapter 1

Introduction

The Standard Model (SM) [2, 3] of particle physics, developed in the middle of the 20^{th} century, describes the interactions of fundamental particles leading to the understanding of the sub-atomic world. It is an extremely successful theory that has been established via the experimental confirmation of all elementary particles with great accuracy. It is described by a gauge invariant theory that explains the particle interactions with three out of four forces of nature (electromagnetism, weak, and strong force). However the theory was initially formulated to describe massless particles in order to maintain the gauge invariance of their interactions. By introducing spontaneous symmetry breaking to the theory, a mass generation mechanism —commonly known as the Higgs mechanism [4–6]— explains that the SM particles acquire mass via their interaction with the Higgs field. After almost 30 years of experimental searches of the particle associated with this field, on the 4^{th} of July 2012, the Higgs boson was discovered [7, 8] by the ATLAS and CMS collaborations at the Large Hadron Collider (LHC), CERN. Following the discovery, several measurements of the particle properties [1, 9–12] show strong evidence that it corresponds to the Higgs boson predicted by the SM. Still, the relative large uncertainty of the current measurements leaves enough room for the discovered boson to be a Beyond the SM (BSM) particle with a behaviour that is different than the SM predictions for the Higgs boson. Numerous precision measurements of the Higgs boson are currently ongoing in order to reveal its true nature.

The Higgs boson couples directly to elementary particles of the SM with a coupling strength which is proportional to the mass of the particle. The coupling

strength of the Higgs boson with the rest of the SM particles according to the theory is directly linked to its production and decay rates. In order to verify the full SM hypothesis, all possible channels need to be measured and compared to the SM prediction. BSM physics can modify the Higgs coupling strength of a given process, by introducing exotic particles in loops either in the production or the decay processes. If these exotic particles have a substantial mass, their impact in the coupling strength can be observed in the Higgs boson high-mass, off-shell sector.

The main part of this thesis presents a measurement of the off-shell Higgs coupling with a further interpretation of the Higgs total width in the $H^* \to ZZ \to 4\ell$ decay channel.

Chapter 2 outlines the incorporation of the Higgs mechanism in a gauge invariant SM theory to explain the mass of the fundamental particles. It begins with a brief summary of the SM elementary particle content and its interactions. An introduction of the symmetries of the SM is given using the Euler-Lagrange method, showing the conservation of each continuous group current. A description of the main characteristics of the SM interactions (Electromagnetic, Strong, and Electroweak) is given explaining the mechanism to obtain gauge invariance. The Goldstone theorem is explained in the context of the spontaneous symmetry breaking in a scalar model, as an introduction to the Higgs mechanism. This mechanism is defined first for a simple electromagnetic model to identify the Higgs boson, and then it is expanded to the EW model. The most important EW interactions with the Higgs boson are explained, including decay couplings, mass and self-interaction terms. Following this, an overview of the observation of the Higgs boson at the LHC, and the current measurements of the main properties are given. The phenomenology of the Higgs boson at the LHC is discussed, including production and decay modes. Lastly, a description of the total decay width and the matrix element are covered as an introduction to the tools used in the main analysis chapter.

Chapter 3 summarises the functionality and experimental setup of the LHC and the ATLAS experiment. A description of each sub-system of the ATLAS detector is given, explaining the mechanism for identifying and reconstructing particles transversing its volume. A detailed explanation of the data recorded by the ATLAS detector is given, following the interactions occurring after a proton-proton collision. Finally, the mechanism for reconstructing the main physics objects within the volume of the ATLAS detector is provided.

There are three upgrade stages of the LHC that will allow the physics programme to be significantly extended by increasing the centre-of-mass energy and the collision rate. The last upgrade in 2021 will increase the collision rate by at least a factor of five beyond the ATLAS detector design rate, with a centre-of-mass energy of $\sqrt{s} = 14$ TeV. This period is known as HL-LHC [13] spanning ten years of operation with the expectation to provide datasets with an integrated luminosity 100 times larger than today's datasets. The current ATLAS detector and trigger systems will be unable to handle the data rates of the HL-LHC. It has been proposed to increase the trigger thresholds of basic physics objecs, such as leptons, in order to cope with the increased collision rate, thus compromising the sensitivity for electroweak scale physics. An alternative method is to take advantage of the upgraded components to be installed in the ATLAS detector, and improve the online selection by employing tracking information earlier in the filtering chain.

Chapter 4 examines the performance of a proposed improvement in the online selection of muons using by isolation algorithms at an early triggering level. A brief overview of the LHC and ATLAS upgrades is given, with details about the new components to be installed. A feasibility study is presented that considers the usage of tracking information at the first (hardware) level of the trigger (Level 1 Track trigger) and compares two isolation algorithms using calorimetric and tracking information.

Chapter 5 describes the main features of the $H \to ZZ^{(*)} \to 4\ell$ decay channel. The kinematic observables that are involved in the multivariate analysis of the next chapter are defined. A complete description of the event selection is given. Lastly, the main backgrounds for this channel are described, and their impact on the final event selection explained.

Chapter 6 presents the main analysis of this thesis that aims to measure the couplings and the total width of the Higgs boson in the off-shell $H^{(*)} \to ZZ \to 4\ell$ decay channel. A theoretical overview is given that introduces an indirect method to measure the total Higgs width by using both on- and off-shell couplings. A detailed description of the simulated signal and background Monte Carlo samples is given, including calculations of corrections and uncertainties. The overall analysis strategy is presented, outlining the baseline selection method employing a multivariate matrix element technique, with a secondary "square cut"-based analysis used as a cross-check. The theoretical and experimental uncertainties are calculated for both signal and background processes. A statistical method

and the fit used to constrain the off-shell coupling and the total width of the Higgs boson are detailed. Results are presented in the form of upper exclusion limits on the off-shell signal strength, with a further interpretation on the Higgs total width. Consistency checks are made with the cut-based analysis method. The statistical significance of the result is calculated in combination with the $ZZ \to 2\ell\,2\nu$ and $WW \to \ell\nu\,\ell\nu$ channels under different production modes assumptions.

Chapter 7 summarises the studies carried out in this thesis and the conclusions that have been made.

Chapter 2

The Standard Model and the Higgs boson

The Standard Model (SM) of particle physics represents our current understanding of the elementary particles and their interactions. It is implemented by using Quantum Field Theory (QFT), and describes successfully experimental observations at the subatomic level.

The following chapter gives an overview of the fundamental ingredients of the Standard Model (SM) and the Higgs mechanism. A brief summary of the particle content and the components of the full SM Lagrangian is given in Sect.2.1, with a brief introduction of the symmetry groups involved in the theory in Sect.2.2. A detailed explanation of the Higgs mechanism is then introduced in Sect.2.3, including the necessary phenomenology and the status of the current experimental measurements of the Higgs boson. It ends with a description of the matrix element reconstruction process at the LHC (Sect. 2.4), as an introduction for the discriminant tools used in the main analysis presented in Chapter.6. Historical facts are introduced in several sections in order the give a better context for the development of the theory.

2.1 Elementary particles and interactions

All known matter in the universe is formed by leptons and quarks. Both particle categories are characterised by Fermi-Dirac statistics, having half-integer

intrinsic angular momentum (spin), a property of a broader group called fermions. The interactions between them is mediated by the exchange of another type of fundamental particle, referred to as gauge boson. These fundamental bosons, which obey Bose-Einstein statistics, have an integer spin. The SM satisfactory explains three out of four forces of nature (electromagnetism, weak, and strong force) via the exchange of a specific gauge boson. Electromagnetism is mediated by the photon (γ), the weak force by the vector bosons Z, W^+, and W^-, and the strong force by eight gluons. While photon and gluons are massless particles, the gauge bosons of the weak interaction are massive. Although not yet experimentally confirmed, the graviton would be the corresponding force-carrying particle of gravity. However, the renormalisable relativistic quantum field theory, implemented by the SM to explain the sub-atomic world, is not compatible with the general theory of relativity, used to explain the kinematics of the macroscopic world. For the moment, it is impossible to fit both theories into a single framework that would include the graviton. Nevertheless, when it comes to the minuscule scale of particles, the effect of gravity is so weak as to be negligible.

Each one of nature's interactions has its own strength that indicates the intensity with which the gauge boson couples to a quark or lepton (g_1: strength of the electromagnetic interaction, g_s: strength of the strong interaction). For instance, when two electrons exchange a photon, the amplitude of the interaction is proportional to g_1^2. The dimensionless quantity that characterises each force interaction in the low energy limit (each constant changes according to the energy of the process, as explained in Sec. 2.2.2), and its range of action are: electromagnetic $\alpha \approx \frac{1}{137}$ with infinite range, strong $\alpha_s \approx 0.12$ with a 10^{-15} m range (diameter of a medium size nucleus), weak $\alpha_w \approx 10^{-7}$ with a 10^{-18} m range (0.1% diameter of a proton), and gravity $\alpha_g \approx 10^{-39}$ with infinite range. The weak and the strong interactions are effective only over a very short range but dominate at the subatomic particle level. As its name suggests, the weak force is the weakest of the SM, but it is still much stronger that gravity.

An elementary particle can participate in a certain interaction, if it carries the charge of the corresponding force. All electrically charged particles interact through the electromagnetic force mediated by the massless photon with no electric charge. Each one of these particles couples to the photon with a slightly different intensity, although always proportional to the electromagnetic interaction strength (e.g. $-e$: electron, $+e$: positron, $+2/3e$: up-type quarks,

$-1/3e$: down-type quarks, 0: neutrino). The elementary fermions of the SM differ in the way in which they interact with the strong force. All quarks carry colour charge (red, green, or blue) and thus interact through the strong force mediated by massless gluons. Gluons exist in eight different versions, each carrying a combination of colour and anti-colour charge. Quarks only mix in such ways as to form colourless objects, as explained in Sec. 2.2.2.

All particles have an intrinsic weak isospin which is a quantum number that describes how a particle behaves in the weak interaction. Fermions have weak isospin of either $+1/2$ for up-type quarks and neutrinos, or $-1/2$ for down-type quarks and charged leptons. A combination of the electromagnetic and the weak theories (electroweak theory) gives rise to another quantum property that relates the electric charge of the particle and its weak isospin: the hypercharge. While some particles have a weak isospin value of zero, all particles, except gluons, have non-zero weak hypercharge. However, possibly the most noticeable effect of the weak interaction is given by the $W^{\pm}$ boson that is responsible for flavour changing, like in the case of the Beta decay. Since the $W^{\pm}$ is the only boson with a non-zero electric charge, it couples pairs of particles which differ by one unit of electric charge. In the case of leptons, it couples only to pairs of the same flavour (e.g. electron and electron-neutrino). However, in the case of quarks, any exchange between up-type and down-type quarks is allowed. The transition probabilities between physical up-type quarks and down-type quarks are given by the Cabibbo-Kobayashi-Maskawa (CKM) matrix [14, 15], which favours transitions within the same quark "generation".

The elementary fermions are grouped in three generations. The higher generation, the larger the mass of the corresponding particles. All stable matter in the universe is made of particles that belong to the first generation; any heavier particle quickly decays to the lowest mass stable particle. The two additional generations appear to be a copy of the first generation with heavier masses.

Each generation is organised in pairs of particles. The six quarks are paired as the "up quark"and the "down quark"for the first generation, followed by the "charm quark"and "strange quark", then the "top quark"and "bottom quark". The six leptons are similarly arranged in three generations, organised as the "electron"and the "electron neutrino", the "muon"and the "muon neutrino", and the "tau"and the "tau neutrino". The electron, muon and tau have a sizeable mass, whereas the neutrinos are massless according to the SM. However, experimental observations of neutrinos oscillations have demonstrated that neutrinos have mass. The

elementary particles of the SM are summarized in Figure 2.1.

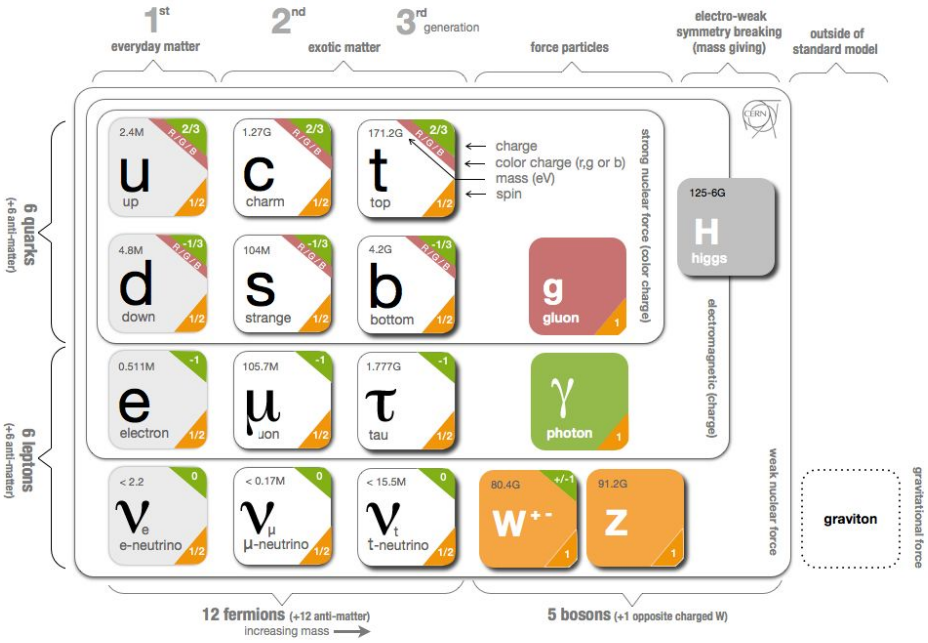

Figure 2.1 *Standard model particle content [16]. The elementary particles are composed by: three generations of leptons and quarks, four force mediating gauge bosons and the Higgs boson*

Even though anti-particles are not explictly mentioned in Figure 2.1, they are an essential part of the SM. Each fundamental fermion has a corresponding anti-particle (e.g. electron-positron). Following the Dirac interpretation, the antiparticles have the same mass and spin as the particles, but opposite charge and magnetic moment relative to the direction of the spin.

All quarks and leptons have spin 1/2, all gauge vector bosons have spin 1, while the scalar Higgs boson has spin 0. The masses of the elementary particles of the SM are acquired via the interaction with the Higgs field, with the minimal excitation state associated with this field being represented by the massive Higgs boson. The proposed mechanism for the generation of mass, Higgs mechanism, is explained by the non-conservation of the vacuum symmetry.

2.2 Symmetries

QFT is the basic mathematical language that is used to describe and analyse the physics of elementary particles. It manages to explain the subatomic interactions using a combination of Classical field theory (CFT), Quantum mechanics (QM) and Special relativity (SR). The evolution of a physical system is described by the solutions to the Euler-Lagrange equation of the system.

The Euler-Lagrange method is used also in simpler cases, as classical mechanics, describing a dynamic system in terms of position coordinates and their time derivatives. The classic action define how physical quantities, such as position and momentum, change continuously in time, written as:

$$S = \int_{t_1}^{t_2} dtL \tag{2.1}$$

The equations of motion (Euler-Lagrange) can be derived by minimizing the action:

$$\frac{d}{dt}(\frac{\partial L}{\partial \dot{q}_i}) - \frac{\partial L}{\partial q_i} = 0 \ , \tag{2.2}$$

which is equivalent to the Newton's laws of motion that is invariant under any system of generalised coordinates. In CFT there is an analogous equation for the calculation of the system's dynamics, with the important difference that the object described is not a particle with a finite number of degrees of freedom, but a continuous function of space and time with an infinite number of degrees of freedom, called "field". The lagrangian is thus generalised to a lagrangian density:

$$L \to \int_{x_0}^{x_1} dx\mathcal{L} \tag{2.3}$$

In the most general case, the lagrangian density is a function of the field ϕ and its space-time derivatives ($\mathcal{L} = \mathcal{L}(\phi, \partial_\mu \phi)$), with the action given by:

$$S = \int dx\mathcal{L} \tag{2.4}$$

As before, the field equations are obtained from the minimization of the action:

$$\frac{\partial \mathcal{L}}{\partial \phi} - \partial_\mu \big(\frac{\partial \mathcal{L}}{\partial(\partial_\mu \phi)} \big) = 0 \tag{2.5}$$

Every local transformation of the fields leaving ∂S unchanged forms a continuous group of CFT. In the SM (described by QFT), these continuous groups are called gauge groups. QFT is a quantum generalisation of CFT, that introduced discrete quantum field states defined by the Hilbert space.

2.2.1 Introduction of the symmetries in the SM

The SM introduces three different continuous gauge groups for the quantum theories that describes a specific force of nature:

- The Electro Weak theory is used to describe the unification of the quantum electrodynamics (QED) and Weak theory by using a combination of the U(1) and SU(2) gauge group.
- Quantum chromodynamics (QCD) is used to describe the strong force by using a SU(3) gauge group.

Gauge group invariance and Noether theorem

All the theories named above must be locally gauge invariant. A simple example is introduced with the lagrangian of a free relativistic fermion field $\psi(x)$:

$$\mathcal{L}_D \;=\; i\bar{\psi}\gamma^\mu \partial_\mu \psi - m\bar{\psi}\psi \tag{2.6}$$

By solving the Euler-Lagrange equation the quantum mechanical field equations are derived. In the case of a non-interacting fermion we end up with the Dirac equation. Interactions appear by requiring local gauge invariance of the lagrangian under the symmetry transformation of the group. For instance, the local phase transformation of the U(1) symmetry of QED is defined by:

$$\psi(x) \to \psi'(x) = e^{iq\chi(x)}\psi(x) \ , \tag{2.7}$$

where $\chi(x)$ is a scalar phase. The local gauge invariance can only be restored by introducing additional fields with the dimension of the given symmetry, which

can be identified with the force-mediating bosons. This is achieved by replacing the derivative ∂_μ with the covariant derivative D_μ. In the case of QED it is given by:

$$\partial_\mu \rightarrow D_\mu = \partial_\mu + ig_1 A_\mu \quad \text{with: } A_\mu \rightarrow A'_\mu = A_\mu - \partial_\mu \chi \ , \tag{2.8}$$

where A_μ is the photon field and g_1 is the charge of the fermion. By adding a kinetic term for the gauge bosons, the QED lagrangian that describes the full dynamics including interactions becomes:

$$\mathcal{L}_{QED} \ = \ \bar{\psi}(i\gamma^\mu \partial_\mu - m)\psi - \frac{1}{4} F_{\mu\nu} F^{\mu\nu} + g_1 \bar{\psi}\gamma^\mu \psi A_\mu \ , \tag{2.9}$$

where $F_{\mu\nu} = \partial_\mu A_\nu - \partial_\nu A_\mu$ is the field strength tensor of QED. While the first term of Eq. 2.9 is the same non-interacting term of the previous lagrangian of Eq. 2.6, the last two terms include photon (second term) and fermion-photon (third term) interactions.

According to Noether's theorem, any continuous symmetry that leaves the action invariant implies the existence of a conserved current S^μ, with $\partial_\mu S^\mu = 0$. For QED, the conserved current is the electric charge, and its given by the third term of Eq. 2.9: $j^\mu = \bar{\psi}\gamma^\mu \psi$.

The same procedure can be done for the Weak and QCD lagrangians in order to obtain the corresponding conserved currents. But, while the generator of the U(1) symmetry of QED is a scalar phase, the generators of SU(2) and SU(3) are represented by the more complex non-commutative Pauli and Gell-Mann matrices. As a consequence, the Weak and QCD symmetries lead to the conservation of the weak isospin and colour charge, respectively.

In summary, the SM lagrangian is invariant under the unified local gauge symmetry group $SU(3) \times SU(2) \times U(1)$. Although not all three theories can be described in a combined way yet, the electroweak (EW) theory by Glashow, Salam and Weinberg [2] is a first succesful attempt at the unification of the electromagnetic and weak interactions into the $SU(2) \times U(1)$ symmetry group (as explained in Sec. 2.2.3). Consequently, the SM lagrangian can be written as a combination of the EW and QCD interactions:

$$\mathcal{L}_{SM} \ = \ \mathcal{L}_{QCD} + \mathcal{L}_{EW} \tag{2.10}$$

Lorentz invariance

The SM implies a consistency of QFT with Einstein's Special Relativity by the conservation of the Lorentz symmetry group. According to SR, the laws of physics stay the same in any inertial system. Thus, the equation of motion must be invariant under rotations and boost velocity.

$$\begin{bmatrix} t^{'} \\ x^{'} \\ y^{'} \\ z^{'} \end{bmatrix} = \begin{bmatrix} \cosh\theta & 0 & 0 & -\sinh\theta \\ 0 & 1 & 0 & 0 \\ 0 & 0 & 1 & 0 \\ \sinh\theta & 0 & 0 & \cosh\theta \end{bmatrix} \begin{bmatrix} t \\ x \\ y \\ z \end{bmatrix} \tag{2.11}$$

where the boost $B = \frac{v}{c}$ is written as $B = \tanh\theta$, or $\gamma = \cosh\theta$. The most general transformation that includes rotations and boosts is:

$$X^{'\mu} = L^{\mu}_{\nu} X^{\nu} \tag{2.12}$$

Where the matrix L^{μ}_{ν} forms the group called: Lorentz group. For example, the space-time interval $(\Delta s)^2 = (\Delta t)^2 - (\Delta x)^2 - (\Delta y)^2 - (\Delta z)^2$ between events x^{μ} and $x^{\mu} + \Delta x^{\mu}$ must be invariant under Lorentz transformations $(\Delta s^{'})^2 = (\Delta s)^2$. Physical quantities that are invariant under Lorentz transformations are called Lorentz scalars The only fundamental particle of the SM that is a scalar is the Higgs boson. The Higgs mechanism keeps the SM lagrangian gauge invariant but the vacuum is not, as explained in Sec. 2.3.2.

Discrete symmetries (CPT)

Apart from the continuous symmetries, three important discrete symmetries that are involved in the SM are: parity, charge conjugation, and time reversal. The changes in these symmetry properties can be thought of as "mirror"transformations under which some property of the particle (space, charge, or time) is reflected or reversed. Parity refers to an operation which takes the space position and reflects it through the origin $x = (t, \vec{x}) \rightarrow x_p = (t, -\vec{x})$. The operation that changes the sign of the charges is called charge conjugation, and it turns a particle into its anti-particle. Both symmetries are conserved in the strong and electromagnetic interactions, but according to experimental observations [17, 18], they are not in the weak interactions. The combination of the two asymmetries is known as CP violation, which, as we believe, is related

to the observation that there is more matter than antimatter in the universe. The time-reversal symmetry refers to the operation that changes the evolution of the system making it move backwards in time $x = (t, \vec{x}) \rightarrow x_T = (-t, \vec{x})$. The combination of these three symmetries, CPT, is observed to be an exact symmetry of nature at the fundamental level. The SM is constructed to be invariant under this symmetry, given that its violation implies the breaking of Lorentz symmetry.

2.2.2 Strong interactions and Quantum chromodynamics

Approximately 60 years ago, many new particles were discovered, in particular the four Δ resonances, the six hyperons, and the four K mesons. Murray Gell-Mann and Yuval Ne'eman succeeded in describing the new particles in a symmetry scheme based on the SU(3) group, the group of unitary 3×3 matrices with determinant 1 [19, 20]. The SU(3) symmetry is an extension of the isospin symmetry, which was introduced in 1932 by Werner Heisenberg and is described by the SU(2) group. Gell-Mann and Ne'eman theory is known as the "Eightfold Way"(because of its organised subatomic baryons and mesons into octets) and led to the subsequent development of the quark model.

However, it was not clear at the time why the members of the simplest SU(3) representation, the triplet representation, were not observed in hadrons. In 1964, Murray Gell-Mann and George Zweig (a PhD student of Richard Feynman) proposed that baryons and mesons are bound states of a hypothetical triplet particles [21]. Gell-Mann called the triplet particles "quarks", using a word that had been introduced by James Joyce in his novel Finnegans Wake. Since the quarks form an SU(3) triplet, there must be three of them: a u quark (with charge 2/3), a d quark (with charge $-1/3$), and a s quark (with charge $-1/3$). For instance, the proton is a bound state of two u quarks and one d quark (uud).

A new problem of the quark model emerged from the observation of a bound state made of three strange quarks (Ω^-). The spatial wave function in this ground state should be symmetric; but since fermions must follow the Pauli principle, the wave function must be anti-symmetric at the same time. This issue was solved in 1971 by Fritzsch and Gell-Mann [**?**] who introduced a model of nine quarks, as Han and Nambu proposed years earlier [22], but by assuming that three quarks of the same type have a new conserved quantum number, called "colour". This colour symmetry is an exact symmetry. The wave functions of

the hadrons were assumed to be singlets of the colour group. For instance, the baryon wave functions are anti-symmetric in the colour indices, denoted by red, green, and blue. Thus the wave function of a baryon changes if two quarks are exchanged, as required by the Pauli principle. The introduction of colour helped also to explain the experimental observation of the neutral pion into two photons. The theory evolved to an interpretation of the colour group as a gauge group. The resulting gauge theory is similar to QED.

The interaction between quarks is generated by an octet of massless colour gauge bosons, which are the gluons. Due to the similarities of the gauge theory with QED, the name adopted was quantum chromodynamics [23] because of the greek word "chroma"($\chi\rho\acute{\omega}\mu\alpha$, meaning colour) that is related to the theory of colour change. The local gauge transformation of the SU(3) symmetry of QCD is defined by:

$$q(x) \rightarrow U(x)q(x) = e^{ig_s\alpha_a(x)\lambda^a}q(x) \ , \tag{2.13}$$

where $q(x)$ are the quark fields, g_s is the QCD coupling strengh, λ^a are the eight Gell-Mann matrices which correspond to the generators of the group, and $\alpha_a(x)$ is an arbitrary function of x on which the quark field depends. As in QED, the local gauge invariance is restored by introducing additional fields by replacing the derivative ∂_μ with the covariant derivative D_μ:

$$\partial_\mu \rightarrow D_\mu = \partial_\mu + it^a A^a_\mu \ , \tag{2.14}$$

where A_μ is the gluon field and $t^a = \lambda^a/2$. A complete description of the strong interactions is given by the QCD lagrangian:

$$\mathcal{L}_{QCD} = \frac{1}{4g_s^2}G^a_{\mu\nu}G^{\mu\nu,a} + \sum_j \bar{q}_j(i\gamma^\mu D_\mu + m_j)q_j \ , \tag{2.15}$$

where $G^a_{\mu\nu} \equiv \partial_\mu A^a_\nu - \partial_\nu A^a_\mu + if^a_{bc}A^b_\mu A^c_\nu$. Here m_j and q_j are the mass and quantum fields of the jth-flavour quark, and A is the gluon field, with spacetime indices μ and ν, and colour indices a, b, c. The numerical coefficients f and t guarantee the SU(3) colour symmetry. Aside from the quark masses, the coupling constant g_s is the only free parameter of the theory.

The non-abelian property of QCD leads to self-interaction terms of the gauge bosons in the lagrangian. This direct gluon-gluon interaction is important since leads to two different behaviors of the quarks according to how the running

coupling constant, $\alpha_s = g_s/4\pi$, changes with respect to the energy of the process. These two features of QCD are known as: "asymptotic freedom"and "confinement".

- Asympotic freedom refers to the high-energy regime, in which the coupling constant α_s is reduced, leading to an asymptotically free theory [24]. Thus, at high energies the quarks and gluons behave almost as free particles. This leads to the approximate "scaling behaviour"of the cross-sections in the deep-inelastic lepton-hadron scattering.

- Confinement refers to the low-energy regime, in which the interaction becomes stronger, leading to the confinement of the quarks, such that no free quarks can be observed. As a consequence, they form hadrons, either consisting of quark-antiquark pairs ($q\bar{q}$ or mesons) or a triplet of quarks or antiquarks (baryons). Following the Pauli exclusion principle, the quarks in a baryon differ in colour charge and hence quarks always form colorless hadrons.

Considering a hypothetical theory of QCD with just one heavy quark Q, the ground-state meson would be a quark-antiquark bound state. The effective potential between the quark and its antiquark at small distances would be a Coulomb potential proportional to $1/r$, with r being the distance between the quark and the antiquark. However, at large distances, the self-interaction of the gluons becomes important. The gluonic field lines at large distances do not spread out as in electrodynamics, instead, they attract each other. Therefore, unlike electrodynamics, the force between the quark and the antiquark is constant, leaving the quarks confined.

In high-energy interactions, virtual particles could produce a quark and an antiquark, which would move away from each other at high speed. Because of confinement, hadrons (referred to as jets) are created, moving roughly in the same direction as the original quarks. The sum of the energies and momenta of the particles in each jet should be equal to the energy of the original quark. QCD predicts that high-energy gluons can be emitted from quarks, creating additional jets. This process is known as "hadronisation". In high-energy experiments, such as those at the LHC, quarks and gluons are only identified by jets. From the measurement of the jet characteristics the type of quarks from which the jets were originated can be inferred with a level of confidence. However, the quark

flavour and momentum inside high-energy hadrons are not fixed quantities, but follow probability density functions.

It was observed in several deep-inelastic scattering (DIS) experiments that the three-quark model made of valence quarks only was not enough to explain the Bjorken scaling [25], leading to a solution based on Feynman's Parton[1] model. In the parton model, partons (e.g. quarks) are defined with respect to a physical scale. For instance, at low energies, a baryon contains three valence quarks and a meson contains a quark and an antiquark. However, at higher energies, observations show the existence of virtual sea (i.e. non-valence) quarks in addition to valence quarks. The sea quarks are produced in pairs from energetic gluons. The momentum distribution functions of the partons within the proton are called Parton Distribution Functions (PDF). They represent the probability densities to find a parton carrying a longitudinal momentum fraction x at a squared energy scale Q^2. Due to the inherent non-perturbative nature of QCD and its description of parton interactions inside a hadron (besides the limitations in present QCD calculations), PDFs are obtained from parametrisations of parton models to experimental data collected from colliders and fixed target experiments (such as DIS). The parametrisation of parton models comes from QCD predictions related to the rate of parton distributions when the Q^2 energy scale varies. It is governed by QCD evolution equations for parton densities in the domain where perturbative calculations can be applied, in the limit where the running coupling constant is very small: $\alpha_s(Q^2) \ll 1$. The equations can be formulated as an approximation, depending on the power of $\alpha_s(Q^2)$ in the perturbative expansion. They are usually referred to as Leading-Order (LO), i.e. first order in $\alpha_s(Q^2)$, Next-to-Leading-Order (NLO) and Next-to-Next to Leading-Order (NNLO). Experimentally determined parton distribution functions are available from various groups worldwide. For example, the MSTW2008 PDF set is given in Figure 2.2, where the PDF of different partons and momentums are shown for two different fixed values of Q^2 energy. DIS experiments have shown that the number of partons increases at low x, and decreases at high x. At low Q^2, the three valence quarks become more dominant in the nucleon. At high Q^2, there are more quark-antiquark pairs which carry a low momentum fraction x, corresponding to the sea quarks. A salient finding of the DIS experiments is that the quarks and antiquarks only carry about half of the nucleon momentum, with the remainder being carried by the gluons. The nucleon momentum fraction

[1]The name parton is a generic term describing any particle constituent within a hadron, and is today referred to as quarks and gluons.

carried by gluons increases with increasing Q^2.

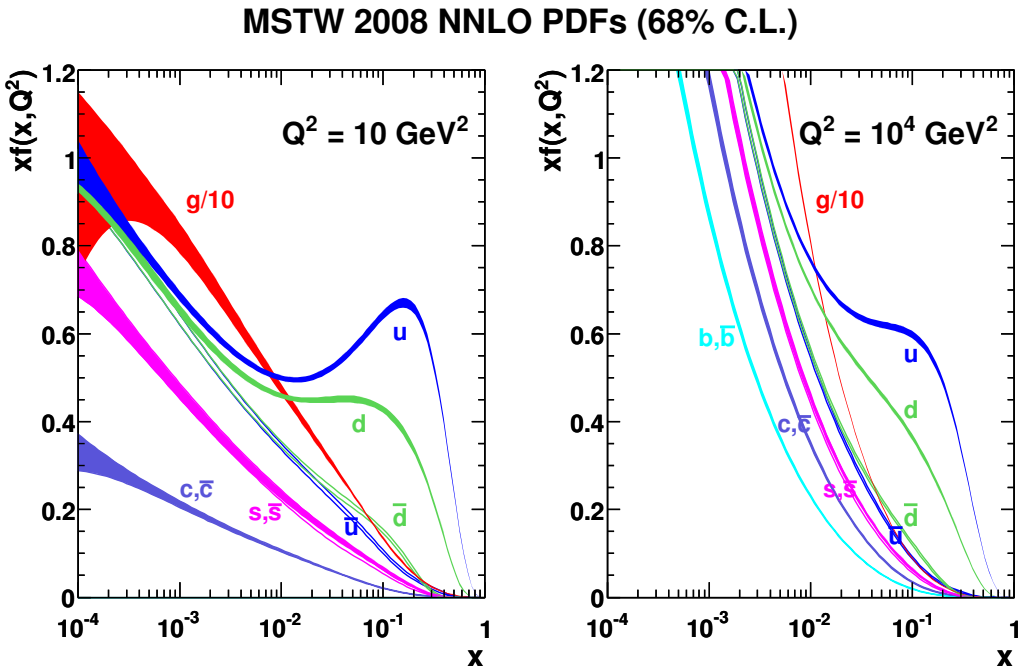

Figure 2.2 *NNLO parton distribution functions calculated from the MSTW2008 PDF set [26] for protons. The momentum fraction x is weighted by its PDF value $f(x, Q^2)$ for two fixed values of Q^2. The bands indicate the 68%-coverage uncertainties.*

In high-energy proton-proton collisions, such as at the LHC, the hard scattering occurs between constituents of the proton. For example, in the production process of a Higgs boson from a quark-antiquark pair, the partonic interaction would be described by p_1, the fraction of momentum of the first proton taken by the quark q, and p_2, the fraction of momentum of the second proton taken by the anti-quark $\bar{q}$. The cross section is then given by:

$$\sigma = \sum_{q,\bar{q}} \int d(p_1)d(p_2)F_1(p_1, Q^2)F_2(p_2, Q^2)\hat{\sigma}(q\bar{q} \to H) \ , \tag{2.16}$$

where $F_1(p_1, Q^2)$ is the probability of finding a particular q quark with a longitudinal momentum fraction p_1 in the first hadron (and similarly for $F_2(p_2, Q^2)$). $F_1(p_1, Q^2)$ and $F_2(p_2, Q^2)$ are commonly known as structure functions, while $\hat{\sigma}(q\bar{q} \to H)$ is the partonic cross section. The cross section is calculated as the sum over all the possible quarks-antiquark interactions that could occur inside the proton.

2.2.3 Electroweak theory

The Electroweak (EW) theory is the unification of the electromagnetic and the weak interactions into a single theory described by the SU(2) × U(1) symmetry group.

The proposal of Feynman and Gell-Mann [27] and Sudarshan and Marshak [28] with the development of the V-A theory was the first attemp at describing the weak interactions. They took the original idea of the EM interactions and replaced the photon with a spin-1 $W^{\pm}$ boson. This led Schwinger [29] to suggest a gauge theory of weak interactions mediated by W^+ and W^-, even questioning a possible unified theory of three spin-1 gauge bosons W^+, W^- and γ. However, there were two main problems with this idea:

1. If there is a symmetry between the gauge bosons, it is clearly severely broken, because there are major mass differences between them.
2. The weak interactions violate parity, whereas the electromagnetic interactions are parity-conserving.

The latter problem was solved in 1961 by Glashow [2], who proposed an extended model with a larger symmetry group, SU(2)×U(1), and a fourth gauge boson Z. With this configuration, the two neutral un-physical gauge bosons, when mixed, give rise to a boson (γ) with parity-conserving interactions and three that violate parity: W^+, W^-, and Z. This model requires the implementation of a new symmetry that combines the electric charge of the particle and its weak isospin, known as hypercharge:

$$Q = I_3 + \frac{Y}{2} , \tag{2.17}$$

where the electric charge Q is expressed as a combination of the third component of the isospin I_3 and the hypercharge Y. All SM particles have non-zero weak hypercharge, except for gluons.

Given that weak interactions distinguish between left-handed and right-handed chiral[2] particles, fermion fields are expressed differently. Left-handed and right-handed fermion fields are represented by doublets and singlets, respectively (with

[2]Chirality is a special version of helicity that considers also massless particles.

doublets containing particles with different flavour). For instance, leptons are expressed as:

$$\psi_{L,i} = \begin{pmatrix} \nu_i \\ \ell_i \end{pmatrix}_L \quad , \quad \psi_{R,i} = \ell_{R,i} \ , \tag{2.18}$$

where i is the lepton generation ($i = 1, 2, 3$), and L or R refers to the chirality of the lepton. An interesting feature of the leptons in the SM is that, in order to keep the neutrinos massless, there is no right-handed neutrino field. Quarks follows the same nomenclature, with the difference that there is an extra singlet for each generation. These fields transforms under the local $SU(2) \times U(1)$ gauge symmetries as:

$$\begin{aligned} \psi_L \rightarrow \psi_L^{'} &= e^{i\alpha(x)\sigma^k/2 + i\beta(x)Y/2}\psi_L \\ \psi_R \rightarrow \psi_R^{'} &= e^{i\beta(x)Y/2}\psi_R \end{aligned} \tag{2.19}$$

where σ^k are the three Pauli matrices, which correspond to the generators of the group. Since the lagrangian must be invariant under local $SU(2) \times U(1)$ gauge transformations, gauge fields B_μ and W_μ are introduced in the covariant derivative to keep the invariance under U(1) and SU(2), respectively.

$$D_\mu = \partial_\mu + \frac{i}{2} g_1 B_\mu + \frac{i}{2} g_2 W_\mu^k \sigma^k \ , \tag{2.20}$$

where g_1 and g_2 are gauge couplings of U(1) and SU(2), respectively. There are in total 4 gauge bosons: B_μ and W_μ^k (k=1,2,3), one for each group generator. The locally gauge invariant lagrangian for EW is defined as:

$$\mathcal{L}_{EW} = i \sum_f \bar{\psi} \gamma^\mu D_\mu \psi - \frac{1}{4} B_{\mu\nu} B^{\mu\nu} - \frac{1}{4} W_{\mu\nu}^a W^{a\mu\nu} \ , \tag{2.21}$$

with $W_{\mu\nu}^a = \partial_\nu W_\mu^a - \partial_\mu W_\nu^b - g_2 \epsilon_{abc} W_\mu^b W_\nu^c$ and $B_{\mu\nu} = \partial_\mu B_\nu - \partial_\nu B_\mu$ as the weak and hypercharge gauge fields, respectively. The non-Abelian property of EW leads to self-interaction terms of the gauge bosons in the lagrangian.

Physics gauge bosons are mixture of the gauge fields B_μ and W_μ^k:

$$\begin{aligned} W_\mu^\pm &= \frac{1}{\sqrt{2}}(W_\mu^1 \mp i W_\mu^2) \\ A_\mu &= \cos\theta_W B_\mu + \sin\theta_W W_\mu^3 \\ Z_\mu &= -\sin\theta_W B_\mu + \cos\theta_W W_\mu^3 \end{aligned} \tag{2.22}$$

the angle θ_W is known as weak angle or Weinberg's angle, and it is given by:

$$\tan\theta_W = \frac{g_1}{g_2} \tag{2.23}$$

Both neutral fields couple to the hypercharge gauge field B_μ and the third component of the weak gauge field W^3_μ, leading to a linear combination of the weak and electromagnetic currents. Unlike the $W^\pm$ boson, the Z boson couples to the two chiralities as it has contributions from both the B_μ and W^3_μ fields.

Despite the successful description of a unified weak and electromagnetic theory, the model still predicts massless $W^\pm$ and Z bosons. As mentioned before, one of the main problems of the theory is that the symmetry between the gauge bosons must be severely broken. The short range of the weak interaction indicates that the force should be mediated by a massive particle. However, inserting mass terms for the gauge bosons directly in the lagrangian would mean in a theory non-renormalisable. The spontaneous symmetry breaking introduced by the Higgs mechanism emerged as the proper solution to explain the mass generation of the gauge fields while keeping the underlying theory gauge invariant.

2.3 The Higgs boson

An important theoretical physics breakthrough after the war period was the development of renormalisation theory. In theories like quantum electrodynamics (QED) this solved the problem of infinities (eliminating them), therefore enabling calculations beyond the lowest order of approximation. The improved precision in the calculations made QED one of the most accurately confirmed theories in the history of physics. An outstanding example of this is the magnetic moment of the electron that has a relative standard uncertainty of 2.6×10^{-13}.

It was natural to assume that the same methods could be used to construct theories that describe the other fundamental interactions, i.e. the strong and the weak forces. Since QED is a gauge theory, many people believed that the other interactions should be described by gauge theories. The first such gauge theory to be developed after QED was the Yang-Mills theory [30], proposed in 1954, which was a theory based on the isospin SU(2) symmetry. The introduction of this symmetry was a natural way to bring new spin-1 fields to the theory that would explain the weak interactions. However, simply adding gauge fields would

break the symmetry and destroy many of the nice properties of gauge theories, like renormalisation. Fortunately, a novel method to introduce gauge fields, while maintaining the symmetry invariance, was develped using spontaneous symmetry breaking (SSB).

2.3.1 Spontaneous symmetry breaking

The first idea of SSB related to particle physics was published in 1961 by Y. Nambu and G. Jona-Lasinio [31][32]. In this study, they explained the SSB of chiral symmetry using a four fermion interaction to describe weak processes, requiring the existence of a zero mass pseudoscalar for symmetry consistency. Months later, J. Goldstone published [33] a simpler illustration of a SSB mechanism using a two component scalar field theory with a quartic interaction, also requiring a zero mass particle. Considering this last publication, the SSB is going to be explained as follows.

A simple lagrangian for a free complex scalar field can be written as:

$$\mathcal{L} \;=\; \partial_\mu \phi \partial^\mu \phi^\dagger - m^2 \phi^\dagger \phi \tag{2.24}$$

with the scalar field defined by two real scalar fields: $\phi = (\phi_1 + i\phi_2)/\sqrt{2}$, and m being the mass term for the field. It can be noticed that that the lagrangian is invariant under the following U(1) gauge transformation:

$$\phi' \;=\; e^{-i\alpha}\phi \tag{2.25}$$

The potential $V = m^2\phi^\dagger\phi$ is constrained from below if $m^2 > 0$, having a minimum energy state when $\phi = 0$ that corresponds to the vacuum state (illustrated in Fig. 2.3a). This specific choice would not be able to perturb the vacuum state and give mass to particles. On the other hand, if $m^2 < 0$, the potential is not constrained from below, so the vacuum state is unstable. However, in this last case the vacuum stability is recovered when a quartic interaction term is introduced to the potential, as follows:

$$V(\phi) \;=\; -\frac{m^2}{2\phi_0^2}(\phi^\dagger\phi - \phi_0^2)^2 \tag{2.26}$$

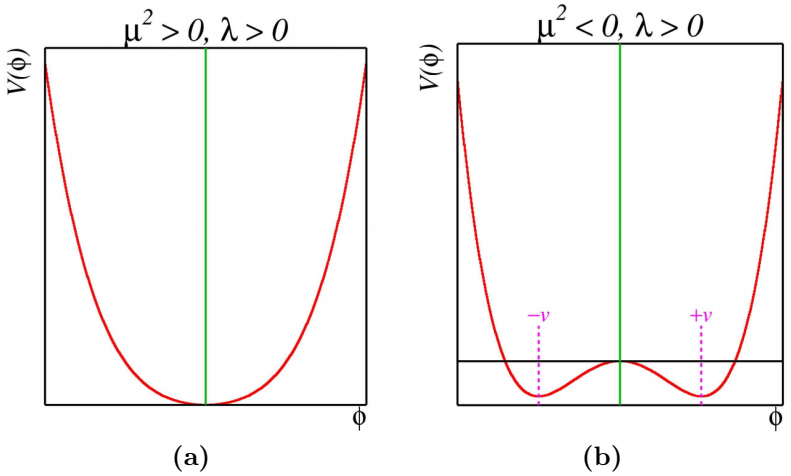

Figure 2.3 *(a) Potential with a single vacuum expectation value (b) Potential with infinite vacuum expectation values, corresponding to a theory with spontaneous symmetry breaking [34].*

When $V(\phi) = 0$ the vacuum state is:

$$\begin{aligned} |\phi|^2 &= \phi_0^2 \\ \phi_1^2 + \phi_2^2 &= 2\phi_0^2 \end{aligned}$$

Now the potential has infinite minima, all located along a circumference in the space defined by ϕ_1 and ϕ_2 (illustrated in Fig. 2.3b). It can be seen that in this case the scalar field ϕ acquires a vacuum expectation value (vev).

The new lagrangian is invariant under the U(1) gauge symmetry but the vacuum value is not, given that if a particular vacuum state is chosen a rotation would change it. When the lagrangian is symmetric under a transformation but the vacuum state is not, it is said that the symmetry has been spontaneously broken.

The vacuum state is the classical solution where there are no particles. Small perturbations around the vacuum state represent the particles. To understand their properties it is convenient to expand around the vacuum state:

$$\phi = \phi_0 + \frac{1}{\sqrt{2}}(\chi + i\psi) \tag{2.27}$$

where χ and ψ are scalar fields. The lagrangian takes the shape:

$$\begin{aligned} \mathcal{L} &= \mathcal{L}_{free} + \mathcal{L}_{int} \\ \mathcal{L}_{free} &= \frac{1}{2}\partial_\mu\chi\partial^\mu\chi - m^2\chi^2 + \frac{1}{2}\partial_\mu\psi\partial^\mu\psi \\ \mathcal{L}_{int} &= -\frac{\sqrt{2}m^2}{2\phi_0}\chi(\chi^2+\psi^2) - \frac{m^2}{8\phi_0^2}(\chi^2+\psi^2)^2 \end{aligned} \tag{2.28}$$

From the free lagrangian it can be noticed that χ is a scalar field of mass "m"and ψ is a scalar with zero mass, known as Goldstone boson.

2.3.2 Higgs mechanism

In 1962 Goldstone, Salam and Weinberg [35] proved that the SSB of a continuous global symmetry in a relativistic theory requires an associated zero-mass excitation. Weinberg commented 'Nothing will come of nothing, speak again', a quote from King Lear. This brought great disappointment to the particle physics community, since the only zero-mass particle seen in nature is the photon and there was no known mechanism to explain how the rest of the fundamental particles could gain mass.

The goal was then to find a mechanism that makes it possible for SSB to be a relativistic theory without producing massless particles. The answer to this problem was solved independently by three different groups [4–6] that used the electrodynamic lagrangian to provide an example of a gauge theory that yields a massive spin-1 particle. The analysis and some conclusions were different in these three studies. The Higgs approach (Abelian Higgs model) has been chosen in the following.

We consider the same scalar Lagrangian from Eq.2.24) but with a local U(1) gauge symmetry:

$$\phi \rightarrow \phi' = e^{-iq\theta(x)}\phi \tag{2.29}$$

As shown in Sect. 2.2.1 the local gauge invariance of the QED Lagrangian is restored by introducing photonic fields A_μ in the covariant derivative D_μ. This

leads to the following lagrangian:

$$\mathcal{L} = D_\mu \phi^\dagger D^\mu \phi - \frac{1}{4} F_{\mu\nu} F^{\mu\nu} - V(\phi^\dagger \phi) \tag{2.30}$$

where:

$$\begin{aligned} F_{\mu\nu} &= \partial_\mu A_\nu \partial_\nu A_\mu \\ V(\phi^\dagger \phi) &= \frac{m^2}{2\phi_0^2} [\phi^\dagger \phi - \phi_0^2]^2 \qquad (2.31) \\ A_\mu \rightarrow A_\mu^{'} &= A_\mu + \partial_\mu \theta \qquad (2.32) \end{aligned}$$

The minimum is obtained when $A_\mu = 0$ and the vacuum state lies again in a circumference defined by the $\phi_1 - \phi_2$ plane. If a particular vacuum state is chosen, a rotation would change it, breaking the vacuum state symmetry. Since the lagrangian was constructed to be invariant under U(1) gauge symmetry, there is a SSB of the U(1) gauge symmetry.

We consider again small perturbations around the vacuum state in order to interpret the new fields:

$$\phi^{'} = \phi_0 + \frac{h(x)}{\sqrt{2}} \tag{2.33}$$

where $h(x)$ is a real scalar field and ϕ is chosen to be real thanks to the gauge freedom. This particular choice of gauge fixing is called unitary gauge [36] [37] and has the property that the Goldstone boson dissapears from the theory. By replacing the field in the lagrangian we obtain

$$\begin{aligned} \mathcal{L} &= \mathcal{L}_{free} + \mathcal{L}_{int} \\ \mathcal{L}_{free} &= \frac{1}{2} \partial_\mu h \partial^\mu h - m^2 h^2 - \frac{1}{4} F_{\mu\nu} F^{\mu\nu} + g_1^2 \phi_0^2 A_\mu A^\mu \qquad (2.34) \\ \mathcal{L}_{int} &= g_1^2 A_\mu A^\mu (\sqrt{2}\phi_0 h + \frac{h^2}{2}) - \frac{m^2 h^2}{2\phi_0^2} (\sqrt{2}\phi_0 h + \frac{h^2}{4}) \end{aligned}$$

and a mass term for the vectorial field ($m_A^2 = 2 g_1^2 \phi_0^2$) has appeared in $\mathcal{L}_{free}$. As a consequence, the gauge boson has acquired mass. The total number of degrees of freedom before and after SSB must be the same for both Lagrangians (Eq. 2.30 and Eq. 2.34, respectively). However, the allocation of the degrees of freedom in the two cases depends on the existing fields.

- Without SSB:

  - massless A_μ: two states of polarization (2 degrees of freedom)
  - complex field: $\phi = \frac{\phi_1 + i\phi_2}{\sqrt{2}}$ (2 degrees of freedom)

- With SSB:
  - massive A_μ: three states of polarization (3 degrees of freedom)
  - real scalar field: h (1 degree of freedom)

The field that dissapears is the Goldstone boson. It is usually said that in the Higgs mechanism, the gauge boson acquires mass when it absorbs the Goldstone boson.

2.3.3 The Higgs boson in the Electroweak model

As mentioned in Sect. 2.2.3, the Higgs mechanism is introduced in the EW theory as a method to give mass to the weak vector bosons while keeping the theory renormalisable.

The fundamental gauge symmetry of the Electroweak (EW) model is SU(2)×U(1). The previous Lagrangian (Eq. 2.30) can be generalised to be invariant under this new symmetry, but given the SU(2) 2×2 matrix representation, the scalar field is constructed using two components.

$$\phi = \begin{pmatrix} \phi_A \\ \phi_B \end{pmatrix} \tag{2.35}$$

where $\phi_A = \phi_1 + i\phi_2$, $\phi_B = \phi_3 + i\phi_4$ (4 real scalar fields).

The EW lagrangian, invariant under local SU(2)×U(1) gauge transformations, and also including a scalar doublet ϕ is:

$$\begin{aligned} \mathcal{L} &= \mathcal{L}_{free} + \mathcal{L}_{int} \\ \mathcal{L}_{free} &= (D_\mu \phi)^\dagger (D^\mu \phi) - V(\phi^\dagger \phi) \\ \mathcal{L}_{int} &= -\frac{1}{4} B_{\mu\nu} B^{\mu\nu} - \frac{1}{4} W^3_{\mu\nu} W^{3\mu\nu} - \frac{1}{2} W^-_{\mu\nu} W^{+\mu\nu} \end{aligned} \tag{2.36}$$

The potential takes the shape:

$$V(\phi^\dagger \phi) = \frac{m^2}{2\phi_0^2} (\phi^\dagger \phi - \phi_0^2)^2 \tag{2.37}$$

where the vacuum fulfils:

$$\phi_1^2 + \phi_2^2 + \phi_3^2 + \phi_4^2 = \phi_0^2 \tag{2.38}$$

The scalar field ϕ transforms under SU(2):

$$\begin{aligned} \phi \rightarrow \phi^{'} &= U\phi_0 \\ U = e^{i\alpha^k\sigma^k} &= \cos\alpha\mathbb{1} + i\sin\alpha(\hat{\alpha}\vec{\sigma}) \end{aligned} \tag{2.39}$$

The SU(2) matrix U has three generators represented by the Pauli matrices σ^k. Therefore, there are three degrees of freedom available for the field ϕ. In order to simplify the vacuum state these can be fixed ($\phi_1^{'} = \phi_2^{'} = \phi_4^{'} = 0$). Then, in the chosen gauge the vacuum becomes:

$$\langle\phi\rangle \;=\; \begin{pmatrix} 0 \\ \phi_0 \end{pmatrix} \tag{2.40}$$

Under this transformation the vacuum breaks the SU(2)×U(1) symmetry but the Lagrangian remains invariant, leading to a SSB of the EW theory. We consider again small perturbations around the vacuum state in order to interpret the fields:

$$\phi \;=\; \begin{pmatrix} 0 \\ \phi_0 + \frac{h}{\sqrt{2}} \end{pmatrix} \tag{2.41}$$

where h is a real scalar field.

The interactions between the Higgs field and the gauge bosons appear after the multiplication of the scalar field with the covariant derivative. The mass terms for the gauge bosons are:

$$\begin{aligned} m_\gamma^2 &= 0 \\ m_Z^2 &= \frac{1}{2}(g_1^2 + g_2^2)\phi_0^2 \\ m_W^2 &= \frac{1}{2}g_2^2\phi_0^2 \end{aligned} \tag{2.42}$$

The photon remains massless, while the Z and $W^{\pm}$ bosons acquire a non-zero mass that is related through the coupling dependence. This parameter ρ is useful for distinguishing quantum corrections in the theory (i.e. deviations from the

tree-level value of 1):

$$\rho = \frac{m_W^2}{\cos^2\theta_W m_Z^2} \tag{2.43}$$

Then, by replacing the physical fields in the lagrangian of Eq. 2.36) we obtain:

$$\begin{aligned}
\mathcal{L} &= \mathcal{L}_{free} + \mathcal{L}_{int} \\
\mathcal{L}_{free} &= \frac{1}{2}\partial_\mu h \partial^\mu h - m^2 h - \frac{1}{4} Z_{\mu\nu} Z^{\mu\nu} + \frac{1}{2}\phi_0^2 (g_1^2 + g_2^2) Z_\mu Z^\mu - \frac{1}{4} A_{\mu\nu} A^{\mu\nu} \\
&- \frac{1}{2}[(D_\mu W_\nu^+)^* (D_\nu W_\mu^+)^*][D^\mu W^{+\nu} - D^\nu W^{+\mu}] + \frac{1}{2} g_2^2 \phi_0^2 W_\mu^- W^{+\mu} \\
\mathcal{L}_{int} &= [\frac{1}{4}h^2 + \frac{1}{\sqrt{2}} h\phi_0][g_2^2 W_\mu^- W_\mu^+ + \frac{1}{2}(g_1^2 + g_2^2) Z_\mu Z^\mu] - \frac{m^2}{\sqrt{2}\phi_0} h^3 - \frac{m^2}{8\phi_0^2} h^4 \\
&+ \frac{1}{4} g_2^2 (W_\mu^- W_\nu^+ - W_\nu^- W_\mu^+)(W^{-\mu} W^{+\nu} - W^{-\nu} W^{+\mu}) \\
&+ \frac{i}{2} g_2 (A_{\mu\nu} \sin\theta_W + Z_{\mu\nu} \cos\theta_W)(W^{-\mu} W^{+\nu} - W^{-\nu} W^{+\mu}) \\
&- g_2^2 \cos\theta_W [(Z_\mu W_\nu^- - Z_\nu W_\mu^-)(D^\mu W^{+\nu} - D^\nu W^{+\mu}) \\
&- (Z_\mu W_\nu^+ - Z_\nu W_\mu^+)(D^\mu W^{+\nu} - D^\nu W^{+\mu})^*]
\end{aligned}$$

where:

$$D_\mu W_\nu^+ = (\partial_\mu + i g_2 \sin\theta_W A_\mu) W_\nu^+ \tag{2.44}$$

Besides the already identified mass terms for the gauge bosons, there is a quadratic term in the free lagrangian ($m^2 h$) that corresponds to the mass of the Higgs boson:

$$m_H = \sqrt{2} m \tag{2.45}$$

Since the variable m is a free parameter of the SM, there is no direct prediction of the Higgs boson mass. However, if the mass is measured and the vev is known, statements about the stability of the Higgs potential can be made.

Within the interacting Lagrangian, the physical Higgs field h interacts with itself, generating self-interaction terms in the form of triplet and quartic couplings. The couplings are defined as a function of the Higgs boson mass and its vev:

$$g_{hhh} = \frac{3 m_H^2}{\sqrt{2}\phi_0} \quad , \quad g_{hhhh} = \frac{3 m_H^2}{2\phi_0^2} \tag{2.46}$$

Since these couplings only depend on the Higgs boson, the measurement of this single property can precisely determine the true nature of the Higgs boson. The possible existence of an extended scalar sector or the presence of new dynamics at higher scales should modify the Higgs self-couplings, yielding different values than the SM predictions. Information on the triple and quartic Higgs coupling can be directly obtained from final states featuring at least two and three Higgs bosons, respectively. However, the cross sections corresponding to these processes are much smaller than those from single Higgs production, due to the suppression induced by a heavier final state and an additional weak coupling. Even with the highest LHC centre-of-mass energy and the event statistics to be collected by the end of the LHC era, any meaningful extraction of quartic Higgs coupling is impossible, but the prospects to observe double-Higgs production with a further determination of the triplet Higgs coupling seems feasible under optimistic assumptions.

The interacting Lagrangian contains triple and quartic interaction terms between the Higgs field and the vector bosons. The couplings are defined as a function of the vector bosons mass and the Higgs vev.

$$g_{hVV} = \frac{m_V^2}{\sqrt{2}\phi_0} \quad , \quad g_{hhVV} = \frac{m_W^2}{2\phi_0^2} \tag{2.47}$$

There is a particular interest in the first coupling g_{hVV}, since it is the coupling of the decay channel that has been used in the study presented in this thesis ($H \to ZZ$).

So far the Higgs mechanism has provided a method to give mass to the vector bosons of the EW theory, but fermions still remain massless.

2.3.4 Fermion mass term

The Higgs field is implemented in the fermion sector by introducing Yukawa terms. These terms are included in the Higgs-fermion interacting lagrangian:

$$\mathcal{L}_{Yf} \;=\; -g_f(\bar{\psi_L}\phi\psi_R + \bar{\psi_R}\phi^\dagger\psi_L) \tag{2.48}$$

where g_f is the dimensionless Yukawa coupling for a given fermion, and ψ_L, ψ_R are the left-handed doublet and right-handed singlet fermion fields, respectively. Using the unitary gauge to expand the Higgs potential around the minimum, we

obtain:

$$\begin{aligned}\mathcal{L}_{Yf} &= -g_f(\bar{\psi_L}\psi_R + \bar{\psi_R}\psi_L)(\phi_0 + \frac{h(x)}{\sqrt{2}}) \\ \mathcal{L}_{Yf} &= -g_f\phi_0(\bar{\psi_L}\psi_R + \bar{\psi_R}\psi_L) - \frac{g_f h(x)}{\sqrt{2}}(\bar{\psi_L}\psi_R + \bar{\psi_R}\psi_L) \end{aligned} \tag{2.49}$$

The first term represents the fermion mass $m_f = g_f\phi_0$, and the second term the interaction between the fermion and the Higgs boson, known as Yukawa term. The same method holds for leptons and quarks.

2.3.5 The observation of the Higgs boson at the LHC

The Higgs boson was discovered in 2012, by two independent experiments, ATLAS [7] and CMS[8], at the Large Hadron Collider (LHC). After the observation, a number of important studies have been made in order to understand the properties of the particle: mass, spin and parity, total decay width, and couplings to the SM particles. These are detailed as follows:

1. Mass: the Higgs boson mass is a free parameter of the theory, but in order to achieve stability in the vacuum state, it is delimited by the SM in a wide mass range. The combined measurement of the Higgs boson mass, by the ATLAS and CMS collaborations [9] using the proton-proton collision data collected in 2011 and 2012, gives $m_H = 125.09 \pm 0.21(\text{stat.}) \pm 0.11(\text{syst.})$ GeV. This value is within the mass range permitted by the SM, while also being favoured by beyond SM (BSM) theories such as super-symmetry (SUSY).

2. Spin and parity: the SM Higgs boson is a scalar particle (spin 0) with CP-even parity ($J^P = 0^+$). The ATLAS [38] and CMS [10] collaborations excluded several alternative spin and parity hypotheses in favour of the SM Higgs boson predictions at a higher than 99.9% confidence level.

3. Total decay width: the Higgs boson is an unstable particle that decays almost instantaneously into other particles. The total decay width is defined as the particle decay probability per unit time, corresponding to the reciprocal of its average decay lifetime. The SM Higgs boson has a narrow total width, approximately 1,000 times smaller than the current detector resolution. The ATLAS Collaboration [11], using data collected in 2011

and 2012, excluded values of approximately 3,000 times the SM prediction. However, by employing a novel indirect-measurement technique to set an exclusion limit on the total width by using non-resonant Higgs boson events, the ATLAS and CMS collaborations have improved the measurement by constraining the total decay width to be smaller than 10 times the SM value hypothesis [1]. This study is the main topic of this thesis and is going to be discussed in Chapter 6.

4. Couplings: the Higgs boson couples to the rest of the SM elementary particles with a strength proportional to their masses. The ATLAS and CMS collaborations performed independent measurements of the Higgs couplings to vector bosons and fermions. The results of these measurements were combined in [12] this year. The couplings with vector bosons are found to be compatible with those expected from the SM within an approximate 10% uncertainty, while in the case of the heavier SM fermions (the top and bottom quarks, and the τ lepton) the uncertainty is of the order 15-20%. The precision of the current measurements therefore still leaves room for deviations of the Higgs boson couplings to the vector bosons and fermions from the SM predictions, and BSM scenarios can only be weakly constrained.

So far, the measurements of the properties of the new particle have strengthened the assumption that the observed particle is indeed the Higgs boson predicted by the SM. For instance, Figure 2.4 shows the agreement of the SM prediction with respect to the strength of the couplings between the Higgs boson and gauge bosons and fermions. The coupling strength of the Higgs boson with the rest of the SM particles is predicted by the theory by looking at the production and decay modes. In order to fully verify the SM hypothesis, all possible channels need to be measured and compared against the SM predictions. The Higgs boson couples directly to all massive SM particles, with a coupling strength that is proportional to the mass of the particle. Couplings to massless gluons and photons are only possible with the help of intermediate loops that contains virtual massive particles. The coupling strength for gauge bosons and fermions scales linearly and quadratically, respectively.

$$g_{HVV} \propto \frac{m_V^2}{\phi_0} \quad , \quad g_{Hff} \propto \frac{m_f}{\phi_0} \tag{2.50}$$

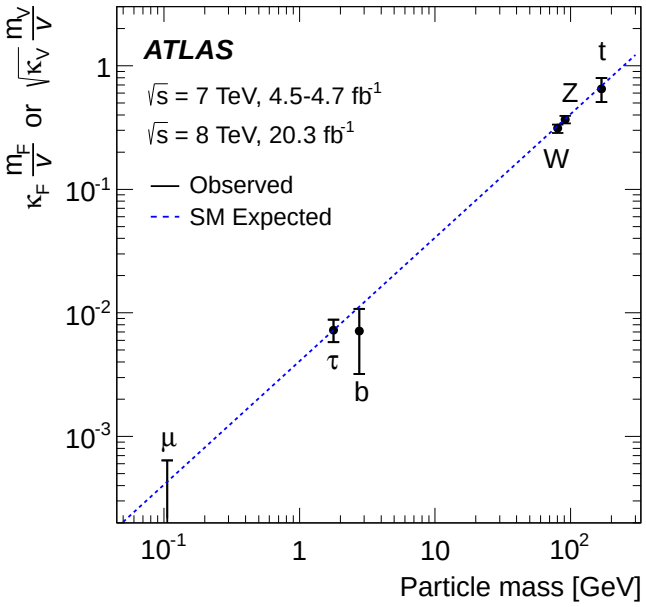

Figure 2.4 *The Higgs boson coupling strength scale factors to bosons and fermions as a function of the particle mass, assuming a SM Higgs boson with a mass of 125.36 GeV by the ATLAS Collaboration [39]. The dashed line indicates the theoretical predictions of the mass dependence for the SM Higgs boson, and the data points correspond to the experimental measurements. The couplings κ_F and κ_V are defined as event yields for fermions and vector bosons, respectively, normalized to the SM predictions.*

Therefore, the Higgs boson production cross section depends mostly on the heaviest particles, such as the top quark. However, even if the mass of the decaying particle plays a strong role in the decay rate, it is not the only kinematic ingredient that contributes to the process.

2.3.6 Higgs boson production

There are four production mechanisms of the SM Higgs boson that dominate at the LHC. These are represented by the Feynman diagrams of Figure 2.5. The production cross section of these processes in proton-proton collisions for a Higgs boson of mass $m_H = 125$ GeV at a centre-of-mass energy range relevant for the LHC is shown in Figure 2.6a, with the relative fractions of these contributions at a centre-of-mass energy of 8 TeV illustrated in Figure 2.6b.

The Higgs boson is mainly produced via the gluon-gluon fusion (ggF) production

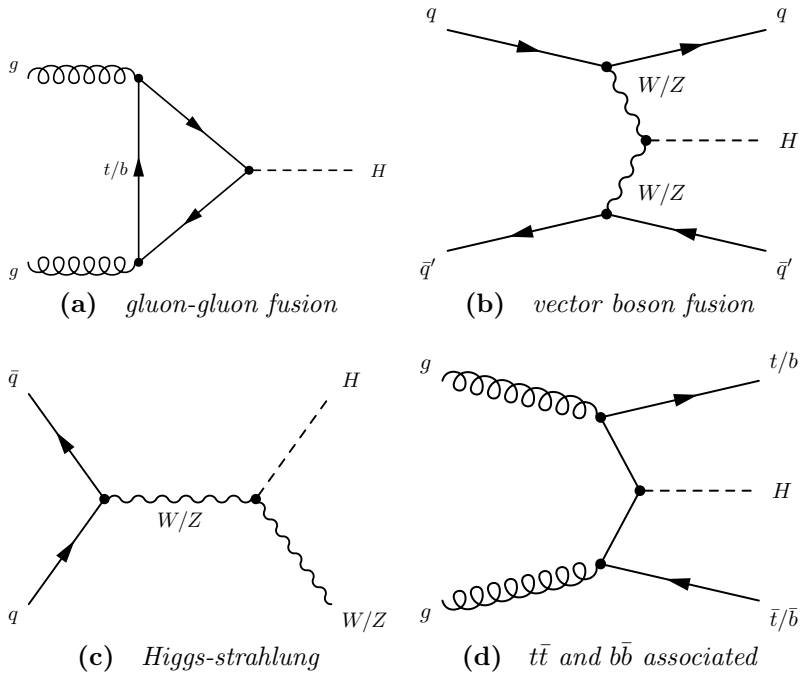

(a) *gluon-gluon fusion* **(b)** *vector boson fusion*

(c) *Higgs-strahlung* **(d)** *$t\bar{t}$ and $b\bar{b}$ associated*

Figure 2.5 *Feynman diagrams of the dominant Higgs boson production mechanisms at the LHC.*

mode at the LHC (Figure 2.5a). This process consists of two merging gluons that interact via a quark loop, resulting in the creation of a Higgs boson. Given that the cross section is proportional to the squared Yukawa coupling, the production is mainly mediated by virtual top quark loops, while other quarks are highly suppressed. The production cross section of 19.47 ± 2.01 pb at $\sqrt{s} = 8$ TeV is know with a NNLO precision [40].

The sub-leading production mode is the vector boson fusion (VBF), that occurs approximately one order of magnitude less often than ggF, with a cross section of 1.6 ± 0.04 pb at $\sqrt{s} = 8$ TeVwith a NNLO precision [40]. This process consists of two scattered quarks that radiate two vector bosons ($W^{\pm}$ or Z) which merge and create a Higgs boson (Figure 2.5b). The scattered quarks undergo a large momentum transfer, forming two hard jets in the forward and backward regions of the detector, while gluon radiation in the central region is highly suppressed. This distinct property is useful for the identification of the process in a clean way.

The Higgs boson can also be produced in association with a W or Z boson (VH), also know as "Higgs-strahlung", being the third most likely production mode at the LHC. The production cross sections for the mediated $W^{\pm}$ and Z bosons are 0.7 ± 0.02 and 0.42 ± 0.02, respectively, at $\sqrt{s} = 8$ TeV with a NNLO precision [40]. A vector boson ($W^{\pm}$ or Z) is produced through $q\bar{q}$ annihilation

which then radiates a Higgs boson (Figure 2.5c). This production mechanism is suppressed with respect to the previous processes because of energy conservation requirements related to the production of a stable massive intermediate vector boson, relatively weak production coupling, and the fact that the anti-quark is originated from a lower interaction probability sea quark. However, due to the advantage of the clear experimental signature of a leptonically decaying vector boson, a further analysis of Higgs decaying to high-statistics and high-background channels (such as a pair of bottom quarks) becomes feasible.

Finally, the Higgs boson can be produced in association with a top quark (ttH) and bottom quark (bbH) pairs. These processes are suppresed by two orders of magnitude compared to ggF. The ttH and bbH production cross sections are 0.13 ± 0.02 and 0.2 ± 0.03 at $\sqrt{s} = 8$ TeV with a NLO precision [40], respectively. The cross section is surprisingly higher for the bbH production mode, given that the probability of producing a smaller mass particle is higher. However, the bbH production is overwhelmed by low-energy multijet background, which is the reason that this channel has not being studied experimentally so far. Both production modes comprise a quark (top or bottom) pair production through gluons and a Higgs boson boson radiated from a virtual quark (Figure 2.5d). The ttH cross section has the strongest dependence on the centre-of-mass energy, as seen in Figure 2.6a, leading to almost five times larger value at $\sqrt{s} = 14$ TeV. Measuring the ttH mode is of particular interest because only this production process allows for a direct measurement of the top quark Yukawa coupling to the Higgs boson. As with the VH production mode, the distinct signature of the $t\bar{t}$ decay provides a relatively clean environment for the identification of the Higgs boson in high-statistics but high-background decay channels.

The contribution of each production mode to the total cross section is illustrated in Figure 2.6b.

2.3.7 Higgs boson decay

The Higgs boson is an unstable particle that decays in several modes known as "decay channels". The probability for a Higgs boson to decay into a specific channel is called branching fraction or branching ratio. Although the Higgs boson mass is not predicted by the theory, the branching fractions are predicted as a function of the Higgs boson mass. The mass region where the Higgs boson has been observed has a rich contribution from several decay modes. The relevant

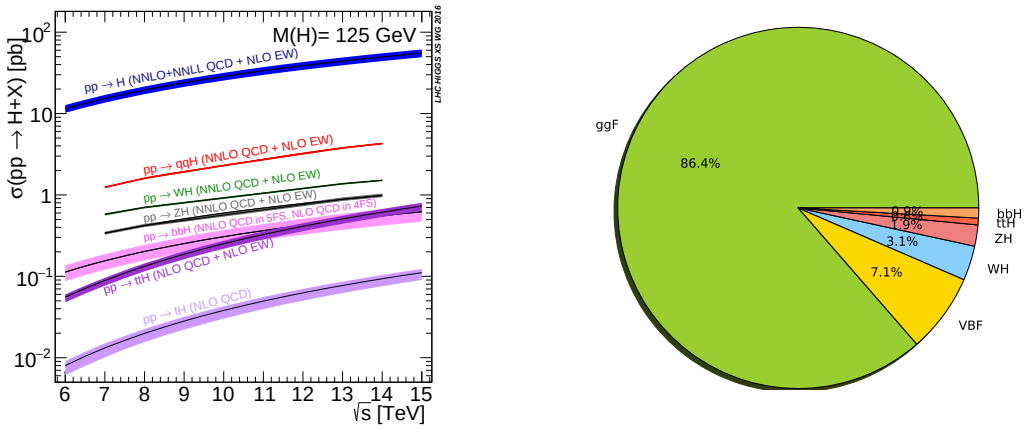

(a) **(b)**

Figure 2.6 *(a) Production cross section of a SM Higgs boson with mass m_H = 125 GeV as a function of the centre-of-mass collision energy [40] (b) Relative fractions of various channels in the production cross section of a SM Higgs boson with mass m_H = 125 GeV at $\sqrt{s} = 8$ TeV.*

branching fractions for Higgs boson masses between 120 GeV and 130 GeV are shown in Figure 2.7a, while the branching fractions for a Higgs boson with mass $m_H = 125$ GeV is illustrated in Figure 2.7b.

The predominant decay mode of the Higgs boson is to a pair of bottom quarks, with a branching fraction of roughly 57%. However, since the final state is affected by an overwhelming multijet background which can easily mimic the signal, this decay channel is extremely challenging to reconstruct. Therefore, we search for $H \to b\bar{b}$ produced in association with vector bosons, which provide a clean signature through their leptonic decays. This decay channel has not been found yet.

The sub-leading decay mode is to a pair of opposite-charge $W^{\pm}$ bosons. Given that the Higgs boson invariant mass is smaller than $2\,m_W$, one of the $W^{\pm}$ bosons is produced off-shell, and the process is called an off-shell Higgs decay. The $W^{\pm}$ boson is not a stable particle either, so experimental analyses reconstruct it through its decays into QCD jets, leptons and neutrinos. Although the $H \to W^{\pm}W^{\mp}$ decay mode did not contribute to the 2012 Higgs boson discovery, the ATLAS collaboration announced a 6.5σ observation [41] last year, and the CMS collaboration reported a clear evidence of 4.7σ [42] for this decay.

Since the tau is the most massive lepton, the main Higgs leptonic decay mode is to a pair of taus, reaching roughly a branching fraction of 6.3%. This decay

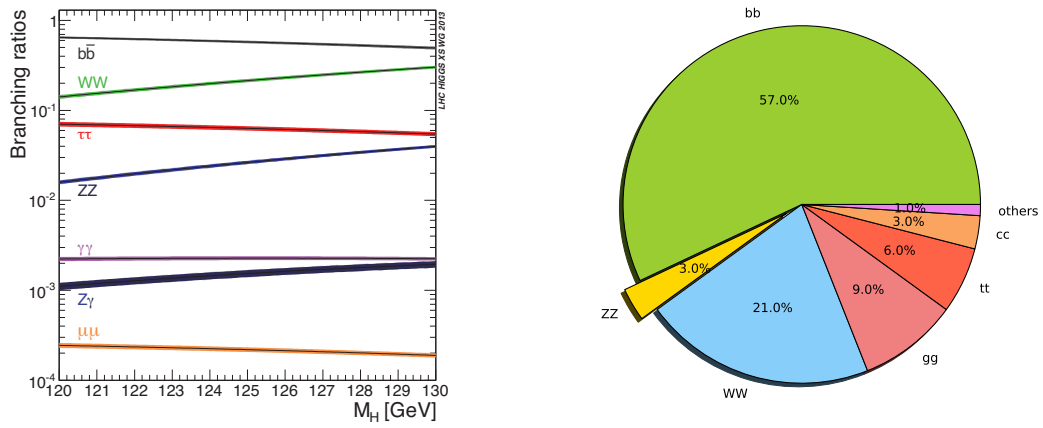

(a) **(b)**

Figure 2.7 *(a) Branching fractions of SM Higgs boson decays for a mass range between 120 GeV and 130 GeV [40] (b) Branching fractions of SM Higgs boson decays with mass $m_H = 125$ GeV.*

mode is also the most promising channel for the measurent of the Higgs boson coupling to fermions, so establishing this measurement is essential. Like the $W^{\pm}$ boson, the τ lepton is not a stable particle but it decays to lighter leptons and hadrons (mostly pions). The experimental reconstruction involves hadronic and leptonic final states. The first evidence of this channel has been reported by the LHC experiments [42, 43].

Despite the relatively small branching fractions of the ZZ and $\gamma\gamma$ decay modes of 2.6% and 2.3%, respectively, the search in these two channels comprised the leading contribution to the Higgs boson discovery [7, 8]. The very clean signature and excellent mass resolution of pairs of photons in $H \to \gamma\gamma$ and four leptons in $H \to ZZ^* \to 4\ell$ led to the discovery and precision measurement of the Higgs properties. Just like in the $W^{\pm}W^{\pm}$ channel, one of the Z bosons has to be produced off-shell. The $H \to ZZ^* \to 4\ell$ is the so-called "golden" channel with a signal to background ratio two orders of magnitude higher than the $H \to \gamma\gamma$ channel. More details about the $H \to ZZ^* \to 4\ell$ channel are given in Chapter 5, which comprises the main topic of this thesis.

Finally, the $Z\gamma$ and $\mu\mu$ are the two decay modes with smaller branching fractions of approximately 0.02%. However, since the signature of both channels is extremely clean (especially in the $\mu\mu$ case), it is expected under optimistic assumptions that they are going to be experimentally acessible during the LHC era.

2.3.8 Total decay width

The lifetime τ of a particle is not a discrete variable, given that the decay is a probabilistic process. The probability per time unit of a particle to decay is called decay width Γ, and it is given by the decay golden rule:

$$d\Gamma = \frac{|\mathcal{M}|^2}{2m_1}(2\pi)^4\delta^{(4)}(p_1 - p_2 - \ldots - p_n)\frac{d^3p_2}{(2\pi)^3 2E_2}\frac{d^3p_3}{(2\pi)^3 2E_3}\cdots\frac{d^3p_n}{(2\pi)^3 2E_n} \quad (2.51)$$

providing the probability of a particle to decay by taking into account the kinematics of the decaying particle and its final decay channels. In general, a particle can decay in several modes. For each one of these modes the partial decay width can be calculated using the previous equation. The total decay width is equals to the sum of the partial decay widths.

$$\Gamma_{total} = \Gamma_{b\bar{b}} + \Gamma_{\tau\tau} + \ldots \quad (2.52)$$

The decay lifetime τ corresponds to the reciprocal of the decay width Γ; the faster the particle decays, the larger its decay width.

$$\tau = \frac{1}{\Gamma} \quad (2.53)$$

For stable particles (like the electron) the lifetime is infinite, while for particles like the Higgs boson the lifetime is relatively small because there are many decay channels available. If the lifetime of a particle is small, the Heisenberg principle states that its mass m is uncertain:

$$\begin{aligned} \Delta t \times \Delta m &\sim \frac{h}{2\pi} \\ \frac{1}{\Gamma} \times \Delta m &\sim \frac{h}{2\pi} \\ \Delta m &\sim \Gamma \end{aligned} \quad (2.54)$$

The Heisenberg principle is able to relate the uncertainty on the mass with the decay width Γ of the particle. For example, the Z boson has a mass of $\sim$91.2 GeV and a width of $\sim$2.5 GeV, whereas the Higgs boson has a mass of $\sim$125.5 GeV and a width of $\sim$4.2 MeV. These numbers shows that the Higgs boson decays $\sim$500 times slower than the Z boson, hence its mass is much better defined.

2.4 Matrix Element

Experimental analyses try to utilise as much information as possible from the final state under study by using multivariate methods (MVA), such as the matrix element method [44]. These MVAs use the full kinematic information of the event to calculate the probability that an observed event is originated from a specific hard scattering process, and decays to a certain final state described by the transition matrix element.

The procedure involves the calculation of the probability density function (pdf) of an event measured in the detector to be consistent with a certain theoretical hypothesis. The pdf for a given event, assuming that its kinematics (Y) has been perfectly measured, is given by integrating over the normalized differential cross-section:

$$\int_{Y\in\Phi} pdf_i(y)dy = \frac{1}{\sigma_i}\int_{\sigma_i(Y)} d\sigma_i(y) \tag{2.55}$$

where it is assumed that Y is contained from the parton-level phase space of the initial and final states y with volume $\Phi = \int dy$. Then, the pdf $pdf_i(y)$ is defined as follows:

$$pdf_i(y)dy = \frac{1}{\sigma_i}\frac{d\sigma_i(y)}{dy} \tag{2.56}$$

In a more realistic scenario, all the physics objects are measured in an experiment with a finite detector resolution that must be taken into account. The detector resolution and bias of the observed kinematics is folded in the calculation by using transfer functions $W(y|x)$ to convolute the differential cross-section. Each object related to a detector component response has an expected value x given the parton level description y:

$$\begin{aligned} pdf_i(x) &= \int pdf_i(y)W(y|x)dy \\ &= \frac{1}{\sigma_i}\int d\sigma_i(y)W(y|x) \end{aligned} \tag{2.57}$$

In order to optimise the identification of the kinematic process under study, the initial and final state particles must be well defined. At the LHC, partons are responsible for the initial state interactions. The phase space of a hard-scattering process is defined by the four-momentum of the two initial partons, q_1 and q_2,

and the four-momentum p_i of the final state N particles.

$$y = (q_1, q_2; p_1, p_2, \ldots, p_N) \tag{2.58}$$

Given that the flavour and momentum of the parton inside the colliding proton cannot be predicted directly, due to the non-perturbative nature of QCD, the parton distribution functions $PDFs$ (explained in Section 2.2.2) for the initial state partons, $f(p_1, Q^2)$ and $f(p_2, Q^2)$ (where q_1 and q_2 are the fractions of longitudinal momentum of the proton carried by each parton), must be included in the full integration:

$$pdf_i(x) = \frac{1}{\sigma_i} \sum_{\text{flavours}} \int dq_1 dq_2 f(q_1, Q^2) f(q_2, Q^2) d\hat{\sigma}_i(y) W(y|x) \tag{2.59}$$

The differential cross-section could depend on several parameters α_j of the theoretical model of interest, as well as the transfer functions can depend on model parameters β_k of instrumental nature. These parameters are included in Equation 2.59, taking also a specific quark color:

$$pdf_i(x|\alpha_j, \beta_k) = \frac{1}{\sigma_i(\alpha_j)} \int dq_1 dq_2 f(q_1) f(q_2) d\hat{\sigma}_i(y|\alpha_j) W(y|x, \beta_k) \ , \tag{2.60}$$

where the experimental and theoretical parameters are modeled by a Gaussian shape when the resolution is non negligible.

The partonic cross section $\hat{\sigma}_i$ is calculated from the matrix element of the hard scattering process according to Fermi's Golden Rule.

$$\hat{\sigma} = \frac{(2\pi)^4}{4[(p_{q_1} \cdot p_{q_2})^2 - m_{q_1}^2 m_{q_2}^2]^{1/2}} \int |\mathcal{M}_{fi}|^2 d\Phi_N, \tag{2.61}$$

with:

$$d\phi_N(q_1 + q_2; p_1, p_2, \ldots, p_N) = \delta^4(q_1 + q_2 - \sum_{i=1}^{N} p_i) \prod_{i=1}^{N} \delta(p_i^2 - m_i^2) \frac{d^4 p_i}{(2\pi)^3} \tag{2.62}$$

where $\mathcal{M}_{fi}$ is the transition matrix element that describes the fundamental physics from the initial and final state particles, while Φ_N is the density of states that contains the kinematics and momentum conservation considered in the process. The differential partonic cross-section is directly proportional to the squared Lorentz-invariant transition matrix element of the process and can be

calculated by using:

$$d\hat{\sigma}_i(y|\alpha) = \frac{(2\pi)^4}{4[(p_{q_1}\cdot p_{q_2})^2 - m_{q_1}^2 m_{q_2}^2]^{1/2}} \int |\mathcal{M}_i(y|\alpha)|^2 d\Phi_N(y), \quad (2.63)$$

Finally, this can be included in Equation 2.60 in order to integrate numerically over the entire phase space of the initial and final state particles to obtain the pdf:

$$\begin{aligned} pdf_i(x|\alpha_j,\beta_k) &= \frac{(2\pi^4)}{\sigma_i(\alpha_j)} \int d\Phi_N(y) f(q_1) f(q_2) \\ &\cdot \frac{|\mathcal{M}_i(y|\alpha_j)|^2}{4[(p_{q_1}\cdot p_{q_2})^2 - m_{q_1}^2 m_{q_2}^2]^{1/2}} W(y|x,\beta_k), \end{aligned} \quad (2.64)$$

The pdf $pdf_i(x|\alpha_j,\beta_k)$ includes kinematic information, such as masses and angular distributions, in addition to the parametrisation of the detector resolution and the event selection uncertainty. The distribution of the pdf $pdf_i(x|\alpha_j,\beta_k)$ for signal and background events are different. Therefore a discriminant can be develop to increase the sensitivity to signal events. This powerful method has been used in the main analysis of this thesis (Sect. 6) with the introduction of a matrix element discriminant.

Chapter 3

The ATLAS detector and the LHC

The main objective of a hadron collider, such as the LHC, is to discover new physics by colliding beams against each other at high energies. For instance, one of the main motivations for designing and building the LHC was to enable the discovery of the predicted Higgs boson for masses up to 1 TeV. A rich research programme is being carried out by seven detectors along the beam circle. There are two general-purpose detectors: ATLAS [45] (A Toroidal LHC Apparatus) and CMS [46] (Compact Muon Solenoid), a heavy flavour physics detector LHCb [47] (Large Hadron Collider beauty), a heavy ion detector ALICE [48] (LArge Ion Collider Experiment), a detector that measures the neutral particle flux in the forward region LHCf [49] (LHC forward), a detector that measures the total proton-proton cross section TOTEM [50] (TOTal Elastic and diffractive cross section Measurement), and a detector that looks for magnetic monopoles MoEDAL [51] (Monopole and Exotics Detector at the LHC).

The analysis presented in this thesis is based on collision data collected by the ATLAS detector. The data is used to reconstruct the particles emerging from the proton-proton collisions, taking place at the centre of the ATLAS detector. Six different subdetectors arranged in layers around the collision point record the paths, momentum, and energy of the particles, allowing them to be individually identified. A strong magnetic system bends the paths of charged particles so that their momentum can be measured.

The following chapter describes the main characteristics of the LHC and the ATLAS detector. Each component of the ATLAS detector is discussed, with an explanation of its role in identifying the the stable particles in the events of

interest for this thesis

3.1 The Large Hadron Collider

The Large Hadron Collider [52] is the most powerful and largest particle collider in the world. It is located at CERN, on the French-Swiss countryside near Geneva. It is a circular proton and heavy ion collider with a 27 km circumference, which was built in the former tunnel of the Large Electron-Positron Collider (LEP) [53], approximately 100 m underground. Is is designed to collide proton beams at a centre of mass energy of $\sqrt{s} = 14$ TeV and lead-ions at $\sqrt{s} = 2.76$ TeV. To achieve such high collision energies, the LHC depends on a long pre-accelerator chain which is schematized in Figure 3.1.

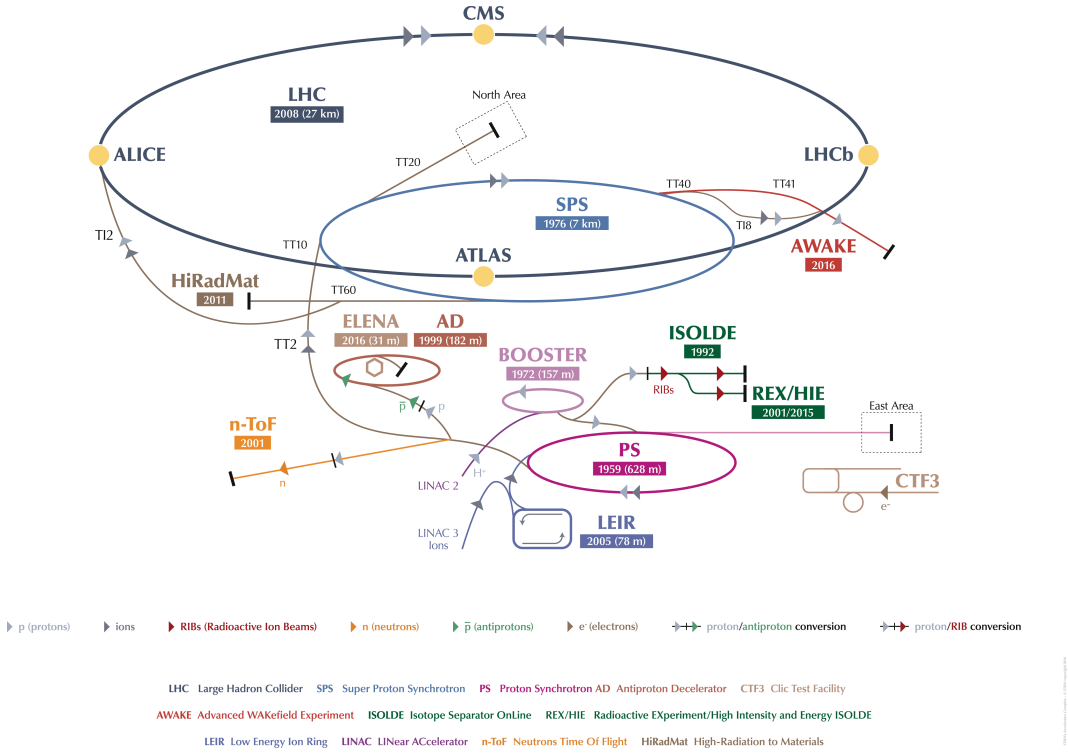

Figure 3.1 *Diagram of the LHC accelerator complex, where the smallest rings are used in a chain to help boost the particles for their injection to the LHC. The main four experiments are shown in the LHC ring [54].*

In proton-proton colliding mode, hydrogen atoms are stripped of their electrons, with the remaining protons getting accelerated in the Linear Particle Accelerator (LINAC2) to an energy of 50 MeV. The protons are then injected into the circular

Proton Synchrotron Booster (PSB) which increases their energy to 1.4 GeV. The protons are passed to the Proton Synchroton (PS) and Super Proton Synchroton (SPS) reaching an energy of 25 GeV and 450 GeV, respectively. In a last step, the two beams of proton are injected into the two beam pipes of the LHC in opposite directions. Inside these beam pipes there is an ultra-high vacuum of 10^{-10} mbar in order to avoid contamination from gas particles. The beams are accelerated by radio frequency cavities along the beam pipes to energies up to 7 TeV per beam. The proton beams are kept on their circular trajectory by 1232 superconducting dipole magnets with field strengths of up to 8.4 T. The beams are focused and stabilised in their trajectory by 400 superconducting quadrupole magnets and their shapes are maintained without distortions by higher order magnets. The superconducting state is achieved by cooling down the structure to 1.9 K by more than 96 tonnes of superfluid helium.

3.2 The ATLAS Detector

The ATLAS detector is one of the two multipurpose detectors located at the LHC. It is designed to search for multiple physics signatures, being suitable for both discoveries of new particles and precision studies of known processes. It can identify a large spectrum of transversing particles, measuring tracks and energies with high precision. Due to the high interaction rate of LHC proton collisions, the ATLAS detector was constructed to to deal with high track multiplicities in a very challenging environment. Its design follows the common onionskin structure of particle detectors at colliders, covering almost the full solid angle using cylindrical nested arrangements around the interaction point, and a symmetric forward-background end-cap. ATLAS is the largest detector at the LHC, around 45 m long, with a 25 m height, and a weight of approximately 7000 tonnes. The main components are the sub-detectors, arranged according to the cylindrical "barrel"and endcaps configuration and the magnets, as illustrated in Figure 3.2.

3.2.1 The ATLAS coordinate system

The ATLAS detector is described by a right-handed cartesian coordinate system (x, y, z) with its origin at the nominal interaction point (IP). The x-axis is

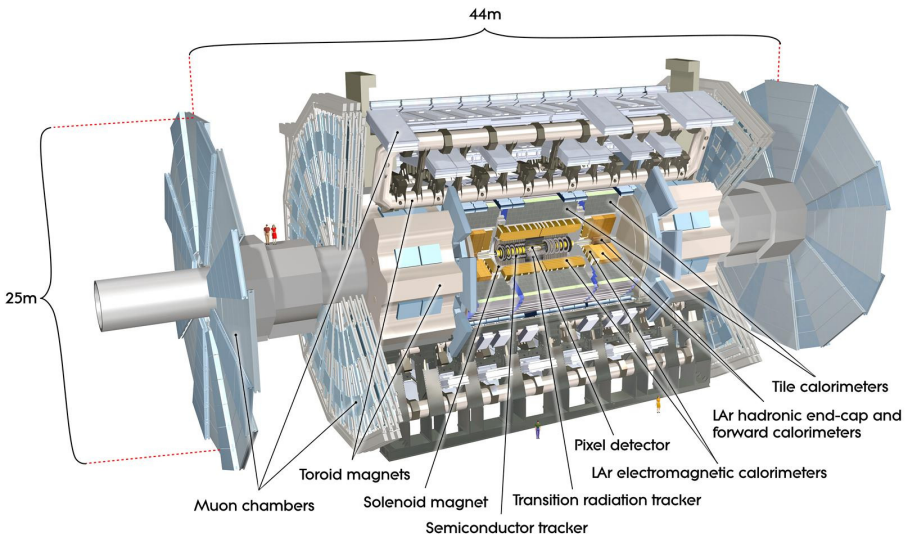

Figure 3.2 *Schematic drawing of the ATLAS detector and its components [45].*

defined pointing towards the centre of the LHC ring, the y-axis points upwards looking from the beam axis, and the z-axis is defined along the beam direction. Spherical coordinates (r, θ, ϕ) are used to describe the transverse plane, where ϕ is the azimuthal angle defined in the x–y plane and the beam z-axis while θ is the longitudinal angle defined in the r–z plane with $r = \sqrt{x^2 + y^2}$. Highly relativistic particles are conveniently described by the pseudorapidity η, which is defined in terms of the longitudinal angle:

$$\eta = -\ln\left[\tan\left(\frac{\theta}{2}\right)\right] \tag{3.1}$$

The pseudo rapidity is a measure of the longitudinal angle against the beam line, that is related to the momentum of the outgoing particle. The relation between η and ϕ is illustrated in Figure 3.3. A particle with a large value of η is going to be found close to the beam line (also known as "forward direction"). The coordinates ϕ and η define a phasespace element that is invariant under Lorentz transformation, with the 2D distance given by:

$$\Delta R = \sqrt{\Delta\eta^2 + \Delta\phi^2} \tag{3.2}$$

There are observables labelled as "transverse" that are projected into the x–y plane, such as the transverse momentum. The transverse momentum of a particle, p_T, is used to define objects which are likely to have originated from interactions

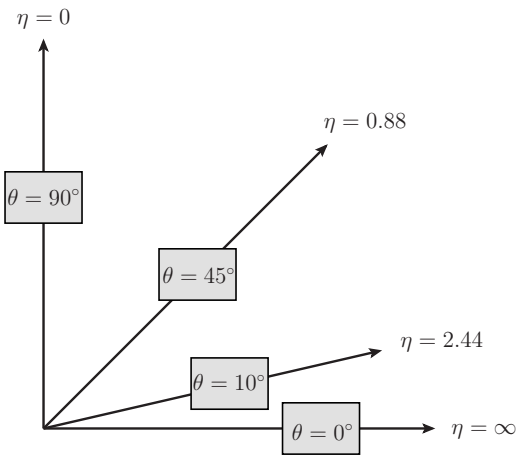

Figure 3.3 *Relation between the coordinates η and θ.*

with high momentum transfer, and it is defined as:

$$p_T = \sqrt{p_x^2 + p_y^2} = |p| \sin\theta \quad , \tag{3.3}$$

where p_x and p_y are the momentum components in the x and y direction, respectively, and $|p|$ is the magnitude of the 3D momentum vector.

3.2.2 The magnet system

The magnet system consists of one solenoid and three toroid superconducting magnets, as seen in Figure 3.4.

The central solenoid magnet surrounds the inner detector tracking system covering a distance of 5.8 m, providing a 2 T axial magnetic field along the beam axis. It has been built by design with the minimal amount of material since it is located in front of the ATLAS calorimeter and it shares the same cooling cryostat with the calorimeter, in order to minimise the energy loss of tranversing particles.

The toroidal magnet system provides the magnetic field for the muon spectrometer and it is composed by one large magnet in the barrel region and two smaller magnets in each end-cap region. Each toroid is constructed using 8 coils, assembled radially with an eight-fold symmetry, which generate strongly varying magnetic fields with a strength of up to 4.1 T.

Both magnets systesm are cooled down by liquid helium to a temperature of 4.5

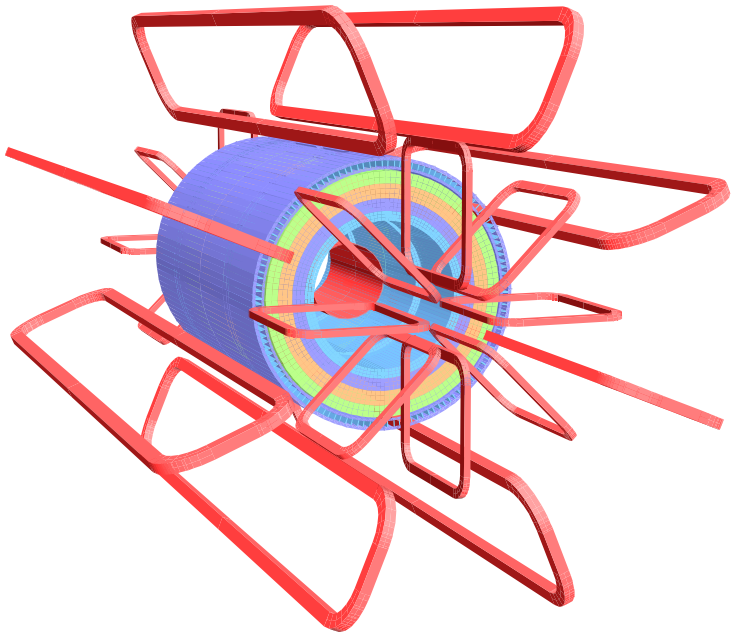

Figure 3.4 *Drawing of the ATLAS magnet system [45].*

K in to achieve superconductivity conditions.

3.2.3 Inner Detector

The Inner Detector (ID) is the part of the detector closest to the interaction point, contained within a cylinder of length 7 m and radius 1.15 m. The function of this subdetector is to enable the track reconstruction of charged particles, and therefore to provide an excellent momentum resolution and precise pattern recognition. The primary and secondary vertices are build from the tracks reconstruced in the ID. The momentum and charge of the particle can be determined by the curvature of its path, bent by the magnetic field produced by the surrounding solenoid magnet. The particle tracks are reconstructed from individual hits from many layers of the ID. A precise measurement of their tracks requires a fine granularity[1] system. The more precise, higher granularity detectors, should be located near the interaction point. Lower granularity sensors can be located, farther from the interaction point where the track density is lower. This is achieved by a three-component system consisting of the Pixel detector, the Semiconductor Tracker (SCT) and the Transition Radiation Tracker (TRT)

[1]Granularity refers to the relative size of the detector material "granule" which defines the level of detail

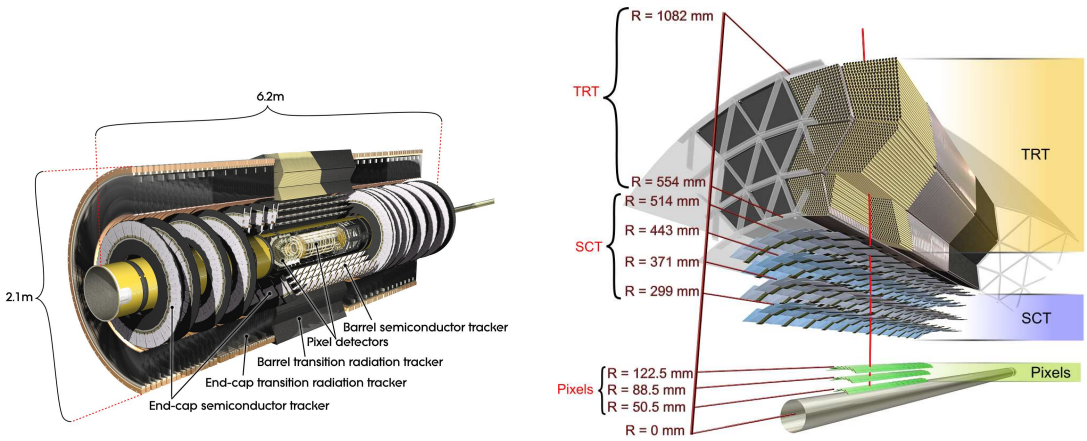

(a) *longitudinal section* **(b)** *layers of the ID*

Figure 3.5 *Drawing of the ATLAS Inner Detector configuration, showing the beam pipe and the ID subsystems: Pixel Detector, Silicon Strup Detector (SCT), and the Transition Radiation Tracker (TRT) [45].*

as illustrated in Figure 3.5.

The Pixel detector is the innermost component of the ID that consists of: three cylindrical barrel layer parallel to the beam, and three disks perpendicular to the beam lying in the forward and backward endcap regions. It has the finest granularity of the ID, having 80 million channels (or pixels) that are arranged into 1744 pixel modules sensors. Each module is a silicon wafer sectioned into pixel which is around 250 μm thick and consists of 47232 readout channels. The pixel system is cooled down to -10°C in order to reduce the thermal noise and to obtain an optimal intrinsic spatial resolution. During the first long shutdown of the LHC, a new beam pipe layer with smaller radius and an additional pixel layer was inserted into the detector [55]. This new Insertable B-layer (IBL) is placed at a distance of 25.7 mm to the beam line and it significantly improve the reconstruction efficiency of secondary vertices caused by heavy flavour decays.

Lying immediately outside the pixel detector is the semiconductor tracker (SCT), which consists of four cylindrical double strip layers parallel to the beam axis and nine endcap disks with radially oriented strips. The double strip layers are considerably further away from the beam line (299-514 mm), and half of their modules are arranged with respect to each other with a small stereo angle of 40 mrad to improve the spatial resolution. Each of the 15912 strip sensors has a length of 6.4 cm, bringing the SCT to a total of 6.3 million readout channels.

Both detectors are based on semiconductor sensors and cover the $|\eta| < 2.5$ region.

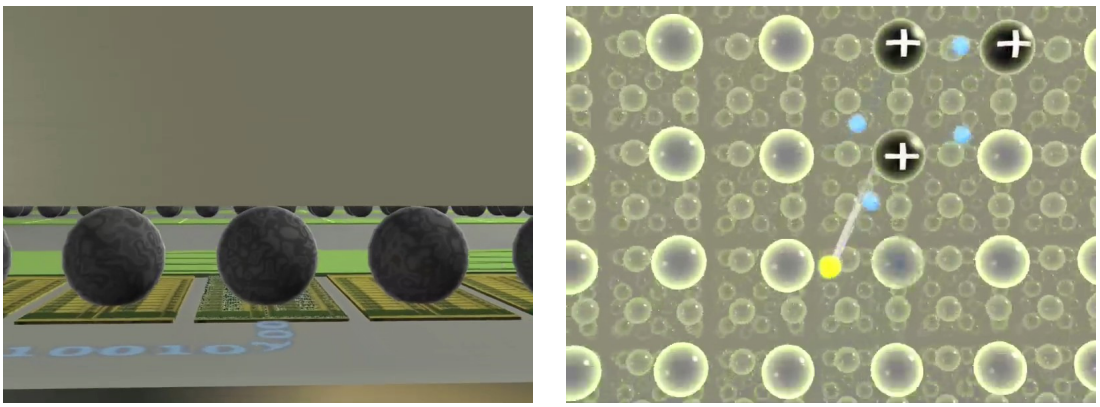

(a) *conducting spheres* **(b)** *charge particle interaction*

Figure 3.6 *Illustration of the pixel modules with its conducting spheres (Figure 3.6a), and interaction of a charged particle in the pixels (Figure 3.6b) [56].*

The hybrid detector consist of silicon sensors connected to electronics readout by bump bonding, illustrated in Figure 3.6a. When a charged particle passes through the silicon it liberates electron-hole pairs; signal that transmited to the electronics readout spheres, as seen in Figure 3.6b. The pixel sensors operate at a bias voltage of 150 V, inducing a current which it is amplified and compared against a given threshold. If this signal lies above the threshold, a hit is recorded, along with a time stamp and the location of the interacting spheres.

The last section of the ID is the TRT. It consist on 370,000 cylindrical drift tubes (straws) with a diameter of 4 mm interleaved with radiators, providing coverage up to $|\eta| < 2$. Each straw is filled with a xenon-based gas, and contains a wire in its centre. This system is called drift detector. The drift detector has a diameter of 30 μm and is made of an alloy of tungsten, gold and silver. In the barrel region the straws are parallel to the beam axis with a length of 144 cm, while in the endcap region the straws are arranged radially in wheels with a length of 37 cm. The space between the tubes is filled with polyethylene with widely varying indices of refraction, which allows the identification of charged particles by making use of the transition radiation. This radiation is emitted when relativistic charged particles cross a boundary between media with different dielectric constants, which the radiation depending on the particle's Lorentz factor γ. Since electrons are highly relativistic, an important method to distinguish electrons from hadrons can be obtained from the transition radiation. A high voltage is applied to each TRT tube in order to attract the electrons, produced by radiated photons, to the central wire. For instance, when the charged pion emits transition radiation

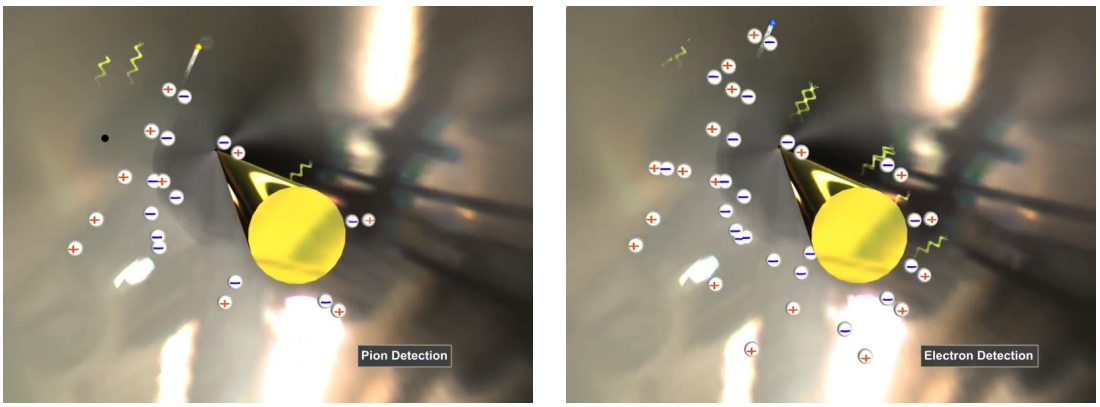

(a) *TRT pion* **(b)** *TRT electron*

Figure 3.7 *Illustration of the transition radiation of a pion (Figure 3.7a), and electron (Figure 3.7b) in the transition radiation tracker cylindrical drift tubes [56].*

it liberates photons that interact with the gas molecules freeing electrons, that are then attracted by the central wire (sketched in Figure 3.7a). If the initial particle, instead, is an electron, a larger number of photons are radiated, bringing a larger negative charge to the central wire (sketched in Figure 3.7b). The TRT straws helps also with the track identification with the reconstruction of the charged particles trajectory from the ionised gas. For the purposes of track reconstruction, this ionisation is more important than the produced transition radiation. Then, the readout of the TRT comprises two discriminators: one acting at a low threshold to detect ionisation, and a second one acting at a high threshold to identify transition radiation. In addition, a measurement of the drift-time is made which may be used to separate ionising radiation, which has a long drift-time, from transition radiation. The measurement of the TRT is around 10 times less accurate than the pixels and the SCT, but the straws are arranged in such a way that it gives a large number of hits per track to compensate for the lack of intrinsic precision.

A good quality track in the ID is reconstructed from three hits in the Pixel detector, eight hits in the SCT, and 36 hits in the TRT. The transverse momentum resolution, that is given by the Glückstern equation [57], and the track reconstruction are particularity good due to the combination of the three different systems of the ATLAS detector. For the pixel detector the resolution is calculated as:

$$\frac{\sigma(p_T)}{p_T} = \frac{\sigma(x) \cdot p_T}{0.3 \cdot L^2 \cdot B} \sqrt{\frac{720}{N+4}} \quad , \tag{3.4}$$

where $\sigma(x)$ is the spatial uncertainty, L the length of the track, B the magnetic field of the solenoid and N the number of measured track points. The ID is designed to reach a resolution of $\frac{\sigma(p_T)}{p_T} = 0.05\%$ [45].

3.2.4 Calorimeters

The ATLAS calorimeter system covers the $|\eta| < 4.9$ region, providing a precise measurement of the energy of electromagnetic and hadronic interacting particles. Electrons, photons, and hadrons are measured in the electromagnetic calorimeter, while neutral jets are measured in the hadronic calorimeter. The calorimeters consist of a cylindrical configuration in the barrel region, and a forward calorimeter (FCal) for particles in the $3.1 < |\eta| < 4.9$ region, as shown in Figure 3.8. Both are sampling calorimeters, which means that they have a structure of sheets of very dense absorber material, alternated by a highly ionisable active material that performs the energy measurement. The absorber material induces particle showers[2], whose energy deposits are measured in the active material via ionisation or scintillation. The energy of the incident particle is reconstructed from the shower remnants, being fully reconstructed only if it is completely absorbed by the calorimeter. Most of the muons produced at high energy collisions act as minimum ionizing particles (MIPs) and escape the calorimeter leaving only small traces of ionisation. The sampling design helps to reduce the size of the calorimeter, but since the energy deposited in the absorber material cannot be measured, the correct incident energy of the particle must be calculated indirectly requiring a proper calibration of the calorimeter system.

The relative energy resolution of the electromagnetic and hadronic calorimeters is given by:

$$\frac{\sigma_E}{E} = \frac{a}{\sqrt{E}} \oplus \frac{b}{E} \oplus c \quad , \tag{3.5}$$

where a (the stochastic term) is related to the sampling of fluctuations related to the particle shower. The variation comes from the number of charged particles produced from the interaction with the active layer, and the energy loss in the absorbing layers. The resolution improves according to the energy of the incident particle as $1/\sqrt{E}$. The stochastic term has been measured in ATLAS,

[2] A "particle shower" refers to the process in which a particle, after colliding against a certain material, breaks down by converting into multiple particles with less energy and momentum.

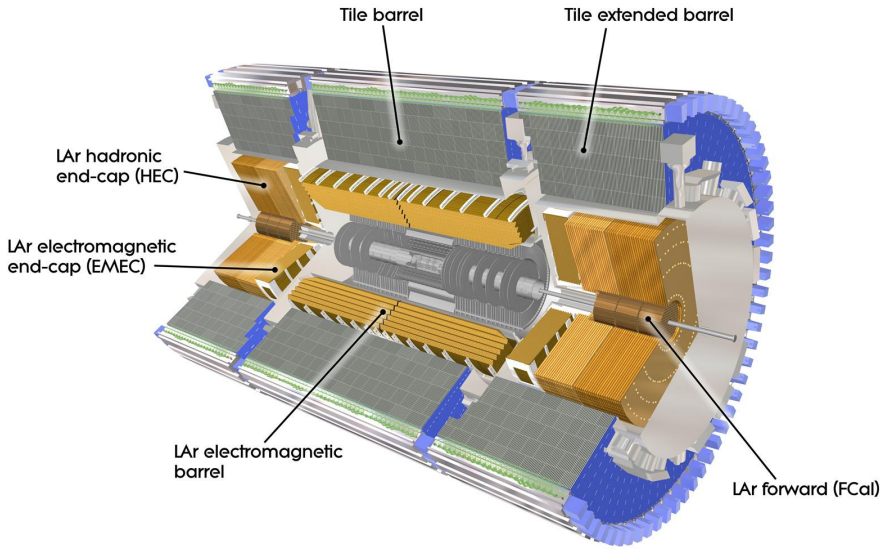

Figure 3.8 *Illustration of the ATLAS calorimeter system [45].*

giving values of: $a = (10.1 \pm 0.4)\%$ for electrons in the EM calorimeter and $a = (52 \pm 0.4)\%$ for pions in the hadronic calorimeter [45]. The second term b (the noise term) originates from the electronic noise in the readout chain. The third term c (the constant term) is independent of the particle energy, but depends on instrumental effects. Calibrations of the noise and constant term are taken into account.

Electromagnetic calorimeter

Particles that interact with the electromagnetic (EM) calorimeter are mostly electrons and photons, that create electromagnetic showers through Bremsstrahlung exchanges and electron-positron pair production. The electromagnetic barrel (EMB) and electromagnetic endcap (EMEC) calorimeters cover a range of $|\eta| < 1.475$ and $1.375 < |\eta| < 3.2$, respectively. An accordion-shaped geometry is used to ensure a complete coverage of ϕ with no cracks. The calorimeter consists of a structure of lead and stainless steel layers of 1.5 mm thick as absorbers, separated by 4 mm of space between them filled with liquid Argon (LAr) as the active material. A copper grid is immersed between the layers, acting as an electrode and measuring the energy of the particles which pass through, as illustrated in Figure 3.9a. The electromagnetic shower interacts with the molecules of the LAr and ionises the atoms, creating (negative-charge)

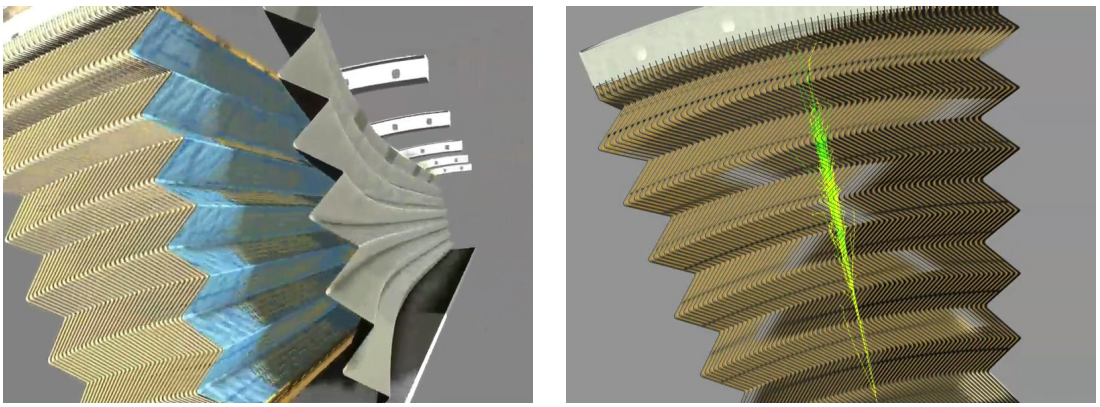

(a) *EM calorimeter* **(b)** *EM shower*

Figure 3.9 *Structure of the Electromagnetic Calorimeter (Figure 3.9a), and electromagnetic shower (Figure 3.9b) of a charged particle interacting with the absorber material of the calorimeter [56].*

electrons and positive ions (as seen in Figure 3.9b). These secondary electrons are collected by the copper electrodes to measure the energy of the original particle. Since the Bremsstrahlung radiation emitted by a charged particle is inversely proportional to the square of its mass, the electrons deposit most of their energy within the EM calorimeter. The EMB has the finest granularity of the calorimeter and is segmented in three longitudinal layers. The first layer acts as a pre-shower detector, enhacing the particle identification, providing a precise position measurement, and contributing to the energy loss due to the ID material in front of the calorimeter. The second and third layers have a refined granularity, and thus offer higher precision for the particle reconstruction. The forward region of $3.1 < |\eta| < 4.9$ is covered by the three layered Forward Calorimeter (FCal), which is designed to cope with high radiation and particle flux due to its vicinity to the beam pipe. The forward wheels are composed of a matrix of concentric copper rods and tubes as absorbers with LAr as active material between the gaps. With a total thickness of approximately 22 radiation lengths X_0, most electromagnetic interacting particles are fully contained in the EM calorimeter

Hadronic calorimeter

The Hadronic calorimeter (HAD calorimeter) consists of a Tile calorimeter in the barrel region and a LAr calorimeter in the hadronic endcap (HEC) and forward regions. The Tile calorimeter is a sampling calorimeter that uses steel as absorber and scintillating tiles as active material, as observed in Figure 3.10a.

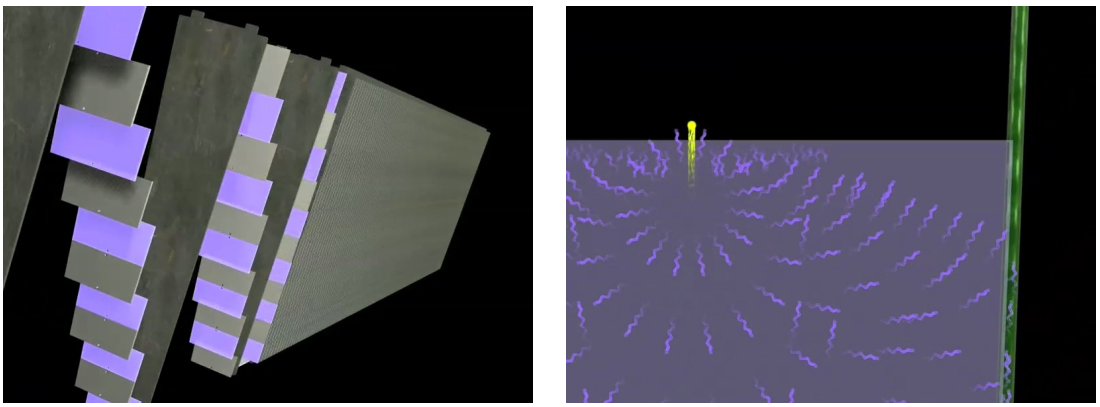

(a) *scintillating tiles* **(b)** *hadronic shower*

Figure 3.10 *Steel scintillating tiles of the Tile calorimeter (Figure 3.10a), and hadronic shower (Figure 3.10b) of a hadron interacting with the atomic nuclei of steel that produced photons upon contact with the scintillating tiles, in the Hadronic calorimeter [56].*

It is composed of one barrel and two extended endcaps, with all of them divided azimuthally in 64 modules, covering the $|\eta| < 1.7$ range. The interaction of high energy hadrons with the atomic nuclei of steel leads to the production of a shower of particles, producing photons upon contact with the scintillating tiles (as seen in Figure 3.10b). Optical fibers carry the photons produced by the scintillating tiles to photomultipliers in order to measure the deposited energy. Since the scintillating tiles get damaged when they are exposed to extreme radiation as in the HEC and forward regions, the sampling calorimeter components in these regions are based in copper. The HEC is a LAr calorimeter with copper as absorber that covers the $1.5 < |\eta| < 3.2$ range. It consists of two wheels with four layers in each endcap. The Forward calorimeter is integrated into the endcap cryostats to reduce the radiation backgound level in the muon spectrometer. It consists of three modules, with two of them using tungsten instead of copper as the absorber material.

3.2.5 Muon Spectrometer

The muon spectrometer (MS) is the outermost component of the ATLAS detector that is designed to measure muons tracks, in addition to the ID. The MS extends over a large radius of approximately 4 m $< r <$11 m, making up most of the volume of the ATLAS detector. The muon momentum is measured from the deflection of muon tracks within the magnetic field of up to 1 T provided by: the

large barrel toroid in $|\eta| < 1.4$, the two smaller endcap magnets in $1.6 < |\eta| < 2.7$, and by a combination of both fields in the transition region of $1.4 < |\eta| < 1.6$. The MS is designed to reach a resolution of $\frac{\sigma(p_T)}{p_T} = 10\%$ at p_T= 1 TeV [45]. The various components of the MS are shown in Figure 3.11.

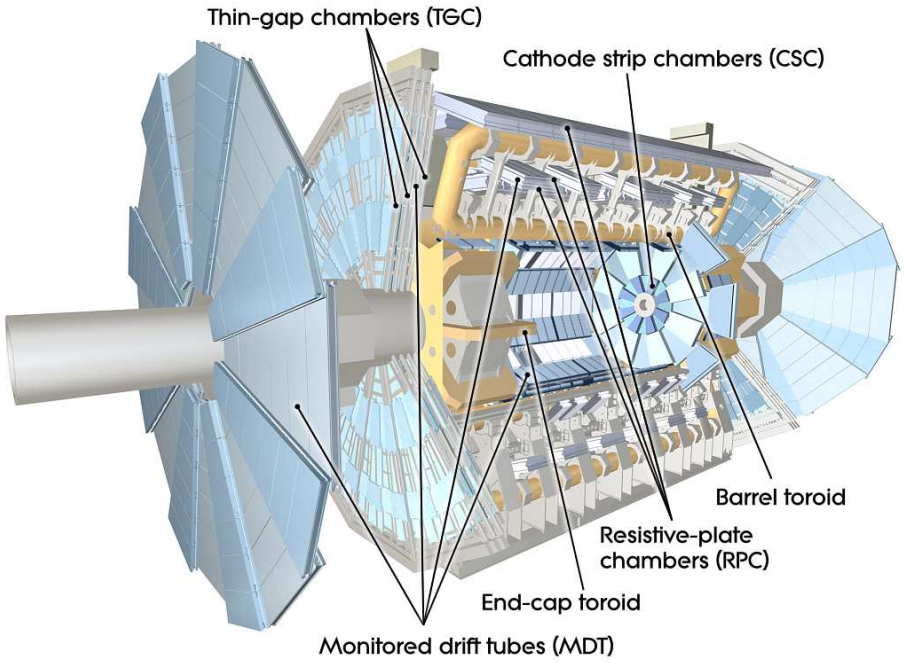

Figure 3.11 *Illustration of the Muon spectrometer with all its components [45].*

Tracks are measured in three layers of chambers which are gaseous detectors sensitive to muon ionisation. For the barrel region these chambers are arranged in cylindrical layers around the beam axis, while in the transition and end-cap region the chambers are installed in planes perpendicular to the beam. Besides a precise determination of the muon momentum, the MS provides fast information to the trigger system. To satisfy both requirements, the system consists of a combination of either high precision spatial resolution, or optimised timing resolution. In the barrel, Monitored Drift Tubes (MDTs) chambers with a high spatial resolution of approximately 40 μm provide precise momentum measurements. While the fast Resistive Plate Chambers (RPCs) provide less precise (but complimentary) tracking information, they give faster readout speeds for the trigger. In the endcaps the precise tracking is performed by Cathode Strip Chambers (CSCs), whereas the quick-response Thin Gap Chambers (TGCs) are used for triggering. The MDTs make up most of the MS detector, and they are made of 30 cm-long aluminium drift tubes. The CSCs are made up of multiwire proportional

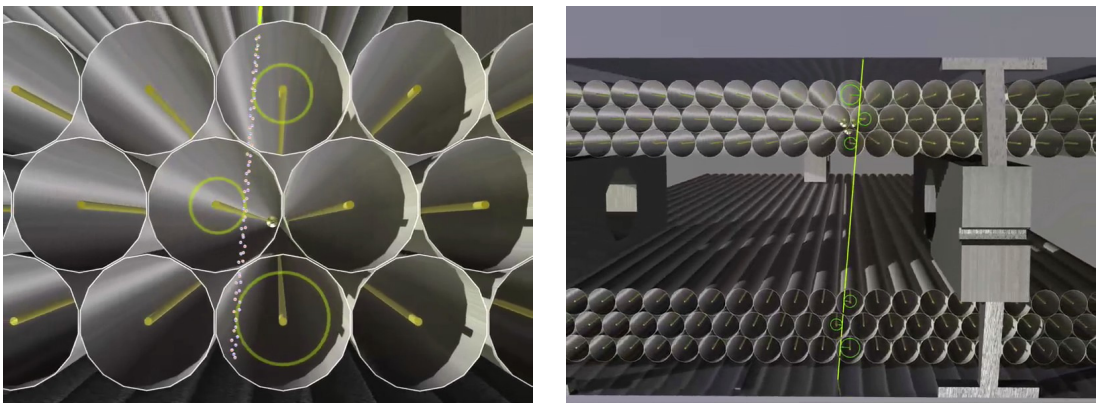

(a) *muon gas trail* **(b)** *muon track*

Figure 3.12 *Trail of charged ions and electrons from the interaction of a muon with the gas within the drift tubes (Figure 3.12a), and the muon track reconstruction from the position of the interaction with each tube (Figure 3.12b) [56].*

chambers with orthogonal planar cathodes. Given that the tolerance for high radiation and counting rate of the MDTs is not very high, CSCs are used instead in the endcaps, where a higher particle flux is expected. RPCs system does not use wires, but employs instead two parallel resistive plates with a 2 mm spacing in each station with a gas mixture in between. It ensures a good time resolution of 1.2 ns [58] and high rate performance. TGCs are thin multiwire proportional chambers similar to the CSCs, except that their wire strip spacing is smaller, allowing a faster charge collection. It has a time resolution of about 2.3 ns [59]. The muon reconstruction in gaseous detectors, such as the MDTs, is based on the interaction of the muon with the gas contained in small tubes, that leaves a trail of charged ions and electrons which drift to the centre or side of the tubes depending on their charge (electrons to the centre and charge ions to the contour of the cylinder), as illustrated in Figure 3.12a. Circles tangent to the trajectories of the muons can be traced from the centre of the tube, and thus used for the determination of the position of the muon track as can be observed in Figure 3.12b.

Muons loose their energy mostly from the ionization coming from the collision with different types of materials. In materials like iron and cooper, the muon loose 5 MeV for every millimeter traversed, so about 5 m of iron will be required to absorb the energy of a 5 GeV muon. On the contrary, most of the hadrons can travel only 1–2 m within iron before they loose their full energy. Therefore, most of the particles, except for muons, are typically absorbed by the preceding

calorimeters.

3.2.6 Trigger and Data Acquisition

The information that would be required for storage by the ATLAS Data Acquisition system [60] without an event-filtering system, would be impossible to handle with the current computing readout and storage capacity. For instance, in the nominal LHC operational conditions the interaction rate in the heart of the ATLAS detector is of the order of 1 GHz, which means a data rate of approximately 60 Tb/s (five orders of magnitude beyond today's capacity). However, most of the bunch crossings lead to "uninteresting", low momentum physics processes which are not wanted for further study. The interesting physics objects have particular characteristics that can be identified by their reconstruction inside the detector, such as an energetic muon. The ATLAS trigger system [61] is designed to select these types of events, reducing the event rate for permanent storage to approximately 200 Hz, resulting in a data rate of a manageable value of 300 Mb/s. There are trigger-selection menus for all the physics objects selected by the Data Acquisition system, such as: electron, photon, muon, tau, jet, missing energy, and minimum bias. The ATLAS trigger in Run-1 is a three-level system, with each level having an ever-increasing refined selection and additional processing time to filter interesting events than the previous stage, as illustrated in Figure 3.13.

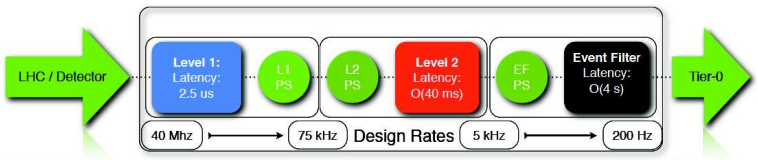

Figure 3.13 *The three trigger levels for ATLAS in Run-1, with the design rates before and after the selection, and the latency for each stage [62].*

The first stage, the Level 1 (L1) trigger, is a hardware-based selection that uses only the calorimeter and the fast trigger section provided by MS. With regard to muons, the identification is made by the RPC and TGC. Since there is limited time for the track reconstruction, the momentum is roughly estimated from the hits using look-up tables. The calorimeter detects high energy deposition of electrons, photons or jets with a coarse granularity. L1 reduces the output rate below 75 kHz, within a 2.5 μs latency, as the data can be stored for a very short

time in the pipeline memory of the trigger system. If an event is accepted by this level, the geometry and position of the candidate physics object are identified as a Region of Interest (RoI), that would be used as input for the next trigger level.

The Level 2 (L2) is a software-based trigger that uses the full granularity of all detector components including the tracking system. The selection process starts from the RoI, including more complex but still relative simple and efficient reconstruction algorithms, such as isolation criteria for leptons. On average the L2 can process a new event every 10 μs, with a further processing time of 40 ms (which includes the data-transfer time). The output rate is reduced from 75 kHz to approximately 2 kHz during nominal operation.

Finally, the information is passed to the software-based Event Filter (EF) trigger level. This level applies sophisticated corrections in the reconstruction algorithms, including noise suppression, alignment, and calibration information. During nominal operation the input event rate is around 2 kHz, with EF providing additional selections that reduce the output rate to approximately 200 Hz, corresponding to 300 Mb/s. The combination of L2 and EF is known as High Level Trigger (HLT). Events that pass the EF selection are stored in local storage elements for a further distribution using the CERN computing network "Grid".

3.3 Performance of ATLAS and the LHC

The number of events N_i produced in a collider for a certain process is given by:

$$N \;=\; \sigma_i \int \mathcal{L} dt \tag{3.6}$$

where σ_i is the cross section of the particular process and $\mathcal{L}$ is the collision rate known as instantaneous luminosity. There are several processes with low cross section, such as the SM Higgs boson production, for which a large integrated luminosity is needed to study their properties in detail. sample. The instantaneous luminosity depends only on beam parameters, which can be written for a Gaussian beam profile as:

$$\mathcal{L} = \frac{N_b^2 \, n_b \, f_{rev} \gamma_r}{4\pi \, \epsilon_n \, \beta^*} F \quad , \tag{3.7}$$

where N_b is the number of particles per bunch, n_b is the number of bunches per beam, f_{rev} is the beam revolution frequency, γ_r is the relativistic gamma factor for a given beam energy, ϵ_n is the normalized transverse beam emittance, β^* is the beta function at the collision point, and F is the geometrical reduction factor that is applied due to the fact that the beams do not collide head-on but with a small crossing angle. The LHC is designed to accommodate up to 2808 bunches of proton per beam at an instantaneous luminosity of $\mathcal{L} = 10^{34}\,\mathrm{cm}^{-2}\,\mathrm{s}^{-1}$, with a bunch space of 25 ns, each bunch containing approximately 10^{11} protons, a beam revolution frequency of $f_{rev} = 11.2$ kHz, a beta function of $\beta^* = 0.55$ m, and with a normalised transverse beam emitance of $\epsilon_n = 3.75$ μm. Most of the parameters stay constant during the proton collisions, except for the number of particles per bunch which is degraded with time.

The LHC era started in 2008 when the first beam circulated successfully. However, the operation was interrupted nine days later due to a faulty electrical connection that provoked a leak of liquid helium in the vacuum which resulted in a magnet damage given the lack of cooling. In November 2009, the operation was resumed with the first proton-proton collisions at the injection energy of 450 GeV , increasing a few days later to a world record of 2.1 TeV. After ensuring the proper operation of the magnets at higher energies, the physics programme started in March 2010 at a centre-of-mass energy of $\sqrt{s} = 7$ TeV. During that year a total integrated luminosity of 48.1 pb^{-1} was delivered by the LHC. At that time, the machine was filled with a maximum of 368 bunches with a spacing of 150 ns and maximum 1.2×10^{11} protons per bunch, leading to a peak luminosity of 2.1×10^{32} $\mathrm{cm}^{-2}\,\mathrm{s}^{-1}$. After a short period of lead ion collisions, LHC started running again in the beginning of 2011 with proton bunches colliding at the same energy but a reduced bunch spacing[3] and β^*, and an increased bunch intensity, resulting in an increased peak luminosity of 3.7×10^{33} $\mathrm{cm}^{-2}\,\mathrm{s}^{-1}$. These conditions lasted until the end of year leading to a total integrated luminosity of 5.46 fb^{-1}.

In April 2012, the collision energy was increased to 8 TeV. In addition, the instantaneous luminosity peak reached 7.7×10^{33} $\mathrm{cm}^{-2}\,\mathrm{s}^{-1}$ which is almost as high as the design luminosity. The improvement was possible due to a much higher bunch intensity, with the bunches being separated by 50 ns (twice the design space). The total integrated luminosity delivered by the LHC after this

[3]Beams are made of trains of proton bunches moving at almost the speed of light around the 27 kilometer ring of the LHC. By sending more bunches around the ring, the LHC will be able to generate more collisions, ultimately maximising the integrated luminosity delivered to the experiments.

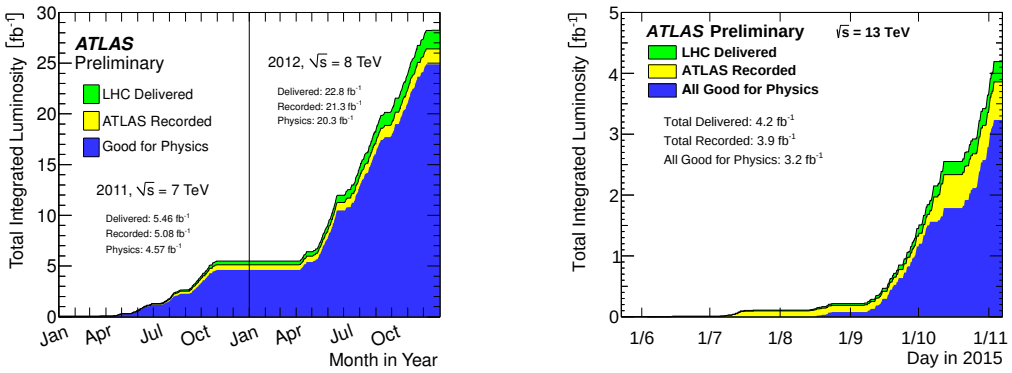

(a) *Integrated luminosity in Run1* **(b)** *Integrated luminosity in Run2*

Figure 3.14 *Integrated luminosity versus time delivered by the LHC (green), recorded by ATLAS (yellow), and certified to be of good quality for physics analyses by ATLAS (blue). 3.14a is the luminosity recorded from proton-proton collisions at 7 and 8 TeV in 2011 and 2012 [63], while 3.14a is the luminosity recorded from proton-proton collisions at 13 TeVin 2015.*

long run was 22.8 fb^{-1}, of which the ATLAS data acquisition (DAQ) system recorded 21.3 fb^{-1}. The difference between these two numbers is mainly because of losses caused by the DAQ system at the starting time of the data-taking period, which is needed for the calibration of the detector settings. Not all the recorded data can be used for physics analyses, since certain parts of the detector might not work as expected in a particular run. The integration of the data-taking periods with good quality physics is called "Good Run List"(GRL). By the end of 2012 the GRL reached an integrated luminosity of 20.3 fb^{-1}, which corresponds to the dataset used for the analysis discussed in Chapter 6.

Following the first scheduled shutdown of the LHC, the data-taking period started in January 2015 with the energy increased to 13 TeV, achieving a peak luminosity beyond the design rate of 1.2×10^{34} $\text{cm}^{-2}\,\text{s}^{-1}$ in July 2016. This became possible mostly because of the decrease of bunch spacing to 25 ns. The integrated luminosity is increasing every day, expecting to exceed 100 fb^{-1} by the end of the Run 2 period. The total integrated luminosity for all the Run 1 period and the first year of Run 2 is shown in Figure 3.14. The green color refers to total integrated luminosity delivered by the LHC, the yellow one is the luminosity recorded by the ATLAS DAQ system, and the green is the GRL.

Over the years, different beam configurations have been used by the LHC, which translates into a variation of the average number of interactions μ per bunch crossing, as shown in Figure 3.15a for Run 1 and Figure 3.15b for Run 2. Each

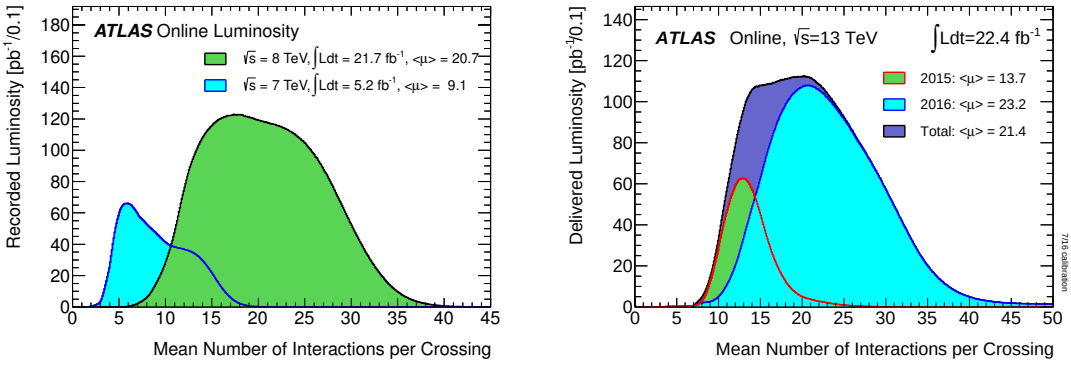

(a) *Pile-up in Run1* **(b)** *Pile-up in Run2*

Figure 3.15 *Number of interactions per bunch crossing (pile-up) weighted by the luminosity for Run 1 [63] (2011 and 2012) and Run 2 (2015-2016) data recorded from proton-proton collisions.*

curve shows a Poisson distribution which a mean equal to the average number of number of interactions per bunch crossing $\langle\mu\rangle$. $\langle\mu\rangle$ has been increasing over the years, having, for example, a value of $\langle\mu\rangle = 21.4$ in the current Run 2 period. The increased number of interactions per bunch crossing increases the chances of finding interesting physics processes, but it also increases the so called pile-up (simultaneous proton-proton interactions) and leads to hits in the detectors that do not originate from the hard scattering. These interactions result in a higher number of electronic signals in the detector which are not originated from the hard scattering process of interest. Pile-up can become an issue if it is not identified accurately when reconstructing physics objects. The mean number of interactions per bunch crossing is calculated as:

$$\langle\mu\rangle = \frac{\mathcal{L}_b \, \sigma_{inel}}{f_{rev} \, n_b} \quad , \tag{3.8}$$

where $\mathcal{L}_b$ is the instantaneous luminosity per bunch, and σ_{inel} is the inelastic cross section. The inelastic cross section varies depending on the collision energy. For instance, the total inelastic cross section at 7 TeV is $\sigma_{inel} = 71.5$ mb, while at 8 TeV is $\sigma_{inel} = 73$ mb.

There are two types of pile-up events: the in-time and the out-of-time pile-up. The in-time pile-up corresponds to additional interactions that are created in the same bunch crossing, while the out-of-time pile-up is related to the overlay of interactions of different bunch crossing due to the limited read-out time of the detector. The in-time pile-up contributions increase with the number of protons in a bunch N_b, whereas the out-of-time pile-up increases when the bunch spacing

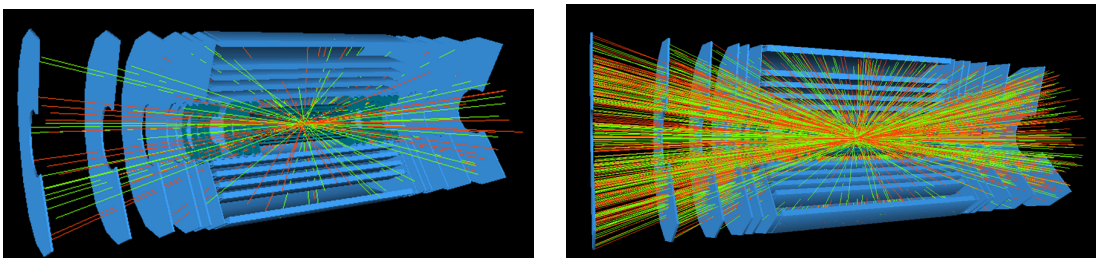

(a) *23 number of interactions* **(b)** *230 number of interactions*

Figure 3.16 *Baseline layout of the ID traverse by 23 and 230 number of interactions per bunch crossing [64].*

is reduced. Both types of pile-up are increased when the number of bunches per beam n_b increases. Figure 3.16 illustrates the number reconstructed vertices in the ATLAS ID under two different pile-up conditions: $\langle\mu\rangle = 23$, the mean number of interactions reached in 2016, and $\langle\mu\rangle = 230$, the pile-up expected during the High Luminosity LHC (HL-LHC).

3.4 Physics objects

Particles created from several physics processes leave different traces in the various subdetectors according to their nature. These include energy deposits in calorimeter cells and hits in the tracking layers. The physics objects are reconstructed with algorithms that try to identify these detector signals. The reconstruction of these physics objects with the ATLAS detector are illustrated in Figure 3.17, and are summarised below.

3.4.1 Track reconstruction

A charge particle track is reconstructed from a sequence of hits in the different layers of the ID. The curve trajectory of the track can suffer deviations due to multiple scattering and energy loss. The hits registered by the Pixel and SCT detectors are converted into clusters and then space-points. The timing information from the TRT is converted into calibrated drift circles. There are two track-finding algorithms which differ in the direction in which they work to identify the candidate track. The inside-out algorithm [65] uses a Kalman filter to seed tracks from hits in the three pixel laters and the first SCT layer. The

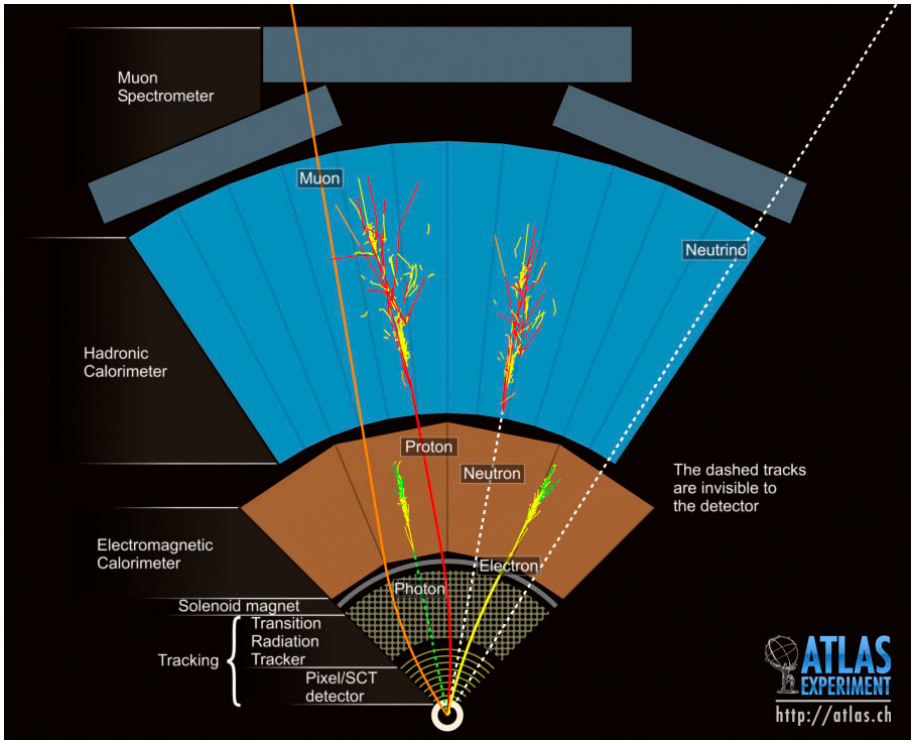

Figure 3.17 *Illustration of the interactions of several particles with the different components of the ATLAS detector [56].*

location of the seed is extrapolated and fitted to the rest of the SCT and the TRT. Further restrictions are applied in order to have a good quality track, such as requiring the track to be originated from the primary vertex. On the contrary, the outside-in algorithm [65] considers seed tracks from the interaction with the TRT, which are then extrapolated to the SCT and Pixel detectors. This method is typically used in displaced vertex signatures, since it improves the tracking of secondary particles. The pattern recognition uses one or the other algorithm, being primarily used the inside-out algorithm.

After the track reconstruction, a vertex finding algorithm is used to determine the primary and secondary vertices of the event. Vertices along the beamline are associated with the interactions of the incoming partons, and are called primary vertices. Vertices originated by particle decays are called secondary vertices.

3.4.2 Electron reconstruction

Electrons are reconstructed from the energy deposits (clusters) in the central region of the EM calorimeter that must satisfy a set of identification criteria so

that the longitudinal and transverse shower profiles are consistent with those expected for electromagnetic showers. The electron candidates must have an ID reconstructed track that points to the respective EM calorimeter cluster. The direction and charge of the electron is taken from this track that is fitted using a Gaussian-Sum filter [66], which allows for Bremsstrahlung energy losses to be taken into account. An electromagnetic cluster is reconstructed by searching for seeds above a transverse energy of 2.5 GeV with a sliding window algorithm [67] defined in the $\eta \times \phi$ plane. A fixed size window is moved across each element of the tower grid in steps of $\Delta\eta \times \Delta\phi = 0.025 \times 0.025$ to look for a seed, as indicated in Figure 3.18. From this seed, an electron cluster is built from longitudinal towers of calorimeter cells with different sizes in the barrel and endcaps. The energy of the electron is calculated from the measured energy deposits inside the cluster by applying correction factors because of the dead material in front of the calorimeter, as well as lateral and longitudinal leakage. The background, composed by non-prompt electrons and jets, is rejected by applying selections on several discriminating variables, such as: good quality tracks (several hits in the ID components) to discriminate against photon conversion, a precise $\eta \times \phi$ matching to discriminate from jets faking electrons, the ratio between the electron energy measured in the cluster and the track momentum in the ID to discriminate from jets faking electrons, the cluster isolation to discriminate from a spread jet distribution, or the ratio between the largest and the sub-leading energy clusters in order to discriminate from jets with one or more neutral particles (such as π^0) which would cause a second maximum in the EM calorimeter. For the first part of the Run 1, a simple selection cut on each one of these variables were made to reconstruct the electron. But for 2012 analyses, as the one from Sect. 6, a multivariate technique (MVA) based on the Maximum Likelihood approach has been chosen for the electron identification, since it allows simultaneous evaluation of several properties when making a selection decision.

$E - p$ combination for electrons

In order to improve the energy resolution of low E_T electrons and electrons in problematic regions of the EM calorimeter (such as the crack region $1.37 < |\eta| < 1.52$ in which the detector response tends to be worse), a combination of the track momentum and the cluster energy is attempted. A combination method that employs a maximum likelihood fit of the p_T measured in the ID and the EM cluster is applied to electrons with $p_T > 30$ GeV and $\eta < 1.52$. This method

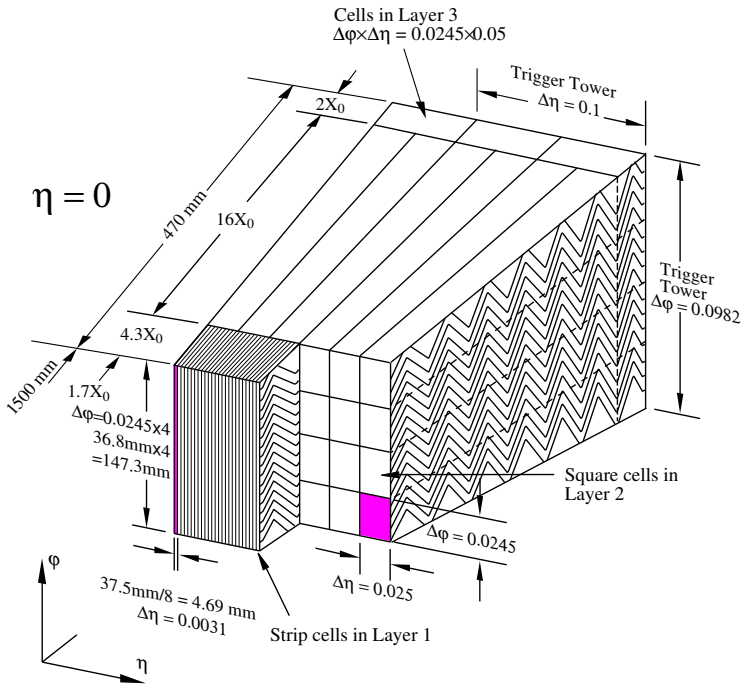

Figure 3.18 *Diagram showing the structure of a barrel module of the electromagnetic calorimeter. An electromagnetic trigger tower is shaded, with its η and ϕ dimensions indicated [64].*

has been applied to the $H \to ZZ^{(*)} \to 4\ell$ analysis selection discussed in Sect. 5, achieving an improvement of 4% when all the final-state leptons are electrons ($4e$), and 3.5% when is a combination of muons and electrons ($2\mu\,2e$). In addition, the likelihood-based combination produces a reduction on the tail of the invariant mass distribution.

Electron calibration

In order to improve the electron and photon calibration, the full procedure have been revisited by invoking MVA techniques. In addition, several subtle experimental corrections has been implemented in the simulation of the detector geometry and the material distribution [68]. The calibration procedure for electrons and photons is described in [69]. The Higgs boson mass measurement critically depends on the precise determination of the scale and resolution of the electron and photon energies.

3.4.3 Muon reconstruction

The reconstruction of muon candidates [70] is made using the track information from the ID and the MS in different regions of the detector. The tracks in the MS are reconstructed by considering the activity in each layer of the chambers for local segments, which are then combined into a single MS track. A track reconstructed in the ID is required to have a certain number of hits in the Pixel, SCT, and TRT detectors, and at most two active Pixel or SCT sensors without a hit corresponding to the transverse muon track candidate. The acceptance varies according to the geometrical coverage of both track sub-detectors, and the momentum of the track. For instance, the ID is not available in the forward region, the MS acceptance region is $|\eta| < 2.7$, low momentum muons are not able to reach the MS given the energy loss in the calorimeters, and there are "dead" regions where there are no active detector material, but plain structure (crack regions). This situation is accounted for by defining four types of muons depending on these limitations:

- Standalone muons (SA): these are muons reconstructed from tracks measured just in the MS. The reconstruction of the full path of the track is extrapolated from the interaction point, taking into account the effect from multiple scattering and energy loss in the transverse material. This selection of muons are used in the region where the ID has no coverage, $|\eta| > 2.5$, to increase the overall acceptance. Some analysis might not use SA muons.

- Combined muons (CB): these are muons whose tracks are reconstructed independently by the ID and MS and are then combined to obtain a muon track, which defines its four-momentum vector. If the MS track can be matched to a ID track, the muon track is obtained by a global refit of all hits assigned to the two reconstructed tracks in the ID and MS. The momentum and direction of the muon candidate is taken from this track. The CB muons have the highest purity, yield reconstruction, and identification efficiency of all the types of muons.

- Segmented-tagged muons (ST): these are muons reconstructed from tracks measured just in the ID. This situation may occur when there is no accurate track match on the MS, mostly because of a low momentum muon candidate.

- Calorimeter-tagged muons (CT): are muons reconstructed from the associ-

ation of a ID track to a calorimeter cluster, in regions where there is no MS coverage. This type of muons helps to cover the crack regions.

The background from non-prompt muons, such as decays of heavy flavour hadrons, is commonly suppressed by requiring that the candidates must satisfy a track-based isolation criteria.

3.4.4 Jet reconstruction

QCD jets are identified in the ATLAS detector as bunches of hadrons that originate from quarks and gluons after fragmentation and hadronization. They are reconstructed from topologically related calorimeter cells, topo-cluster [71], using the anti-k_T algorithm [72]. The topo-cluster method looks for a seed cell with a significant contribution of signal above noise (that can be originated from electronic or pile up effects). The resulting topo-cluster contains shape and location information, which is used to apply a local energy calibration and corrections depending on the nature of the cluster. In this, the clustering algorithm implicitly performs a topological noise suppression by removing cells with insignificant signals which are not in close proximity to cells with significant signals. The resulting topological cell clusters have shape and location information, which is exploited to apply a local energy calibration and corrections depending on the nature of the cluster.

The topo-cluster may contain more than one local maxima of energy deposits, in which case the topo-cluster can be split into several topo-clusters with a considerable separation between them in order to break up overlapping showers. Cells inside the topo-cluster are calibrated using the local cluster weighting (LCW) method [73], which distinguishes between electromagnetic and hadronic topo-clusters based on their energy density and longitudinal shower depth. Energy corrections, due to crack regions, are taken into account from simulated electromagnetic and hadronic showers. The topo-cluster is defined by the sum of the energy deposited in the cells and the direction, that is calculated from the weighted average position of the single cells. This calibrated topo-cluster is given as an input to the anti-k_T algorithm with a distance parameter of $R = 0.4$ using the Fastjet [74] software package. This jet reconstruction method yields stable results, which means that is insensitive to collinear splitting of the initial parton (collinear safe) and additional soft gluon radiation (infra-red safe). Further

calibrations of the jet are made in order to take into account experimental and detector corrections.

Contribution from additional pile-up interactions cause an offset of the jet energy, which is corrected by applying scale factor derived from MC simulation. These simulations are calculated in bins of η and p_T, taking into account the number of reconstructed primary vertices and the average of the expected number of interactions. The direction of the jet is corrected according to its relation with the position of the primary vertex. Jets coming from pile-up events tend to be rather soft and are rejected by making a selection on the jet vertex fraction (JVF) [75], which exploits the fraction of tracks within the jet coming from the primary vertex. Any jet with $p_T < 50$ GeV and $|\eta| < 2.4$ is required to have at least 50% of its summed track p_T of all tracks with $p_T > 1$ GeV originating from the primary vertex.

For the energy losses inside the detector, the jet energy scale (JES) corrections [71] are applied to the energy and η of the jet by comparing reconstructed jets to generator-level jets formed from stable particles in MC simulations. Since there is no distinction between electrons reconstructed as jets and proper jets, the single closest-to-an-electron jet within $\Delta R < 0.2$ is removed. After all these selections and corrections, the total four-momentum of the jet is calculated by summing the four-momenta of all its constituents.

3.4.5 Missing energy reconstruction

Processes than involve particles that do not interact with the detector, such as neutrinos, are identified by the missing transverse energy E_T^{miss}. The initial state collision has, in good approximation, zero transverse momentum. Therefore, the E_T^{miss} [76] is defined as the magnitude of the negative vector sum of the momentum of all reconstructed and calibrated objects taking into account correction terms from the calorimeter and tracking. The measurement of E_T^{miss} relies on the precise identification of all the physics objects in an event. These objects are represented by energy deposits of tracks corresponding to electrons, photons, hadronically decaying tau leptons, jets, muons, and soft calorimeter topo-cluster ("soft"). The $x-$ and $y-$component of the E_T^{miss} is calculated by:

$$E_{x(y)}^{miss} = E_{x(y)}^{miss,e} + E_{x(y)}^{miss,\gamma} + E_{x(y)}^{miss,\tau} + E_{x(y)}^{miss,\mu} + E_{x(y)}^{miss,jets} + E_{x(y)}^{miss,soft} \quad (3.9)$$

where each term is the negative sum of the $x-$ and $y-$component of all objects' energies. The E_T^{miss} is then given by:

$$E_T^{miss} = \sqrt{(E_x^{miss})^2 + (E_y^{miss})^2} \tag{3.10}$$

Corrections must be taken into account to include sources that could be misinterpreted as true E_T^{miss}, such as: limited detector coverage, finite detector resolution, electronic noise, crack detector regions, and pileup events. Pileup contributions, in particular to the jet and soft terms, can be suppressed by applying selection cuts based on track properties.

Chapter 4

Muon isolation studies for the Phase-II Level-1 Track Trigger

The last scheduled LHC phase will experience an increase in the instantaneous luminosity and pp collision rate beyond the LHC design and the current ATLAS detector capabilities. Several upgrades to the ATLAS detector will be made in order to withstand the high radiation collisions and maintain an optimal physics performance. The large detector occupancies will require the implementation of a more restrictive event selection, compared to Run-1 and Run-2. The preliminary study presented here examines the performance of a track-based isolation algorithm for muons at the first stage (hardware level) of the trigger in order to reduce the rate of events to be processed by the High Level Trigger (HLT) farm. A secondary objective of the study is to compare the performance of the track-based isolation algorithm (implemented in the first trigger stage, known as L1 Track Trigger) with the performance of a calorimetric-based isolation for a trigger system that does not involve tracking information at the first stage of the filtering system. This study has been performed in the context of the R&D that is being carried out in the ATLAS collaboration for the design of the Phase-II trigger.

4.1 LHC and ATLAS Upgrade

After the first major LHC upgrade in 2013 (which increased the collision energy from $\sqrt{s} = 8$ to 13 TeV), there are several phases of new upgrades scheduled that will enable the extension of the physics programmes of the LHC experiments. The timeline of the LHC and its upgrade is shown in Figure 4.1. Three long shutdowns (LS) are scheduled for maintenance and upgrade work on the accelerator and the detectors. This will allow for a continuous increase of the instantaneous luminosity, and, therefore, the collection of very large datasets over the years. Following the first LHC shutdown (LS1), the 2015 data-taking period began with a collision energy increase to 13 TeV and with an instantaneous luminosity that eventually exceeded the design value of 10^{34} cm^{-2} s^{-1}. After the second long shutdown (LS2) in 2018, the instantaneous luminosity will increase by another factor of two, allowing the detectors to collect 100 fb^{-1} of collision data per year of operation. A second upgrade [**?**] is planned, which will make significant changes to the interaction point region in addition to improvements to other parts of the accelerator complex, such as crab cavities and installation of 11 T superconducting quadrupoles. These improvements will result in an instantaneous luminosity increase to at least 5×10^{34} cm^{-2}s^{-1}, with a projected integrated luminosity of 3000 fb^{-1} after about 10 years of operation. This period is known as the High Luminosity LHC era (HL-LHC). These conditions are ideal for measurements of low cross-section processes, such as the Higgs boson self-couplings or searches of dark matter candidates of BSM theories. However, the nominal instantaneous luminosity in the HL-LHC period corresponds to an average of at least 140 pp interactions in every beam crossing (so called "pile-up" interactions). In order to take advantage of the improved LHC operation the ATLAS detector must be upgraded in order to deliver the same excellent physics performance at higher luminosities, as the one achieved in the Run-1 and Run-2 data-taking periods.

4.1.1 Phase-I ATLAS upgrade

The main focus of the Phase-I ATLAS upgrade [78] in 2018 (LS2) is on the event selection at the first stage of the filtering system (the hardware-based Level-1 trigger). The objective is to sharpen the selection efficiency while maintaining the low transverse momentum (p_T) threshold for single charged leptons (electrons

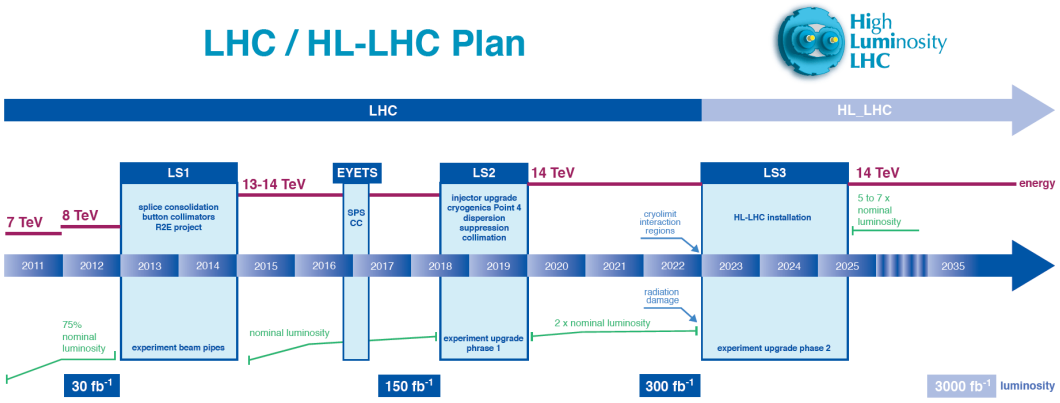

Figure 4.1 *Timeline of the LHC with planned shutdowns, projected instantaneous and integrated luminosity levels [77].*

and muons) and keeping the Level-1 (background) rate at a manageable level. Upgrades are planned for both the muon and the calorimeter trigger systems, without which the single lepton Level-1 trigger p_T thresholds would have to be raised, resulting in a significant loss of acceptance for many interesting physics processes.

The Phase-I upgrade of the ATLAS muon spectrometer [79] focuses on the forward region of the detector. The performance of the muon tracking chambers (in particular in the forward region) degrades with the expected increase of cavern background rate. The Phase-I high luminosity and high energy conditions are expected to create a substantial degradation of tracking performance, both in terms of efficiency and resolution in the inner forward part of the detector, the (so called) "Small Wheels". Given that the high resolution muon momentum measurement crucially depends on the presence of hits at the Small Wheel level, this degradation is detrimental for the performance of the ATLAS detector. Besides this, one has to take into account that a significant part of the muon trigger rate in the forward region is (non-muon) background. Low energy particles, mainly protons, generated in the material located between the Small Wheel and the calorimeter station, produce fake muons by hitting the forward chambers at an angle similar to that of real high p_T muons. The ATLAS Collaboration will replace the existing Small Wheel with a New Small Wheel (NSW), which improves the L1 trigger tracking capabilities for higher luminosities. The NSW consists of a set of precision tracking and trigger detectors able to cope with high event rates with excellent real-time spatial and time resolution. These detectors can provide the L1 muon trigger system with track

segments of good angular resolution to confirm that muon tracks are originated from the interaction point. The rate of forward-region fake muons is considerably reduced by this addition. With the proposed NSW the ATLAS muon system will maintain the excellent muon tracking over the full acceptance at the highest LHC luminosity expected. At the same time, the low-p_T (typically $p_T > 20$ GeV) single muon L1 trigger rates will be kept at an acceptable level. For instance, the rate for this trigger menu is expected to be reduced from 60 kHz to 22 kHz [79] for an instantaneous luminosity of 3×10^{34} cm^{-2} s^{-1} at $\sqrt{s} = 14$ TeV and with a bunch spacing of 25 ns.

The proposed upgrades to the L1 hardware trigger allow the experiment to send events with relatively-low p_T physics objects to the HLT farm for further processing. Tracking information is typically employed at the HLT to further discriminate between the interesting physics and background, and select the most promising events for offline analysis. However, extensive tracking in such high-multiplicity environments [80] is prohibitively expensive in terms of processing time and computing cores needed. Therefore, it is used sparsely for specific RoI's which have been identified as potentially interesting by the L1 trigger and at a much lower rate for full-event tracking reconstruction. This approach has its limitations, given that a finite number of RoI's can be considered at the HLT, and that information that requires full-event tracking (such as the number of primary vertices in a collision event) is useful for object selections or detector corrections. The Fast TracKer (FTK) [81] is a hardware-based pattern recognition trigger component which performs a "global" (i.e. full-event) track reconstruction after a L1 trigger accept, giving to HLT algorithms early access to tracking information. It employs a massively parallel processing scheme that simultaneously compares multiple hits in sections of the ID detector against millions of pre-calculated patterns [82]. FTK tracks, freed from the CPU constraints of HLT-tracking, will be an important tool for the ATLAS HLT in Run-2 and beyond.

4.1.2 Phase-II ATLAS upgrade

With the last scheduled LHC upgrade in 2023, the instantaneous luminosity is projected to increase to at least 5×10^{34} cm^{-2} s^{-1}. This record luminosity value would create very challenging operational conditions for the current ID detector. The ATLAS Collaboration is preparing to install a new ID detector, besides the trigger and calorimeter upgrades.

After the LS2, the increase in the instantaneous luminosity is achieved at the expense of a much higher pile-up enviroment, with the average number of multiple collisions within the same bunch crossing increasing from approximately 28 to 140 — 200. This large detector occupancy is already beyond the current TRT specifications, even before taking into account the degraded performance of the ID system (Pixel and SCT included) due to the radiation damage of their sensors and the front-end electronics. The ATLAS Collaboration has decided to replace the entire ID subdetector by an all-silicon Inner Tracker (ITk) [83, 84]. In addition to the requirements of robust operation, efficient readout and tolerance to both integrated radiation dose and accumulated activation, the ITk is designed to improve the tracking performance of the existing ID with the expected level of pile-up. Several layouts have been simulated to study their tracking performance in order to find the optimal architecture. The available space is a major constraint on the design, with the maximum radius of 1 m being determined by the current ID volume (without taking into account the existing gaps for services which further limit the design). The current baseline design of the ITk includes four Pixel and five silicon-strip layers in the barrel section, and six Pixel and five silicon-strip layers in the two endcap regions.

The pixel modules in the innermost layers are expected have approximately 638×106 pixels with size 25×150 μm and 50×250 μm (to be compared to the current layout of 80×106 pixels of size 50×400 μm), while the size of the outer silicon strip modules will be a rectangle of 24×96 mm. The silicon-strip modules are designed in a similar fashion to the current SCT, where a pair of modules are glued back-to-back in order to provide a 2D topology. The ITk is expected to be read out at a nominal 1 MHz rate.

Research and design studies are currently ongoing to determine the most suitable pixel sensor technology (e.g. silicon planara and 3D) and the optimal layout of the silicon-strip modules.

The extreme radiation conditions in the HL-LHC will cause damage on the active material of the whole calorimetry system, as well as the on-detector readout electronics, and a decision has been made by the ATLAS Collaboration to replace them. The major upgrades for this subdetector are to be made in the TileCal and the Forward Calorimeters, and will include new radiation tolerance electronics.

The finer granularity of the upgraded detector will improve the performance of the Trigger system. Studies are being carried out in order to determine how the

Trigger can best exploit the upgrades of the Phase-II ATLAS detector. One of the major proposals with a large impact on the performance of the Phase-II Trigger is the option to include tracking information at the first (hardware) level of the trigger. This project is known as the Level 1 Track Trigger and is currently under review within the ATLAS collaboration. The challenge is to mitigate the effects of the high-occupancy on the filtering system without raising the p_T thresholds for the main physics objects of the online selection.

4.2 Level 1 Track trigger

The Level 1 trigger in the HL-LHC era must provide a higher background rejection because of the higher instantaneous luminosity and the increased detector occupancies. A first study concluded that, if no improvements are made to the trigger and data acquisition systems, the p_T threshold for single leptons must be increased to 25 GeV [85, 86]. Raising the leptonic thresholds is not ideal since it would compromise electroweak physics, in particular since the mediocre L1 p_T resolution is not optimal for high momentum selection. An alternative, improved Level 1 trigger architecture has been proposed [87, 88], which includes the possibility of employing low latency and high accuracy tracking information at the first level of the trigger.

The online selection for the HL-LHC has not been finalised but will most likely focus on physics objects in kinematic proximity to the electroweak scale. In order to maximise the full trigger efficiency at these scales, it is imperative to have the ability to identify and select events with charged leptons with momentum of the order of 10 GeV. The L1 Track trigger offers the option of implementing a hardware-based track reconstruction that will match the (muon or calorimetric) candidate's RoI with nearby tracks. This improved selection reduces the single lepton background by a factor of five compared to the non-L1 Track (baseline) method, while maintaining a 95% efficiency. An optimal track reconstruction is essential for obtaining such high charged-lepton efficiencies, requiring tracks with p_T as low as 4 GeV.

The L1 Track trigger will use the L1 RoI of the candidate lepton as a seed for reconstructing the track. This approach is similar to the way the current trigger system reconstructs software-based HLT tracks, with the important difference that in the L1 Track Trigger scheme the RoI input is being processed by the

hardware-based ITk system layers. The "early" muon or calorimetric information must be identified fast enough so that it can serve as a seed to the readout of specific ITk regions at a high rate. The first level decision that is used to reduce the information to be read out by the ITk for processing is known as the Level 0 (L0) trigger level.

The proposed hardware-based track trigger is divided into two stages, the L0 RoI determination and the L1 Track identification. The L1 Track trigger will be fed by a L0 decision based on calorimeter and fast trigger MS information. The output of the L0 processing includes the identification of L0 RoIs for regional track identification as an input for the L1 decision. The combined (L0 and L1) track trigger system must arrive at a decision with a latency of less than 24 μs. The allocated time to the individual steps is as follows: 6 μs for the regional ITk readout request, 12-15 μs for the track identification and reconstruction, and 3-6 μs for the data transfer and global L1 decision. Currently there are several studies that are exploring potential architecture options that could fulfill these constraints.

4.3 Muon Isolation

There are several characteristics that can be used to differentiate between charged leptons and other hadronic activity in the ATLAS detector. For instance, a particle that has a wide interacting area, such as a quark or a gluon hadronising into a jet, produces a large number of tracks in the ID and a broad energy deposition in the calorimeter. On the other hand, the trace of charged leptons is typically that of a single track with a narrow energy deposition in the calorimeter. A method to quantify this experimental signature is through the measurement of the "isolation" of the particle [89]. This is evaluated with the construction of a cone around the direction of the candidate minimum ionising particle, designed to give a measure of the (lack of) detector activity around its trajectory. For example, muons from W or Z boson decays are highly isolated particles that appear with a small number of tracks around them, if any. There are two qualitatively different approaches that can be used to define the isolation criterion: the track-based and the calorimeter-based algorithms.

The track-based isolation algorithm uses the transverse momenta of the reconstructed tracks from the ID as a measure of activity around the candidate's

trajectory, while the calorimeter-based isolation algorithm considers the energy deposited in the calorimeter cells around the candidate's direction. An improved discriminant is obtained using the energy deposit or the sum of transverse momenta (measured within the isolation cone, as explained above) divided by the transverse momentum of the candidate particle, effectively measuring a "normalised" activity around the particle's direction.

The main objective of this section is to quantify the performance of these isolation algorithms for candidate muons when employed within the L1 trigger system. The goal is to improve the overall background rejection for muon triggers while retaining a high overall selection efficiency at the HL-LHC. The muon isolation will be studied in two different scenarios with algorithms employing:

- calorimeter-based isolation using the existing L1 trigger information
- track-based isolation using the proposed L1 Track trigger

The track-based isolation algorithm uses a discriminant defined as the ratio of the sum of the tracks transverse momenta p_T^i inside a $\Delta R < 0.2$ cone centered around the muon candidate (excluding the muon candidate itself) to the muon candidate p_T^μ:

$$R_{iso,p_T} = \frac{\sum p_T^i}{p_T^\mu} \tag{4.1}$$

whereas the calorimeter-based isolation discriminant is defined as the ratio of the sum of the energy clusters E_T^i inside a $\Delta R < 0.2$ cone around the muon candidate (excluding the energy deposits linked to the muon candidate itself) to the muon candidate p_T^μ:

$$R_{iso,E_T} = \frac{\sum E_T^i}{p_T^\mu} \tag{4.2}$$

The tracks considered must be of good quality; i.e., they need to have at least four hits in the pixel and silicon strip detectors (silicon hits) and $p_T > 1$ GeV for muons, and at least nine silicon hits, incliding one hit in the innermost pixel layer (the b-layer). Electrons are required to have $p_T > 0.4$ GeV.

The performance comparison of the two isolation methods is presented in the following section.

4.4 Muon Isolation performance studies

4.4.1 Monte Carlo samples

The $Z \to \mu^+\mu^-$ process has been chosen for the evaluation of the signal muon efficiencies. The choice of this Monte Carlo (MC) sample was made because the muon momentum range is similar to the EW kinematic region of interest, and the muonic final state can be fully reconstructed with a combination of ID and MS measurements in the detector. The $Z \to \mu^+\mu^-$ sample is modelled at LO with the POWHEG MC generator [90], and interfaced with PYTHIA8 [91] for the parton shower and hadronisation. The CT10 PDF set [92] is used with values fixed according to the AU2 tune [93].

For the determination of background rates, a minimum bias[1] (MB) MC sample has been chosen to simulate fake or mismeasured low-p_T muons mostly from soft processes. It is modeled at LO with the POWHEG MC generator [90], and interfaced with PYTHIA8 [91] for the parton shower and hadronisation.

The detector simulation for all generated MC event samples is done with Geant4 [94, 95]. The samples used for these studies were generated with a centre of mass energy of $\sqrt{s} = 14$ TeV, a bunch crossing of 25 ns, and a pile-up of 80, in order to emulate the experimental conditions at the HL-LHC startup. At the time the study was performed, there were no additional large-statistics samples with different pile-up values available.

4.4.2 Isolation discriminant variables

The track-based R_{iso,p_T} and calorimeter-based R_{iso,E_T} discriminating variables are plotted in Figure 4.2 separately for the signal and background processes. The range of the R_{iso} values shown are between 0, corresponding to no activity around the muon trajectory inside the isolation cone, and 1, where the sum of the surrounding tracks p_T or energy clusters E_T inside the cone is numerically equal to the p_T of the muon candidate. The signal distribution peaks at $R_{iso} \to 0$ since

[1]Minimum bias are collision events with the minimum activity in the detector, occuring at a much higher rate than the typical hard process of interest at the LHC. They are sampled in the most unbiased way possible, given the detector's geometric acceptance and operational thresholds.

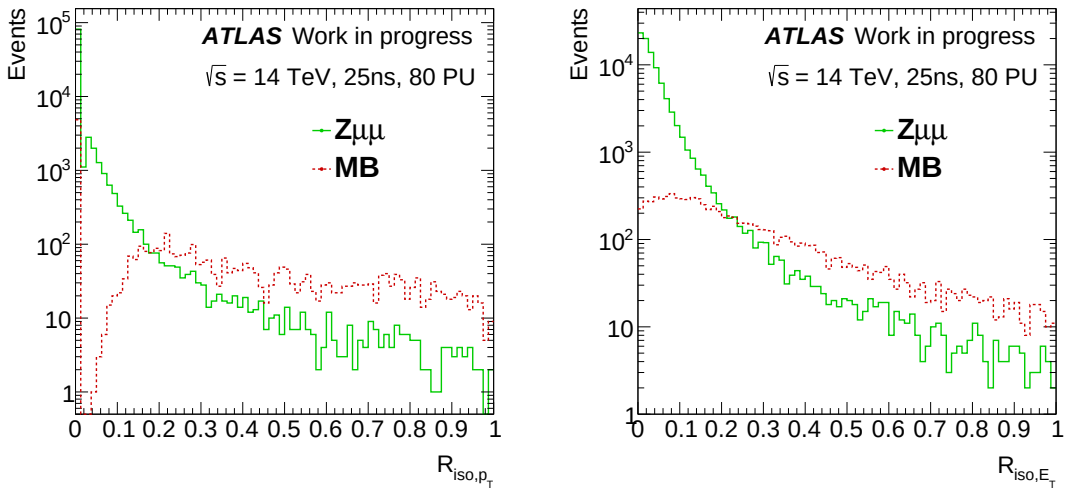

(a) *track-based isolation* **(b)** *calorimeter-based isolation*

Figure 4.2 *Distributions of the discriminating variables R_{iso,p_T} (left, Eq. 4.1) and R_{iso,E_T} (right, Eq. 4.2) for the $Z \to \mu\mu$ signal (green solid line) and MB background samples (red dashed line).*

most of the muon candidates have a single isolated track, whereas the background demonstrates much higher activity within the isolation cone, which results into an almost flat distribution for the whole range of the discriminant. This behaviour of the isolation variable for $R_{iso} \ll 1$ values will be used for further signal-background separation.

4.4.3 Event selection

The event selection is divided into three different steps.

The first step is a loose selection that corresponds to the Phase-II L0 trigger level, requiring a muon with $p_T > 2$ GeV to be within the $|\eta| < 2.7$ region. The kinematic information is obtained from the simulation of the existing L1 trigger (i.e. ignoring any Phase-I upgrades) using coarse-resolution measurements from the calorimeter and the fast trigger MS.

The second step is an emulation of the proposed L1 Track trigger that includes track information and an $\eta - \phi$ matching with the L0 RoI of the muon candidate. Since a full simulation of the L1 Track trigger is not available in the ATLAS software yet, we kept selection cuts using the existing ID (not considering the improved simulation of the ITK), and the selection of the muon track candidates

is made using offline variables that must fulfill the following requirements:

- number of hits in the Pixel detector > 0
- number of hits in the SCT > 0
- number of Pixel and SCT missing hits < 3
- $|\eta| < 2.7$
- $p_T > 5$ GeV
- number of TRT hits within the $0 < |\eta| < 1.9$ region must be > 5
- $|d_0| < 1$ mm, $|z_0| < 10$ mm
- geometric matching with the L0 RoI: $\Delta R(\text{L1Trk } \mu, \text{L0 } \mu) < 0.1$

A feasibility study that employs offline quality tracks can be used to demonstrate the performance of the L1 Track trigger in an optimal-case scenario. In the studies presented here, the track reconstruction of the muon candidate must coincide with the offline muon selection. This assumption has been taken, requiring a combined muon reconstructed by the (so-called) "third muon chain"[2].

Finally, the third step of the event selection is the isolation requirement either using the calorimeter-based or the track-based discriminant. Various selection cuts on the isolation discriminant R_{iso} between 0.06 and 1 are made, in order to find the optimal value.

4.4.4 Results

The analysis is divided in two parts.

The first study is a comparison of the track-based and the calorimeter-based isolation discriminants for an upgraded ATLAS detector that includes a L1 Track Trigger providing tracks matched to the L0 muon candidates. The idea is to test whether a track-based isolation algorithm offers better performance than the calorimeter-based isolation algorithm for a system with an installed L1 Track

[2]The "third muon chain" is one of the available offline ATLAS muon reconstruction options (the first two being the so-called MUID and STACO options) and the current recommendation by the Muon group. It employs a method that combines the first and second options for the muon reconstruction.

trigger. The isolation requirement is applied on top of the simple requirement of a good-quality track matched to the muon candidate (which is expected to provide some non-negligible background rate reduction).

The second study goes a step further, and examines the performance of the two isolation algorithms for two different detector scenarios, one with and a second one without an installed L1 Track trigger. In the scenario of a detector with (without) a L1 Track trigger, the track (calorimeter), -based isolation algorithm is used. In this second study, we evaluate the overall improvement in the trigger performance that combines a track-based isolation algorithm with the matching of a good-quality track to a L0 muon candidate.

Each one study is done by evaluating signal efficiencies for different p_T-bins in order to test the trigger performance for various physics cases. The chosen values are: $p_T > 5$, 15, 30, 50 GeV. This selection is applied only for the calculation of signal efficiencies, and uses offline muon reconstruction information.

First study: Isolation for the track- and calorimeter-based algorithms

In this section we compare the performance of the two isolation discriminants for a common detector architecture including a L1 Track trigger. The RoI is defined initially by the L0 trigger level, followed by varying thresholds of the isolation discriminant variables.

Signal efficiency and rejection plots are used to check the performance of each algorithm. Efficiency is calculated using the $(Z \to \mu\mu)$ signal sample, while the rejection is calculated using the (MB) background sample. The efficiencies are calculated per muon with respect to the L0 selection. In this section the signal efficiency and rejection are defined as:

$$\begin{aligned} \text{Efficiency} &= \frac{\#\text{ events surviving L0 + L1Trk} + R_{iso}}{\#\text{ events surviving L0}} \\ \text{Rejection} &= \frac{\#\text{ events surviving L0}}{\#\text{ events surviving L0 + L1Trk} + R_{iso}} \ , \end{aligned} \tag{4.3}$$

Figure 4.3 shows the efficiency and rejection for the two isolation discriminant variables as a function of the R_{iso} threshold for various p_T-bin groups. The overall performance of the two isolation algorithms is similar.

The efficiency is slightly higher for the track-based isolation algorithm for every

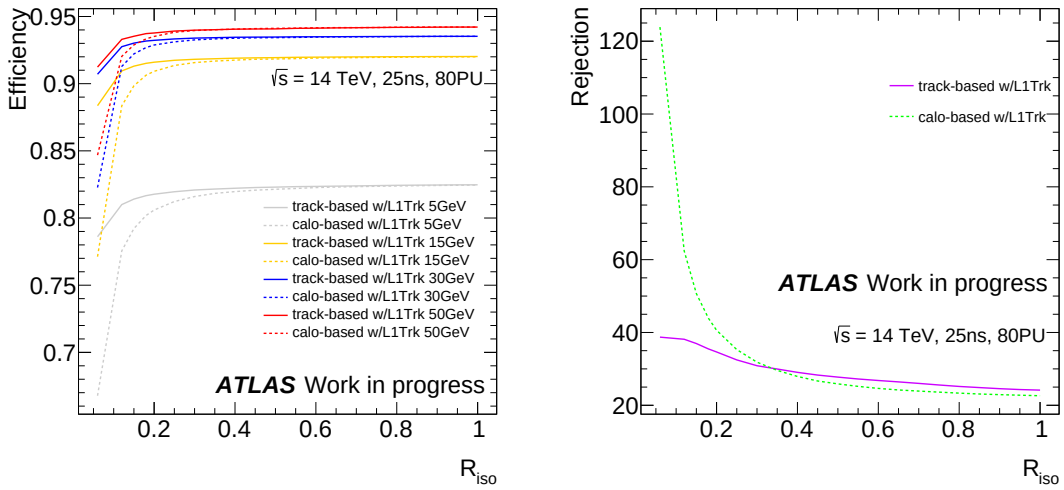

(a) *Efficiency* **(b)** *Rejection*

Figure 4.3 *(a) Efficiency and (b) Rejection comparisons between the p_T - (solid lines) and E_T - (dashed lines) based isolation algorithms for a system including a L1 Track trigger as a function of the R_{iso} selection cut for different p_T-bin groups of signal muons.*

p_T-bin group considered. The p_T-based isolation algorithm has a steeper turn-on curve, which translates into an approximate 5% difference in the efficiency for the $p_T > 5$ GeV selection in the $R_{iso,p_T} < 0.25$ area and below the plateau region. After that point the two distributions get closer to each other. This efficiency difference tends to be smaller for higher p_T-bin groups. The efficiency plateau for muons with $p_T > 15$ GeV is reached approximately at $R_{iso,p_T} \sim 0.2$ and $R_{iso,E_T} \sim 0.35$ for the track- and calorimeter-based isolation algorithms, respectively. The plateau efficiency for all p_T-bin muon groups (except muons with $p_T > 5$ GeV) tends to reach the same value, pointing to the observation that any inefficiencies of the isolation algorith are independent from the muon p_T.

The background rejection can increase by a factor between 120 and 38 (depending on the isolation selection cut) with respect to the default selection by using the calorimeter-based or the track-based isolation algorithms, respectively. Even though the calorimeter-based algorithm appears to offer better rejection, one notes that the high rejection values are achieved for R_{iso} values that are below the signal efficiency plateau region. When considering only R_{iso} values in the plateau region, the two isolation algorithms show similar rejection. Since the operational point of the isolation discriminant would need to lie in the efficiency plateau region, the background rejection of both isolation algorithms brings an improvement of about a factor of 30 with respect to not requiring isolation. The

trigger performance increases considerably compared to a detector without a Level-1 Track trigger.

Second study: Isolation with and without a L1 Track trigger

In this section we will be comparing the combined performance of the track-based isolation algorithm with the matching of the L0 muon candidate to a track, to the calorimeter-based isolation algorithm performance for a system without a L1 Track trigger (and for which, there is no tracking information available). In both cases the L0 trigger level defines the RoI, but the isolation algorithm is applied over a different group of muon candidates (since the matching of L0 muon candidates to tracks occurs only for the system that includes a Level-1 Track Trigger).

As discussed previously, the efficiencies are calculated per muon with respect to the L0 selection. For the scenario including the L1 Track trigger, one can factor out the efficiency for the isolation selection alone (i.e. excluding the step in which the L0 muon candidate is matched to a track). Eq. 4.3 shows the efficiency and rejection when the L1 Track selection is included, whereas when it is not included is defined as:

$$\begin{aligned} \text{Efficiency} &= \frac{\#\text{ events surviving L0} + R_{iso}}{\#\text{ events surviving L0}} \\ \text{Rejection} &= \frac{\#\text{ events surviving L0}}{\#\text{ events surviving L0} + R_{iso}} \end{aligned} , \tag{4.4}$$

Figure 4.4 shows the comparison in the performance (efficiency and rejection) of the isolation selection for the two cases (a L1 Track trigger is included/not included in the system) as a function of the R_{iso} threshold for various p_T-bins.

For the system without the L1 Track trigger, the background rejection increases on average by a factor of 3 when the (calorimeter-based) isolation selection is applied. For the system including the L1Track trigger, the rejection increases by a factor of 30 times on average. Therefore, we observe that the step of matching the L0 muon candidate to a track improves the rejection of the trigger by a factor of 10, at an efficiency cost of about 7% (reducing the number of muons that reach the isolation filtering stage). The inefficiency is different for muons of different p_T-bins, as can be clearly seen in the plateau region. On the other hand, the selection efficiency of the isolation algorithm with respect to the previous level of

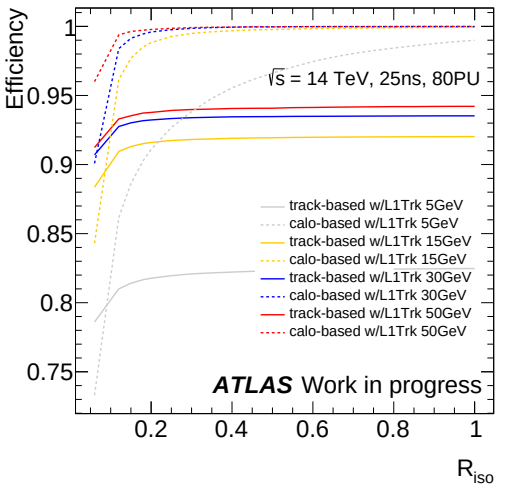

(a) *Efficiency*

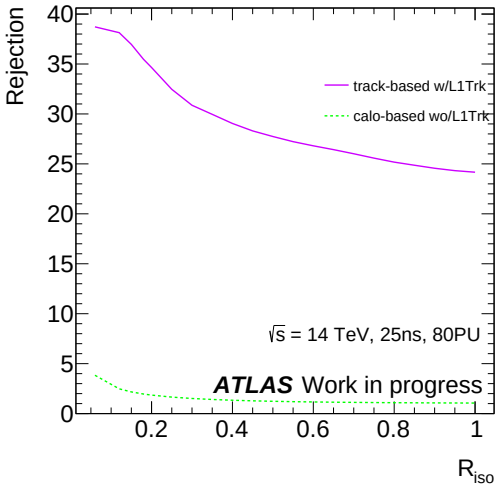

(b) *Rejection*

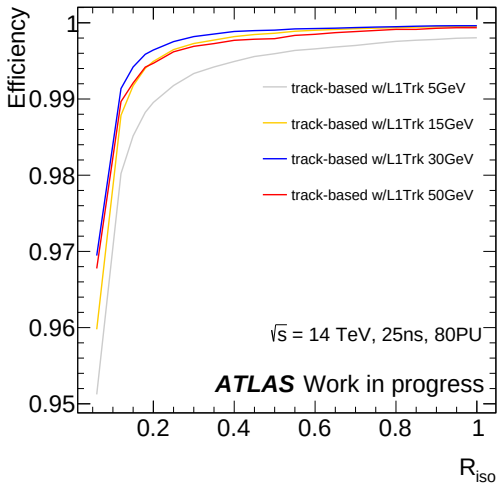

(c) *Efficiency Isolation*

Figure 4.4 *(a) Efficiency and (b) Rejection isolation algorithm comparisons between a system that includes a L1 Track trigger (solid lines) and a system that does not (dashed lines) as a function of the R_{iso} selection cut for different p_T-bin groups of signal muons. (c) Efficiency of the p_T -based isolation algorithm with respect to the track-matching step, as a function of the R_{iso} selection cut for different p_T-bin groups of signal muons.*

matching the L0 candidate to a track is above 99%, as can be seen in Figure 4.4c.

Conclusion of muon isolation studies with a L1 Track trigger

We conclude that the inclusion of a L1 Track trigger improves the trigger performance for muon events by providing access to tracking information (that reduces the number of fake muons) and by giving the option of an additional isolation algorithm. The step of matching L0 muon candidates to tracks gives an average rejection of a factor of 10, with an inefficiency of about 7%. Applying an isolation algorithm on top of the track-matching step gives an additional rejection of about 20% for a negligible efficiency loss. We find no significant difference on the isolation algorithm performance between track-based and calorimeter-based algorithms, however these studies should be repeated for a wider range of pile-up signal and background samples.

Chapter 5

The phenomenology of the Higgs to four lepton channel

The Higgs to four lepton analysis was one of the main channels that contributed to the Higgs boson discovery [96] and the measurement of its properties, such as spin/parity [38] and couplings [97]. This chapter presents an overview of the main phenomenological features of the $H \to ZZ^{(*)} \to 4\ell$ search, highlighting the kinematic variables of the final state that can be reconstructed and used as discriminants. It also includes the theoretical description of the off-shell mass process which forms the basis of the analysis presented at the next chapter.

5.1 Overview of the $H \to ZZ^{(*)} \to 4\ell$ process

The $H \to ZZ^{(*)} \to 4\ell$ search considers a final state with four (charged) leptons[1] that must be highly isolated. This is the golden mode to study the Higgs boson since leptons provide a clean final state with rich kinematic information. This final state is quite distinct from the typical QCD multi-jet process, which is the dominant background at the LHC. Taus are not considered in this analysis since they are not, strictly speaking,"final state" particles but decay rapidly to smaller-mass leptons (approximately 35% of the time) or hadrons (approximately 65% of the time), leading unfortunately to a more complicated final state to be

[1]In this document we are using the simplified term "leptons" instead of the more accurate "charged leptons".

reconstructed. Since each pair of leptons comes from a Z boson decay, they must have opposite charge (± 1) and same flavour (ee or $\mu\mu$) in order to be invariant under the discrete charge and lepton number symmetries. Every Higgs *candidate* event requires two intermediate Z bosons, each decaying to a pair of leptons. Since the (by now measured) mass of the Higgs boson is smaller than the sum of the mass of two Z bosons (approximately 190 GeV), one of the Z bosons has to be produced off-shell because of energy conservation. The Z boson candidate that has a reconstructed mass closer to the actual Z pole mass value is labelled Z_1, while the second one is labelled Z_2.

The probability of the Higgs boson with mass $m_H = 125$ GeV to decay to a pair of Z bosons is already very small (3%) before taking into account the further decay of the Z boson to a pair of leptons. Figure 5.1a shows that the branching fraction (BF) of a Z boson to a pair of charged leptons is 10.3% (by excluding the τ lepton the BF becomes 6.7%), leaving a combined branching fraction of the Higgs decay to four leptons of just 0.01%. For example, in an analysis that considers Higgs boson decays into pairs of vector bosons (WW or ZZ) as intermediate particles, the $H \to ZZ^{(*)} \to 4\ell$ golden channel represents just 0.1% of the full decay rate. (Figure 5.1b).

Nevertheless, one of the advantages of the $H \to ZZ^{(*)} \to 4\ell$ channel is that the signal is easily identified, the background is very small, and the energy resolution to reconstruct the Higgs is excellent. The main background consists of misidentified pairs of leptons that originate from QCD jets and other processes that mimic the same final state as the signal. The contribution of these processes after the analysis selection is very low, resulting in a channel with the highest signal/background ratio of all the Higgs analyses.

5.2 Kinematic observables

The $H \to ZZ^{(*)} \to 4\ell$ channel has the great advantage of having a fully reconstructed final state with high-precision kinematic information due to the excellent lepton reconstruction efficiency and resolution of the ATLAS detector. The four-body final state offers a rich range of kinematic observables that can be used to distinguish between the signal and background processes, and to extract the properties of the Higgs boson.

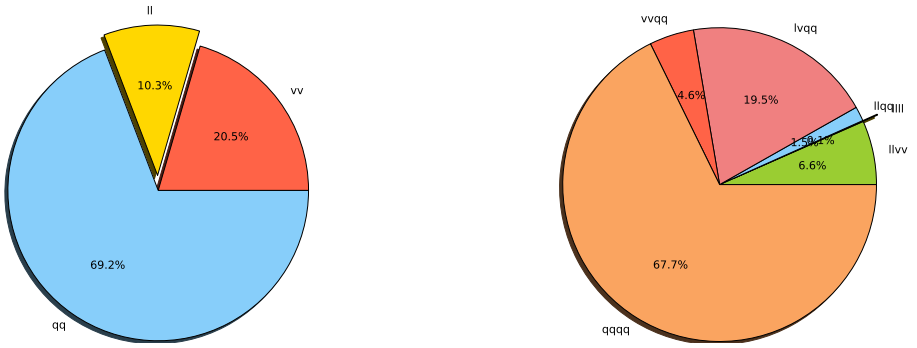

(a) **(b)**

Figure 5.1 *(a) Leptonic and hadronic branching fractions of Z boson decays. (b) Breakdown of the leptonic, semileptonic and hadronic final states in the $H \to VV$ channel with $V = W,\ Z$, for a Higgs boson mass of $m_H = 125$ GeV.*

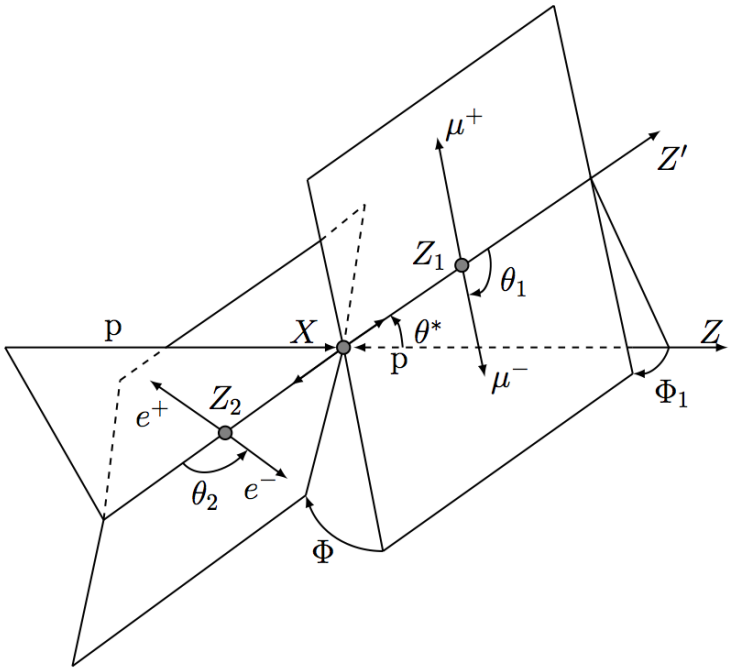

Figure 5.2 *Definition of the production and decay angles in an $X \to ZZ^{(*)} \to 4\ell$ decay, where the X could be a Higgs boson. The illustration is drawn with the beam axis in the lab frame, the Z_1 and Z_2 in the X rest frame and the leptons in their corresponding parent rest frames.*

The final state can be described with the 3D momentum components of each lepton. By making the good approximation that the leptons are massless, this results in $4 \times 3 = 12$ degrees of freedom. By considering the initial state before the Higgs boson decay, we have four degrees of freedom from its four-momentum (p_T,

η, ϕ and m_H), which relates the Lorentz boost of the Higgs boson rest frame with respect to the initial partonic state. Two additional degrees of freedom appear from the invariant masses of the two Z bosons, m_{Z_1} and m_{Z_2}. This leaves six degrees of freedom available for the angles between the particles of the process. Five of these angles are illustrated in Figure 5.2, while the sixth angle (Φ^*) defines the global rotation of an event in the plane transverse to the collision axis, so its offset is arbitrary and therefore not shown. These angles are defined in the rest frame of the four leptons. They are defined explicitly [98] through the momentum of the leptons as follows:

- $\theta^* \in [0, \pi]$ is the production angle defined through the unit vector of the Z_1 direction, $\hat{q_1} = (\sin\theta^* \cos\Phi^*, \sin\theta^* \sin\Phi^*, \cos\theta^*)$, in the rest frame of the Higgs boson. In this reference frame, the collision axis is aligned with the z axis, $\hat{n_z} = (0, 0, 1)$, taken as the direction of one of the colliding hadrons.

- $\Phi \in [-\pi, \pi]$ and $\Phi_1 \in [-\pi, \pi]$ are the two azimuthal angles between the three planes constructed from the Higgs boson decay products and the two Z bosons, in the Higgs rest frame, defined as:

$$\begin{aligned} \phi &= \frac{q_1 \cdot (\hat{n}_1 \hat{n}_2)}{|q_1 \cdot (\hat{n}_1 \hat{n}_2)|} \times \cos^{-1}(-\hat{n}_1 \cdot \hat{n}_2) \\ \phi_1 &= \frac{q_1 \cdot (\hat{n}_1 \hat{n}_{sc})}{|q_1 \cdot (\hat{n}_1 \hat{n}_{sc})|} \times \cos^{-1}(-\hat{n}_1 \cdot \hat{n}_{sc}) \end{aligned} \tag{5.1}$$

  where the normal vectors for the three planes are defined as:

$$\begin{aligned} \hat{n}_1 &= \frac{q_{11} \times q_{12}}{|q_{11} \times q_{12}|} \\ \hat{n}_2 &= \frac{q_{21} \times q_{22}}{|q_{21} \times q_{22}|} \\ \hat{n}_{sc} &= \frac{\hat{n_z} \times q_1}{|\hat{n_z} \times q_1|} \end{aligned} \tag{5.2}$$

  where the three-momenta q_i and q_{ii} are defined as in Figure 5.3 in the Higgs rest frame.

- $\theta_1 \in [0, \pi]$ and $\theta_2 \in [0, \pi]$ are the decay angles, defined as:

$$\begin{aligned} \theta_1 &= cos^{-1}(-\frac{q_2 \cdot q_{11}}{|q_2||q_{11}|}) \\ \theta_2 &= cos^{-1}(-\frac{q_1 \cdot q_{21}}{|q_1||q_{21}|}) \end{aligned} \tag{5.3}$$

where the three-momenta are defined in their respective Z boson rest frame.

The transverse momentum and the rapidity of the Higgs boson depend on the details of the production mechanism. They are not considered here because they introduce additional uncertainties due to QCD effects. Further details are mention in Sect. 6.1.5.

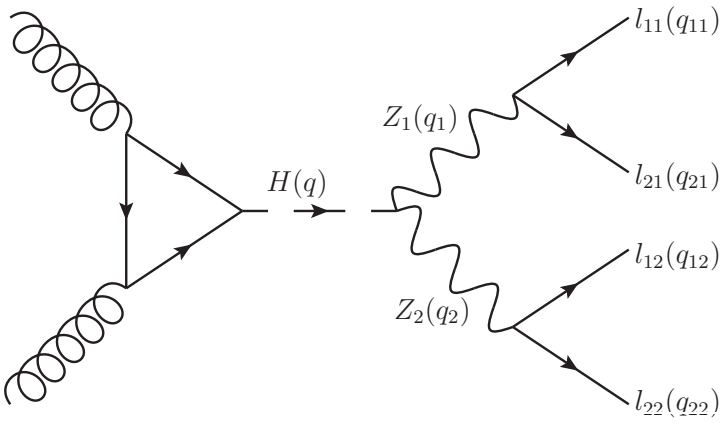

Figure 5.3 *Feynman diagram for the $gg \to H \to ZZ^{(*)} \to 4\ell$ signal process. The labels identify the four-momenta of the Higgs and Z bosons, and the leptons, as used in the text.*

5.3 The off-shell mass processes

5.3.1 Introduction to the off-shell $H^{(*)} \to ZZ$ processes

The differential cross-section of the Higgs boson production through gluon fusion with a subsequent decay into Z boson pairs at an energy scale $\hat{s}$ is given by:

$$\frac{d\sigma(gg \to H^* \to ZZ)}{dm_{4\ell}}(\hat{s}) \sim \frac{\kappa_g^2(\hat{s}) \cdot \kappa_Z^2(\hat{s})}{(m_{4\ell}^2 - m_H^2)^2 + m_H^2 \Gamma_H^2} \tag{5.4}$$

where $\kappa_g(\hat{s})$ and $\kappa_Z(\hat{s})$ are the couplings associated with the $gg \to H^*$ production and the $H^* \to ZZ$ decay, respectively; $m_{4\ell}$ is the invariant mass of the dilepton pairs from the Z boson decays, and m_H is the mass of the Higgs boson.

The equation can be worked on separately for two different cases, depending on whether the Higgs boson is produced on-shell or off-shell. In the off-shell case, the

invariant mass $m_{4\ell}$ is larger than the Higgs boson mass m_H, and the denominator becomes: $(m_{4\ell}^2 - m_H^2)^2 + m_H^2\Gamma_H^2 \sim m_{4\ell}^4$. Then, the cross-section $\sigma_{\text{off-shell}}^{gg\to H^*\to VV}$ for the off-shell Higgs boson is:

$$\sigma_{\text{off-shell}}^{gg\to H^*\to ZZ}(\hat{s}) \sim \kappa_{g,\text{off-shell}}^2(\hat{s}) \cdot \kappa_{Z,\text{off-shell}}^2(\hat{s}) \quad , \tag{5.5}$$

The cross-section for on-shell Higgs production depends on the total width Γ_H.

$$\mu_{\text{on-shell}} \equiv \frac{\sigma_{\text{on-shell}}^{gg\to H\to ZZ}}{\sigma_{\text{on-shell, SM}}^{gg\to H\to ZZ}} = \frac{\kappa_{g,\text{on-shell}}^2 \cdot \kappa_{Z,\text{on-shell}}^2}{\Gamma_H/\Gamma_H^{\text{SM}}}, \tag{5.6}$$

On the contrary, the off-shell Higgs boson production, $\sigma_{\text{off-shell}}^{gg\to H^*\to ZZ}$, is independent of the total Higgs boson decay width Γ_H [99, 100].

Using the framework for Higgs boson coupling deviations as described in Ref. [40], the off-shell signal strength in the high-mass region, can be expressed as:

$$\mu_{\text{off-shell}}(\hat{s}) \equiv \frac{\sigma_{\text{off-shell}}^{gg\to H^*\to ZZ}(\hat{s})}{\sigma_{\text{off-shell, SM}}^{gg\to H^*\to ZZ}(\hat{s})} = \kappa_{g,\text{off-shell}}^2(\hat{s}) \cdot \kappa_{Z,\text{off-shell}}^2(\hat{s}) \quad , \tag{5.7}$$

The on-shell propagator follows the narrow-width approximation [101], where the denominator becomes: $(m_{4\ell}^2 - m_H^2)^2 + m_H^2\Gamma_H^2 \sim m_H^2\Gamma_H^2$. Then, the cross-section $\sigma_{\text{on-shell}}^{gg\to H^*\to ZZ}$ for the on-shell Higgs boson is:

$$\sigma_{\text{on-shell}}^{gg\to H\to ZZ} = \frac{\kappa_{g,\text{on-shell}}^2 \cdot \kappa_{Z,\text{on-shell}}^2}{\Gamma_H} \quad , \tag{5.8}$$

Assuming that the on-shell and off-shell couplings are identical in the analysis region, the Higgs boson total width can be calculated as the ratio of $\mu_{\text{off-shell}}$ with $\mu_{\text{on-shell}}$.

$$\Gamma_H/\Gamma_H^{\text{SM}} = \frac{\mu_{\text{off-shell}}}{\mu_{\text{on-shell}}} \tag{5.9}$$

However, the previous assumption does not consider possible new physics that could be included in the $gg \to H$ loop production process, changing the running value of the effective coupling $\kappa_g(\hat{s})$. Futher studies that consider exotics fields in the off-shell signal region are given in Refs. [102–106]. Given the current sensitivity of the analysis, the most conservative assumption in the measurement of an upper limit on the total width is:

$$\kappa_{g,\text{on-shell}}^2 \cdot \kappa_{Z,\text{on-shell}}^2 \leq \kappa_{g,\text{off-shell}}^2 \cdot \kappa_{Z,\text{off-shell}}^2 \, , \tag{5.10}$$

meaning that the on-shell couplings are the same or smaller than the off-shell ones. In the hypothetical case that there are new fields in the high-mass region that modify the signal couplings, it is assumed that the background predictions remain the same. In this case, there are no sizable kinematic modifications to the off-shell signal, nor new signals unrelated to this analysis that alter the off-shell signal strength [107, 108].

5.3.2 Signal and background processes

The signal and background processes considered in the analysis are illustrated in the Feynman diagrams of Fig. 5.4. The main background is the $q\bar{q} \to ZZ$ process (Fig. 5.4c). The $gg \to ZZ$ background process (Fig. 5.4b) shares the same initial and final states as the $gg \to H^* \to ZZ$ signal (Fig. 5.4a). This means that the signal cannot be treated independently from the $gg \to ZZ$ background process since there is a sizable negative interference between the two terms [99]. The interference term also depends on the off-shell coupling, since the amplitude includes a signal component:

$$\begin{aligned} < \mathcal{M} >^2 &= < \mathcal{M}_{gg\to H^*\to ZZ} >^2 + < \mathcal{M}_{gg\to ZZ} >^2 \\ &+ 2 < \mathcal{M}_{gg\to H^*\to ZZ} >< \mathcal{M}_{gg\to ZZ} >, \end{aligned} \tag{5.11}$$

then, the interference term is proportional to $\sqrt{\mu_{\text{off-shell}}} = \kappa_{g,\text{off-shell}} \cdot \kappa_{Z,\text{off-shell}}$.

In the following, the notation $gg \to (H^* \to)ZZ$ is used for the combined signal plus background process, including the Higgs boson signal (S) $gg \to H^* \to ZZ$ component, the continuum background (B) $gg \to ZZ$ component, and their interference. For the vector-boson fusion (VBF) production, the analogous notation VBF $(H^* \to)ZZ$ is used for the full signal plus background process, with VBF $H^* \to ZZ$ representing the Higgs boson signal and VBF ZZ denoting the background.

While higher-order QCD and EW corrections have been calculated for the off-shell signal process $gg \to H^* \to ZZ$ [109] in the form of a next-to-next-to-leading-order (NNLO) K-factor ($\mathrm{K}^{H^*}(m_{4\ell}) \equiv \sigma^{\text{NNLO}}_{gg\to H^*\to ZZ}/\sigma^{\text{LO}}_{gg\to H^*\to ZZ}$), no higher-order QCD calculations were available for the leading-order (LO) $gg \to ZZ$ background process at the time of the analysis.

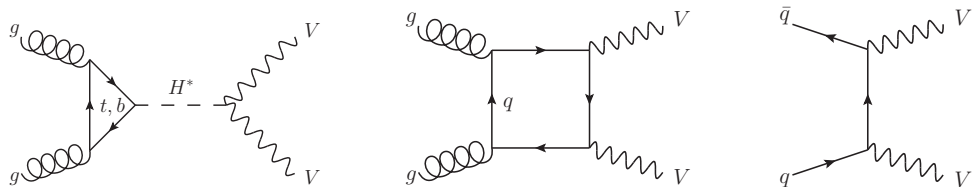

Figure 5.4 *The leading-order Feynman diagrams for 5.4a the $gg \to H^* \to VV$ signal, 5.4b the continuum $gg \to VV$ background and 5.4c the $q\bar{q} \to VV$ background.*

5.4 Data and Monte Carlo samples

The dominant processes contributing to the high-mass signal region in the $ZZ \to 4\ell$ chanel are:

- $gg \to (H^*) \to ZZ$, that includes the off-shell signal $gg \to H^* \to ZZ$, the continuum background $gg \to ZZ$, and the interference between these two
- ZZ production, in association with two jets through VBF and VH-like production modes, $pp \to VV + 2j$ ($s-$, $t-$ and $u-$channels)
- $q\bar{q} \to ZZ$ (irreducible background)
- Z+jets and $t\bar{t}$ (reducible background)

In the following, a Higgs boson mass of $m_H = 125.5$ GeV, close to the ATLAS-measured Higgs boson mass value of 125.36 GeV [11], is assumed for the off-shell signal processes. This small difference has a negligible impact on the predicted off-shell production yields, as shown in Appendix A.

Signal and background distributions are generated and used in this study. The detector simulation for all generated Monte Carlo (MC) event samples is done with Geant4 [94, 95]. The signal and background differential cross-sections as a function of the four-lepton invariant mass ($m_{4\ell}$) is shown in Figure 5.5. The plot illustrates the gluon-induced distributions in the $2e2\mu$ final state after applying the event selections from the analysis discussed later in this thesis on generator-level quantities. The signal plus background process $gg \to (H^* \to)ZZ \to 2e2\mu$ is shown with the SM parameters ($\mu_{\text{off-shell}} = 1$) and amplified by a factor of 10 with respect to the SM case ($\mu_{\text{off-shell}} = 10$). The $gg \to H^* \to ZZ$ signal contribution

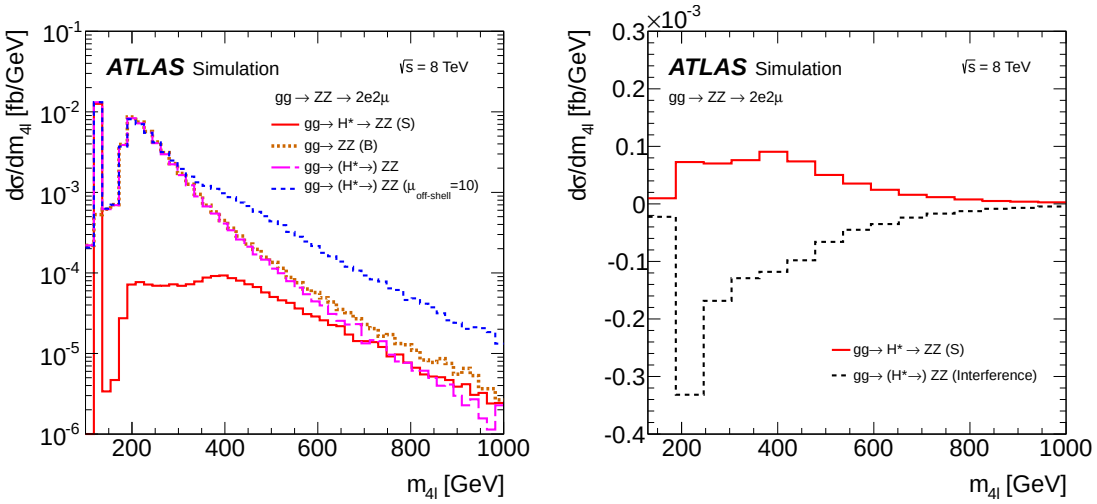

(a) **(b)**

Figure 5.5 *(a) Differential cross-sections as a function of the four-lepton invariant mass $m_{4\ell}$ in the range of 100 GeV $< m_{4\ell} <$ 1000 GeV for the $gg \to (H^* \to)ZZ \to 2e2\mu$ process at the parton level, the $gg \to H^* \to ZZ$ signal (red solid line), the $gg \to ZZ$ continuum background (thick brown dotted line), the $gg \to (H^* \to)ZZ$ with SM Higgs couplings (magenta long-dashed line, including a $\mu_{off\text{-}shell} = 1$ signal plus background plus interference) and $gg \to (H^* \to)ZZ$ with $\mu_{off\text{-}shell} = 10$ (blue long-dashed line, including a $\mu_{off-shell} = 10$ signal plus background plus interference.) (b) Differential cross-section as a function of $m_{4\ell}$ in the range of 130 GeV $< m_{4\ell} <$ 1000 GeV for the $gg \to H^* \to ZZ \to 2e2\mu$ signal (solid red line) and its interference with the $gg \to ZZ \to 2e2\mu$ continuum background (black dashed line).*

becomes negligible above the Higgs boson mass peak and up to the $m_{4\ell} \sim 2m_t$ region, where it is comparable to the continuum $gg \to ZZ$ component. The interference between the $gg \to H^* \to ZZ$ signal and the $gg \to ZZ$ background processes has a negative sign over the whole mass range.

The present analysis is performed on data corresponding to an integrated luminosity of 20.3 fb^{-1} at a collision energy of $\sqrt{s} = 8$ TeV.

5.4.1 Simulation of $gg \to (H^* \to)ZZ$

We have used the LO MC generators gg2VV [99, 110] and MCFM [111, 112] integrated with PYTHIA8 [91] for showering, and SHERPA+OpenLoops [113–116] to generate the $gg \to H^* \to ZZ$ and $gg \to ZZ$ processes, including the

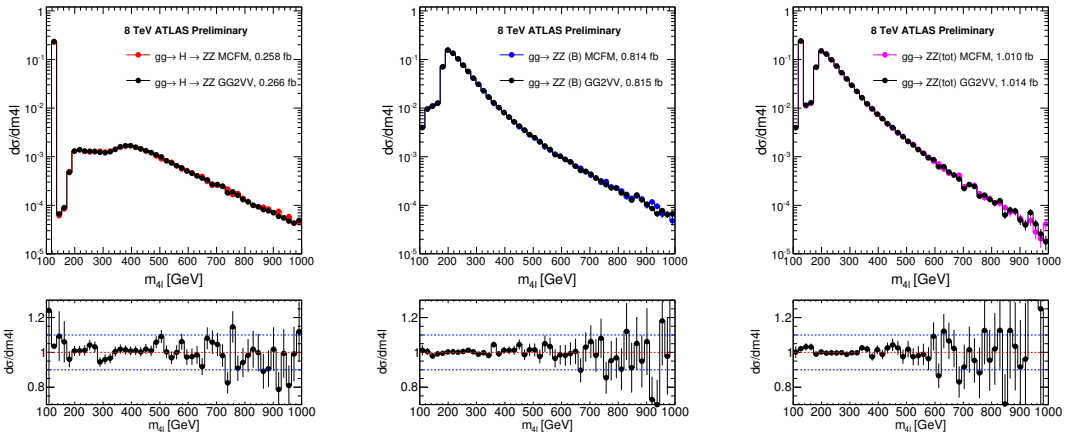

Figure 5.6 *Comparison of the $m_{4\ell}$ distributions between gg2VV and MCFM in the $gg \to ZZ \to 2e2\mu$ channel at the matrix element level for (a) the Higgs signal $gg \to H^* \to ZZ$, (b) background continuum $gg \to ZZ$, and (c) the total $gg \to (H^* \to)ZZ$ process.*

interference. The two signal generators, gg2VV and MCFM, are consistent with each other in the cross-section prediction and the description of the distribution in the off-shell region; MCFM is chosen as baseline for this analysis. The QCD renormalisation and factorisation scales are set to $m_{4\ell}/2$ [111]. The CT10 next-to-next-to-leading-order (NNLO) PDF set [92] is used, as the LO $gg \to ZZ$ process is part of the NNLO calculation for $pp \to ZZ$. The default parton showering and hadronisation option for the events processed with the full detector simulation is PYTHIA8 with the "power shower" parton shower option [91].

For the $gg \to H^* \to ZZ$ signal, a NNLO/LO K-factor[2] including the next-to-leading-order (NLO) electroweak corrections, $\mathrm{K}^{H^*}(m_{4\ell}) = \sigma^{\mathrm{NNLO}}_{gg\to H^*\to ZZ}/\sigma^{\mathrm{LO}}_{gg\to H^*\to ZZ}$, is applied. The K-factor and associated uncertainties are calculated in Ref. [109] as a function of the Higgs boson virtuality $m_{4\ell}$ for m_H ∼125.5 GeV, using the MSTW2008 PDF set [26] (see Fig. 5.7a). However in the MC simulation, the CT10(NNLO) PDF set is used for consistency with the NNLO $qq \to ZZ$ calculation giving the LO cross-section $\sigma_{\mathrm{LO,CT10(NNLO)}}(m_{4\ell})$. To account for the difference in the PDF sets used in the simulation and the higher order QCD calculations, a $m_{4\ell}$-dependent PDF re-weighting is applied first to calculate the

[2]The shorter $gg \to X$ notation is used also in the context of higher-order QCD calculations with qg and qq initial states also contributing to the full $pp \to X$ process.

higher order QCD predictions of the $gg \to H$ cross-sections, as follows:

$$\begin{aligned}\sigma_{\text{NNLO,CT10NNLO}}(m_{4\ell}) &= \sigma_{\text{LO,CT10NNLO}}(m_{4\ell}) \cdot \mathrm{K}^{H*}_{\text{NNLO,MSTW}}(m_{4\ell}) \\ &\cdot \frac{\text{MSTW(LO)}(m_{4\ell})}{\text{MSTW(NNLO)}(m_{4\ell})}\end{aligned} \tag{5.12}$$

The re-weighting function MSTW(LO)/MSTW(NNLO) is shown in Figure 5.7c. A factor CT10(NNLO)/MSTW(NNLO) was incorrectly omitted in the derivation of this PDF re-weighting. This missing correction, shown in Figure 5.7d, has a negligible impact compared to the large uncertainties and is therefore neglected. Figure 5.7e shows the resulting NNLO/LO K-factor for the CT10NNLO PDF.

As mentioned earlier, for the $gg \to ZZ$ continuum processes, Matrix Element (ME) calculations are only available at LO. As a workaround, we note that the effect of the NLO QCD corrections are studied for the WW final state in Ref. [117] in the soft-collinear approximation. This approximation is considered suitable for the Higgs boson production at high-mass. In particular, studies show that the soft-collinear approximation can be used for both the $gg \to WW$ background and the $gg \to H \to WW$ signal processes, and therefore the signal-background interference term as well, within an uncertainty of about 30%. The same approximation should also be applicable for the ZZ final state and the off-shell Higgs process as well.

Given that the K-factor $\mathrm{K}(gg \to ZZ)$ for the $gg \to ZZ$ background process and subsequently the interference with the signal process are not known, the results of this study are given as a function of the ratio, R, of unknown K-factors for the $gg \to ZZ$ background and the $gg \to H^* \to ZZ$ signal, defined as:

$$\mathrm{R}^{B}_{H^*} = \frac{\mathrm{K}(gg \to ZZ)}{\mathrm{K}(gg \to H^* \to ZZ)} = \frac{\mathrm{K^B}(m_{4\ell})}{\mathrm{K}^{H^*}_{gg}(m_{4\ell})}\,, \tag{5.13}$$

where $\mathrm{K^B}(m_{4\ell})$ is the unknown mass-dependent K-factor for the $gg \to ZZ$ background, and $\mathrm{K}^{H^*}_{gg}(m_{4\ell})$ is the gluon-initiated K-factor [109] for the signal[3] as motivated by the soft-collinear approximation in Ref. [117]. Since the K-factor $\mathrm{K}^{H^*}_{gg}(m_{4\ell})$ changes by less than 10% as a function of $m_{4\ell}$ in the relevant region of phase space, no mass dependence on $\mathrm{R}^{B}_{H^*}$ is assumed. We choose the

[3]Numerically, $\mathrm{K}^{H^*}_{gg}(m_{4\ell})$ differs from $\mathrm{K}^{H^*}(m_{4\ell})$ by $\sim$ 2%, as the higher-order QCD contributions from qg and qq production are small. However, $\mathrm{K}^{H^*}_{gg}(m_{4\ell})$ has substantially larger uncertainties than $\mathrm{K}^{H^*}(m_{4\ell})$. Therefore, the 2% shift in the central value is ignored here, and the difference is taken into account in the treatment of the systematic effects.

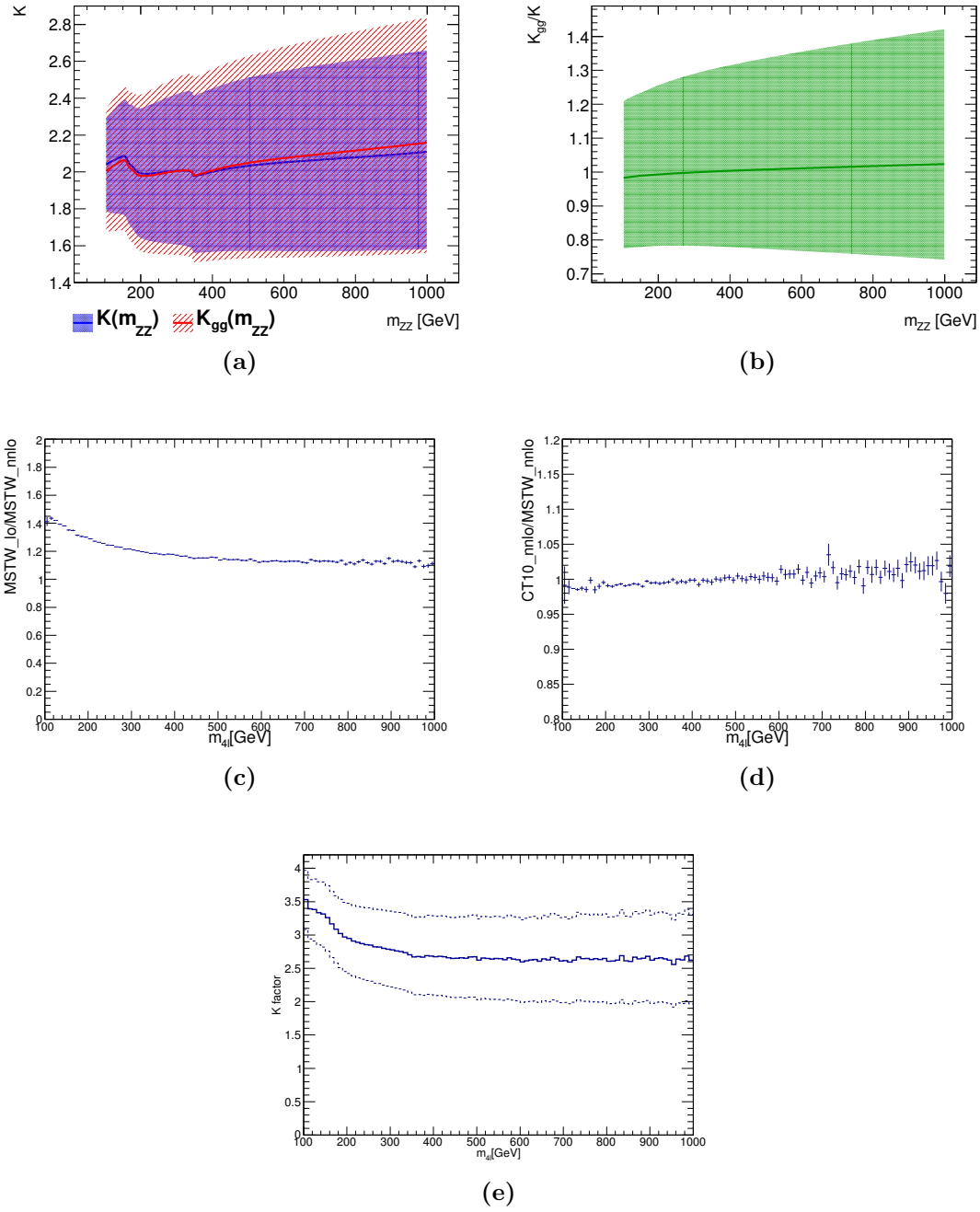

Figure 5.7 *(a): K-factors $K^{H^*}(m_{4\ell})$ and $K^{H^*}_{gg}(m_{4\ell})$ from Ref. [109]. (b): ratio of the K-factors $K^{H^*}_{gg}(m_{4\ell})$and $K^{H^*}(m_{4\ell})$ from Ref. [109]. (c): PDF re-weighting function for the off-shell $gg \to H$ K-factor ($m_H = 125.5$) between the MSTW and MSTWNNLO PDF sets. (d): The CT10(NNLO)/MSTW(NNLO) factor that was incorrectly omitted in the PDF re-weighting of Fig. (c), see text for details. (e): Differential K-factors in the Higgs production for $m_H = 125.5$ GeV using the CT10NNLO PDF. The solid line represents the predictions for the nominal $\mu_R = \mu_F = m_{4\ell}/2$ set of parameter values, with the two dashed lines representing the theoretical uncertainty bands obtained by varying the QCD scales between $m_{4\ell}/4$ and $m_{4\ell}$.*

range 0.5–2 for the variation of the K-factor ratio $\mathrm{R}^{B}_{H^*}$ in order to include the full correction from the signal K-factor $\mathrm{K}^{H^*}_{gg}(m_{4\ell}) \sim 2$ in the variation range. With respect to the LO $gg \to ZZ$ process, this corresponds to an absolute variation in the approximate range 1–4. The ansatz of using $\mathrm{R}^{B}_{H^*}$ to parametrise the uncertainty on missing higher order corrections leads to large cancellations between the interference and the background terms. We choose to apply the 30% uncertainty, derived in Ref. [117] for the interference component, on the $\mathrm{R}^{B}_{H^*}$ itself. Likely, this constitutes an overestimate of the uncertainties; however, without additional theory input one cannot disentangle the effects, and albeit conservative, this is a safe approach in the treatment of the $\mathrm{R}^{B}_{H^*}$ uncertainties.

Using the K-factors discussed above, the cross-section for the $gg \to (H^* \to)ZZ$ process for an arbritary off-shell Higgs boson signal strength $\mu_{\text{off-shell}}$ can be parameterised as:

$$\begin{aligned} \sigma_{gg\to(H^*\to)ZZ}(\mu_{\text{off-shell}}) &= \mathrm{K}^{H^*}(m_{4\ell}) \cdot \mu_{\text{off-shell}} \cdot \sigma^{\text{SM}}_{gg\to H^*\to ZZ} \\ &+ \sqrt{\mathrm{K}^{H^*}_{gg}(m_{4\ell}) \cdot \mathrm{K}^{\mathrm{B}}(m_{4\ell}) \cdot \mu_{\text{off-shell}}} \cdot \sigma^{\text{SM}}_{gg\to ZZ,\,\text{Interference}} \\ &+ \mathrm{K}^{\mathrm{B}}(m_{4\ell}) \cdot \sigma_{gg\to ZZ,\,\text{cont}}\,. \end{aligned} \tag{5.14}$$

More details are given in Appendix B.1. This expression can be used to construct MC samples for arbitrary values of $\mu_{\text{off-shell}}$ from three basic samples generated at different fixed values of $\mu_{\text{off-shell}}$.

5.4.2 Simulation of electroweak ZZ production through VBF and ZH-like processes

The electroweak[4] $pp \to ZZ + 2j$ process contains both VBF-like events and ZH-like events, which are simulated using MadGraph5 [118], and cross-checked using the PHANTOM [119] generator. The QCD renormalisation and factorisation scales are set to m_W, following the recommendation in Ref. [120]. The CTEQ6L1 PDF set [121] is used. PYTHIA6 [122] is used for parton showering and hadronisation.

The high-mass range, which is the focus of this analysis, includes Higgs boson signal events arising from:

[4]In this context, "electroweak" refers to the fact that QCD NNLO corrections are not included in the description of the $pp \to ZZ$ process.

- the off-shell VBF $H \to ZZ$ process, which scales with $\kappa^4_{Z,\text{off-shell}}$ and is independent of Γ_H,
- the VBF-like ZZ process with a t-channel Higgs boson exchange, which scales with $\kappa^4_{Z,\text{off-shell}}$ and is independent of Γ_H,
- the ZH process with an on-shell Higgs boson, in the $Z \to 2\ell$ and $H \to 2\ell 2j$ or $H \to \ell\nu 2j$ channels, which scales with $\kappa^4_{Z,\text{on-shell}}/\Gamma_H$,

where we have assumed the same coupling strength $\kappa_{Z,\text{off-shell}}$ for the two VBF-like contributions, although the energy scale of the Higgs boson propagator is different in the two cases. Due to the different Γ_H dependence, the on-shell and off-shell Higgs boson production processes are separated in the analysis by requiring that the generated Higgs boson mass satisfies $|m_H^{\text{gen.}} - 125.5\text{ GeV}| < 1\text{ GeV}$. This requirement is fully efficient in selecting the on-shell ZH process. The NNLO QCD corrected cross-section in Ref. [40] is used for the on-shell ZH production process. The cross-section $\sigma_{pp\to ZZ+2j}(\mu_{\text{off-shell}})$ for the electroweak $pp \to ZZ + 2j$ process for any off-shell Higgs boson signal strength $\mu_{\text{off-shell}}$ is parameterised in the same way as for the $gg \to (H^* \to)ZZ$ process.

MC event samples for the electroweak $pp \to (H^* + 2j \to)ZZ + 2j$ process with an arbitrary value of the off-shell Higgs boson signal strength $\mu_{\text{off-shell}}$ can be constructed from a pure $pp \to ZZ + 2j$ continuum background MC sample, a full SM Higgs boson signal plus background $pp \to (H^* + 2j \to)ZZ + 2j$ MC sample and a third Higgs boson signal plus background $pp \to (H^* + 2j \to)ZZ + 2j$ MC sample with $\mu_{\text{off-shell}} = \kappa_V^4 = \Gamma_H/\Gamma_H^{\text{SM}} = 10$. Using $\Gamma_H/\Gamma_H^{\text{SM}} = 10$ for the last sample ensures that the on-shell VH events are generated with SM-like signal strength.

The following weighting function is used:

$$\begin{aligned}\sigma_{pp\to(H^*+2j\to)ZZ+2j}(\mu_{\text{off-shell}}) &= \mu_{\text{off-shell}} \cdot \sigma^{\text{SM}}_{pp\to(H^*+2j\to)ZZ+2j} \\ &+ \sqrt{\mu_{\text{off-shell}}} \cdot \sigma_{pp\to ZZ+2j,\text{ Interference}} \\ &+ \sigma_{pp\to ZZ+2j,\text{ cont}}\,,\end{aligned} \tag{5.15}$$

where the signal and interference samples are implicitly defined through the SM $pp \to (H^* + 2j \to)ZZ + 2j$ MC sample:

$$\begin{aligned}\sigma^{\text{SM}}_{pp\to(H^*+2j\to)ZZ+2j} &= \sigma^{\text{SM}}_{pp\to H^*+2j\to ZZ+2j} + \sigma_{pp\to ZZ+2j,\text{ Interference}} \\ &+ \sigma_{pp\to ZZ+2j,\text{ cont}}\end{aligned} \tag{5.16}$$

and a $\mu_{\text{off-shell}} = 10$ MC sample:

$$\begin{aligned}\sigma^{\kappa_V^4=10}_{pp\to(H^*+2j\to)ZZ+2j} &= 10\cdot\sigma^{\text{SM}}_{pp\to H^*+2j\to ZZ+2j} + \sqrt{10}\cdot\sigma_{pp\to ZZ+2j,\ \text{Interference}} \\ &+ \sigma_{pp\to ZZ+2j,\,\text{cont}}\,. \end{aligned} \tag{5.17}$$

Solving for the generated MC samples yields:

$$\begin{aligned}\sigma_{pp\to(H^*+2j\to)ZZ+2j}(\mu_{\text{off-shell}}) &= \frac{\mu_{\text{off-shell}} - \sqrt{\mu_{\text{off-shell}}}}{10-\sqrt{10}}\sigma^{\kappa_V^4=10}_{pp\to(H^*+2j\to)ZZ+2j} \\ &+ \frac{10\sqrt{\mu_{\text{off-shell}}} - \sqrt{10}\mu_{\text{off-shell}}}{10-\sqrt{10}}\sigma^{\text{SM}}_{pp\to(H^*+2j\to)ZZ+2j} \\ &+ \frac{(\sqrt{\mu_{\text{off-shell}}}-1)\cdot(\sqrt{\mu_{\text{off-shell}}}-\sqrt{10})}{\sqrt{10}}\sigma_{pp\to ZZ+2j,\,\text{cont}}\,. \end{aligned} \tag{5.18}$$

5.5 Simulation of $q\bar{q} \to ZZ$ background

The $q\bar{q} \to ZZ$ background is simulated at NLO in QCD using the POWHEG-BOX [123] generator with dynamic QCD renormalisation and factorisation scales of m_{ZZ} and the CT10 NLO PDF set. Please note that this scale choice is not identical to the choice of $Q = m_{ZZ}/2$ used for the signal and the $gg \to ZZ$ background. This difference will be corrected with the NNLO/NLO K-factor. Parton showering and hadronisation are done with PYTHIA8 for $q\bar{q} \to ZZ$.

As the full 4-fermion matrix element is used by POWHEG-BOX, all final state decay correlations are taken into account.

5.5.1 Higher order QCD correction and uncertainties

The cross-section for the $q\bar{q} \to ZZ$ process is calculated in Ref. [124] for two on-shell Z bosons in the final state with a NNLO QCD accuracy, and it is valid in the high mass region. The $gg \to ZZ$ process is included as part of these NNLO calculations, and therefore a different K-factor is provided by the authors of Ref. [124], excluding the $gg \to ZZ$ component and using a QCD renormalisation and factorisation scale μ_{QCD} of $m_{4\ell}/2$ in order to consistently

match the simulation of the $gg \to (H^* \to)ZZ$ process:

$$\begin{aligned} \mathrm{K}_{q\bar{q}}(m_{4\ell}) &= \frac{\sigma^{\mathrm{NNLO}}_{q\bar{q}\to ZZ}(m_{4\ell}, \mu_{QCD} = m_{4\ell}/2)}{\sigma^{\mathrm{NLO}}_{q\bar{q}\to ZZ}(m_{4\ell}, \mu_{QCD} = m_{4\ell})} \\ &- \frac{\sigma^{\mathrm{LO}}_{gg\to ZZ}(m_{4\ell}, \mu_{QCD} = m_{4\ell}/2)}{\sigma^{\mathrm{NLO}}_{q\bar{q}\to ZZ}(m_{4\ell}, \mu_{QCD} = m_{4\ell})}. \end{aligned} \tag{5.19}$$

This K-factor can be directly applied to the Powheg NLO $qq \to ZZ$ sample. The correction increases the $qq \to ZZ$ cross section in the high mass region by 6-8%, with a factor of approximately 4% coming from the NNLO calculation and the remaining increase from the change of the central scale with respect to the POWHEG sample. The function used to implement the K-factor in the analysis is:

$$\begin{aligned} \mathrm{K}_{q\bar{q}}(m_{4\ell}) &= 1.0113 + 0.000310203 \cdot m_{4\ell}/\ \mathrm{GeV} \\ &- 9.2014 \cdot 10^{-8} \cdot (m_{4\ell}/\ \mathrm{GeV})^2 \end{aligned} \tag{5.20}$$

and the functional form is depicted in Fig. 5.9.

The uncertainties for the $qq \to ZZ$ process are taken from Ref. [120], Sec. 11.3.1 and are based on $\sqrt{s}$=7 TeV calculations with MCFM 6.1 using a fixed scale of m_Z. Fig. 5.8 shows the shape uncertainties corresponding to the PDF and the strong running coupling (PDF$\pm\alpha_s$) and QCD scale variations. QCD scale uncertainties are derived by varying Q in the range $[m_Z/2, m_Z]$. PDF$\pm\alpha_s$ uncertainties are derived using the envelope of CT10, MSTW and NNPDF. The PDF uncertainty functional forms for the $qq \to ZZ \to 4\ell$ and $gg \to ZZ \to 4\ell$ processes are given by:

$$\begin{aligned} qq \to ZZ \to 4\ell : \kappa(m_{4\ell}) &= 1 + 0.0035\sqrt{m_{4\ell}/\ \mathrm{GeV} - 30} \\ gg \to ZZ \to 4\ell : \kappa(m_{4\ell}) &= 1 + 0.0066\sqrt{m_{4\ell}/\ \mathrm{GeV} - 10} \end{aligned} \tag{5.21}$$

The QCD scale uncertainty for $qq \to ZZ \to 4\ell$, parametrised as function of $m_{4\ell}$ is given by:

$$qq \to ZZ \to 4\ell : \kappa(m_{4\ell}) = 1 + 0.01\sqrt{(m_{4\ell}/\ \mathrm{GeV} - 20)/13} \tag{5.22}$$

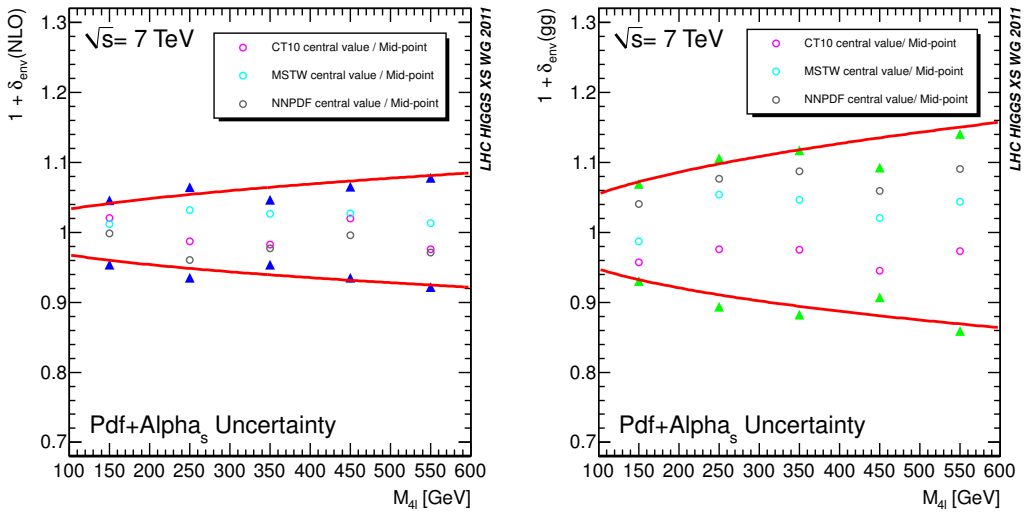

(a)

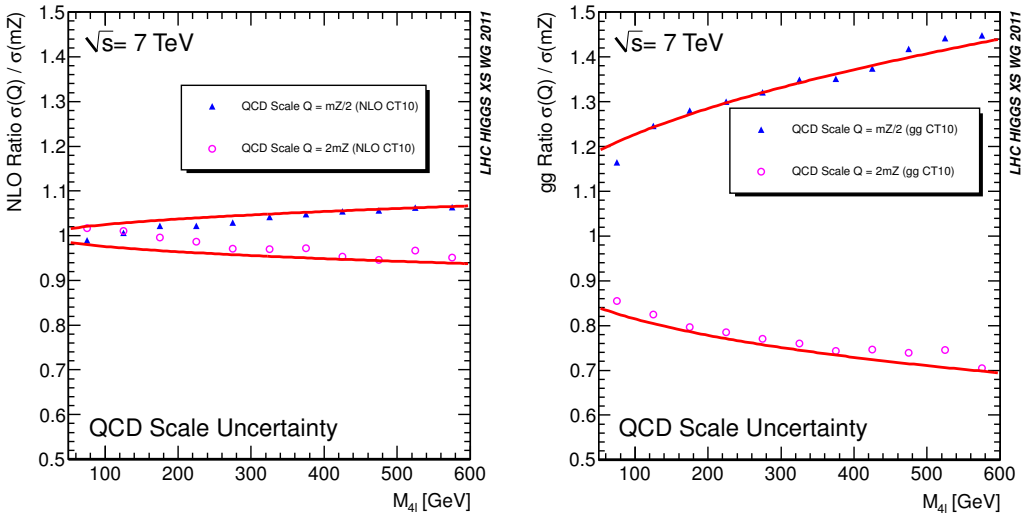

(b)

Figure 5.8 *(a) Pdf$\pm\alpha_s$ correction, and (b) QCD correction scale induced shape uncertainties for the $qq \to ZZ$ (left) and the $gg \to ZZ$ (right) processes, as function of $m_{4\ell}$, taken from Ref. [120].*

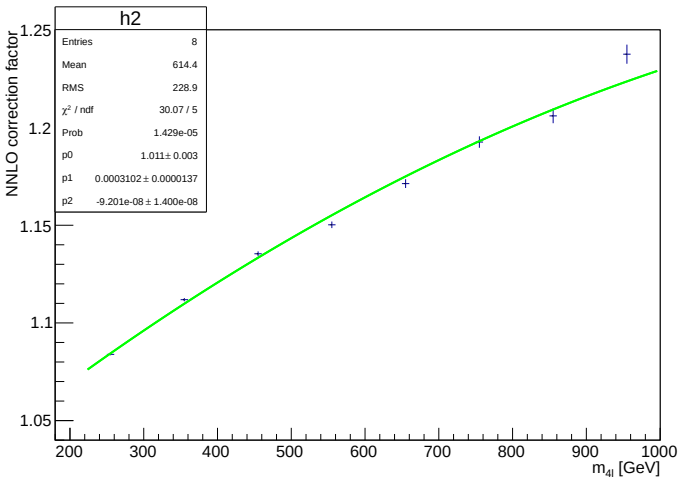

Figure 5.9 *NNLO/NLO K-factor $K(m_{ZZ})$ for the $qq \to ZZ$ and $qq \to ZZ$ processes calculated by the authors of Ref. [124].*

5.5.2 Electroweak high order corrections and uncertainties

Electroweak higher-order corrections are not included in POWHEG-BOX, or any officially released generator. These corrections are calculated in Refs. [125, 126] for on-shell outgoing vector bosons and found to be about -10% in the high-mass ZZ region of this analysis. To account for these corrections, the POWHEG-BOX events are re-weighted using a procedure similar to the one described in Ref. [127], based on the kinematics of the diboson system and the initial state quarks. The derived corrections are validated in Ref. [128].

Strictly speaking, the corrections are only valid for the $qq \to ZZ$ LO process above the corresponding diboson production threshold and with both vector bosons on-shell. To enforce this, we require that $s > \sqrt{\left(m_{Z_1}^{PDG} + m_{Z_2}^{PDG}\right)^2}$ in the centre-of-mass frame of the diboson system. For this analysis this is simplified to $m_{4\ell} > 2\, m_Z^{PDG}$. The requirement does not comprise a rigorous on-shell cut. Therefore, the correction is applied without any modification only for $|m_{2\ell} - m_Z^{PDG}| < 25$ GeV. However, because electroweak effects are expected to be of the same size in events with either off- or on-shell bosons, we apply the same correction in both cases. We conservatively assume a 100% uncertainty which should adequately cover these effects. In any case, the fraction of events with off-shell bosons amounts to only 0.02% of the selected events for $ZZ \to 4\ell$.

Weights are computed at LO QCD because the (NLO QCD)×(NLO EW) correc-

tions are unknown. In events with high QCD activity an additional systematic uncertainty is considered, as suggested in Ref. [127]. A new variable is introduced to take into account this effect: $\rho \equiv \left|\sum_i \vec{\ell}_{i,T} + \vec{p}_{T,miss}\right| / \left(\sum_i \left|\vec{\ell}_{i,T}\right| + |\vec{p}_{T,miss}|\right)$. Generator-level quantities are used for this calculation (as opposed to reconstructed quantities that include resolution effects). Following the recommendation of Ref. [127] a value of $\rho < 0.3$ is used to select the region of phase space where both the LO and NLO QCD predictions are dominated by recoiling vector bosons, and therefore the weights are applicable without an additional uncertainty. For events with $\rho > 0.3$, the correction is applied with a 100% systematic uncertainty since corrections of the same order are expected, but remain unknown.

Figure 5.10 shows the ρ distribution in the $ZZ \to 4\ell$ channel for different numbers of jets. The fraction of events with $\rho < 0.3$ is about 100% in the 0-jet final state, 70% in the 1-jet event and 42% in the events with more than 1 jets. Summing over all jet final states, this fraction is about 85%. Figure 6.10 shows the impact of these corrections on the kinematic distributions.

The applied corrections are limited in the sense that they exclusively comprise virtual corrections and do not include polarisation effects. In the case of two Z bosons, the sum of both effects is within $\mathcal{O}(1\%)$ (rather small), with more detailed studies presented in Ref. [127] and with the more important distribution reproduced in Fig. 5.12. Since the ATLAS simulation software treats final-state leptons with PHOTOS, a substantial portion of real-radiation effects are treated properly, whereas photon radiation originating from W bosons remains absent. It is assumed that the electroweak effects are modelled with an accuracy of the order of the uncertainty of the complete calculation. The uncertainty of the full calculation can be estimated to be about one order of magnitude smaller than higher order QCD uncertainties considered in this analysis. Thus, there is no reason to include other uncertainty besides the ones already mentioned.

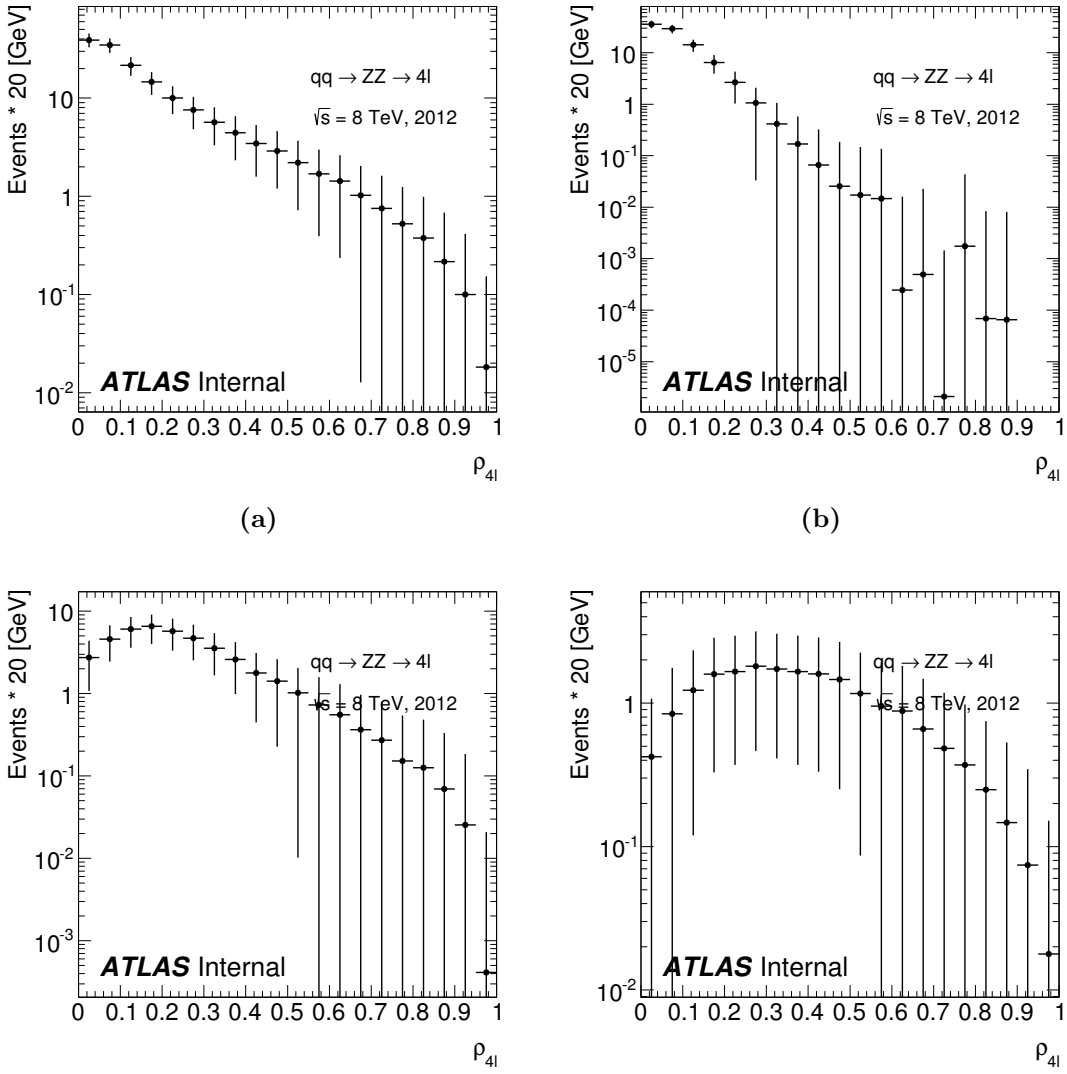

Figure 5.10 *ρ distributions in the $ZZ \to 4\ell$ channel for events with (a) any jets (inclusive) (b) 0 jets (c) 1 jet (d) more than one jets.*

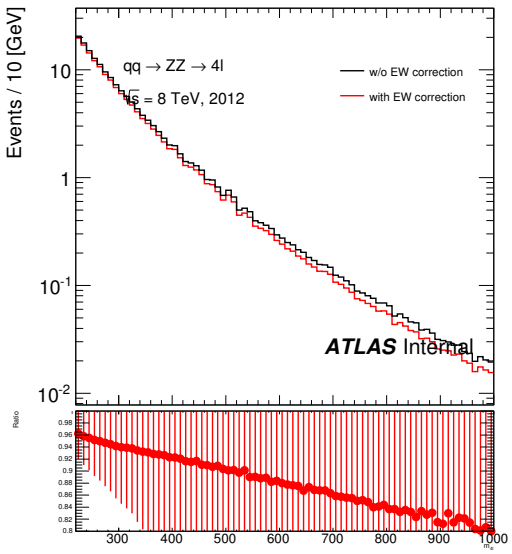

(a)

Figure 5.11 *Effect of the electroweak corrections on the $m_{4\ell}$ distribution in the $ZZ \to 4\ell$ analysis.*

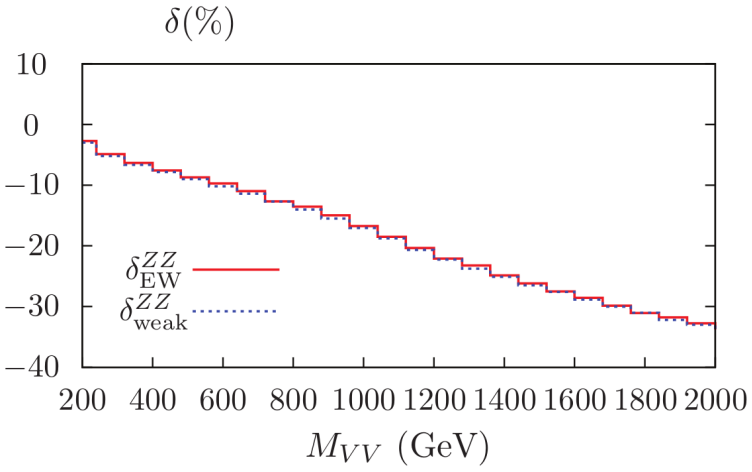

Figure 5.12 *NLO electroweak corrections on the four lepton (diboson) invariant mass distribution in the $ZZ \to 4\ell$ channel. Relative weak (δ^{ZZ}_{weak}) and the full set of electroweak (δ^{ZZ}_{EW}) corrections are included. The selection criteria are somewhat different than the ones employed in this analysis, and the calculation has been done at $\sqrt{s}$=14 TeV. The results are nevertheless applicable to this analysis. (Plot reproduced from Ref. [127], Figure 4).*

Chapter 6

Couplings and total width of the Higgs boson in the off-shell $H^{(*)} \to ZZ \to 4\ell$ channel

Even though there is strong evidence that the particle observed in 2012 by the ATLAS and CMS collaborations [129, 130] is the Higgs boson predicted by the SM, there is still place for BSM physics to change our understanding of the Higgs sector. A crucial precision measurement is the coupling of the Higgs boson to the rest of the fundamental particles, providing key information about the validity of the Higgs mechanism as formulated in the SM. The ATLAS and CMS collaborations have performed independent measurements [42, 131] of the Higgs coupling to vector bosons and fermions, with a combined measurement published earlier this year [12]. Decay channels with vector bosons have the advantage of higher statistics, and have been found to be compatible with the SM expectations with an uncertainty of about 10%. The achieved precision is not yet sufficient to make a strong statement about the true nature of the Higgs boson. Nevertheless, most of the couplings measurements have been taken in a narrow mass window around the resonance. For instance, the measurement of the Higgs couplings in the $H \to ZZ^{(*)} \to 4\ell$ channel by the ATLAS collaboration was made within the on-shell region of 110 GeV$< m_{4\ell} <$ 140 GeV [11, 42]. However, about 20% of the Higgs production corresponds to the region above the on-shell threshold. An interesting feature is that the high-mass off-shell region in the $H \to ZZ$ channel, well above the measured resonance mass (i.e. beyond $2\,m_Z$), is sensitive to the Higgs boson production through the interference of the off-shell production and

background processes. The high-mass region is also sensitive to new physics that could alter our understanding of the interactions between the Higgs boson and other fundamental particles [102–107, 132]. Therefore, the measurement of the off-shell coupling is an excellent method to test the validity of the SM predictions on the Higgs boson. A special property of the Higgs boson that relates its on-shell and off-shell couplings to its total width, offers an alternative, indirect way to measure these couplings.

The theoretical total width of the 125.5 GeV SM Higgs boson is extremely small (4.2 MeV) compared to the experimental resolution of the LHC experiments (approximately 1 GeV). In fact, the last publication of the ATLAS collaboration on the direct measurement[1] of the Higgs boson width [11], obtained a 95% CL upper limit of 5.0 GeV using the $H \to \gamma\gamma$ channel, and 2.6 GeV using the $H \to ZZ^{(*)} \to 4\ell$ channel. It is obvious that a direct measurement has approximately a factor of 1,000 worse sensitivity than the SM prediction. Consequently, a direct measurement of the Higgs total width is not a feasible task for the ATLAS and CMS experiments, even with the full dataset expected at the end of the HL-LHC era. Nevertheless, there is still hope that a future muon collider could have enough resolution to achieve a direct measurement of the SM Higgs total width.

Recent publications (Refs. [99, 100, 111, 112]) have introduced a novel and powerful method to probe a total width measurement by using both off-shell and on-shell production measurements of the Higgs boson. This approach was used by the CMS Collaboration [133] to set an indirect limit on the total width. The analysis presented in this thesis is complementary to direct searches for Higgs boson to invisible matter [134, 135] and to constraints imposed by measurements of the Higgs boson couplings [42, 131].

This thesis chapter presents a determination of the off-shell Higgs boson coupling and a futher interpretation of the Higgs total width in the $ZZ \to 4\ell$ channel ($\ell = e, \mu$). The results are presented in terms of the off-shell event yields, normalised to the SM-predicted cross section (referred to as signal strength, μ), and the associated off-shell Higgs boson couplings. The results are based on pp collision data collected by the ATLAS experiment at the LHC, corresponding to an integrated luminosity of 20.3 fb^{-1} at a collision energy of $\sqrt{s} = 8$ TeV.

[1]The direct measurement of the width in the $H \to ZZ^{(*)} \to 4\ell$ channel uses a Breit-Wigner curve fitted to the observed invariant mass of candidate Higgs events convoluted with the detector resolution, as explained in Sect. 2.3.8.

6.1 Analysis strategy

The analysis follows closely the Higgs boson on-peak (110-140 GeV) measurements in the same final state. The methodology adopted in this analysis follows closely the strategy adopted for the measurement of Higgs boson on-shell decaying into the same final state, as described in Ref. [136]. It has been used the same physics object definitions, trigger and event selections, and background estimation methods. A Matrix Element (ME)-based discriminant is constructed to enhance the separation between the $gg \to H^* \to ZZ$ signal and the $gg \to ZZ$ and $q\bar{q} \to ZZ$ backgrounds (discussed in Section 6.1.5), and is subsequently used in a binned maximum-likelihood fit for the final result. A cut-based analysis (discussed in Section 6.1.4), comparing the data event yield in a signal-enriched region to theoretical expectations, is also performed, both as a cross-check and to enable the re-interpretation of the results in models where the ME-based discriminant cannot be applied.

6.1.1 Event selection

The final state comprises highly isolated leptons (e or μ) with restricted transverse momentum and topological selections, in order to keep an optimal signal efficiency and background rejection. A proper selection of jets for the production modes is made according to the characteristics of each production mechanism. Events are required to come from the primary interaction using the standard primary vertex reconstruction[2], in order to avoid minimum bias contamination. After a Higgs boson candidate is reconstructed from the two Z boson candidates, further statistical and kinematic selections are applied in order to improve the resolution and efficiency of the channel.

Trigger

Since the analysis depends on two pairs of (same-flavour) leptons in the final state, single- or di-lepton triggers are used, depending on the characteristics of the leptons. Isolation cuts have been introduced for single lepton triggers in the 2012 data-takinng due to the high instantaneous luminosity and pile-up levels.

[2]The standard primary vertex selection reconstructs the vertex that has the highest Σp_T of associated tracks in the event, with at least three associated tracks.

The isolation cut is applied at the Event Filter (EF) level only, requiring the scalar sum of p_T of the tracks (with $p_T > 1$ GeV) within a $\Delta R < 0.2$ cone around the lepton track, to be less than 10% of the lepton candidate's p_T. A summary of the triggers used in this analysis is shown in Table 6.1, with triggers marked with an "i"indicating the ones that use the isolation selection.

channel	single lepton	di-lepton
4e	`e24vhi_medium1`, `e60_medium1`	`2e12Tvh_loose1`, `2e12Tvh_loose1_L2StarB` (only data)
4μ	`mu24i_tight`, `mu36_tight`	`mu18`, `mu8_EFFS`
2e2μ	4μ or 4e trigger menus	`e12Tvh_medium1_mu8` or `e24vhi_loose1_mu10`

Table 6.1 *Summary of the triggers that are used during the 2012 data taking for the three analysis channels presented in this thesis. When multiple chains are listed, it is intended that they have been combined with a logic "or".*

After the four lepton (for the reconstruction of the Higgs boson candidates) have been identified in a given event, we require that either one of these leptons matches the single lepton trigger, or that two of the leptons match the di-lepton trigger. The requirement of trigger matching has a negligible impact on the total event selection efficiency of the four-lepton analysis. The trigger efficiencies for the 2012 analysis in the different channels, evaluated with a simulated sample of Higgs bosons generated with mass $m_H = 130$ GeV produced via gluon fusion are as follows:

- 4μ: 97.6%
- $2e\,2\mu$: 97.3%
- $4e$: 99.7%

Differences between the trigger efficiency measured in the data and the one predicted in MC is accounted for by re-weighting MC events with scale factors according to the observed single-lepton efficiency. There is no correction applied for the dilepton triggers.

Leptons

The lepton tracks must have a longitudinal distance parameter of $|\Delta z_0| < 10$ mm from the primary vertex along the proton beam pipe.

Electrons

Electron candidates consist of EM clusters matched with an ID track using the distance between the cluster position and the extrapolated position of the track at the calorimeter. Electrons are identified using a maximum likelihood method according to the loose selection criteria. Variables that characterise the electromagnetic shower in the calorimeter and track hits in the ID serve as input for the likelihood discriminant, as defined in Sect. 3.4.2. Electrons are required to have $E_T > 7$ GeV and a pseudorapidity range of $\eta < 2.47$.

Muons

The muon momentum is measured independently by the ID and the MS detector systems. Four types of muon candidates are reconstructed, depending on the available information from the ID, the MS, and the calorimeters, as described in Section 3.4.3. The selection cuts differ depending on the type of muon reconstructed. Combined muons (CB) that are in the region $|\eta| < 2.5$ and standalone muons (SA) within the region $2.5 < |\eta| < 2.7$ must have $p_T > 6$ GeV. Standalone muons are required to also have hits in all three stations of the muon spectrometer. Calorimeter-tagged muons (CT) are used in the central region $|\eta| < 0.1$ in order to fill the acceptance gap of the MS, requiring that they have $p_T > 15$ GeV and that they do not share the same ID track with any reconstructed electron. To reduce the cosmic background, an additional selection on the transverse impact parameter is required: $|\Delta d_0| < 1$ mm.

Jets

Jets can arise from various production mechanisms: gluon-gluon Fusion (ggF), Vector Boson Fusion (VBF), and associated production with a Vector boson (VH). Depending on the kinematics of the Higgs candidate, a selected event will be assigned to one of the three categories (VBF-like, VH-like, or ggF-like). The jets are reconstructed from topological clusters using an anti-k_t algorithm [72] with a distance parameter $R = 0.4$. Jets within the ID acceptance ($|\eta| < 2.47$) are required to have more than 50% of the sum of the scalar p_T of their associated tracks coming from the primary vertex, so that pile-up background is minimised. The analysis first identifies events belonging to the VBF category, by selecting events with two high p_T jets widely separated in rapidity. The VBF jets that are in the $|\eta| < 2.5$ region must have $p_T > 25$ GeV , while the jets in $2.5 < |\eta| < 4.5$

must have $p_T > 30$ GeV. The two highest p_T jets are required to be separated by more than 3 units in pseudorapidity and have an invariant mass greater than 350 GeV. The events that do not satisfy these requirements are then considered for the second category (VH-like). These events must have an extra lepton (e or μ) with $p_T > 8$ GeV, in addition to the four leptons forming the Higgs boson candidate, which satisfies the same lepton requirements. Finally, events that are not classified by the two previous selections are assigned to the ggF-like category.

Higgs boson signal selection

The Higgs candidate is reconstructed from two pairs of leptons (di-leptons) with opposite sign and same leptonic flavour in an event, forming a lepton quadruplet. The highest p_T lepton in the quadruplet must have $p_T > 20$ GeV, the second highest $p_T > 15$ GeV, and the third highest $p_T > 10$ GeV. The lepton combination is allowed to have at most one muon of the stand-alone and calorimeter tagged type. The rejection of misidentified electrons that comes from the emission of photons proceeding from muon bremsstrahlung, is achieved by requiring that the leptons must be separated by $\Delta R > 0.1$ when they have the same flavour, and $\Delta R > 0.2$ when they have different flavours. Each event is required to have the triggering lepton(s) matched to one or two of the selected leptons.

Each lepton pair is ordered by di-lepton mass according to the proximity to the Z boson mass. For each channel, the lepton pair with invariant mass closest to the Z boson mass is selected as the leading di-lepton pair and its invariant mass, m_{12}, is required to be between 50 GeV and 106 GeV. The second lepton pair is known as the sub-leading di-lepton pair. Its invariant mass, m_{34}, must be within the range $m_{min} < m_{34} < 115$ GeV. Here m_{min} varies between 12 GeV for $m_{4\ell} < 140$ GeV and rises linearly to 50 GeV for $m_{4\ell} \geq 190$ GeV. The results are classified according to the four final states: $4e$, $2e\,2\mu$, $2\mu\,2e$, 4μ, ordered by the flavour of the leading di-lepton. To remove events with $J/\Psi \to \ell^+\ell^-$ candidates, all the di-lepton candidate combinations must satisfy $m_{\ell\ell} > 5$ GeV. In the case that more than one quadruplets survives the kinematic selection, the one with the m_{12} mass value closest to the Z boson mass is retained. If multiple combinations have the same m_{12} mass value, the one with the highest m_{34} mass value is selected.

The inclusive Z (Z + jets) and $t\bar{t}$ background contributions are further reduced by applying impact parameter and track -and calorimeter- based isolation requirements to the leptons. The impact parameter selection is based on

the parameter significance $|d_0|/\sigma_{d_0}$. It is required that the impact parameter significance has values less than 3.5 for muons and 6.5 for electrons; this difference can be explained by the broader distribution for electrons due to bremsstrahlung effects. The size of the cone used for both the track and calorimeter isolation discriminants is $\Delta R < 0.2$, but the track-based isolation discriminant is required to be smaller than 0.15 and the calorimeter-based discriminant to be smaller than 0.3 (0.15 for standalone muons). The tracks considered in the isolation cone must come from the primary vertex and fulfil good quality criteria; i.e. they must have at least four hits in the pixel and silicon strip detectors, at least nine silicon hits, one hit in the innermost pixel layer (the b-layer), $p_T > 1$ GeV for muon isolation and $p_T > 0.4$ GeV for electron isolation.

The physics object quality and kinematic selections are summarized in Table 6.2.

	Event Pre-selection
Electrons	LOOSE LH quality electrons with $E_T > 7$ GeV, $\|\eta\| < 2.47$
Muons	combined or segmented-tagged muons with $p_T > 6$ GeV, $\|\eta\| < 2.7$ maximum one calo-tagged or standalone muon calo-tagged muons: $p_T > 15$ GeV, $\|\eta\| < 0.1$ standalone muons: $p_T > 6$ GeV, $2.5 < \|\eta\| < 2.7$ and $\Delta R > 0.2$ separation from closest segmented-tagged muon
	Event Selection
Kinematic Selection	at least two pairs of same-flavour opposite-charge leptons p_T thresholds for three leading leptons: 20, 15, 10 GeV leading di-lepton: the one closest to Z mass subleading di-lepton: the second closest to Z mass leading di-lepton: 50 GeV $< m_{12} <$ 106 GeV sub-leading di-lepton: $m_{min} < m_{34} <$ 115 GeV remove H candidate if either same-flavour, opposite-charge dilepton candidate has $m_{\ell\ell} < 5$ GeV $\Delta R(\ell, \ell') > 0.10$ (0.2) for all same (different) flavour leptons
Isolation	isolation cut in $\Delta R = 0.20$ cone applied on all H leptons lepton track-based: $\Sigma p_T/p_T < 0.15$ electron calorimeter-based: $\Sigma E_T/E_T < 0.20$ muon calorimeter-based: $\Sigma E_T/E_T < 0.30$ standalone muon calorimeter-based: $\Sigma E_T/E_T < 0.15$
Impact parameter significance	significance cut applied on all H leptons electrons: $d_0/\sigma_{d_0} < 6.5$ muons: $d_0/\sigma_{d_0} < 3.5$

Table 6.2 *Summary of the physics object quality and kinematic selection requirements for the analysis. The choice of the m_{min} value threshold for m_{34} is discussed in the text.*

Final State Radiation

Given that leptons radiate via bremsstrahlung, there can be secondary photons that complicate the task of reconstructing the final state. To account for the impact of Final State Radiation (FSR) [137] on the calculation of the Z invariant mass, we use MC-based corrections. The FSR recovery is performed by allowing at most one photon to be added per event. All leading di-muon candidates with invariant masses within the range 66 GeV $< m_{12} <$ 89 GeV (i.e. below the Z boson mass) are corrected for collinear FSR by incorporating any reconstructed photon with $E_T > 1$ GeV lying close ($\Delta R < 0.08$ to 0.15, depending on E_T^{γ}) to one of the muon tracks, as long as the corrected mass, $m_{\mu\mu\gamma}$, remains below 100 GeV. In other words, a FSR photon is retained and associated with the closest lepton in a lepton pair only if the dilepton-plus-photon mass is closer to the nominal Z boson mass. This recovers 70% of the FSR photons within the selected fiducial region. About 85% of the corrected events have genuine collinear FSR photons, with the remaining incorrectly associated (or misidentified) photons originating from pileup and muon ionisation. For events without collinear FSR, non-collinear FSR photons with a significant E_T are included for both the leading di-muon and di-electron candidates, an improvement introduced since Ref. [131]. The expected fraction of events with a collinear (non-collinear) FSR correction is 4% (1%). These studies are discussed in detail in Ref. [39].

Z-mass constraint

The mass resolution is improved by applying a kinematic fit, named Z-mass constraint, to constrain the mass of the leading di-lepton pair if $m_{4\ell} < 190$ GeV, and of both di-leptons for higher masses. The invariant mass shape of the reconstructed leading di-lepton should follow a distribution peaked at the Z boson pole mass with its intrinsic width (convoluted with the experimental resolution). A function can then be used to fit the shape of the Z boson mass distribution. The Z-mass constraint fit is implemented by using a single Gaussian resolution model and a Breit-Wigner line shape for the reconstructed di-lepton mass, including FSR photons, if applicable. The $m_{4\ell}$ resolution is improved with this method by approximately 15%.

6.1.2 Background estimation

There are two types of background processes included in the analysis: the reducible and the irreducible background.

Reducible background

The reducible background consists of at least one misidentified pair of leptons that is produced by a QCD jet or events with a single low-p_T Z boson. This type of background is more dominant in the low-mass ($m_{4\ell} < 130$ GeV) region, since the kinematic selection on the leptons is looser in order to keep a high signal efficiency. The electron final states are affected the most by this type of background since jets can create fake electron candidates. In the high-mass ($m_{4\ell} > 200$ GeV) region the contribution of this background is expected to be negligible, since high-energy electrons have a narrow shape deposition, and the isolation selection removes fake electrons from jets. The following types of processes are included in this category:

- Z bosons in association with jets
- Z bosons in association with heavy flavour particles
- $t\bar{t}$

Irreducible background

The irreducible background shares the same well-defined four-leptons final state with the signal process. It includes the following processes:

- pairs of Z bosons via quark annihilation: $q\bar{q} \to ZZ \to 4\ell$
- pairs of Z bosons via gluon fusion: $gg \to ZZ \to 4\ell$

The contribution of this type of background is considerably larger than the reducible background in the low-mass region; and has an increasingly higher impact in the high-mass region, since the signal process is much weaker above the Higgs boson mass peak. The discrimination between signal and background processes in the low-mass region is obtained by taking into account the difference in the shapes of a narrow signal distribution and a flat background distribution.

In the high-mass region, where the signal cross section is dramatically reduced, further kinematic variables have to be considered in order to discriminate against background processes.

After all selection cuts described above, the background contribution is kept at a low level. For example, the $H \to ZZ^{(*)} \to 4\ell$ analysis by ATLAS using collision data with an integrated luminosity of 20.3 fb^{-1} at $\sqrt{s} = 8$ TeV, was estimated to have 13.8 ± 1.4 signal and 8.24 ± 6.2 background events in the $120 < m_{4\ell} < 130$ GeVregion, with a signal-to-background ratio of about 1.7.

6.1.3 Off-shell event selection and background estimations

The analysis is split into four categories ($2\mu\,2e$, $2e\,2\mu$, $4e$, 4μ) as in Ref. [136]. The off-shell analysis includes an additional event selection that defines the mass region of study: 220 GeV $< m_{4\ell} <$ 1000 GeV. A shape-based analysis is chosen as it is demonstrated to achieve a better sensitivity. The same background estimation procedures are applied for the $q\bar{q} \to ZZ \to 4\ell$ and reducible backgrounds.

The signal NNLO/LO K-factor is calculated as a function of the invariant mass $m_{4\ell}$, independently of the jet multiplicity, or non-zero $p_T(4\ell)$ values that are induced by the higher-order QCD corrections. The experimental analysis is, therefore, performed in an inclusive jet-observable category, and the event selections are designed to minimise the dependence on the boost of the ZZ system, which is sensitive to the jet multiplicity.

Table 6.3 shows the expected number of events for the signal and background processes for an integrated luminosity of 20.3 fb^{-1} at $\sqrt{s} = 8$ TeV. The corresponding $m_{4\ell}$ distributions are shown in Figure 6.1. In the off-peak region, the dominant background is from the $q\bar{q} \to ZZ$ process. The contribution of the reducible backgrounds, such as Z+jets, top and double parton interactions, is less than 1% of the total background in the full off-shell region, and is, therefore, not included in this analysis.

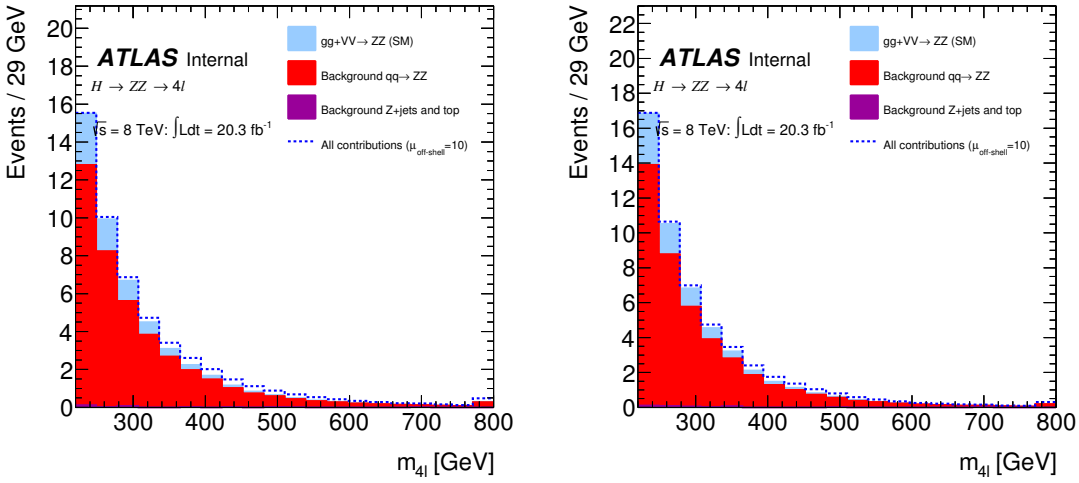

(a) $2e2\mu$ **(b)** $2\mu2e$

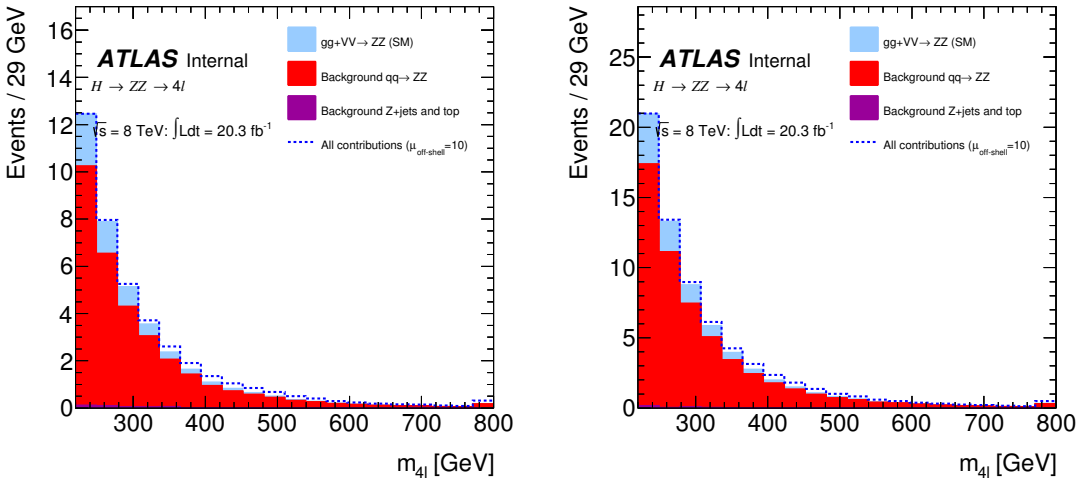

(c) $4e$ **(d)** 4μ

Figure 6.1 *Expected $m_{4\ell}$ distributions for all signal and background processes after the baseline off-peak selections, for the four different lepton final states: (a) $2e\,2\mu$ (b) $2\mu\,2e$ (c) $4e$ (d) 4μ. The dashed line corresponds to the total expected event yield, for a Higgs boson with $\mu_{off\text{-}shell} = 10$. A relative $gg \to ZZ$ background K-factor of $R^{B}_{H^*}$=1.0 is assumed. The Z+jets and top-quark backgrounds are barely visible in the plot (with a background fraction of less than 1%). Note that the last bin includes the overflow.*

	$2\mu\,2e$	$2e\,2\mu$	4μ	4e	Total
$gg \to H^* \to ZZ$ (S)	0.48 ± 0.11	0.60 ± 0.14	0.62 ± 0.14	0.45 ± 0.10	2.2 ± 0.5
$gg \to ZZ$ (B)	7.64 ± 1.74	7.57 ± 1.73	9.50 ± 2.17	5.94 ± 1.36	30.7 ± 7.0
$gg \to (H^* \to)ZZ$	7.32 ± 1.67	7.17 ± 1.64	9.05 ± 2.07	5.69 ± 1.30	29.2 ± 6.7
$gg \to (H^* \to)ZZ$ ($\mu_{\text{off-shell}} = 10$)	9.73 ± 2.22	10.3 ± 2.4	12.2 ± 2.8	7.95 ± 1.81	40.2 ± 9.2
VBF $H^* \to ZZ$ (S)	0.04 ± 0.00	0.05 ± 0.01	0.06 ± 0.01	0.05 ± 0.00	0.2 ± 0.0
VBF ZZ (B)	0.51 ± 0.03	0.56 ± 0.03	0.66 ± 0.03	0.44 ± 0.02	2.2 ± 0.1
VBF ZZ (S+B+I)	0.48 ± 0.03	0.53 ± 0.03	0.60 ± 0.03	0.40 ± 0.02	2.0 ± 0.1
VBF ZZ (S+B+I, $\mu_{\text{off-shell}} = 10$)	0.69 ± 0.04	0.79 ± 0.04	0.91 ± 0.05	0.61 ± 0.03	3.0 ± 0.2
$q\bar{q} \to ZZ$	42.0 ± 3.3	40.7 ± 3.2	53.8 ± 4.2	31.3 ± 2.5	167.9 ± 13.1
Reducible backgrounds	0.38 ± 0.06	0.30 ± 0.06	0.32 ± 0.06	0.38 ± 0.06	1.4 ± 0.1
Total Expected (SM)	50.1 ± 3.7	48.7 ± 3.6	63.8 ± 4.7	37.8 ± 2.8	200.5 ± 14.7

Table 6.3 *Expected number of events for the $ZZ \to 4\ell$ channel for signal and background processes for an integrated luminosity of 20.3 fb^{-1} at $\sqrt{s}$ = 8 TeV. The $gg \to ZZ$ (S+B+I) process with $\mu_{\textit{off-shell}} = 10$ is shown for illustration. Both statistical and systematic uncertainties are included. A relative $gg \to ZZ$ background K-factor of $R^B_{H^*}$=1 is assumed.*

6.1.4 Cut based analysis

As a cross-check to the shape-based analysis, a simpler, cut-based analysis is performed using $m_{4\ell}$. To optimise the sensitivity on the $m_{4\ell}$ selection, the following figure of merit is used:

$$\mathcal{S} = \frac{N_{s+b(r)} - N_{s+b(r=1)}}{\Delta_{s+b(r)}}, \tag{6.1}$$

where $r = \Gamma_H/\Gamma_H^{SM}$. In calculating $\Delta_{s+b(r)}$, both statistical and systematic uncertainties on the total number of $q\bar{q} \to ZZ$ ($N_{q\bar{q}}$) background events and the continuum background (N_{gg}) are included. In this optimisation, a 10% systematic uncertainty on the main background ($q\bar{q} \to ZZ$) is used, to account for the main theoretical uncertainties due to the QCD scale variations and PDF variations. The 1-side 95% C.L. upper limit on the Γ_H/Γ_H^{SM} can be roughly estimated as the value that corresponds to a significance $S = 1.645$ (as it is explained in Section 6.3). After varying the $m_{4\ell}$ cut between 200 and 450 GeV in steps of 50 GeV, the best value for the $m_{4\ell}$ cut, namely the one that minimises the 95% C.L. upper limit, is found to be 400 GeV, shown in Table 6.4.

In Table 6.5, the number of expected events for the combination of all lepton final states in the signal region are shown. The event yields in the off-shell signal region are compared to the Higgs on-shell region and a $q\bar{q} \to ZZ$ background-enriched region. The upper limits are calculated using the CL_s method, with the null

hypothesis $\mu_{\text{off-shell}} = 1$. The results are based on Asimov data sample from the pdf shape. Futher details about the statistical tools can be seen in Section 6.3.

$m_{4\ell}$ threshold (GeV)	250	300	350	400	450
1-side 95% C.L. upper limit on Γ_H/Γ_H^{SM}	19.8	15.2	13.0	12.6	13.2

Table 6.4 *1-side 95% C.L. upper limit on Γ_H/Γ_H^{SM} for different cuts on $m_{4\ell}$ for the combination of all lepton final states.*

mass region (GeV)	Higgs on-peak $110 < m_{4\ell} < 140$	Background $160 < m_{4\ell} < 220$	Signal $400 < m_{4\ell} < 1000$
$gg \to H \to ZZ$	14.2	0.22	1.1
$gg \to ZZ$ (B)	1.2	26.1	2.8
$gg \to ZZ$ (S+B+I)	16.1	25.3	2.4
$q\bar{q} \to ZZ$	17.5	112.2	21.31

Table 6.5 *Expected number of events for 20.3 fb^{-1} at $\sqrt{s}$=8 TeV for the combination of all leptonic final states in the various $m_{4\ell}$ regions.*

6.1.5 Matrix-element-based kinematic discriminant

The matrix-element kinematic discriminant fully exploits the event kinematic information in the centre-of-mass frame of the 4ℓ system, based on eight observables: $\{m_{4\ell}, m_{12}, m_{34}, \cos\theta_1, \cos\theta_2, \phi, \cos\theta^*, \phi_1\}$ [136, 138], introduced in Sect. 5.2, and shown in Figure 5.2. These observables are used to simulate the four-momenta of the leptons and incoming partons (as explained in Section 2.4), which are then used to calculate matrix elements for different processes, provided by the MCFM program [111]. The following matrix elements are calculated for each event in the mass range 220 GeV $< m_{4\ell} <$ 1000 GeV:

- $P_{q\bar{q}}$: matrix element squared for the $q\bar{q} \to ZZ \to 4\ell$ process
- P_{gg}: matrix element squared for the $gg \to (H^* \to)ZZ \to 4\ell$ process including the Higgs boson ($m_H = 125.5$ GeV) with SM couplings, continuum background and their interference
- P_H: matrix element squared for the $gg \to H^* \to ZZ \to 4\ell$ process ($m_H =$ 125.5 GeV)

The kinematic discriminant is defined as in Ref. [111]:

$$\mathrm{ME} = \log_{10}\left(\frac{P_H}{P_{gg} + c \cdot P_{q\bar{q}}}\right), \tag{6.2}$$

where $c = 0.1$ is an empirical constant, to approximately balance the overall cross-sections of the $q\bar{q} \to ZZ$ and $gg \to (H^* \to)ZZ$ processes. The exact value of c has a very small effect on the analysis sensitivity.

Figure 6.2 shows the shape comparisons of the key input variables to the ME-based discriminant, $m_{4\ell}$, $\cos\theta_1$, $\cos\theta_2$ and $\cos\theta^*$. Figure 6.3 shows the shape comparisons of the ME-based discriminant for the main processes considered. Events with the ME-based discriminant value between -4.5 and 0.5 are selected with a signal efficiency over 99%. Figure 6.4 shows the 2D distributions of the ME-based discriminant and $m_{4\ell}$. As $m_{4\ell}$ is the most important input variable for the ME, there is a strong correlation between them.

In order to illustrate the impact of the selection on QCD related quantities, we produce distributions for the jet multiplicity and $p_T(4\ell)$ before and after the selection cuts for fixed $m_{4\ell}$ bins. Figure 6.5 shows the distributions of $p_T(4\ell)$ and the number of jets before and after a matrix element discriminant cut of -1.5 for the $gg \to H \to 4\ell$ process in three distinct $m_{4\ell}$ ranges. The matrix element discriminant is independent of the ZZ system boost for each $m_{4\ell}$ bin.

In the default analysis, the re-weighting procedure is only used to account for the acceptance effects, as the matrix-element-based discriminant is insensitive to the p_{T} and the jet multiplicity of the ZZ system (inclusive analysis).

In addition, an alternative multivariate discriminant based on a boosted decision tree (BDT) algorithm was studied to further separate the $gg \to H^* \to ZZ$ signal from the main $q\bar{q} \to ZZ$ background, by exploiting additional kinematic information (p_{T} and η) of the ZZ system. It has been found that the analysis sensitivity improves only marginally (by approximately 2%) compared to the ME-based discriminant alone. Due to the method's dependence on the p_{T} of the ZZ system, the BDT-based discriminant introduces additional systematic uncertainties from the higher-order QCD corrections. For these reasons, the BDT-based discriminant is not used for the final result.

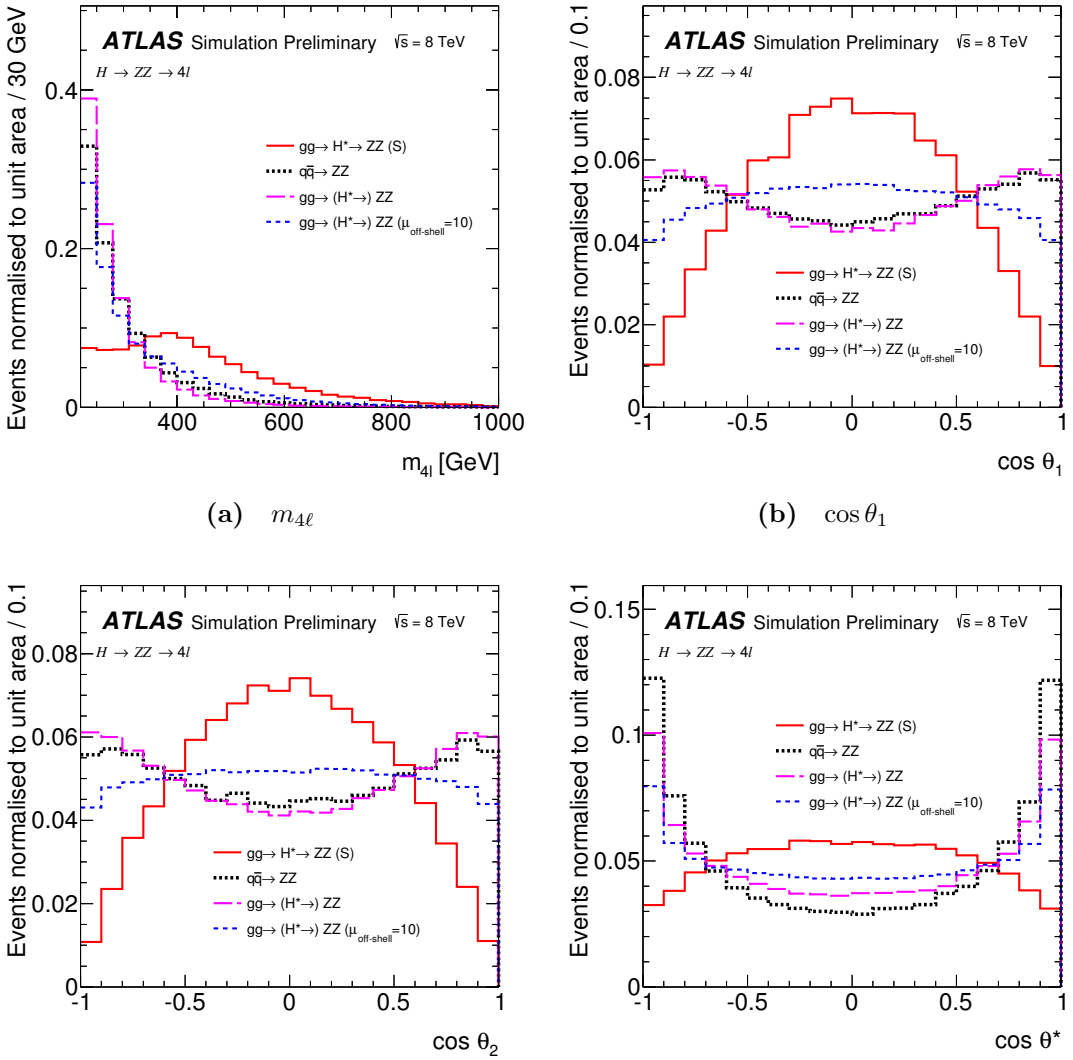

(a) $m_{4\ell}$ **(b)** $\cos\theta_1$

(c) $\cos\theta_2$ **(d)** $\cos\theta^*$

Figure 6.2 *Distributions of the key input variables to the ME-based discriminant for the off-peak region (220 GeV $< m_{4\ell} <$ 1000 GeV) and for all lepton final states combined: (a) $m_{4\ell}$ (b) $\cos\theta_1$ (c) $\cos\theta_2$ (d) $\cos\theta^*$. The distributions are normalised to unit area for shape comparisons. The thick black dotted line represents the $q\bar{q} \to ZZ$ background, the red solid line the $gg \to H^* \to ZZ$ signal with SM couplings, the magenta long-dashed line the $gg \to (H^* \to)ZZ$ with SM $\mu_{off\text{-}shell}$, and the blue dashed line is for $gg \to (H^* \to)ZZ$ with $\mu_{off\text{-}shell} = 10$. A relative $gg \to ZZ$ background K-factor of $R^B_{H^*}$=1.0 is assumed.*

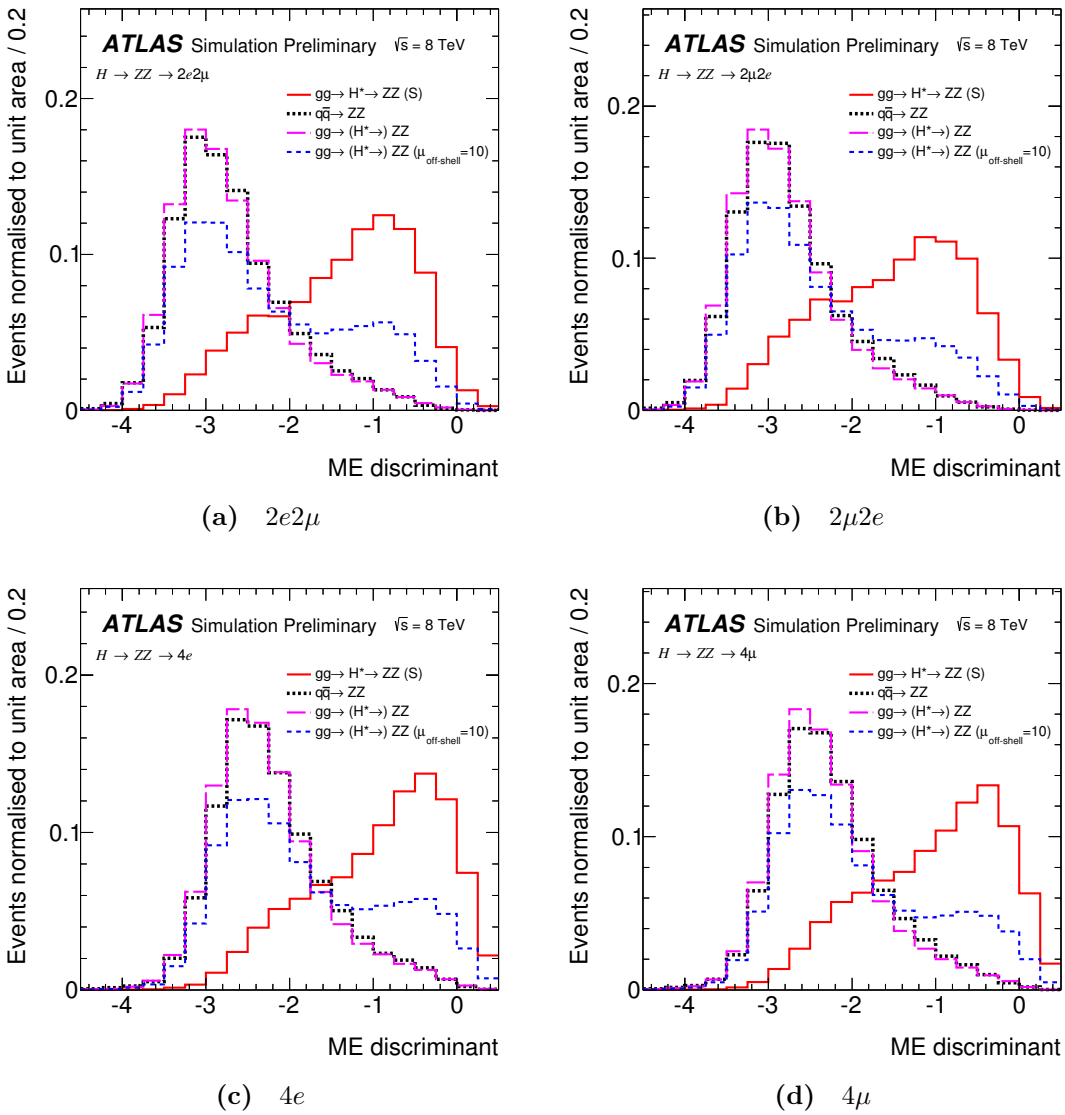

Figure 6.3 *Distributions of the ME-based discriminant for the off-peak region ($220\ GeV < m_{4\ell} < 1000\ GeV$) in the four lepton final states: (a) $2e\,2\mu$ (b) $2\mu\,2e$ (c) $4e$ (d) 4μ. The distributions are normalised to unit area for shape comparisons. The thick black dotted line represents the $q\bar{q} \to ZZ$ background, the red solid line the $gg \to H^* \to ZZ$ signal with SM couplings, the magenta long-dashed line the $gg \to (H^* \to)ZZ$ with SM $\mu_{off\text{-}shell}$, and the blue dashed line is for $gg \to (H^* \to)ZZ$ with $\mu_{off\text{-}shell} = 10$. A relative $gg \to ZZ$ background K-factor of $R^B_{H^*}$=1.0 is assumed.*

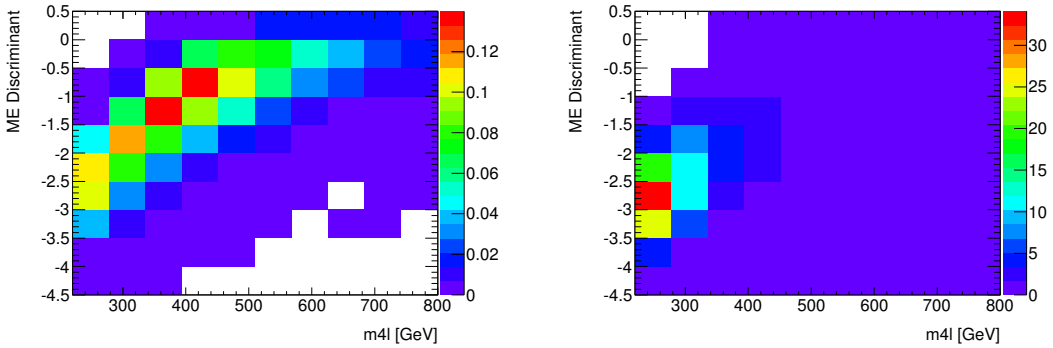

(a) $gg \to H \to ZZ$ **(b)** $q\bar{q} \to ZZ$

Figure 6.4 *Distributions of the ME-based discriminant vs. $m_{4\ell}$ for the (a) $gg \to H \to ZZ$ and (b) $q\bar{q} \to ZZ$ processes. A relative $gg \to ZZ$ background K-factor of $R^{B}_{H^*}$=1.0 is assumed.*

6.2 Systematics uncertainties

The largest systematic uncertainties for this analysis arise from theoretical uncertainties on the $gg \to H^* \to ZZ$ signal, the $gg/q\bar{q} \to ZZ$ background and the interference between the $gg \to ZZ$ signal and background processes. The electroweak $H^* \to ZZ$ process in association with two jets contributes about 10–30% to the total signal uncertainties. The associated theoretical uncertainties due to missing higher-order corrections and PDF variations are small for VH-like and VBF-like processes $pp \to ZZ + 2j$, and are therefore not included in the analysis. Compared to the theoretical uncertainties, the experimental uncertainties are negligible.

6.2.1 Systematic uncertainties on $gg \to (H^* \to)VV$

Uncertainty on the $gg \to H^* \to ZZ$ signal

The uncertainty from missing higher-order QCD and EW corrections to the off-shell $gg \to H^* \to ZZ$ signal as a function of the Higgs boson virtuality, $m_{4\ell}$, is estimated in Ref. [109] and adopted by this analysis. The uncertainty is 20–30% for the high-mass region. The PDF uncertainty for the $gg \to (H^* \to)ZZ$ process as a function of $m_{4\ell}$ is found to be 10–20% in the high-mass region, relevant for this analysis. This is consistent with an earlier study at $\sqrt{s} = 7$ TeV [120].

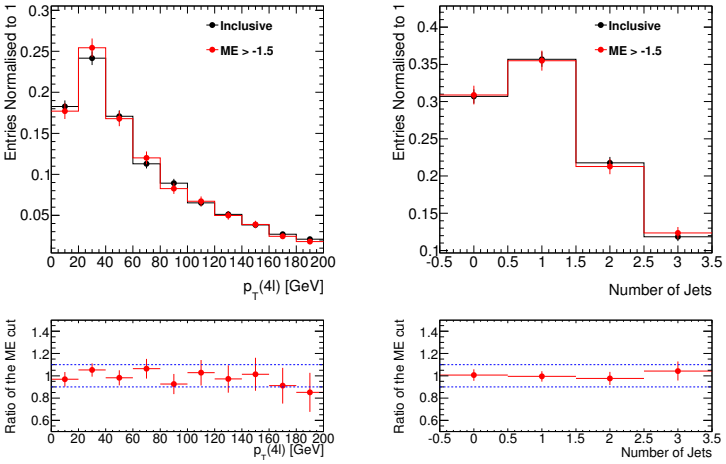

(a) $p_T(4\ell)$, *300-350 GeV*

(b) *# of jets, 300-350 GeV*

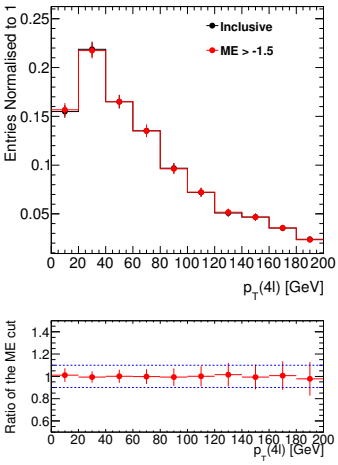

(c) $p_T(4\ell)$, *400-450 GeV*

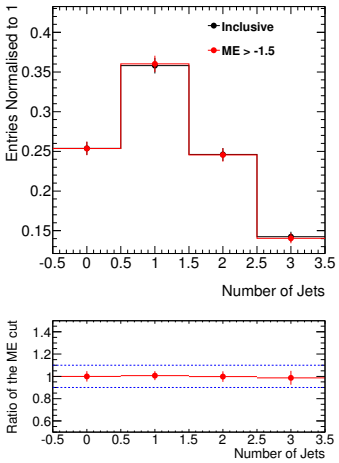

(d) *# of jets, 400-450 GeV*

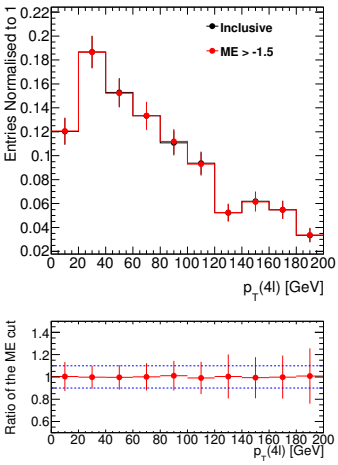

(e) $p_T(4\ell)$, *600-650 GeV*

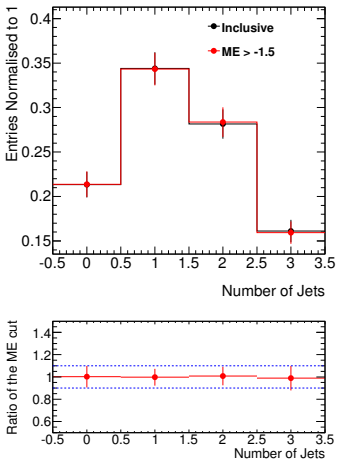

(f) *# of jets, 600-650 GeV*

Figure 6.5 *Distributions of $p_T(4\ell)$ (left) and the number of jets (right) for the $gg \to H \to ZZ \to 4\ell$ process before (black) and after (red) a ME discriminant cut of -1.5 has been applied, in $m_{4\ell}$ ranges of: 300-350, 400-450 and 600-650 GeV.*

Treatment of the $gg \to ZZ$ continuum background uncertainty

For the $gg \to ZZ$ background, higher-order QCD calculations are not available. In Ref. [117], a soft-collinear approximation is used to estimate the next-to-leading-order (NLO) and NNLO corrections to the $gg \to WW$ background process, indicating that the signal K-factor may also be applied to the signal-background interference term at the cost of adding an additional uncertainty of ∼30%. Then, the gluon-induced part of the signal K-factor $\mathrm{K}_{gg}^{H^*}(m_{4\ell})$ is applied to the background, and results are then presented as a function of the unknown K-factor ratio $\mathrm{R}_{H^*}^{B}$ between background and signal. The uncertainty on $\mathrm{K}_{gg}^{H^*}(m_{4\ell})$ is larger than the uncertainty on $\mathrm{K}^{H^*}(m_{4\ell})$ because some contributions to the full signal NNLO QCD K-factor are not present in $\mathrm{K}_{gg}^{H^*}(m_{4\ell})$. Therefore, the following correlation treatment of uncertainties is applied: the uncertainty on the signal K-factor $\mathrm{K}^{H^*}(m_{4\ell})$ is applied as an uncertainty correlated with $\mathrm{K}_{gg}^{H^*}(m_{4\ell})$. The difference in quadrature between the uncertainty on $\mathrm{K}_{gg}^{H^*}(m_{4\ell})$ and $\mathrm{K}^{H^*}(m_{4\ell})$ is added as an uncorrelated uncertainty component only to $\mathrm{K}_{gg}^{H^*}(m_{4\ell})$.

The 0.5–2 range is chosen for the variation of the K-factor ratio $\mathrm{R}_{H^*}^{B}$ in order to include the full corrections from the signal K-factor $\mathrm{K}_{gg}^{H^*}(m_{4\ell}) \sim 2$ in the variation range. With respect to the LO $gg \to ZZ$ process, this corresponds to an absolute variation in the range 1 to 4.

Treatment of the $gg \to (H^* \to)ZZ$ interference uncertainty

In Ref. [117], a soft-collinear approximation is used to calculate the cross-section for the sum of a heavy Higgs boson ($gg \to H \to WW$) and its interference with the background. The uncertainty on this calculation is estimated to be about 10%, which leads to a ∼ 30% uncertainty on the interference term alone. We use the same method employed for the missing higher-order QCD calculations in the $gg \to ZZ$ continuum background process to deal with the interference term here (namely, a similar K-factor and a 30% uncertainty on the interference alone). Within the ansatz of using an unknown K-factor ratio between background and signal (see Eq. (5.14)), this additional uncertainty of roughly 30% on the interference term can be represented by an approximately 60% variation of the K-factor ratio $\mathrm{R}_{H^*}^{B}$ for the background around the nominal value of 1.0. The approximation of scaling the interference term in Equation B.1 with the square root of an inclusive background K-factor K^B is valid only if the variation of this

K-factor over the phase-space being integrated in the analysis is sufficiently small to be factorised out of the integration.

For the Higgs boson signal component, Ref. [117] suggests that the soft-collinear approximation is expected to account for the dominant part of the full signal K-factor and shows little variation across phase space. Hence, this approximation is justified for the signal. It is estimated that this is also the case for the background, but this can only be confirmed once a full NLO calculation for the background is available. Therefore, the variation of $\mathrm{R}^{B}_{H^*}$ from 0.5 to 2 should cover both the leading corrections and uncertainties for the interference and the background component taken individually.

However, with respect to the expected results shown in Table 6.3 and the values $\mu^{95\%}_{\text{off-shell}}$ for the various expected limits at 95% CL presented in Section 6.4, the uncertainty on the negative interference component given by the $\sqrt{\mathrm{R}^{B}_{H^*}}$ variation and the uncertainty on the positive background component given by the $\mathrm{R}^{B}_{H^*}$ variation cancel each other to a large extent:

$$-\sqrt{\mu^{95\%\text{ CLs limit}}_{\text{off-shell}}} \cdot N^{gg\to(H^*\to)ZZ}_{\text{interference}} \quad \sim \quad 2 \cdot N^{gg\to ZZ}_{\text{background}}, \tag{6.3}$$

where $N^{gg\to(H^*\to)ZZ}_{\text{interference}}$ and $N^{gg\to ZZ}_{\text{background}}$ are the expected event yields for the interference and background components after the event selection. As the induced variation from the $\sqrt{\mathrm{R}^{B}_{H^*}}$ scaling on the interference component is approximately half the variation on the background component from the $\mathrm{R}^{B}_{H^*}$ scaling, no variation is expected at first order for the sum of interference and background as a function of $\mathrm{R}^{B}_{H^*}$ close to the point where the limit on $\mu_{\text{off-shell}}$ is expected:

$$-\sqrt{\mathrm{R}^{B}_{H^*}} \cdot \sqrt{\mu^{95\%\text{ CLs limit}}_{\text{off-shell}}} \cdot N^{gg\to(H^*\to)ZZ}_{\text{interference}} + \mathrm{R}^{B}_{H^*} \cdot N^{gg\to ZZ}_{\text{background}} \quad \sim \quad \text{const.} \tag{6.4}$$

Essentially, the leading uncertainty on the $gg \to ZZ$ background represented by the $\mathrm{R}^{B}_{H^*}$ variation is self-subtracting when the interference is enhanced by $\sim \sqrt{\mu^{95\%\text{ CLs limit}}_{\text{off-shell}}}$.

This raises the question on whether the chosen ansatz of scaling the interference term with $\sqrt{\mathrm{R}^{B}_{H^*}}$, although apparently a good approximation, is sufficient. Additional uncertainties on the interference component, which are not covered by the soft-collinear approximation could have an impact on the analysis. Therefore, in order to conservatively account for these additional contributions, the 30% uncertainty on the interference derived in Ref. [117] is applied to the

interference component in addition to the $\sqrt{\mathrm{R}^{B}_{H^*}}$ variation, which is assume to be uncorrelated. This is a conservative treatment which most likely results in a slight overestimation of uncertainties for the interference term.

6.2.2 Systematic uncertainties on $q\bar{q} \to ZZ$

The missing higher-order and PDF uncertainties for the $q\bar{q} \to ZZ$ background, as a function of $m_{4\ell}$, are taken from Ref. [120], and are based on NLO 7 TeV calculations using a fixed scale of m_Z. Slightly smaller systematic uncertainties are found for 8 TeV using a dynamic scale of $m_{4\ell}/2$. Therefore, applying the uncertainties from Ref. [120] can be considered a conservative choice. Both the QCD scale and the PDF uncertainties are 5–10% for the high-mass region used in this analysis. The NNLO calculation in Ref. [124] does not yield a significantly reduced QCD scale systematic uncertainty. An evaluation of the PDF uncertainty correlations shows that the $q\bar{q} \to ZZ$ background PDF uncertainties are anti-correlated with the PDF uncertainties for the $gg \to (H^* \to)ZZ$ process, and this is taken into account in the analysis. Acceptance uncertainties on the $q\bar{q} \to ZZ$ background are evaluated by comparing PYTHIA8 and HERWIG6 [139] samples and found to be negligible. Both the QCD scale and the PDF uncertainties are estimated to be ∼5–10% for the high-mass region used in this analysis.

Systematic uncertainty on the EW correction for $q\bar{q} \to ZZ$

The EW corrections for the $q\bar{q} \to ZZ$ process described in Sect. 5.5 are strictly valid only for the LO QCD $q\bar{q} \to ZZ$ process above the diboson production threshold, where both vector bosons are on shell.

The EW corrections are computed at LO QCD because calculations for the mixed QCD-EW corrections are not yet available. In events with high QCD activity, an additional systematic uncertainty is considered by studying the variable ρ introduced in Section 5.5.2, where a phase space region with $\rho < 0.3$ is selected. Figure 6.10 shows the impact of these corrections on the ME-based discriminant. For events with $\rho > 0.3$, the correction is applied with a 100% systematic uncertainty to account for the missing mixed QCD–EW corrections which are expected to be of the same order of magnitude. The applied corrections are partial in that they include only virtual corrections, and do not include polarisation

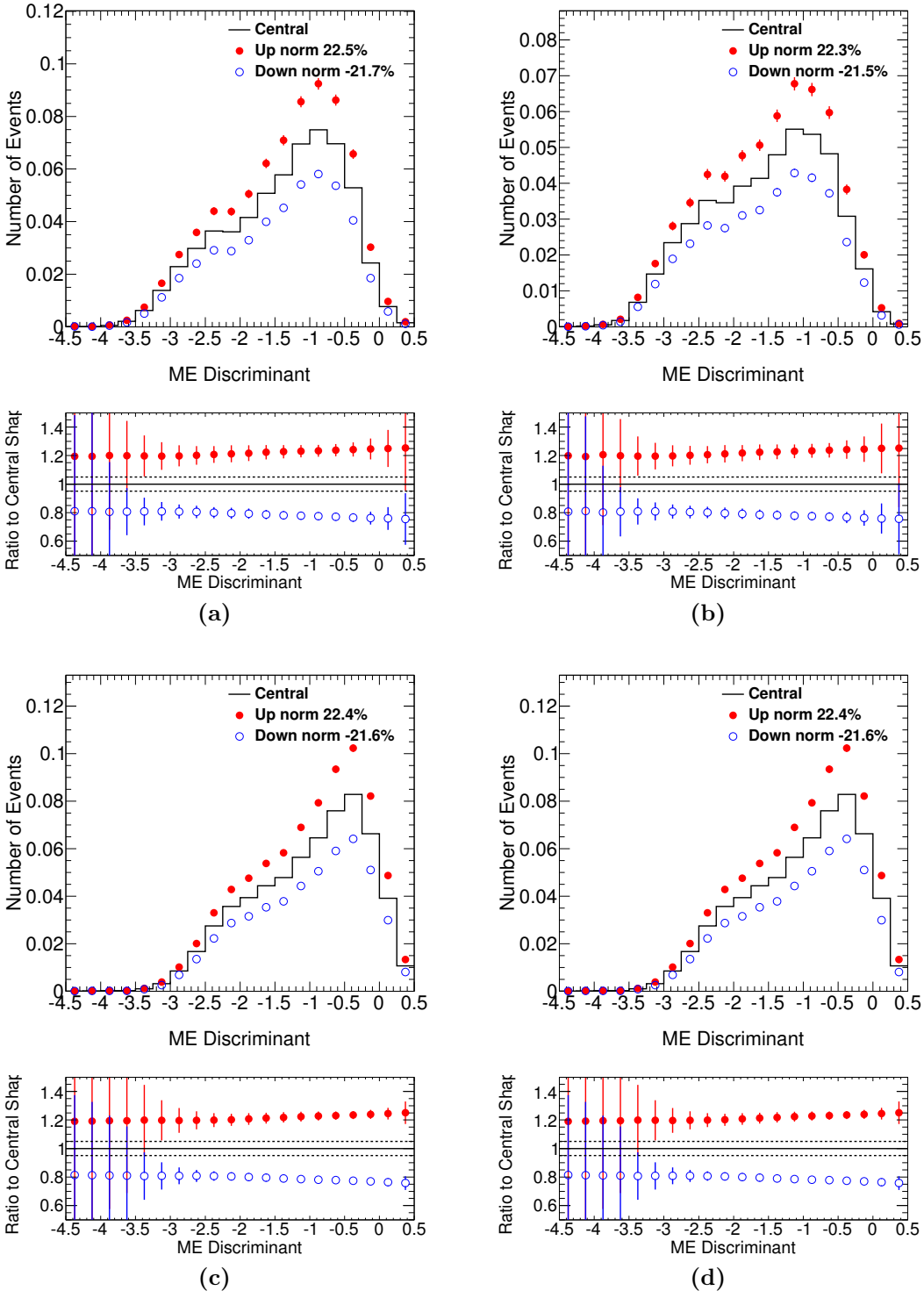

Figure 6.6 *Systematic uncertainties related to QCD corrections for the ME discriminant shapes in the four different lepton final states for the $gg \to H \to ZZ$ process: (a) $2e\,2\mu$ (b) $2\mu\,2e$ (c) $4e$ (d) 4μ.*

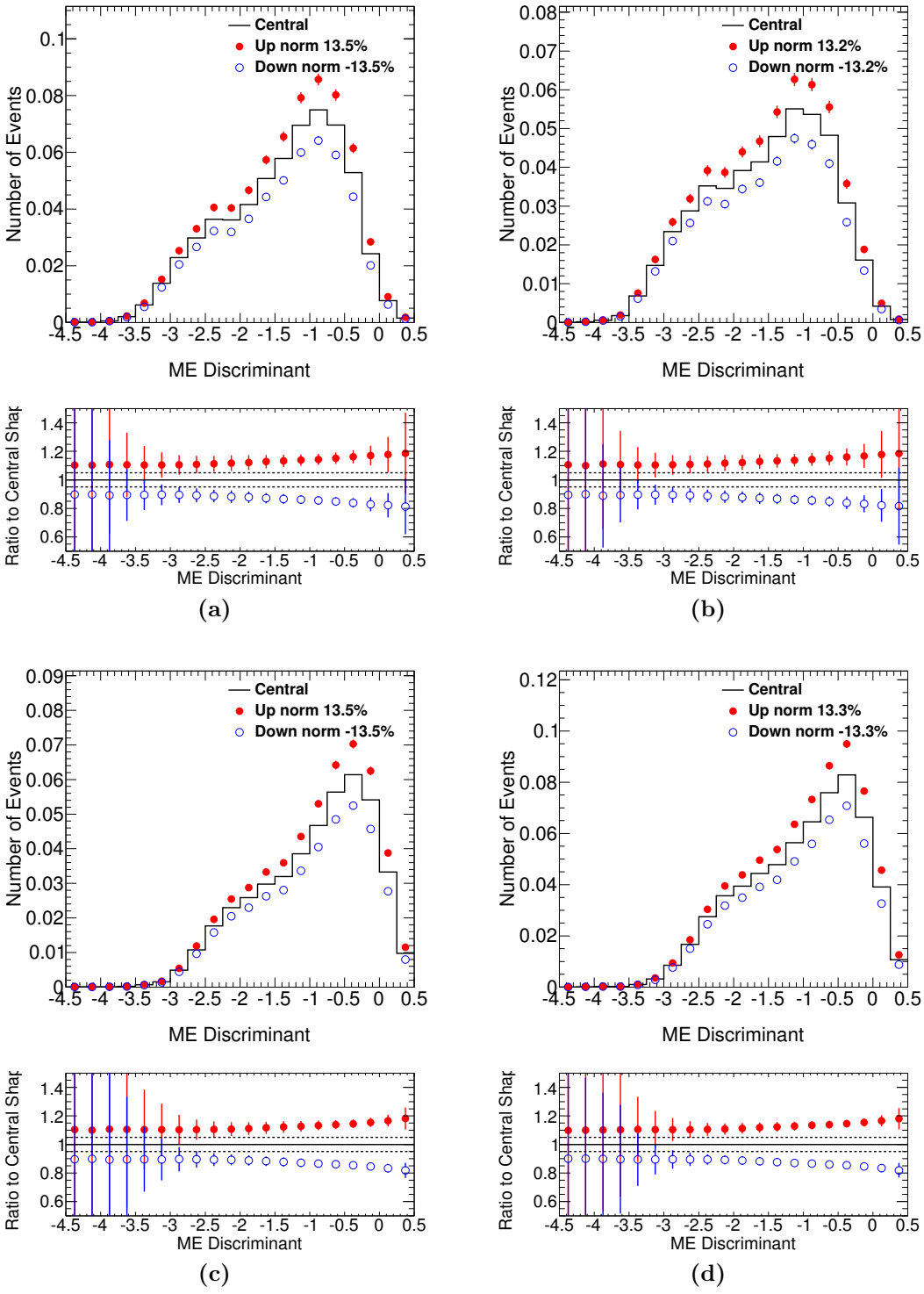

Figure 6.7 *Systematic uncertainties related to the PDF for the ME discriminant shapes in the four different lepton final states for the $gg \to H \to ZZ$ process: (a) $2e\,2\mu$ (b) $2\mu\,2e$ (c) $4e$ (d) 4μ.*

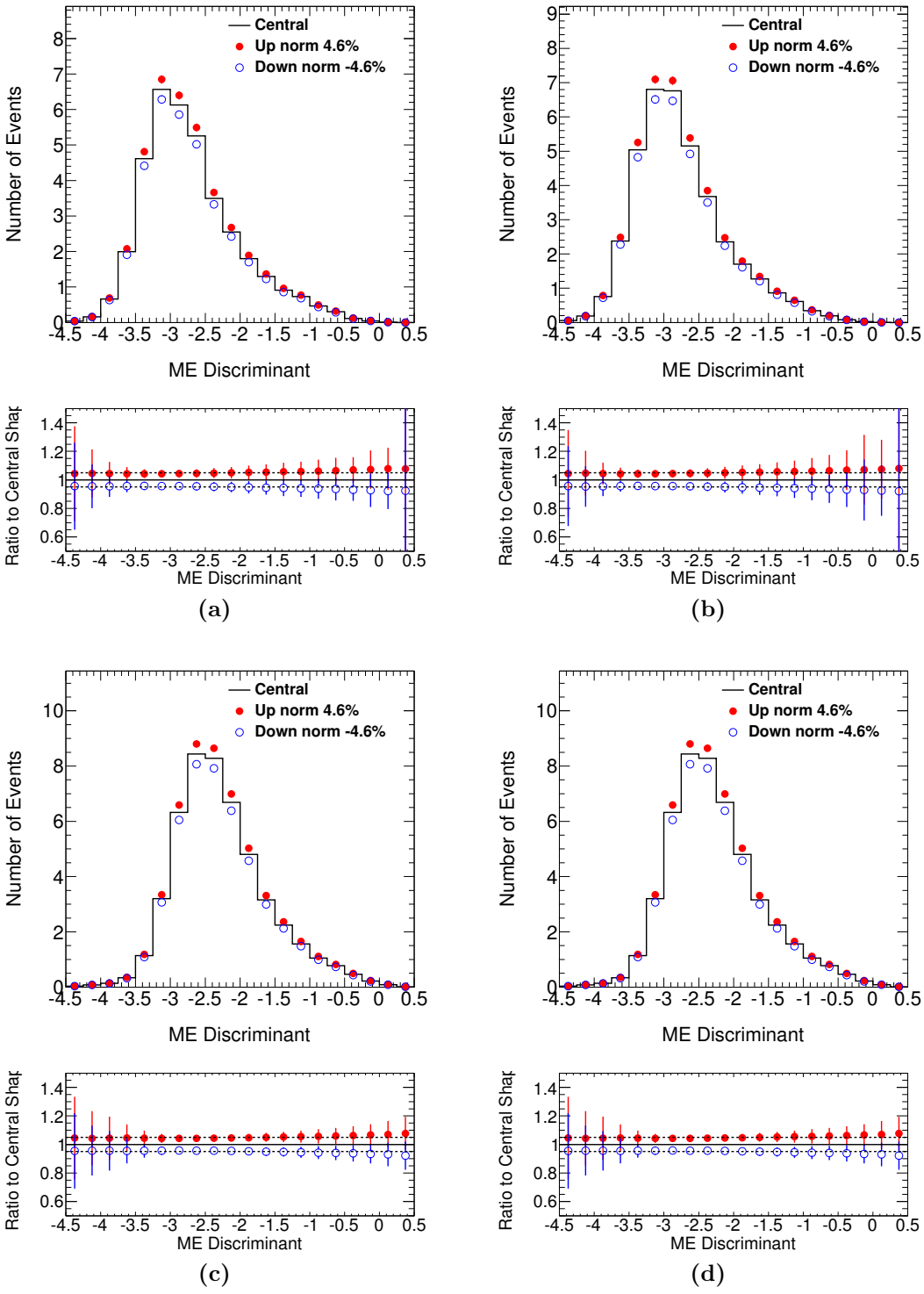

Figure 6.8 *Systematic uncertainties related to the QCD corrections for the ME discriminant shapes in the four different lepton final states for the $q\bar{q} \to ZZ$ process: (a) $2e\,2\mu$ (b) $2\mu\,2e$ (c) $4e$ (d) 4μ.*

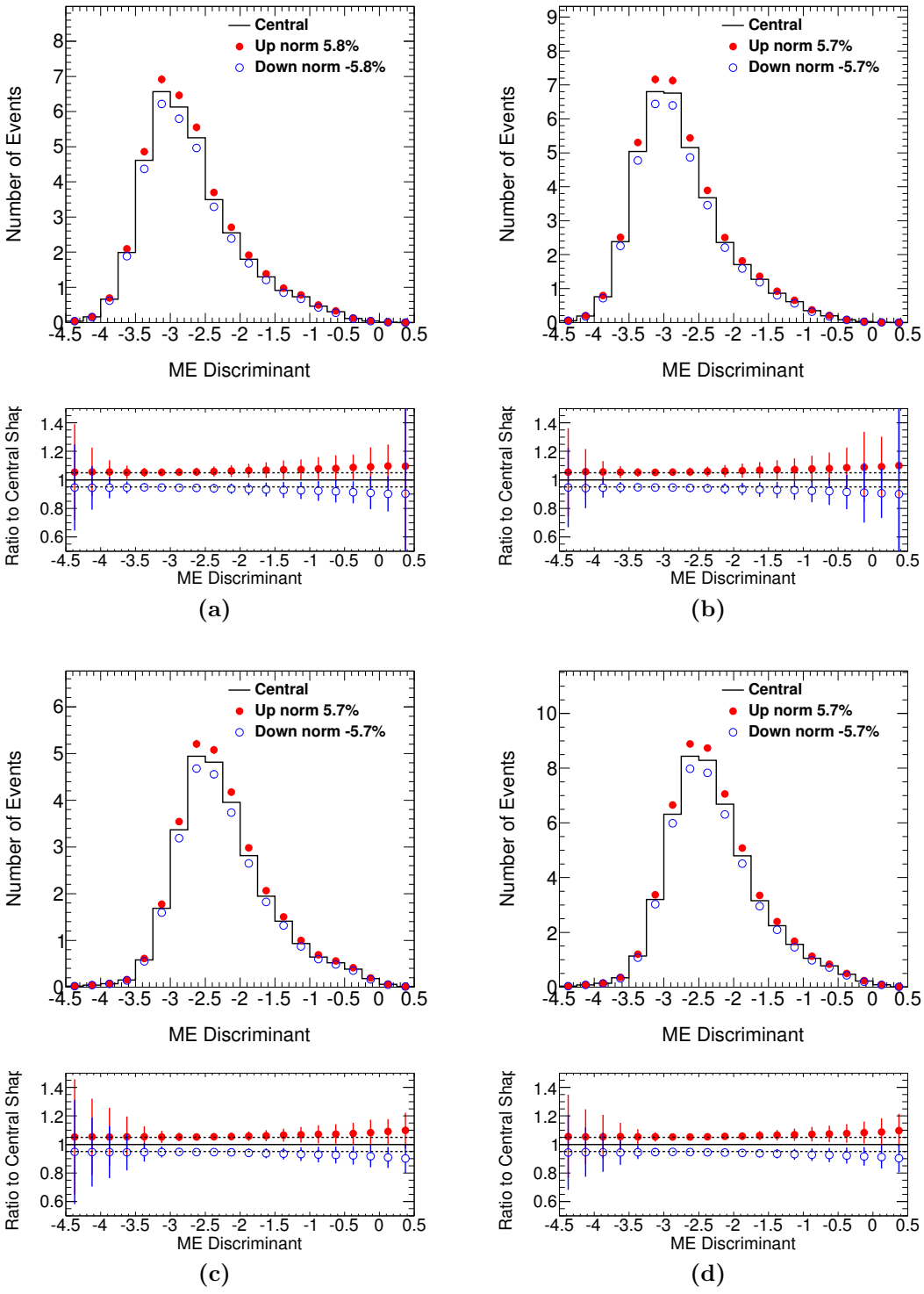

Figure 6.9 *Systematic uncertainties related to the PDF for the ME discriminant shapes in the four different lepton final states for the $q\bar{q} \to H \to ZZ$ process: (a) $2e\,2\mu$ (b) $2\mu\,2e$ (c) $4e$ (d) 4μ.*

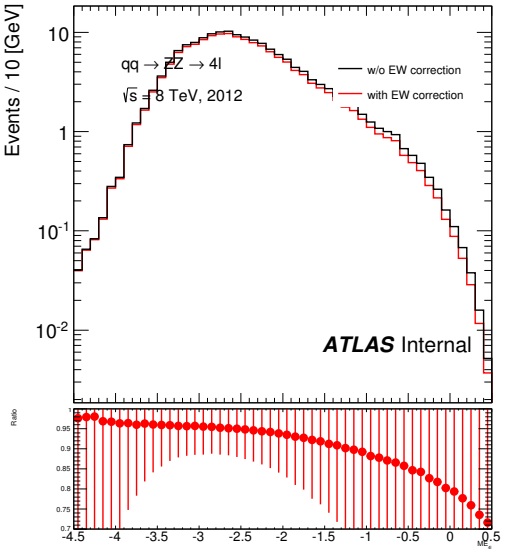

(a)

Figure 6.10 *Impact of the electroweak corrections for the ME discriminant in the $ZZ \to 4\ell$ analysis.*

effects. The sum of both of these effects is estimated to be $\mathcal{O}(1\%)$ [127] and is neglected in this analysis.

6.2.3 Systematic uncertainties on EW ZZ signal and background production in association with two jets

As the electroweak production modes are only a small contribution to expected signal yields, and the missing higher-order and PDF uncertainties are estimated to be small for the VH-like and VBF-like processes $pp \to ZZ + 2j$, these uncertainties are neglected in the analysis.

6.2.4 Experimental systematic uncertainties

The same sources of experimental uncertainty as in Ref. [136] are evaluated. In the off-shell Higgs boson region, the leptons come from the decay of on-shell Z bosons; hence the lepton-related systematic uncertainties are small compared to those for the leptons from on-shell Higgs boson production. Among the many experimental uncertainties, only two have a visible effect on the expected sensitivity, systematics due to electron reconstruction efficiency uncertainties for

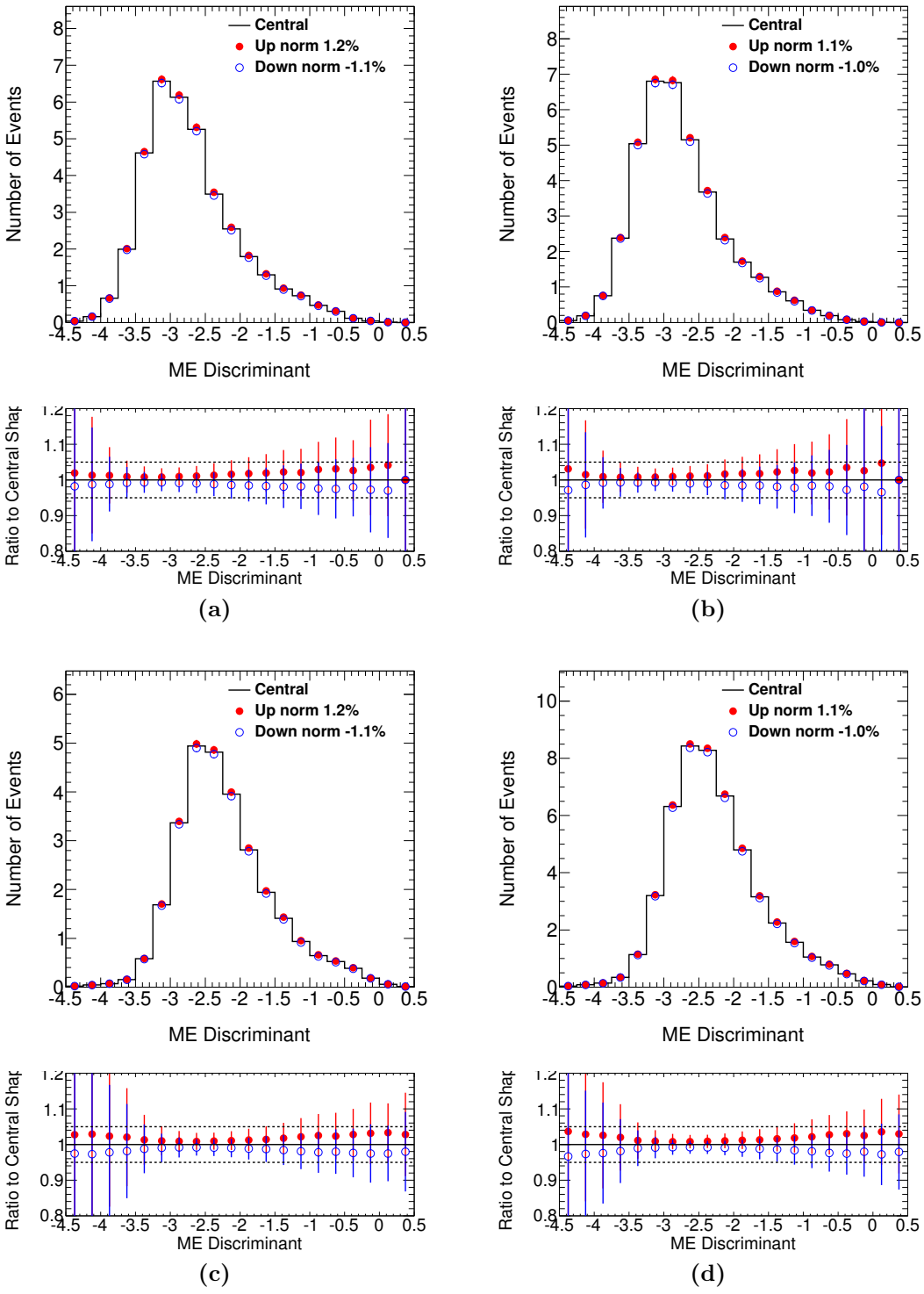

Figure 6.11 *Systematic uncertainties related to the electroweak corrections for the ME discriminant shapes in the four different lepton final states for the $q\bar{q} \to ZZ$ process: (a) $2e\,2\mu$ (b) $2\mu\,2e$ (c) $4e$ (d) 4μ.*

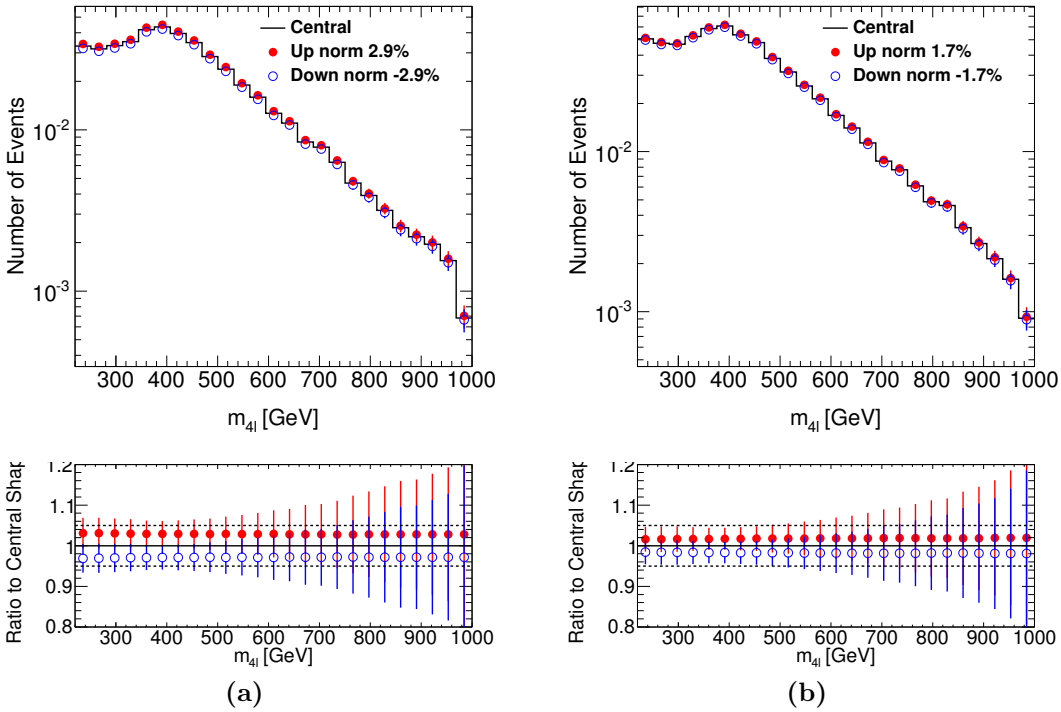

Figure 6.12 *Experimental systematic uncertainties related to the (a) electron and (b) muon reconstruction efficiency in the* $4e$ *and* 4μ *channels for the* $gg \to H \to ZZ$ *process.*

the high p_T (> 20 GeV) electron and muon efficiencies. Figure 6.12 shows the effect of those two systematics on the signal, as a function of the $m_{4\ell}$. There is no visible shape dependence and therefore only normalisation uncertainties are included. The impact of the experimental uncertainty to the expected sensitivity of the $\mu_{\text{off-shell}}$ is about a few percent.

6.3 Statistical analysis

After applying the same set of selection cuts on events from simulated MC and measured datasets, we create models for the description of probability density functions (PDFs) for the signal and background processes. The parameters of the likelihood function are estimated by comparing the model predictions against the experimental data in a fitting process that maximises the likelihood function. A parameter of interest is defined under a specific hypothesis, and its agreement with the observed data is obtained by using a statistical test. The statistical significance of this test defines the upper limit of the parameter of interest with a

value that should be within a confidence interval. This section gives an overview of the statistical tools used in the analysis to extract the upper limit of the off-shell signal strength.

6.3.1 Likelihood

The agreement between a proposed model and the measured data is done by first defining the hypotheses. Usually two contradictory hypotheses are defined, known as the null hypothesis and the alternative hypothesis, with the intent to be tested against each other. The null hypothesis corresponds to the "known" or "established" model or background-only hypothesis. For example, in a search for the SM Higgs, this hypothesis would correspond to all the SM interactions excluding the Higgs boson. On the other hand, the alternative hypothesis corresponds to a proposed signal model and is sometimes referred to as the signal+background hypothesis. In the same SM Higgs search example, it would correspond to the SM interactions including the Higgs boson (to be discovered).

The hypotheses are tested according to the measurement of a particular variable that is called the observable, x. For instance, this study uses two different observables, the invariant mass of the four leptons, $m_{4\ell}$ and the matrix element discriminant, ME. We assume that for a dataset of n events, s and b correspond to the expected number of signal and background events, respectively. The number of events observed can be modeled by a Poisson distribution whose mean can be expressed as $\mu s + b$, with μ being the signal strength. The probability to observe n events is given by:

$$P(n|\mu) = \prod_{i=1}^{n} \frac{(\mu s_i + b_i)^{n_i}}{n_i!} e^{-(\mu s_i + b_i)} \tag{6.5}$$

where the probability P is calculated from the number of signal, background and total events (n_i) in the i-th bin. The signal strength μ is the parameter of interest (POI), which, following the same Higgs boson search example, would vary between 0 for the null hypothesis and 1 for the alternative hypothesis. The values of the observable follow a PDF according to the probabilities for a signal or background event to occur:

$$f(x|\mu) = \frac{\mu s}{\mu s + b} f(x|s) + \frac{b}{\mu s + b} f(x|b) \tag{6.6}$$

where the coefficients of the signal and backround components above correspond to the fraction of signal and background events, respectively. Hence, the likelihood function that measures the observable x in every bin in a dataset with n events is:

$$\begin{aligned} L(\mu,\theta) &= P(n|\mu)\prod_{i=1}^{n} f(x_i|\mu) \\ &= \prod_{i=1}^{n} \frac{(\mu s_i + b_i)^{n_i}}{n_i!} e^{-(\mu s_i + b_i)} \frac{\mu s f(x_i|s) + b f(x_i|b)}{\mu s + b} \end{aligned} \tag{6.7}$$

where $\theta = (\theta_s; \theta_b)$ contains the nuisance parameters. The signal and background PDFs depend on these parameters: $f(x|s) = f_s(x;\theta_s)$ and $f(x|b) = f_b(x;\theta_b)$, respectively. Systematic uncertainties are introduced as nuisance parameters described by the PDFs $\rho(\theta,\tilde{\theta})$, where $\tilde{\theta}$ is the best estimate of the nuisance parameter θ with a width σ. The analysis in this thesis includes both normalization and shape systematic uncertainties as described in Sect. 6.2.1, with correlations between different components and processes as indicated therein. In the case of shape systematic uncertainties, the usual choice is a Gaussian PDF, as it suits well situations in which a parameter can have both positive and negative values. It is defined as:

$$\rho(\theta) = \frac{1}{\sqrt{2\pi}\sigma} exp\Big(- \frac{(\theta - \tilde{\theta})^2}{2\sigma^2} \Big) \tag{6.8}$$

The complete likelihood that takes into account the nuisance parameters is written as:

$$\begin{aligned} L(\mu,\theta) &= P(n|\mu)\prod_{i=1}^{n} f(x_i|\mu)\prod_{j=1}^{m}\rho(\theta_{ij}) \\ &= \prod_{i=1}^{n} \frac{(\mu s_i + b_i)^{n_i}}{n_i!} e^{-(\mu s_i + b_i)} \prod_{j=1}^{m} \frac{\mu s f_s(x_i;\theta_s) + b f_b(x_i;\theta_b)}{\mu s + b} \\ &\cdot \quad \frac{1}{\sqrt{2\pi}\sigma_{ij}} exp\Big(- \frac{(\theta_{ij} - \tilde{\theta}_{ij})^2}{2\sigma_{ij}^2} \Big) \end{aligned} \tag{6.9}$$

where j runs over all $(= m)$ nuisance parameters. The binned likelihood of the analysis is the same as in Eq. 6.9, where the POI is the off-shell signal strength $\mu = \mu_{\text{off-shell}}$ and the baseline observable is the ME-discriminant $x = ME$. However, since the goal of the analysis is to measure an upper limit of $\mu_{\text{off-shell}}$, the POI would vary freely, starting from the value 1 for the SM+Higgs hypothesis, and until it reaches an upper limit under a given threshold, as explain in Sect. 6.3.2.

The estimation for each parameter is obtained by maximising the value of the likelihood function, i.e. in the so-called maximum likelihood maximisation.

$$\frac{\partial L}{\partial \theta_i} = 0 \quad , \quad i = 1, \ldots, n \tag{6.10}$$

Despite the dependency on and the complications brought in by the nuisance parameters, the goal of the analysis is simply to evaluate the likelihood as a function of $\mu_{\text{off-shell}}$, and determine when it is maximised. The analysis uses a profile likelihood method that expresses the nuisance parameters in terms of $\mu_{\text{off-shell}}$, estimating the maximum likelihood without determining the optimal values for them. Statistical methods to measure the best $\mu_{\text{off-shell}}$-fit are explained in the following section.

6.3.2 p-value and confidence intervals

To quantify the statistical significance of the agreement level between the observed data and a given hypothesis, a p-value is computed. The p-value is the probability, under a specific hypothesis assumption, of finding data of equal or greater incompatibility with the predictions of the hypothesis. The measure of incompatibility can be based on the corresponding profile likelihood ratio for the signal and background models. One can regard the hypothesis as "excluded" if its p-value is observed to be below a specified threshold.

The p-value is usually converted into an equivalent significance, Z, defined as a Gaussian distributed variable which is lying Z standard deviations (σ) above the mean value with an upper-tail probability equal to the p-value (p).

$$Z = \Phi^{-1}(1-p), \tag{6.11}$$

where Φ^{-1} is the inverse of the cumulative distribution of the standard Gaussian. A signal discovery is claimed if the significance to reject a background hypothesis reaches at least $Z = 5$, which corresponds to a p-value[3] of $p = 2.87 \times 10^{-7}$. The signal hypothesis is generally excluded if the probability of signal absence reach a p-value threshold of 0.05, or 95% CL, which corresponds to $Z = 1.64$. A widely used procedure to establish discovery (or exclusion) is based on a significance test using the profile likelihood ratio [140] as a test statistic. A hypothetical value of

[3]Estimated by using a one-sided fluctuation of a Gaussian variable.

the POI μ is tested using the profile likelihood ratio:

$$\Lambda(\mu) = \frac{L\big(\mu, \hat{\hat{\vec{\theta}}}(\mu)\big)}{L(\hat{\mu}, \hat{\vec{\theta}})} \quad , \tag{6.12}$$

where $\hat{\hat{\vec{\theta}}}$ and $\hat{\vec{\theta}}$ are the nuisance parameter values that maximize the likelihood for a specific μ, (or conditional fit), and the ones that maximize the likelihood (or unconditional fit), respectively. The parameter μ in the numerator is not determined by a fixed fit, while $\hat{\mu}$ is a parameter of the maximum likelihood fit. The range of the profile likelihood ratio $\Lambda(\mu)$ varies between $0 \leq \Lambda(\mu) \leq 1$, with $\Lambda(\mu) \to 1$ implying a good agreement between the data and the hypothesized value of μ. The level of the agreement for a distribution for a given μ can be tested by using a test statistic t_μ:

$$t_\mu \equiv -2 \ln \Lambda(\mu) \quad , \tag{6.13}$$

High values of t_μ thus correspond to an increased incompatibility between the data and μ. Even though the observed number of events can fluctuate below the expected value, usually the signal process is such that only positive values of μ are considered. For the purpose of measuring an upper limit for the parameter μ, Eq. 6.13 can take the following values:

$$t_\mu = \begin{cases} -2 \ln \Lambda(\mu) & \text{if } \hat{\mu} \leq \mu \\ 0 & \text{if } \hat{\mu} > \mu \end{cases} \tag{6.14}$$

Values with $\hat{\mu} > \mu$ would not be taken into account for the measurement of an upper limit since they correspond to a reduced μ-compatibility with the data obtained, therefore $t_\mu = 0$. To quantify the level of disagreement between data and the hypothesis obtained by the previous test, the p-value is calculated as:

$$p_\mu = \int_{t_{\mu,obs}}^{\infty} f(t_\mu|\mu, \theta) dt_\mu \tag{6.15}$$

where $t_{\mu,obs}$ is the value of t_μ observed in the data and $f(t_\mu|\mu, \theta)$ is the PDF of t_μ under the assumption of μ. After testing several values of μ, the upper limit becomes the highest p-value of a given μ that can be defined within the CL region. For instance, the current analysis aims to set an upper limit on $\mu_{\text{off-shell}}$ within a 95% CL interval, under the assumption of a null hypothesis of the (SM plus) Higgs interactions $\mu_{\text{off-shell}}$=1.

The p-value from Eq. 6.15 is obtained by simulating the distribution of the PDF $f(t_\mu|\mu,\theta)$, being are several ways to do it. A common choice is to use an approximate method that is computationally less demanding. For instance, assuming relatively large data samples, the distribution approaches asymptotically a form that can be approximed by a chi-square χ^2 distribution [141] with the number of degrees of freedom being equal to the number of parameters of interest. In the specific case of the current analysis there is only one POI, $\mu_{\text{off-shell}}$. The approximate method is based on the theorems of Wilks [142] and Wald [143], where the asymptotic approximation of the test statistic t_μ is given by:

$$-2\ln\Lambda(\mu) \;=\; \frac{\mu-\hat{\mu}}{\sigma^2} + O(1/\sqrt{N})\ , \tag{6.16}$$

with the $\hat{\mu}$ distribution following a Gaussian with mean $\mu^{'}$, and N being the size of the data sample. Neglecting the $O(1/\sqrt{N})$ term, the PDF of t_μ follows a non-central χ^2 distribution:

$$f(t_\mu|\mu) \;=\; \frac{1}{2\sqrt{2\pi t_\mu}}\Big[\exp\Big(-\frac{1}{2}(\sqrt{t_\mu}+\frac{\mu-\mu^{'}}{\sigma})^2 \tag{6.17}$$

$$+\;\exp\Big(-\frac{1}{2}(\sqrt{t_\mu}-\frac{\mu-\mu^{'}}{\sigma})^2\Big)\Big] \tag{6.18}$$

The upper limit can be calculated numerically as the maximum value of μ that is constrained by the CL region. However, the standard deviation σ, that depends on the hypothesis value μ, has not been calculated. This quantity can be estimated by using an artificial dataset such as the Asimov dataset[4]. The Asimov dataset is an approximate method that obtains the expected values by evaluating the estimators for the parameter. Then, according to the Asimov estimation, the POI in the profile likelihood corresponds to the mean of the gaussian $\mu = \mu^{'}$. Therefore, given that $t_\mu = -2\ln\Lambda(\mu)$, the standard deviation can be estimated from Eq. 6.16:

$$\sigma \;=\; \frac{(\mu-\mu^{'})^2}{t_\mu} \tag{6.19}$$

The results presented in this study rely on the asymptotic approximation [140] for the test statistic $\Lambda(\mu)$. This approximation was cross-checked with Monte Carlo ensemble tests that confirm its validity in the range of the parameters for

[4]The name of the Asimov data set is inspired by the short story Franchise, by Isaac Asimov. In it, elections are held by selecting the single most representative voter to replace the entire electorate.

which the 95% CL limits are derived. Deviations appear close to the boundary of $\mu_{\text{off-shell}} \geq 0$ imposed by Eq. (5.14), and hence the 1σ quoted uncertainties can only be seen as approximate.

The interpretation of the p-value for searches of phenomena near the sensitivity limit of an experiment is a common problem in particle physics. But the introduction of the CL_s method [144], as a modification of a purely classical statistical analysis method, can avoid excluding (or discovering) signals for which the search has no sensitivity. The CL_s method is based not on the usual p-value, but rather on a test that considers the background-only hypothesis:

$$CL_s = \frac{p_{s+b}}{1 - p_b} \tag{6.20}$$

In the case in which the analysis sensitivity is high, the classical frequentist procedure is recovered, corresponding to the negligible-background scenario. In the current analysis, the final results are calculated using the CL_s method and are cross-checked with the statistical test t_μ. In the case of the CL_s method, the p-value p_{s+b} corresponds to the test of a given $\mu = \mu_{\text{off-shell}}$ or $\mu = \Gamma_H/\Gamma_H^{\text{SM}}$ (the non-SM hypothesis, or null hypothesis). The p-value p_b is derived from the same test statistic under the SM hypothesis of $\mu_{\text{off-shell}} = 1$ in the first case, and $\Gamma_H/\Gamma_H^{\text{SM}} = \mu_{\text{on-shell}} = 1$ in the second.[5] The 95% CL_s upper limit is calculated by solving $CL_s(\mu^{95\%}) = 5\%$, with the $\mu > \mu^{95\%}$ values regarded as excluded at 95% CL. A detailed description of the implementation of the CL_s procedure can be found in Ref. [145].

At first instance, the likelihood fits and the estimation of the parameters of interest are calculated using MC samples in order to validate the statistical methods.

6.3.3 Fit validation

As a first step, the distribution of the binned maximum likelihood for the ME-based discriminant is validated by comparing the expected PDF distribution to the one from simulation. The fit model accounts for signal and background processes, including $gg \to (H^* \to)ZZ$, VBF$(H^* \to)ZZ$ and $q\bar{q} \to ZZ$. The PDF of the signal-related processes $gg \to (H^* \to)ZZ$ and VBF $(H^* \to)ZZ$

[5] In the context of this analysis, the alternative hypothesis is given by the SM value(s) for all relevant parameters of the fit model.

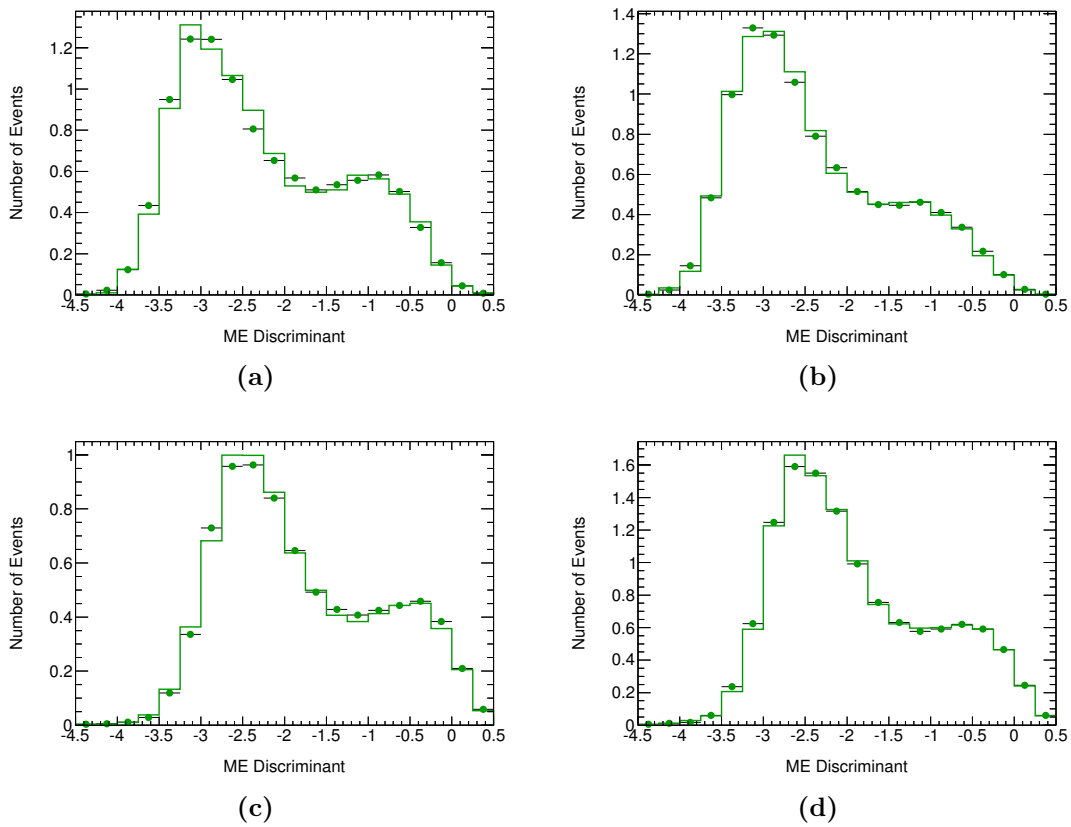

Figure 6.13 *Comparison between the distributions of the ME discriminant for the $gg \to (H^*) \to ZZ$ PDF parametrisation (histograms) and simulation (data points) for the $gg \to ZZ \to 4\ell$ process including a Higgs boson ($\mu_{\textit{off-shell}} = 10$), the continuum background and their interference, after the baseline selections for the off-peak analysis, in the four lepton final states: (a) 2e2μ (b) 2μ2e (c) 4e (d) 4μ.*

are parameterised as a function of both the off-shell Higgs boson signal strength $\mu_{\text{off-shell}}$ and the unknown background K-factor ratio $\mathrm{R}^{B}_{H^*}$, given in Eqs. (B.3) and (5.18). This parametrisation is validated using MC samples with $\mu_{\text{off-shell}} = 10$ for the $gg \to (H^* \to)ZZ$ process (distributions of which can be seen in Figure 6.13), with no significant deviations found. In the case of the cut-based analysis, the ME-based discriminant observable is replaced by $m_{4\ell}$.

In the following results, one must note that the final 95% CL limits are given as a function of the unknown background K-factor ratio $\mathrm{R}^{B}_{H^*}$. This is in contrast to some of the figures and tables, for which the $\mathrm{R}^{B}_{H^*}$=1 assumption is made.

The fit is validated in the presence of large $\mu_{\text{off-shell}}$ (with values of 10 and 25). Asimov datasets are created from both PDF and MC samples, which are then fitted without the systematic effects. Fit results are shown in Table 6.6, indicating

no bias in the fitting procedure for the datasets created from either the PDF or the MC samples.

Asimov dataset	$\mu_{\text{off-shell}} = 10$	$\mu_{\text{off-shell}} = 25$
PDF	$10.0^{+4.3}_{-3.8}$	$25.0^{+5.2}_{-4.8}$
MC samples	$10.0^{+4.3}_{-3.8}$	$25.0^{+5.2}_{-4.8}$

Table 6.6 *Fit results of $\mu_{\text{off-shell}}$ on Asimov datasets generated from both PDF and MC samples for the ME discriminant-based shape analysis excluding systematic effects. The corresponding t_μ likelihood scans are shown in Figure 6.14.*

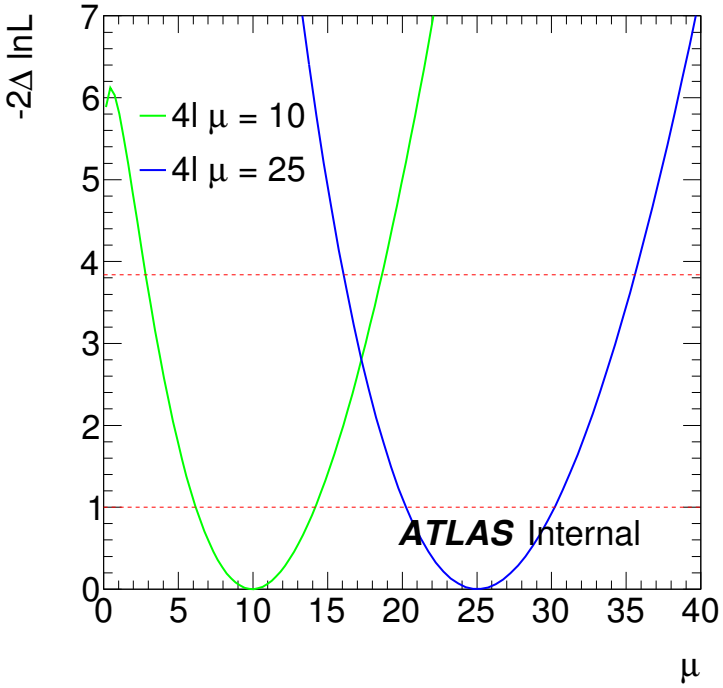

Figure 6.14 *t_μ (-2lnΛ) likelihood scan as a function of $\mu_{\text{off-shell}}$ in the fit to Asimov data generated from MC samples with $\mu_{\text{off-shell}} = 1$, using the ME discriminant-based shape analysis.*

The expected sensitivity of the 95% CL upper limits on $\mu_{\text{off-shell}}$ is evaluated using the statistical test t_μ, assuming SM Higgs couplings. The results can be seen in Figure 6.15 and Table 6.7. A double-minimum structure is observed between 0 and 1, due to the expected double solution to the second order polynomial dependence of the $gg \to ZZ$ yield on $\mu_{\text{off-shell}}$.

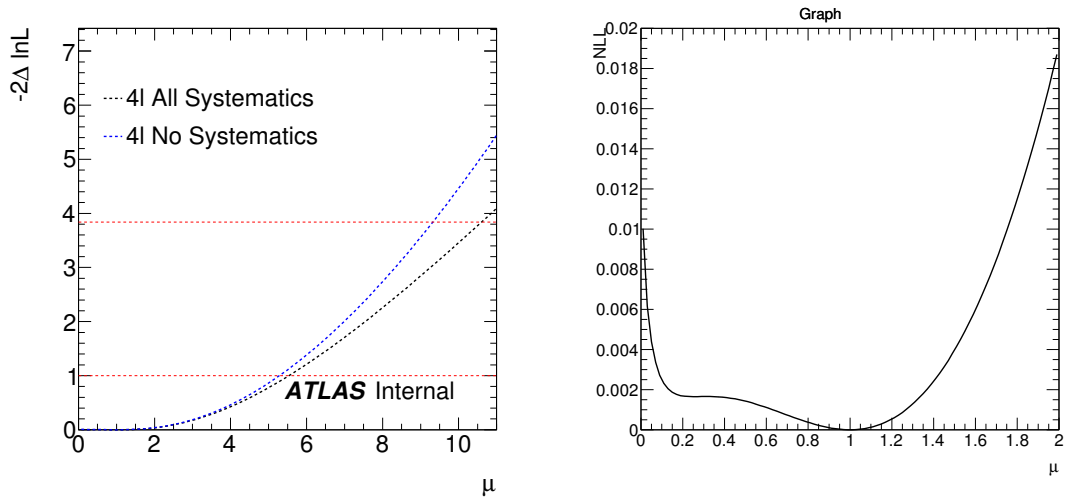

(a) **(b)**

Figure 6.15 *(a) t_μ (-2lnΛ) likelihood scan as a function of $\mu_{off\text{-}shell}$ in the fit to Asimov data generated from MC samples with $\mu_{off\text{-}shell} = 1$, using the ME discriminant-based shape analysis for the gg fusion channel (b) Zoom-in of the scan near the minimum for the fit to MC samples.*

Asimov dataset	Without systematics	With systematics
PDF	1.0 (9.3)	1.0 (10.6)
MC samples	1.0 (9.3)	1.0 (10.6)

Table 6.7 *The fitted (expected) mean 95% C.L. upper limits on $\mu_{off\text{-}shell}$ with Asimov datasets generated from both PDF and MC samples for the ME discriminant shape-based analysis for gg fusion, assuming the SM Higgs couplings, with and without systematic uncertainties. The corresponding t_μ likelihood scan plots are shown in Figure 6.15.*

6.4 Results

This section presents the fit results expressed as upper limits on the off-shell signal strength and with an additional interpretation on the Higgs boson total width. First, the consistency between the total background prediction and the actual measurement of the off-peak region is checked. Then, the event distribution are checked with the cut-based and ME shape-based analyses, calculating the significance of the upper limit on the off-shell signal strength. The full systematic uncertainties are included in the calculation for the baseline ME shape-based analysis. Then, a combination with the results from the $ZZ \to 2\ell\,2\nu$ and $WW \to \ell\nu\ell\nu$ channels is performed, in order to calculate the significance of the upper limit on the off-shell signal strength across all diboson channels. Finally, the Higgs boson total width is interpreted from the on-shell and off-shell signal strength measurements. The off-shell signal strength and the Higgs boson total width are calculated using two different assumptions related to the production modes.

6.4.1 Observed yield and kinematics in the background region

To cross-check the background predictions, we define two $q\bar{q} \to ZZ$ background enriched regions:

- Control region A: 160 GeV $< m_{4\ell} <$ 220 GeV
- Control region B: 220 GeV $< m_{4\ell} <$ 1000 GeV and ME $<$ -1.5

Table 6.8 and Table 6.9 show the expected number of events in control region A and B, respectively. The corresponding $m_{4\ell}$ and ME discriminant distributions are shown in Figure 6.16 and Figure 6.17 for control region A, and Figure 6.18 and Figure 6.19 for control region B. In all four lepton final states, the observed (background-enriched) data is found to be consistent with the total background prediction within $1 - 2\sigma$.

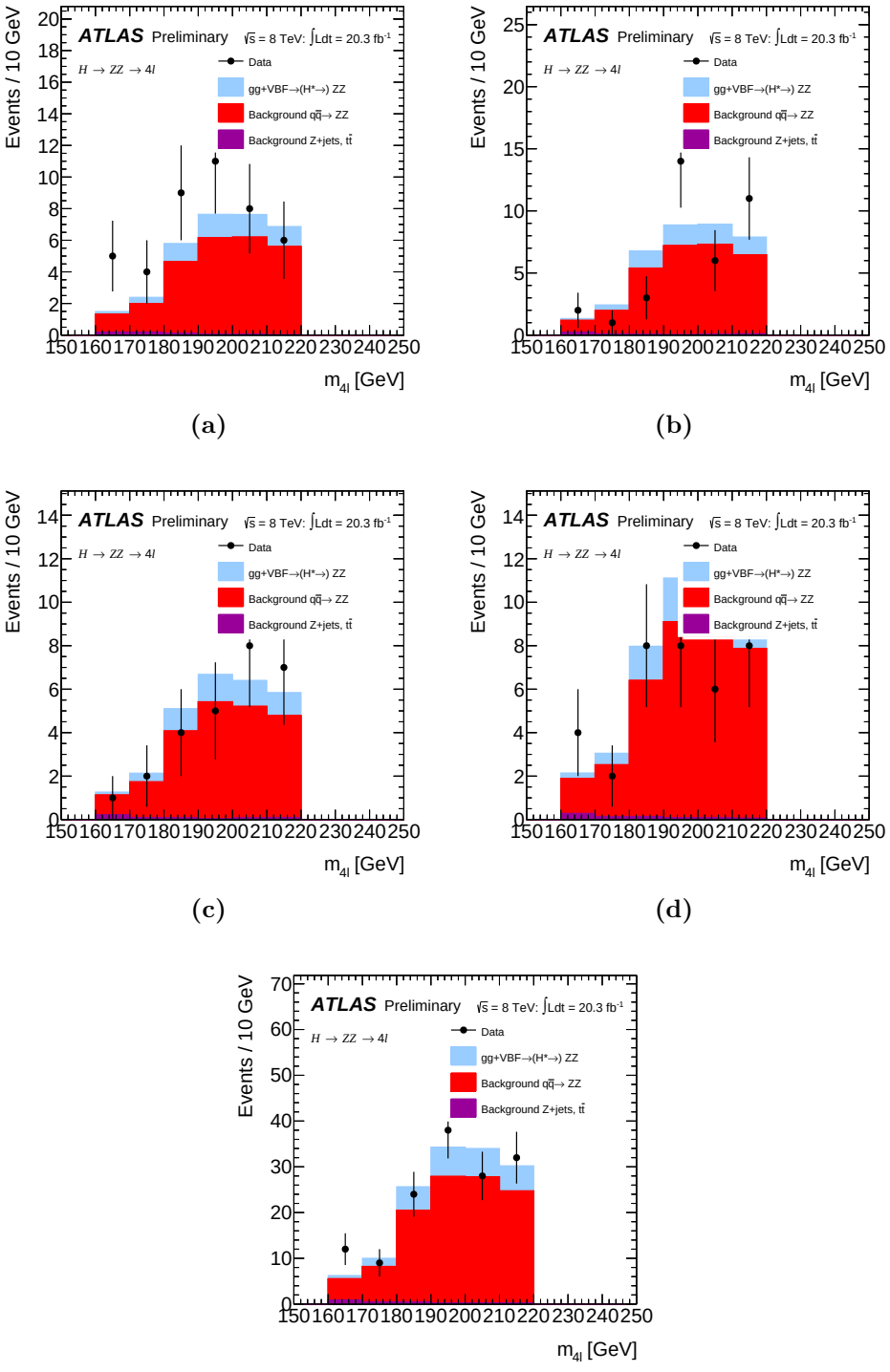

Figure 6.16 *$m_{4\ell}$ distributions in the "Control A" $q\bar{q} \to ZZ$ background enriched region (160 GeV $< m_{4\ell} <$ 220 GeV) for all processes in the four leptonic final states: (a) $2e2\mu$ (b) $2\mu 2e$ (c) $4e$ (d) 4μ (e) all combined.*

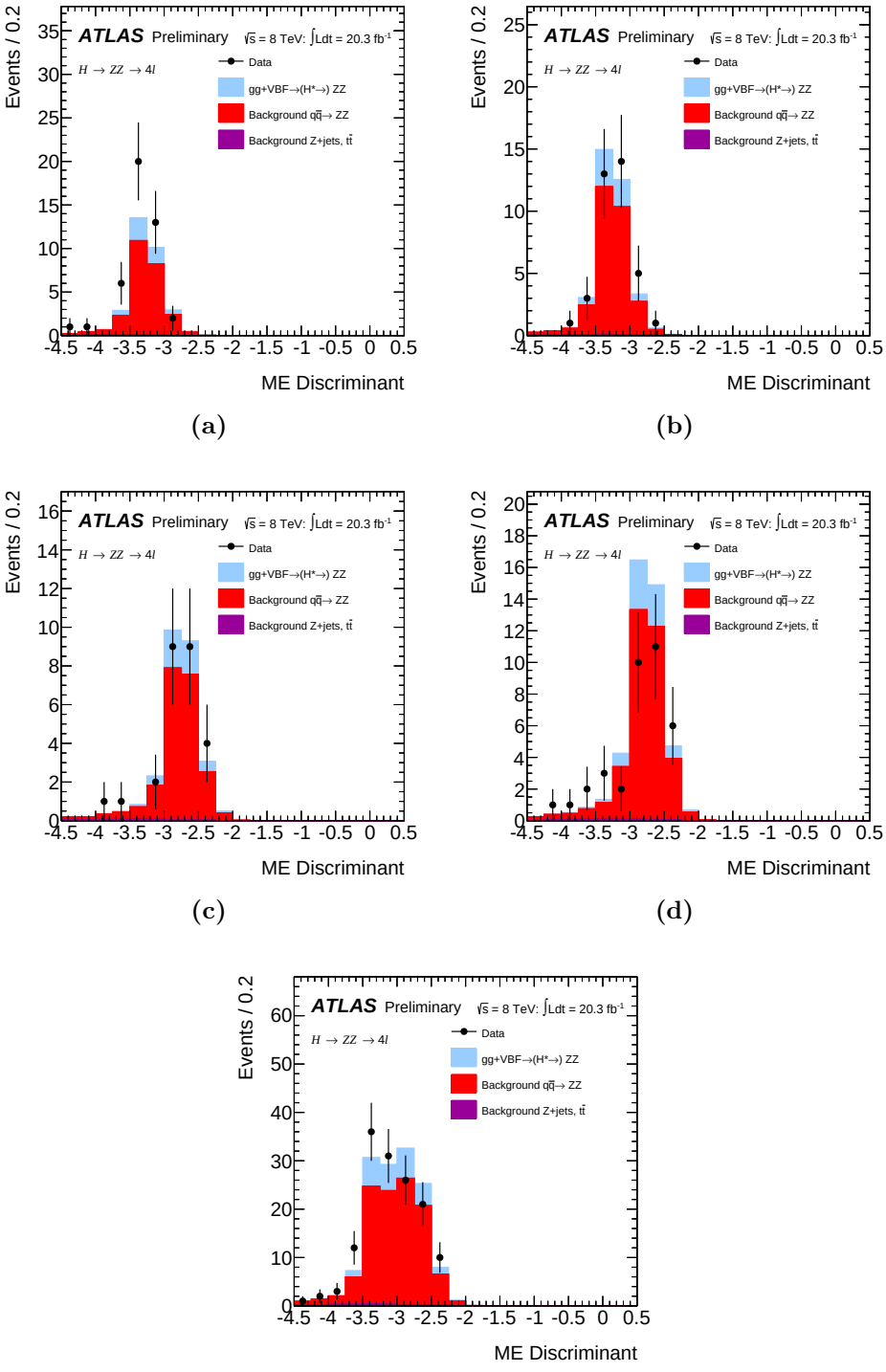

Figure 6.17 *ME discriminant distributions in the "Control A" $q\bar{q} \to ZZ$ background enriched region ($160\ GeV < m_{4\ell} < 220\ GeV$) for all processes in the four leptonic final states: (a) $2e\,2\mu$ (b) $2\mu\,2e$ (c) $4e$ (d) 4μ (e) all combined.*

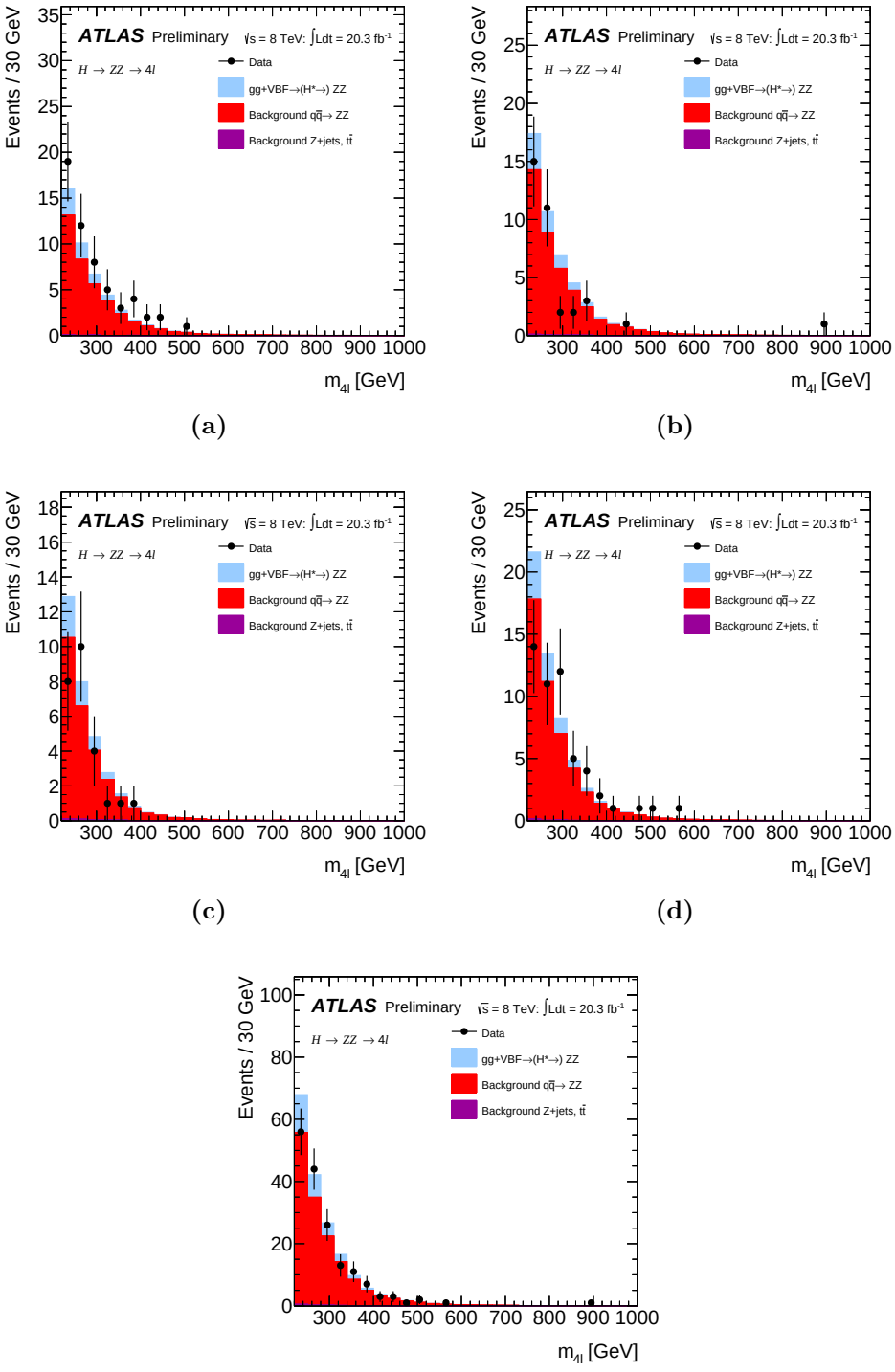

Figure 6.18 *$m_{4\ell}$ distributions in the "Control B" $q\bar{q} \to ZZ$ background enriched region (220 GeV < $m_{4\ell}$ < 1000 GeV, and ME discriminant <-1.5) for all processes in the four leptonic final states: (a) $2e\,2\mu$ (b) $2\mu\,2e$ (c) $4e$ (d) 4μ (e) all combined.*

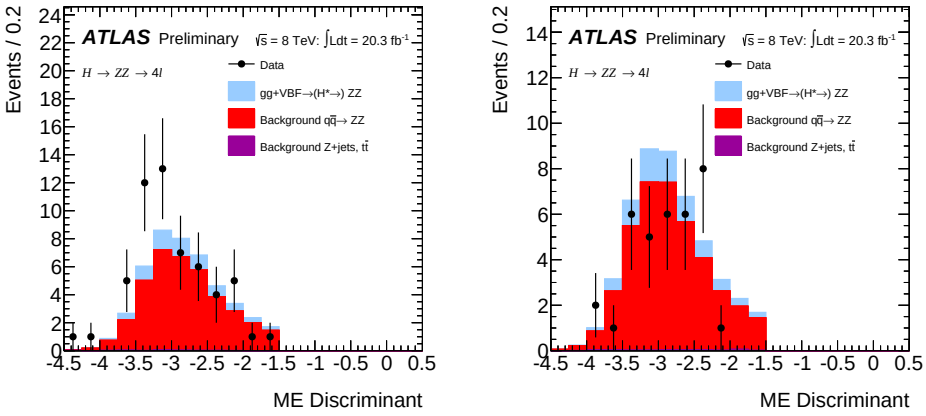

(a) (b)

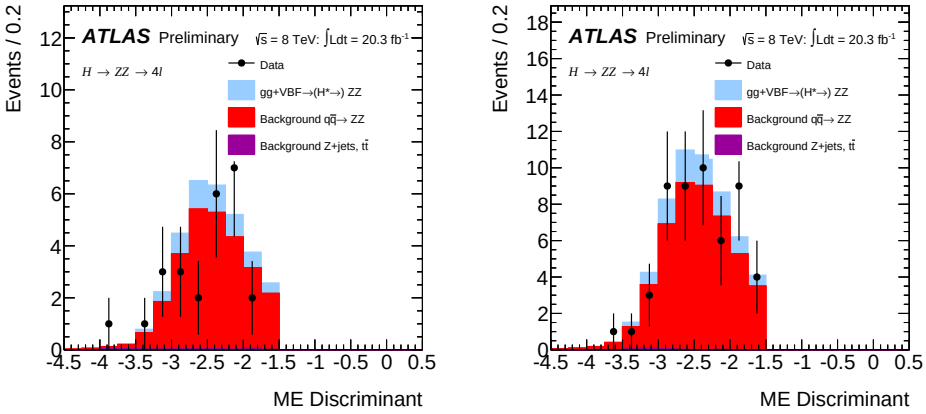

(c) (d)

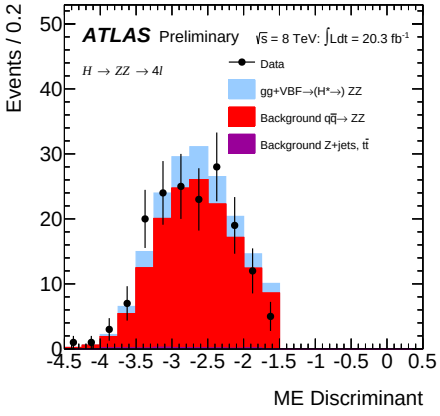

(e)

Figure 6.19 *ME-discriminant distributions in the "Control B" $q\bar{q} \to ZZ$ background enriched region (220 GeV < $m_{4\ell}$ < 1000 GeV, and ME discriminant <-1.5) for all processes in the four leptonic final states: (a) $2e\,2\mu$ (b) $2\mu\,2e$ (c) $4e$ (d) 4μ (e) all combined.*

sample	$2\mu2e$	$2e2\mu$	4μ	4e	TOTAL
$gg \to H^* \to ZZ$ (S)	0.06 ± 0.00	0.05 ± 0.00	0.07 ± 0.00	0.04 ± 0.00	0.2 ± 0.0
$gg \to ZZ$ (B)	6.75 ± 0.03	6.01 ± 0.03	8.15 ± 0.03	5.17 ± 0.02	26.1 ± 0.1
$gg \to (H^* \to)ZZ$	6.58 ± 0.04	5.79 ± 0.03	7.87 ± 0.03	4.99 ± 0.02	25.2 ± 0.1
$gg \to (H^* \to)ZZ$ ($\mu_{\text{off-shell}} = 10$)	6.24 ± 0.03	5.53 ± 0.03	7.48 ± 0.03	4.76 ± 0.02	24.0 ± 0.1
VBF $H^* \to ZZ$ (S)	0.01 ± 0.00	0.01 ± 0.00	0.01 ± 0.00	0.00 ± 0.00	0.0 ± 0.0
VBF ZZ (B)	0.13 ± 0.00	0.11 ± 0.00	0.16 ± 0.00	0.10 ± 0.00	0.5 ± 0.0
VBF $(H^* \to)ZZ$	0.12 ± 0.00	0.11 ± 0.00	0.15 ± 0.00	0.10 ± 0.00	0.5 ± 0.0
VBF $(H^* \to)ZZ$ (S+B+I, $\mu_{\text{off-shell}} = 10$)	0.16 ± 0.00	0.15 ± 0.00	0.19 ± 0.01	0.12 ± 0.00	0.6 ± 0.0
$q\bar{q} \to ZZ$	28.9 ± 0.3	25.3 ± 0.2	36.1 ± 0.2	21.8 ± 0.2	112.2 ± 0.5
Reducible backgrounds	0.59 ± 0.08	0.59 ± 0.07	0.76 ± 0.06	0.58 ± 0.08	2.5 ± 0.1
Total Expected (SM)	36.2 ± 0.3	31.8 ± 0.2	44.9 ± 0.2	27.4 ± 0.2	140 ± 0
Observed	37	43	36	27	143

Table 6.8 *Expected number of events for the $ZZ \to 4\ell$ channel in the "Control A" $q\bar{q} \to ZZ$ background enriched region (160 GeV $< m_{4\ell} <$ 220 GeV) for all processes in the four leptonic final states. Only statistical uncertainties are shown. The corresponding $m_{4\ell}$ and ME discriminant distributions are shown in Figure 6.16 and Figure 6.17.*

sample	$2\mu2e$	$2e2\mu$	4μ	4e	TOTAL
$gg \to H^* \to ZZ$ (S)	0.23 ± 0.00	0.24 ± 0.00	0.18 ± 0.00	0.11 ± 0.00	0.8 ± 0.0
$gg \to ZZ$ (B)	7.47 ± 0.03	7.24 ± 0.03	8.64 ± 0.03	5.28 ± 0.02	28.6 ± 0.1
$gg \to (H^* \to)ZZ$	7.20 ± 0.04	6.94 ± 0.04	8.31 ± 0.03	5.12 ± 0.02	27.6 ± 0.1
$gg \to (H^* \to)ZZ$ ($\mu_{\text{off-shell}} = 10$)	7.88 ± 0.04	7.75 ± 0.04	8.58 ± 0.03	5.24 ± 0.02	29.4 ± 0.1
VBF $H^* \to ZZ$ (S)	0.02 ± 0.00	0.01 ± 0.00	0.02 ± 0.00	0.01 ± 0.00	0.1 ± 0.0
VBF ZZ (B)	0.41 ± 0.01	0.43 ± 0.01	0.44 ± 0.01	0.28 ± 0.00	1.6 ± 0.3
VBF $(H^* \to)ZZ$	0.40 ± 0.01	0.43 ± 0.01	0.42 ± 0.01	0.27 ± 0.01	1.5 ± 0.4
VBF $(H^* \to)ZZ$ (S+B+I, $\mu_{\text{off-shell}} = 10$)	0.49 ± 0.01	0.51 ± 0.01	0.51 ± 0.01	0.32 ± 0.01	1.8 ± 0.4
$q\bar{q} \to ZZ$	39.5 ± 0.3	37.8 ± 0.3	46.6 ± 0.3	26.6 ± 0.2	150.6 ± 0.5
Reducible backgrounds	0.38 ± 0.06	0.29 ± 0.06	0.32 ± 0.06	0.38 ± 0.06	1.4 ± 0.1
Total Expected (SM)	47.5 ± 0.3	45.5 ± 0.3	55.6 ± 0.3	32.4 ± 0.2	181 ± 1
Observed	35	56	52	25	168

Table 6.9 *Expected number of events for the $ZZ \to 4\ell$ channel in the "Control B" $q\bar{q} \to ZZ$ background enriched region (220 GeV $< m_{4\ell} <$ 1000 GeV, and ME discriminant $<$ -1.5) for all processes in the four leptonic final states. Only statistical uncertainties are shown. The corresponding $m_{4\ell}$ and ME discriminant distributions are shown in Figure 6.18 and Figure 6.19.*

6.4.2 Results in cut-based signal region

Table 6.10 shows the observed and expected numbers of events in the cut-based signal region. Figure 6.20 shows the observed and expected 95% C.L. upper limit on $\mu_{\text{off-shell}}$ as a function of $\mathrm{R}^{B}_{H^*}$. The numerical values for these limits are tabulated in Table 6.12.

	$2\mu2e$	$2e2\mu$	4μ	4e	Total
$gg \to H^* \to ZZ$ (S)	0.23 ± 0.06	0.33 ± 0.09	0.32 ± 0.09	0.24 ± 0.07	1.1 ± 0.3
$gg \to ZZ$ (B)	0.63 ± 0.17	0.78 ± 0.21	0.84 ± 0.23	0.57 ± 0.16	2.8 ± 0.8
$gg \to (H^* \to)ZZ$	0.54 ± 0.15	0.65 ± 0.18	0.71 ± 0.19	0.48 ± 0.13	2.4 ± 0.7
$gg \to (H^* \to)ZZ$ ($\mu_{\text{off-shell}} = 10$)	1.98 ± 0.55	2.65 ± 0.73	2.66 ± 0.73	1.93 ± 0.53	9.2 ± 2.5
VBF $H^* \to ZZ$ (S)	0.02 ± 0.00	0.04 ± 0.00	0.04 ± 0.00	0.03 ± 0.00	0.1 ± 0.0
VBF ZZ (B)	0.15 ± 0.01	0.19 ± 0.01	0.21 ± 0.01	0.15 ± 0.01	0.7 ± 0.0
VBF $(H^* \to)ZZ$	0.14 ± 0.01	0.16 ± 0.01	0.18 ± 0.01	0.12 ± 0.01	0.6 ± 0.0
VBF $(H^* \to)ZZ$ (S+B+I, $\mu_{\text{off-shell}} = 10$)	0.24 ± 0.01	0.34 ± 0.02	0.35 ± 0.02	0.25 ± 0.01	1.2 ± 0.1
$q\bar{q} \to ZZ$	5.00 ± 0.51	5.53 ± 0.56	6.90 ± 0.70	3.88 ± 0.39	21.3 ± 2.1
Reducible backgrounds	0.03 ± 0.02	0.06 ± 0.03	0.00 ± 0.00	0.03 ± 0.02	0.1 ± 0.0
Total Expected (SM)	5.7 ± 0.5	6.4 ± 0.6	7.8 ± 0.7	4.5 ± 0.4	24.4 ± 2.2
Observed	2	6	8	2	18

Table 6.10 *Expected and observed numbers of events in the $ZZ \to 4\ell$ channel for the signal region ($400\ GeV < m_{4\ell} < 1000\ GeV$) with the cut-based analysis. The reducible background includes contributions from Z+jets and top quark production. As the contribution is less than 1% of the total background, this component is ignored in the final analysis. The expected numbers of events for the $gg \to ZZ$ and VBF ZZ processes, including the Higgs signal, background and their interference, are reported for both the SM prediction and for $\mu_{off\text{-}shell} = 10$. Both statistical and systematic uncertainties are included. A relative $gg \to ZZ$ background K-factor of $R^B_{H^*}$=1 is assumed.*

Observed	Median Expected
[10.3–14.5] (11.8)	[13.6–20.1] (15.7)

Table 6.11 *Observed and expected 95% C.L. upper limits on $\mu_{off\text{-}shell}$ obtained with the cut-based analysis in the 4ℓ channel, with $0.5 < R^B_{H^*} < 2$ ($R^B_{H^*} = 1$). The upper limits are calculated with the CLs method, with $\mu_{off\text{-}shell} = 1$ being the null hypothesis.*

6.4.3 Results in the ME shape analysis

Table 6.13 shows the observed and expected numbers of events in the ME discriminant shape-based signal region. Figure 6.21 shows the $m_{4\ell}$ and ME-discriminant distributions observed in the data and their comparison to the expectations for the combination of the four leptonic final states, whereas the ME distributions for the individual states are shown in Figure 6.22.

Figure 6.23 shows the scan of the negative log-likelihood, $-2\ln\Lambda$, as a function of $\mu_{\text{off-shell}}$ for data, overlaid with the expected curve for a SM Higgs boson for the ME-based discriminant analysis. A relative $gg \to ZZ$ background K-factor of $R^B_{H^*}$=1 is assumed.

Table 6.14 and Figure 6.24 show the observed and expected 95% C.L. upper limits

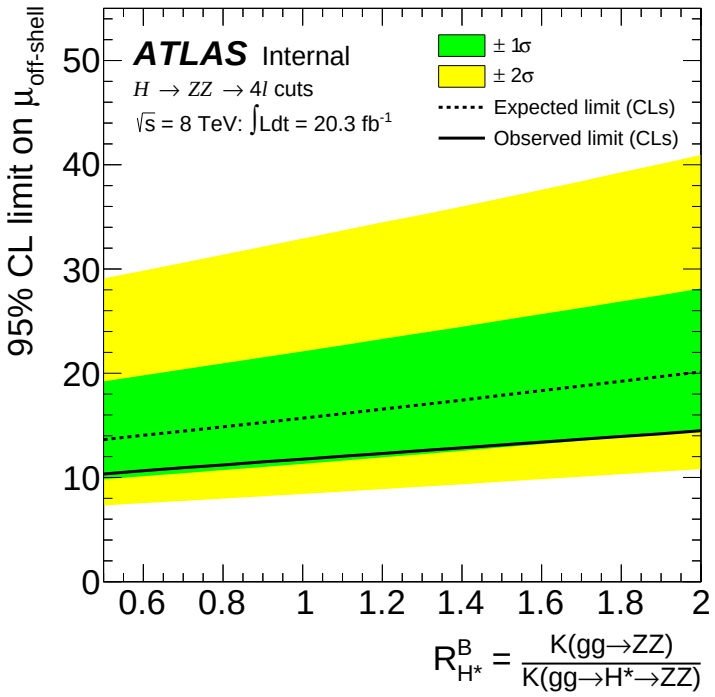

Figure 6.20 *Observed and expected 95% C.L. upper limits on $\mu_{off\text{-}shell}$ as a function of $R^B_{H^*}$, obtained with the cut-based analysis. The limits are calculated with the CLs method, with $\mu_{off\text{-}shell} = 1$ being the null hypothesis. The numerical values for these limits are tabulated in Table 6.12.*

on $\mu_{\text{off-shell}}$ as a function of $\mathrm{R}^B_{H^*}$, calculated with the CL_s method with $\mu_{off-shell} = 1$ being the null hypothesis. The result obtained with the experimental data is consistent with the SM expectations. The numerical values for these limits are tabulated in Table 6.15.

To understand the impact of the systematic effects, each uncertainty is added independently and the corresponding expected upper limit of $\mu_{\text{off-shell}}$ shown in Table 6.16 is re-evaluated. We find that the QCD scale uncertainty in the $gg \to ZZ$ production has the largest impact on the sensitivity of the search.

6.4.4 Combined results

The $ZZ \to 4\ell$ analysis is combined with that of the $ZZ \to 2\ell\,2\nu$ and $WW \to \ell\nu\,\ell\nu$ channels in order to improve the search sensitivity in the off-peak Higgs mass region (NB: the analysis of the last two channels was carried out by other teams and is not part of this thesis). The observed and expected 95% CL upper

$R^B_{H^*}$	Observed	Median	1 σ band	2 σ band
0.5	10.3	13.6	[9.8, 19.2]	[7.3, 29.1]
0.6	10.6	14.1	[10.1, 19.8]	[7.5, 29.8]
0.7	10.9	14.4	[10.4, 20.4]	[7.8, 30.6]
0.8	11.2	14.9	[10.7, 20.9]	[8.0, 31.4]
0.9	11.5	15.3	[11.0, 21.5]	[8.2, 32.1]
1.0	11.8	15.7	[11.3, 22.1]	[8.4, 32.9]
1.1	12.0	16.1	[11.6, 22.7]	[8.6, 33.7]
1.2	12.3	16.6	[11.9, 23.3]	[8.9, 34.5]
1.3	12.6	17.0	[12.2, 23.9]	[9.1, 35.2]
1.4	12.8	17.4	[12.5, 24.5]	[9.3, 36.0]
1.5	13.1	17.9	[12.9, 25.1]	[9.6, 36.8]
1.6	13.4	18.3	[13.2, 25.7]	[9.8, 37.6]
1.7	13.7	18.8	[13.5, 26.3]	[10.1, 38.4]
1.8	13.9	19.2	[13.9, 26.9]	[10.3, 39.3]
1.9	14.2	19.7	[14.2, 27.5]	[10.6, 40.1]
2.0	14.5	20.1	[14.5, 28.1]	[10.8, 40.9]

Table 6.12 *Observed and expected 95% C.L. upper limits on $\mu_{\text{off-shell}}$ as a function of $R^B_{H^*}$, obtained with the cut-based analysis. The limits are calculated with the CLs method, with $\mu_{\text{off-shell}} = 1$ being the null hypothesis. The expected results are based on an Asimov data sample obtained from PDFs.*

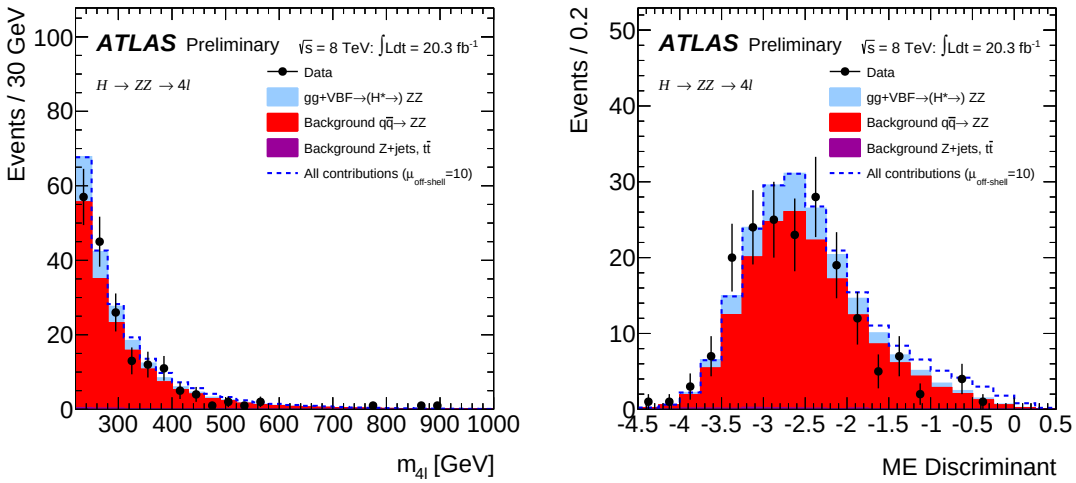

(a) **(b)**

Figure 6.21 *(a) $m_{4\ell}$ and (b) ME discriminant distributions observed in the data, and their comparison to the SM expectations, including a $gg \to H \to ZZ$ signal and its interference with the background (stacked histogram), for the combination of the four leptonic final states. The dashed line corresponds to a $\mu_{\text{off-shell}}$=10 Higgs model, including the interfence with the backround.*

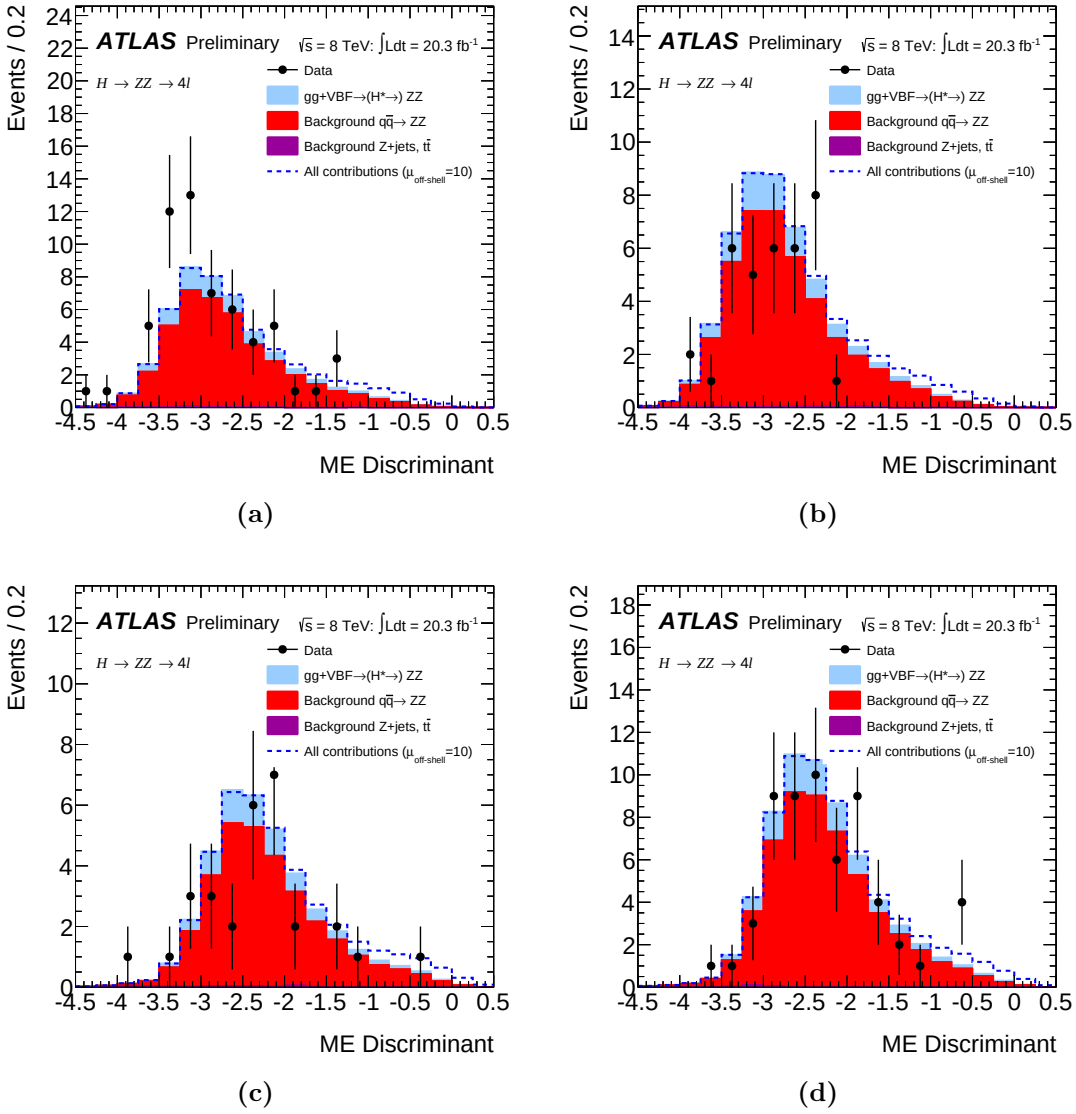

Figure 6.22 *ME discriminant distributions observed in the data, and their comparison to the SM expectations, including a $gg \to H \to ZZ$ signal and its interference with the background (stacked histogram), for the four leptonic final states: (a) $2e\,2\mu$ (b) $2\mu\,2e$ (c) $4e$ (d) 4μ. The dashed line corresponds to a $\mu_{off\text{-}shell}$=10 Higgs model, including the interfence with the backround.*

	$2\mu\,2e$	$2e\,2\mu$	4μ	4e	Total
$gg \to H^* \to ZZ$ (S)	0.48 ± 0.11	0.60 ± 0.14	0.62 ± 0.14	0.45 ± 0.10	2.1 ± 0.5
$gg \to ZZ$ (B)	7.94 ± 1.81	7.87 ± 1.80	9.88 ± 2.25	6.18 ± 1.41	31.9 ± 7.3
$gg \to (H^* \to)ZZ$	7.61 ± 1.74	7.45 ± 1.70	9.41 ± 2.15	5.91 ± 1.35	30.4 ± 6.9
$gg \to (H^* \to)ZZ$ ($\mu_{\text{off-shell}} = 10$)	9.92 ± 2.27	10.5 ± 2.4	12.4 ± 2.8	8.10 ± 1.85	41.0 ± 9.4
VBF $H^* \to ZZ$ (S)	0.04 ± 0.00	0.05 ± 0.01	0.06 ± 0.01	0.04 ± 0.00	0.2 ± 0.0
VBF ZZ (B)	0.51 ± 0.03	0.56 ± 0.03	0.66 ± 0.03	0.44 ± 0.02	2.2 ± 0.1
VBF $(H^* \to)ZZ$	0.48 ± 0.03	0.53 ± 0.03	0.60 ± 0.03	0.40 ± 0.02	2.0 ± 0.1
VBF $(H^* \to)ZZ$ (S+B+I, $\mu_{\text{off-shell}} = 10$)	0.69 ± 0.04	0.79 ± 0.04	0.91 ± 0.05	0.60 ± 0.03	3.0 ± 0.2
$q\bar{q} \to ZZ$	41.9 ± 3.3	40.7 ± 3.2	53.8 ± 4.2	31.3 ± 2.5	167.7 ± 13.1
Reducible backgrounds	0.36 ± 0.06	0.30 ± 0.06	0.29 ± 0.06	0.35 ± 0.06	1.3 ± 0.1
Total Expected (SM)	50.4 ± 3.7	49.0 ± 3.6	64.1 ± 4.7	37.9 ± 2.8	201 ± 15
Observed	35	59	59	29	182

Table 6.13 *Expected and observed number of events in the $ZZ \to 4\ell$ channel in the signal region (220 GeV $< m_{4\ell} <$ 1000 GeV and -4.5 <ME< 0.5), obtained with the ME discriminant-based shape analysis for the four leptonic final states. The reducible background includes contributions from Z+jets and top quark production. As the contribution is less than 1% of the total background, this component is not used in the final analysis. The expected events for the $gg \to ZZ$ and VBF ZZ processes, including the Higgs signal, background and interference, are reported for both the SM predictions and $\mu_{off\text{-}shell} = 10$. Both statistical and systematic uncertainties are included. A relative $gg \to ZZ$ background K-factor of $R^B_{H^*}$=1 is assumed.*

channel	Observed	Median	1 σ band	2 σ band
$2e\,2\mu$	12.6	17.8	[12.8, 25.7]	[9.6, 40.6]
$2\mu\,2e$	14.0	22.3	[16.1, 32.5]	[12.0, 51.3]
$4e$	16.2	21.4	[15.4, 31.2]	[11.5, 49.5]
4μ	17.4	18.6	[13.4, 26.9]	[10.0, 42.1]
combined	6.7	10.2	[7.4, 14.2]	[5.5, 21.3]

Table 6.14 *Observed and expected 95% C.L. upper limits on $\mu_{off\text{-}shell}$ obtained with the ME discriminant-based shape analysis. The limits are calculated with the CLs method, with $\mu_{off\text{-}shell} = 1$ being the null hypothesis. The expected upper limits are based on an Asimov data sample from PDF.*

limits on $\mu_{\text{off-shell}}$ as a function of $\mathrm{R}^B_{H^*}$ for the combination of the three channels are summarised in Table 6.17. The $ZZ \to 4\ell$ and $ZZ \to 2\ell 2\nu$ analyses have very similar expected sensitivities. The $ZZ \to 4\ell$ analysis is statistics limited, while the sensitivity in the $ZZ \to 2\ell 2\nu$ analysis is significantly reduced because of further theoretical systematic uncertainties. The similar expected CL_s limits for the two channels for $\mathrm{R}^B_{H^*} = 0.5$ and 1.0 reported in Table 6.17 is a coincidence, and a result of different statistical and systematic uncertainty components for the two analyses.

$R^B_{H^*}$	Observed	Median	1 σ band	2 σ band
0.5	5.5	8.8	[6.3, 12.2]	[4.7, 18.7]
0.6	5.8	9.0	[6.5, 12.5]	[4.8, 19.1]
0.7	6.0	9.3	[6.7, 12.9]	[5.0, 19.6]
0.8	6.2	9.6	[6.9, 13.3]	[5.1, 20.1]
0.9	6.5	9.9	[7.1, 13.7]	[5.3, 20.7]
1.0	6.7	10.2	[7.4, 14.2]	[5.5, 21.3]
1.1	7.0	10.6	[7.6, 14.7]	[5.7, 21.9]
1.2	7.2	11.0	[7.9, 15.2]	[5.9, 22.6]
1.3	7.5	11.4	[8.2, 15.8]	[6.1, 23.3]
1.4	7.8	11.8	[8.5, 16.3]	[6.3, 24.0]
1.5	8.1	12.2	[8.8, 16.9]	[6.5, 24.7]
1.6	8.4	12.6	[9.1, 17.4]	[6.8, 25.5]
1.7	8.6	13.0	[9.4, 18.0]	[7.0, 26.2]
1.8	8.9	13.4	[9.7, 18.5]	[7.2, 27.1]
1.9	9.2	13.8	[10.0, 19.1]	[7.4, 27.7]
2.0	9.5	14.3	[10.3, 19.7]	[7.7, 28.5]

Table 6.15 *Observed and expected 95% C.L. upper limit on $\mu_{\textit{off-shell}}$ obtained with the ME discriminant-based shape analysis as a function of $R^B_{H^*}$. The limits are calculated with the CLs method, with $\mu_{\textit{off-shell}} = 1$ being the null hypothesis. The expected results are based on an Asimov data sample from PDF.*

Source of systematic uncertainty	95% C.L. on $\mu_{\text{off-shell}}$
QCD scale for $gg \to ZZ$	9.6
QCD scale for the $gg \to (H^* \to)ZZ$ interference	9.3
QCD scale for $q\bar{q} \to ZZ$	8.9
PDF for $pp \to ZZ$	8.8
EW for $q\bar{q} \to ZZ$	8.8
luminosity	8.9
electron reconstruction efficiency	8.8
muon reconstruction efficiency	8.8
All systematic effects	10.2
No systematic effects	8.8

Table 6.16 *Expected 95% C.L. upper limits on $\mu_{\textit{off-shell}}$ obtained with the ME discriminant-based shape analysis in the 4ℓ channel, and result comparison for various uncertainty hypotheses: including each systematic effect separately, vs. including no and all systematic uncertainties. The upper limits are evaluated from the CL_s method, assuming $R^B_{H^*}$=1.*

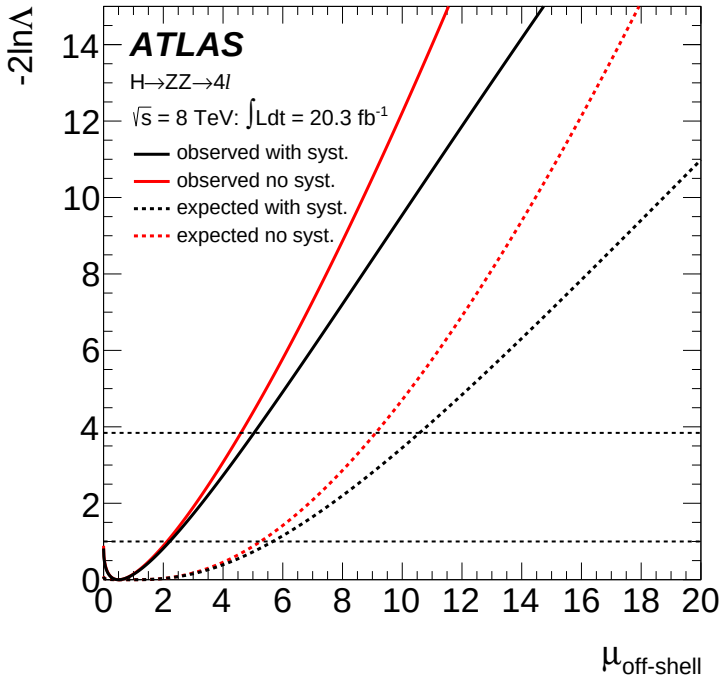

Figure 6.23 *Scan of the negative log-likelihood, $-2\ln\Lambda$, as a function of $\mu_{\textit{off-shell}}$, in the $ZZ \to 4\ell$ channel. The black solid (dashed) line corresponds to the observed (expected) likelihood function incorporating all systematic uncertainties, while the red solid (dashed) line corresponds to the observed (expected) likelihood function without any systematic uncertainties. A relative $gg \to VV$ background K-factor of $R^B_{H^*}$=1 is assumed in the calculations.*

	Observed			Median expected		
$R^B_{H^*}$	0.5	**1.0**	2.0	0.5	**1.0**	2.0
$ZZ \to 4\ell$ analysis	6.1	**7.3**	10.0	9.1	**10.6**	14.8
$ZZ \to 2\ell\,2\nu$ analysis	9.9	**11.0**	12.8	9.1	**10.6**	13.6
$WW \to \ell\nu\,\ell\nu$ analysis	15.6	**17.2**	20.3	19.6	**21.3**	24.7

Table 6.17 *Observed and expected 95% CL upper limits on $\mu_{\textit{off-shell}}$ for assumed values of $R^B_{H^*}$= 0.5, 1.0 (bold font) and 2.0. The limits have been evaluated with the CL_s method, with $\mu_{\textit{off-shell}} = 1$ being the alternative hypothesis.*

Combination of the off-shell ZZ and WW analyses

The analyses described in the previous sections are combined to obtain a limit on $\mu_{\text{off-shell}}$. In combining the off-shell results, the main systematic uncertainties related to the theory uncertainties on the $gg \to (H^* \to)VV$ (including signal and interference contributions) and $q\bar{q} \to VV$ processes are treated as correlated

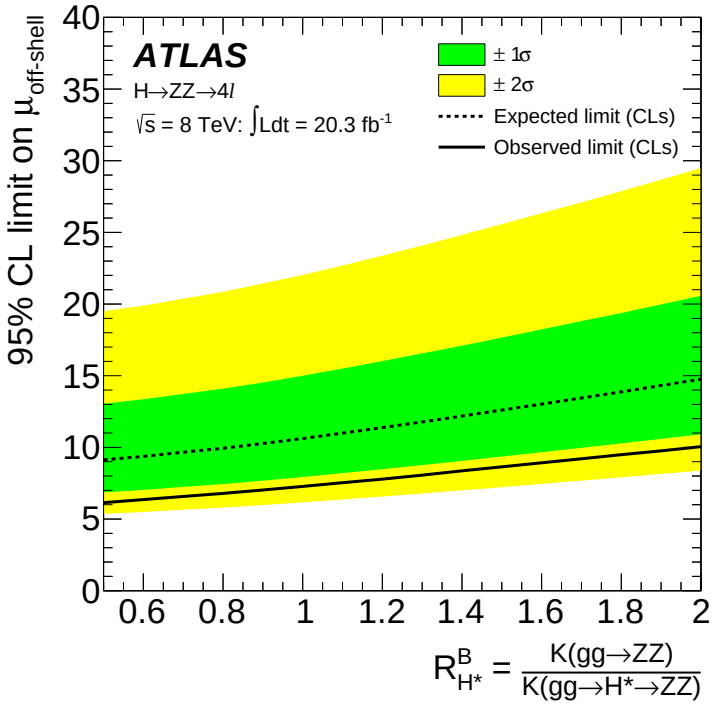

Figure 6.24 *Observed and expected 95% CL upper limits on $\mu_{off\text{-}shell}$ as a function of $R^B_{H^*}$, for the $ZZ \to 4\ell$ channel. The limits are evaluated using the CL_s method, with $\mu_{off\text{-}shell} = 1$ being the alternative hypothesis. The green (yellow) bands represent the 68% (95%) confidence intervals for the CL_s expected limit.*

between the different channels. The same K-factor ratio $R^B_{H^*}$ is assumed for the $gg \to ZZ$ and $gg \to WW$ backgrounds. When appropriate, the experimental systematic uncertainties are also treated as correlated. However, these assumptions are found to have a very small impact on the combined result.

The limits on $\mu_{\text{off-shell}}$ are obtained under two different assumptions:

- Determination of the signal strength $\mu_{\text{off-shell}}$ when fixing the ratio of the signal strength in $gg \to H^*$ and VBF to the SM prediction, namely $\mu^{gg\to H^*}_{\text{off-shell}}/\mu^{VBF}_{\text{off-shell}}$=1. This is equivalent to the assumption that the ratio of the off-shell production rates via the process $gg \to H$ to those via the VBF process are as predicted in the SM.

- Determination of the signal strength $\mu^{gg\to H^*\to VV}_{\text{off-shell}}$ when fixing the VBF off-shell signal strength to the SM prediction, i.e. $\mu^{\text{VBF } H^*\to VV}_{\text{off-shell}}$=1. In this case the combined signal strength $\mu^{gg\to H^*\to VV}_{\text{off-shell}}$ can be interpreted as a constraint on the off-shell coupling strength $\kappa_{g,\text{off-shell}}$ associated with the $gg \to H^*$

production mode.

The scan of the negative log-likelihood, $-2\ln\Lambda$, as a function of $\mu_{\text{off-shell}}$ for data and the expected curve for a SM Higgs boson for the two cases described above are shown in Fig. 6.25. The limits on $\mu_{\text{off-shell}}$ and $\mu^{gg\to H^*}_{\text{off-shell}}$ are computed with the

	Observed			Median expected			Assumption
$R^B_{H^*}$	0.5	**1.0**	2.0	0.5	**1.0**	2.0	
$\mu_{\text{off-shell}}$	5.1	**6.2**	8.6	6.7	**8.1**	11.0	$\mu^{gg\to H^*}_{\text{off-shell}}/\mu^{VBF}_{\text{off-shell}}$=1
$\mu^{gg\to H^*\to VV}_{\text{off-shell}}$	5.3	**6.7**	9.8	7.3	**9.1**	13.0	$\mu^{\text{VBF } H^*\to VV}_{\text{off-shell}}$=1

Table 6.18 *Observed and expected 95% CL upper limits on $\mu_{off\text{-}shell}$ and $\mu^{gg\to H^*\to VV}_{off\text{-}shell}$ for the combination of the ZZ and WW analyses, for values of $R^B_{H^*}$= 0.5, 1.0 (bold font) and 2.0, and two different assumptions. The limits are evaluated with the CL_s method, with $\mu_{off\text{-}shell} = 1$ being the alternative hypothesis.*

CL_s method, with the alternative hypothesis being that the off-shell rates are described by the SM predictions. These limits are derived as a function of the $gg \to VV$ background K-factor ratio $R^B_{H^*}$. The results are reported in Table 6.18 and shown in Fig. 6.26, assuming either a common scale factor for both the $gg \to H^*$ and VBF processes, or by using a scale factor for the $gg \to H^*$ process and fixing the VBF production to the SM prediction.

The impact of the various systematic uncertainties on the combined expected limit in the off-shell fit can be seen in Table 6.19 when fixing the ratio of the signal strength in $gg \to H^*$ and VBF to the SM prediction. The values in this table were derived by fixing all nuisance parameters associated with the systematic uncertainties to the values derived from the SM-conditional fit to the data, with the exception of the uncertainty under study.

6.4.5 Interpretations for the Higgs boson total width

In this section, the off-shell results reported earlier are combined with the on-shell $H \to ZZ^* \to 4\ell$ [136] and $H \to WW^* \to \ell\nu\ell\nu$ [41] analyses based on the 8 TeV data taken in 2012. In these analyses a Higgs boson mass value of 125.36 GeV [11] is assumed. For the on-shell ZZ and WW combination, the main common sources of theoretical and experimental systematic uncertainties are treated as correlated [131].

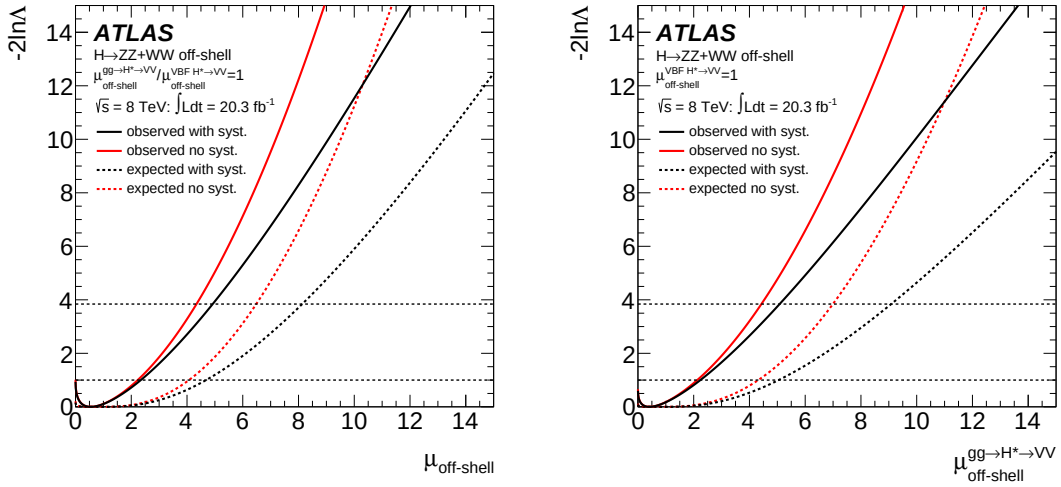

(a) **(b)**

Figure 6.25 *Scan of the negative log-likelihood, $-2\ln\Lambda$, as a function of $\mu_{off\text{-}shell}$, for the combined ZZ and WW analyses. (a) A common signal strength $\mu_{off\text{-}shell}$ is applied to both $gg \to H^*$ and VBF processes. The ratio of the $gg \to H^*$ and VBF processes is assumed to be equal to the SM prediction. (b) Signal strength $\mu^{gg\to H^*\to VV}_{off\text{-}shell}$ is used for the $gg \to H^* \to VV$ process. The production rate for the VBF off-shell process is fixed to the SM prediction. The black solid (dashed) line corresponds to the observed (expected) likelihood function when incorporating all systematic uncertainties, while the red solid (dashed) line corresponds to the observed (expected) likelihood function without any systematic uncertainties. A relative $gg \to VV$ background K-factor of $R^B_{H^*}$=1 is assumed in these figures.*

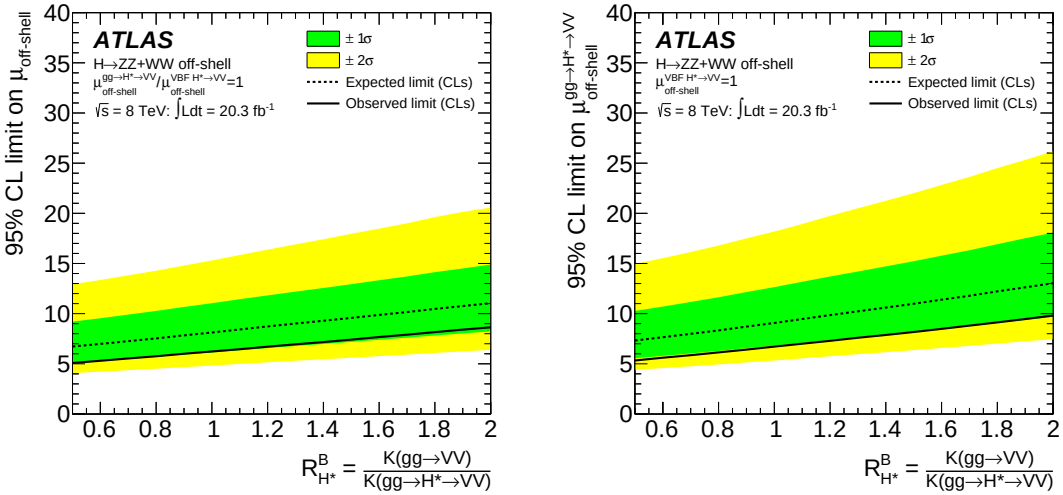

Figure 6.26 *Observed and expected combined 95% CL upper limits on $\mu_{off\text{-}shell}$ as a function of $R^B_{H^*}$ for the combined ZZ and WW analyses. The limits are calculated with the CL_s method, with the SM being the alternative hypothesis. (a) Limits on a common signal strength $\mu_{off\text{-}shell}$ applied to both $gg \to H^*$ and VBF processes. The ratio of the $gg \to H^*$ and VBF processes is assumed to be equal to the one predicted in the SM. (b) Limits on the signal strength $\mu^{gg\to H^*\to VV}_{off\text{-}shell}$ for the $gg \to H^* \to VV$ process. The production rate for the VBF off-shell process is fixed to the SM prediction. The green (yellow) bands represent the 68% (95%) confidence intervals for the CL_s expected limit.*

Systematic uncertainty	95% CL limit on $\mu_{\text{off-shell}}$
Interference $gg \to (H^* \to)VV$	7.2
QCD scale $\mathrm{K}^{H^*}(m_{VV})$ (correlated component)	7.1
PDF $q\bar{q} \to VV$ and $gg \to (H^* \to)VV$	6.7
QCD scale $q\bar{q} \to VV$	6.7
Luminosity	6.6
Drell–Yan background	6.6
QCD scale $\mathrm{K}_{gg}^{H^*}(m_{VV})$ (uncorrelated component)	6.5
Remaining systematic uncertainties	6.5
All systematic uncertainties	8.1
No systematic uncertainties	6.5

Table 6.19 *Expected 95% CL upper limits on $\mu_{\textit{off-shell}}$ for the combined ZZ and WW analyses, with a ranked list of the individual systematic uncertainties, and comparison with the results obtained by incoporating all or no systematic uncertainties. The limits are evaluated with the CL_s method, assuming $R^B_{H^*}$=1. The ratio of the $gg \to H^*$ and VBF processes is assumed to be equal to the one predicted in the SM.*

The uncertainties from the impact of higher-order QCD corrections on the $gg \to H^{(*)}$ and $q\bar{q} \to VV$ processes are considered correlated between the on-shell and off-shell measurements. The PDF uncertainties are treated as uncorrelated between the on-shell and off-shell analyses. The correlations between the PDF uncertainties for the on-shell and off-shell analyses are expected to be small, with the exception of the ones for the $q\bar{q} \to VV$ process, which has a negligible impact on the on-shell results.

In addition to the main theoretical uncertainties, the common experimental systematic uncertainties are treated as correlated.

The results reported in the following are based on two different assumptions:

- Determination of $\Gamma_H/\Gamma_H^{\mathrm{SM}}$ when profiling the coupling scale factors κ_g and κ_V associated with the on- and off-shell $gg \to H^{(*)}$ and VBF production and the $H^{(*)} \to VV$ decay, assuming $\kappa_g = \kappa_{g,\text{on-shell}} = \kappa_{g,\text{off-shell}}$ and $\kappa_V = \kappa_{V,\text{on-shell}} = \kappa_{V,\text{off-shell}}$ [6]. In other words, the fit is performed using different signal strengths for the $gg \to H^{(*)}$ and the VBF production modes [7].

[6] To set an upper limit, the assumption in Eq. (5.10), and the equivalent assumption for the VBF production mode, is sufficient.

[7] In all results, the signal strength for VH is assumed to scale as the VBF production, while the $b\bar{b}H$ and $t\bar{t}H$ processes scale with $gg \to H$. These additional production modes are expected to give negligible contributions to the off-shell measurements, but have small contributions to

- Determination of $R_{gg} = \kappa^2_{g,\text{off-shell}}/\kappa^2_{g,\text{on-shell}}$ when profiling the coupling scale factor $\kappa_V = \kappa_{V,\text{on-shell}} = \kappa_{V,\text{off-shell}}$ associated with the VBF production and the $H^{(*)} \to VV$ decay. The ratio $\Gamma_H/\Gamma_H^{\text{SM}}$=1 is fixed to the SM prediction. The parameter R_{gg} is sensitive to possible modifications of the gluon couplings in the high-mass range with respect to the on-shell value.

The negative log-likelihood scans for the fitting configurations described above, as well as the combined upper limit at 95% CL on $\Gamma_H/\Gamma_H^{\text{SM}}$ and R_{gg} are illustrated in Figs. 6.27 and 6.28, with the corresponding limits listed in Table 6.20. The limits are all computed with the CL_s method, taking the SM values as the alternative hypothesis.

The limit on $\Gamma_H/\Gamma_H^{\text{SM}}$ can be translated into a limit on the total width of the Higgs boson, assuming the value of $\text{R}^B_{H^*}$=1 and under the assumptions described above. It corresponds to an observed (expected) 95% CL upper limit on the Higgs boson total width of 22.7 (33.0) MeV.[8]

	Observed			Median expected			Assumption
$\text{R}^B_{H^*}$	0.5	**1.0**	2.0	0.5	**1.0**	2.0	
$\Gamma_H/\Gamma_H^{\text{SM}}$	4.5	**5.5**	7.5	6.5	**8.0**	11.2	$\kappa_{i,\text{on-shell}} = \kappa_{i,\text{off-shell}}$
$R_{gg} = \kappa^2_{g,\text{off-shell}}/\kappa^2_{g,\text{on-shell}}$	4.7	**6.0**	8.6	7.1	**9.0**	13.4	$\kappa_{V,\text{on-shell}} = \kappa_{V,\text{off-shell}}$, $\Gamma_H/\Gamma_H^{\text{SM}}$=1

Table 6.20 *Observed and expected 95% CL upper limits on Γ_H/Γ_H^{SM} and R_{gg} for the combined on- and off-shell ZZ and WW analyses. Results are shown for values of $R^B_{H^*}$= 0.5, 1.0 (bold font) and 2.0, and two different assumptions.*

6.5 Prospects for Run 2

The schedule of the LHC spans long periods of data-taking (the Runs), with three long shutdowns (LS) scheduled in between them. The second LHC run (Run 2) started in 2015 with an energy increase to $\sqrt{s} = 13$ TeV, and with the aim to achieve $\sqrt{s} = 14$ TeV collisions in 2018. The bunch spacing was reduced from 50 ns (Run 1) to 25 ns. During 2016, LHC will provide one billion collisions per second to the experiments, with the objective of reaching an integrated luminosity of around 25 fb^{-1} by the end of the year. The ATLAS detector expects to record

the on-shell signal yields.

[8] We use the value of the SM Higgs boson width of 4.12 MeV at a mass of 125.4 GeV [40] to convert the $\Gamma_H/\Gamma_H^{\text{SM}}$ limit into a total width limit.

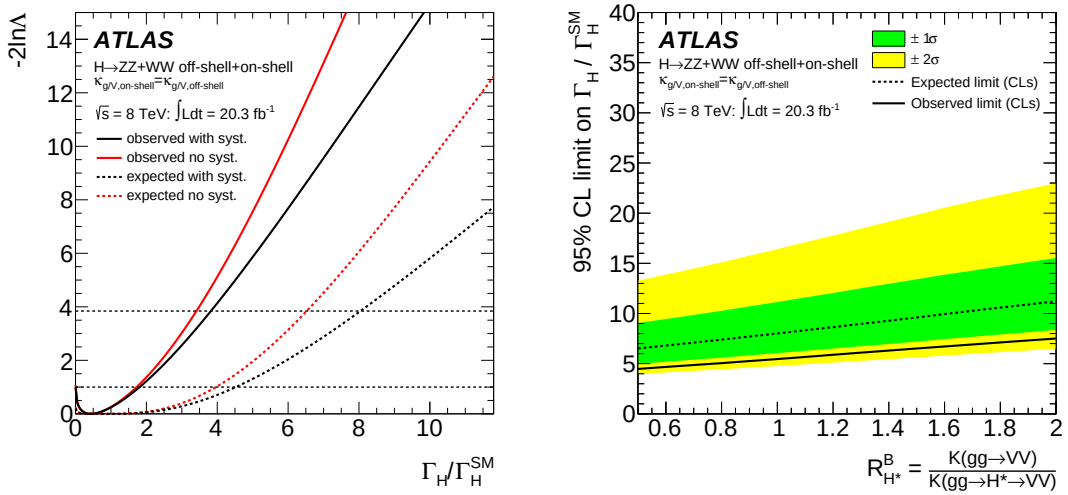

(a) **(b)**

Figure 6.27 *(a) Scan of the negative log-likelihood as a function of Γ_H/Γ_H^{SM} when the coupling scale factors κ_g and κ_V for the on- and off-shell $gg \to H^{(*)}$ and VBF production and the $H^{(*)} \to VV$ decay are assumed to be the same. The black solid (dashed) line corresponds to the observed (expected) likelihood function when incorporating all systematic uncertainties, while the red solid (dashed) line corresponds to the observed (expected) likelihood function without any systematic uncertainties. (b) Observed and expected combined 95% CL upper limits on Γ_H/Γ_H^{SM} as a function of $R^B_{H^*}$ under the same assumption as (a). The limits are calculated with the CL_s method, with the SM being the alternative hypothesis. The green (yellow) bands represent the 68% (95%) confidence intervals for the CL_s expected limit.*

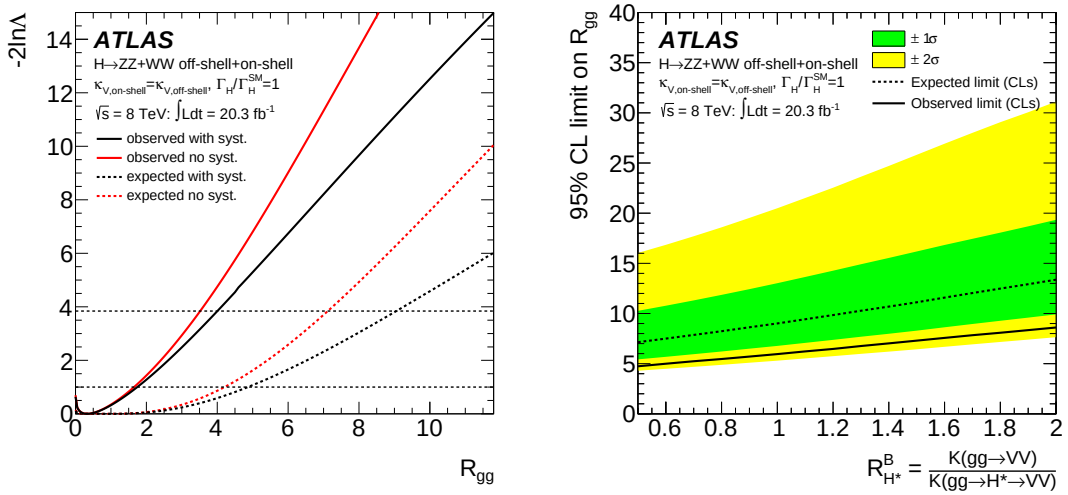

(a) **(b)**

Figure 6.28 *(a) Scan of the negative log-likelihood as a function of* $R_{gg} = \kappa^2_{g,off\text{-}shell}/\kappa^2_{g,on\text{-}shell}$ *when profiling the coupling scale factor* κ_V *associated with the on- and off-shell VBF production and the* $H^{(*)} \rightarrow VV$ *decay. The ratio* Γ_H/Γ_H^{SM} *is set to 1.0. The black solid (dashed) line correponds to the observed (expected) likelihood function when incorporating all systematic uncertainties, while the red solid (dashed) line corresponds to the observed (expected) likelihood function without any systematic uncertainties. (b) Observed and expected combined 95% CL upper limits on* R_{gg} *as a function of* $R^B_{H^*}$ *under the same assumption as (a). The limits are calculated with the* CL_s *method, with the SM being the alternative hypothesis. The green (yellow) bands represent the 68% (95%) confidence intervals for the* CL_s *expected limit.*

an integrated luminosity of 100 fb^{-1} by the end of Run 2 (2018). This new scenario opens up unexplored regions for the production of high-mass new particles, but also precision measurement can greatly benefit by the large increase in the size of the collected datasets.

The Higgs total width is one of the precision measurements that will benefit from the new Run 2 conditions. The following study checked the sensitivity in Run 2 under two different scenarios, by assuming integrated luminosities of 10 fb^{-1} and 100 fb^{-1}. Signal and background MC samples simulated for the Run 2 conditions were not available, so the Run 1 8 TeV samples were extrapolated to the upgraded settings. The signal and background cross section were scaled according to the parton luminosity ratios when moving from $\sqrt{s} = 8$ TeV to 14 TeV [146]. The main assumption in this extrapolation to a higher energy and luminosity, is that the signal and background experimental efficiencies computed with the 8 TeV fully simulated samples are preserved in the Run 2 scenario. The event selection, analysis strategy, and systematic uncertainties used for Run 1 analysis [1] are identical in this study. NLO calculations for the $gg \to ZZ$ continuum process are expected to be available, so the results are not presented as a function of $\mathrm{R}^{B}_{H^*}$. The upper limits are calculated considering just the Run 2 simulated data.

Table 6.21 shows the expected 95% CL upper limits on $\mu_{\text{off-shell}}$ and $\Gamma_H/\Gamma_H^{\text{SM}}$ using the scan of the negative log-likelihood, $-2\ln\Lambda$, for the $ZZ \to 4\ell$ and $ZZ \to 2l2\nu$ channels. Figure 6.29 shows the projected $\mu_{\text{off-shell}}$ upper limit, by taking into account the result without systematics uncertainties and considering only the $ZZ \to 4\ell$ channel. The $\mu_{\text{off-shell}}$ limits are calculated considering a ratio of the off-shell production rates $gg \to H$ and VBF equal to that predicted by the SM, namely an off-shell signal strenght parameter equal to 1. The $\Gamma_H/\Gamma_H^{\text{SM}}$ is calculated assuming that the off- and on-shell couplings are the same for both $gg \to H$ and VBF production modes (i.e., $\kappa_{g,\text{on-shell}} = \kappa_{g,\text{off-shell}}$ and $\kappa_{V,\text{on-shell}} = \kappa_{V,\text{off-shell}}$). The upper limits are calculated at 95% CL using a cut-based analysis method, and by assuming a 10% background uncertainty.

The sensitivity obtained in the Run 2 analysis with an integrated luminosity of 10 fb^{-1} is similar to the one achieved with double the luminosity of Run 1. This improvement is due to the increased cross section. The sensitivity achieved with an integrated luminosity of 10 fb^{-1} in the $ZZ \to 2\ell\,2\nu$ channel is higher than in the $ZZ \to 4\ell$ channel. However, at 100 fb^{-1} the roles are reversed. This indicates that the four lepton final state benefits to a larger degree by an increase in statistics. The upper limit at an integrated luminosity of 100 fb^{-1} is improved

by approximately 60% compared to the Run 1 result in the same $ZZ \to 4\ell$ channel.

	$\mu_{\text{off-shell}}$		$\Gamma_H/\Gamma_H^{\text{SM}}$	
	$\mathcal{L} = 10$ fb^{-1}	$\mathcal{L} = 100$ fb^{-1}	$\mathcal{L} = 10$ fb^{-1}	$\mathcal{L} = 100$ fb^{-1}
$ZZ \to 4\ell$ analysis	9.1	4.4	9.0	4.3
$ZZ \to 2\ell\,2\nu$ analysis	8.5	5.7	8.4	5.6

Table 6.21 *Projected expected 95% CL upper limits on $\mu_{\textit{off-shell}}$ and Γ_H/Γ_H^{SM} in the Run 2 scenario for the $ZZ \to 4\ell$ and $ZZ \to 2\ell\,2\nu$ channels, obtained assuming $\sqrt{s} = 14$ TeV and integrated luminosities of 10 fb^{-1} and 100 fb^{-1}. The limits are evaluated with the scan of the negative log-likelihood, $-2\ln\Lambda$. The $gg \to ZZ$ background K-factor is assumed to be known.*

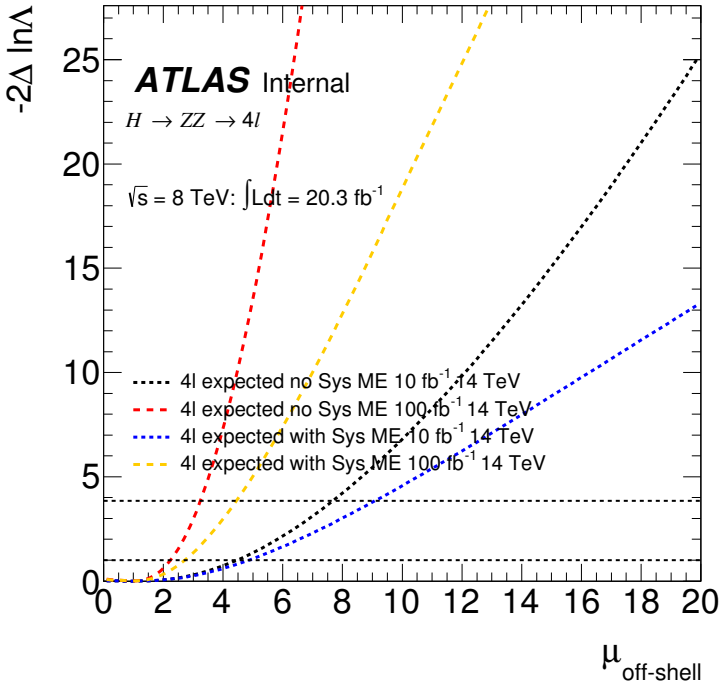

Figure 6.29 *Scan of the negative log-likelihood, $-2\ln\Lambda$, as a function of $\mu_{\textit{off-shell}}$, in the $ZZ \to 4\ell$ channel. The black and red lines correspond to the expected likelihood function without any systematic uncertainties, while the blue and yellow lines correspond to the expected likelihood function incorporating all systematic uncertainties. The black and blue lines limits are calculated with an integrated luminosity of 10 fb^{-1}, while the red and yellow are calculated with 100 fb^{-1}. The $gg \to ZZ$ background K-factor is assumed to be known.*

One of the limitations in the evaluation of the Higgs boson total width in the

	$\mathcal{L} = 10$ fb^{-1}	$\mathcal{L} = 100$ fb^{-1}
VBF $H^* \to ZZ$ (S)	0.07	0.88
VBF ZZ (B)	0.49	6.23
VBF $(H^* \to)ZZ$	0.41	5.35
$q\bar{q} \to ZZ$	1.69	16.6

Table 6.22 *Expected number of events in the $ZZ \to 4\ell$ channel in the analysis signal region (220 GeV $< m_{4\ell} <$ 1000 GeV), in the Run 2 with $\sqrt{s} = 14$ TeV and integrated luminosities: 10 fb^{-1} and 100 fb^{-1}. The expected events for VBF ZZ processes, including the Higgs signal, background and interference, are reported for the SM predictions. The VBF ZZ background K-factor is assumed to be known.*

current analysis, is that it has been assumed that the off-shell and on-shell couplings are the same. There is a possibility that new physics may contribute at higher energy scales in the $gg \to H$ loop production process, changing the value of the effective coupling. However, the VBF production mode is less sensitive since it is a tree-level process. The main challenge is that the VBF production mechanism is approximately ten times smaller than the $gg \to H$ process. It is expected that at the end of Run 2, the increased statistics will give us the opportunity to obtain promising results.

Table 6.22 shows the expected number of events in the analysis signal region (220 GeV $< m_{4\ell} <$ 1000 GeV) for the VBF production mode, for the combination of all lepton channels and with integrated luminosities of 10 fb^{-1} and 100 fb^{-1}. The $gg \to ZZ + 2j$ background process is not included due to its small contribution. The expected 95% CL upper limit on $\Gamma_H/\Gamma_H^{\mathrm{SM}}$ can be calculated using the same cut-based analysis method and by assuming a 10% background uncertainty. Table 6.23 shows the expected 95% CL upper limit on $\Gamma_H/\Gamma_H^{\mathrm{SM}}$ using the same method as before, but by including only the VBF production mode. The sensitivity reached by using just the VBF production process for the combined ZZ channel is comparable to the result obtained in the $ZZ \to 4\ell$ channel using all production modes in the Run 1 analysis, and the same cut-based analysis method. The VBF production mode was not taken into account independently in the Run 1 analysis, since it is a low cross section process. This channel can enjoy a significantly improvement using an MVA technique, such as the ME method.

	$\Gamma_H/\Gamma_H^{\mathrm{SM}}$ $\mathcal{L} = 100$ fb^{-1}
$ZZ \to 4\ell$ analysis	25
$ZZ \to 4\ell + ZZ \to 2l2\nu$ analysis	15

Table 6.23 *Expected 95% CL cut-based upper limits on Γ_H/Γ_H^{SM} using the scan of the negative log-likelihood, $-2\ln\Lambda$, for the $ZZ \to 4\ell$ and $ZZ \to 2\ell\,2\nu$ channels using the VBF production mode.*

Chapter 7

Conclusion

There is strong evidence that the particle observed in 2012 by the ATLAS and CMS collaborations is the Higgs boson predicted by the SM. The measurements of its properties have so far all been consistent with the SM hypothesis. However, there is still some room for a scenario in which a BSM candidate (with different properties than those of the SM Higgs boson) is what has been discovered. Improving the precision on the measurements of the couplings of the Higgs boson to the other SM particles could unveil deviations from the SM expectations and give evidence for new physics. This couplings of the Higgs boson with the rest of the SM particles can vary if an unknown exotic particle interacts in a particular Higgs boson production or decay mode, which is a plausible scenario at higher energies, or equivalently, invariant masses.

The measurement of the ZZ final state in the mass range above the $2m_Z$ threshold provides a unique opportunity for the measurement of the off-shell coupling strength of the observed Higgs boson. By assuming the same on-shell and off-shell couplings, this can be interpreted as a measurement for the Higgs boson total width. In this thesis we have presented the determination of the off-shell Higgs boson signal strength in the $ZZ \to 4\ell$ final state, which has then been combined with the analysis of the $ZZ \to 2\ell\,2\nu$ and $WW \to e\nu\,\mu\nu$ channels to provide a measurement with increased sensitivity. The result is based on pp collision data collected by the ATLAS experiment at the LHC, corresponding to an integrated luminosity of 20.3 fb^{-1} at a collision energy of $\sqrt{s} = 8$ TeV.

Using the CL_s method, the observed 95% confidence level (CL) upper limit on the off-shell signal strength is in the range 5.1–8.6, with an expected range of

6.7–11.0. In each case, the range has been determined by varying the value of the unknown $gg \to ZZ$ and $gg \to WW$ background K-factor, which is due to a higher-order QCD correction, between half and twice the value of the known signal K-factor.

Assuming that the relevant Higgs boson couplings are independent of the energy scale of the Higgs production, a combination of the on-shell measurements of ZZ and WW in the same dataset yields an observed (expected) 95% CL upper limit on $\Gamma_H/\Gamma_H^{\mathrm{SM}}$ in the range 4.5–7.5 (6.5–11.2) under the same assumptions for the background K-factor. By using the value of $\mathrm{R}_{H^*}^{B}$=1 and the assumptions summarised above, this translates into an observed (expected) 95% CL upper limit on the Higgs boson total width of 22.7 (33.0) MeV.

If the total width of the Higgs boson is equal to the value predicted by the SM, the same combination can be interpreted as a limit on the ratio of the off-shell to the on-shell couplings to gluons $R_{gg} = \kappa^2_{g,\text{off-shell}}/\kappa^2_{g,\text{on-shell}}$. An observed (expected) 95% CL upper limit on R_{gg} in the range 4.7–8.6 (7.1–13.4) is found, using the same assumptions for the background K-factor.

The measurement of the off-shell signal strength of the Higgs boson using ZZ events in the $ZZ \to 4\ell$ channel has been explored in the Run 2 scenario, i.e. $\sqrt{s} = 14$ TeV for integrated luminosities between 10 fb^{-1} and 100 fb^{-1}. At 100 fb^{-1}, the sensitivity is improved by approximately 60% with respect to today's measurements. The VBF channel is less sensitive to the assumption of same on-shell and off-shell couplings, due to the absence of a quark loop, but has a smaller cross-section than the ggF process. The statistics available at the end of Run 2 would be enough to carry out an independent analysis using just VBF production mode.

The second study of this thesis presented a proposal for a more efficient filtering of muons at the trigger in order to reduce the large background rates in the high-occupancy environment of the HL-LHC era. A significant redesign of the ATLAS detector and TDAQ system will be required that will be implementing an improved rejection at early trigger stages to cope with the very high pile-up interactions. An isolation discriminant (that could be implemented via a hardware based track reconstruction, known as Level-1 Track trigger) will provide an essential component for the implementation of this algorithm.

We have carried out a preliminary study, showing that the background for single-muon selection can be reduced by a factor of ten with respect to the current

selection by matching a muon candidate with a track identified by the Level-1 Track trigger system, for an inefficiency increase of about 7%. An additional isolation discriminant improves the background rejection by another 20% for a negligible efficiency loss. We have found no significant performance difference between a calorimeter- and a track-based isolation algorithms. These studies should be repeated for a wider range of pile-up conditions.

Appendix A

Impact of Higgs mass to the off-peak shapes

In this section we document the studies of the off-peak kinematic shapes varying the Higgs boson mass. Figure A.1 shows the main kinematic distributions for the $gg \to H \to ZZ \to 4\ell$ process with different Higgs mass. Varying the Higgs mass from the nominal choice of 125.5 GeV by 1 GeV has little effect on the off-peak shapes.

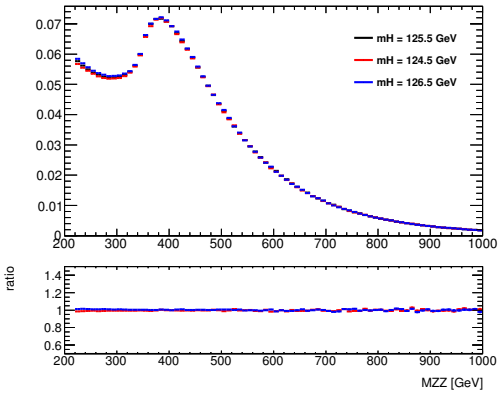

(a)

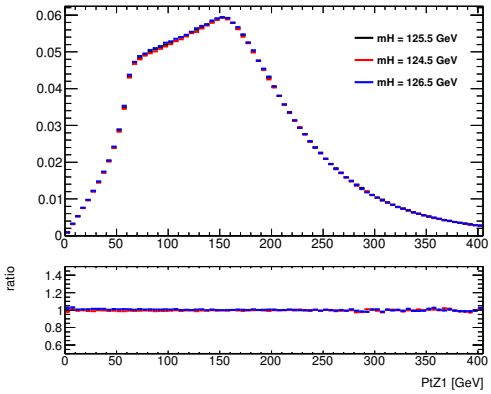

(b)

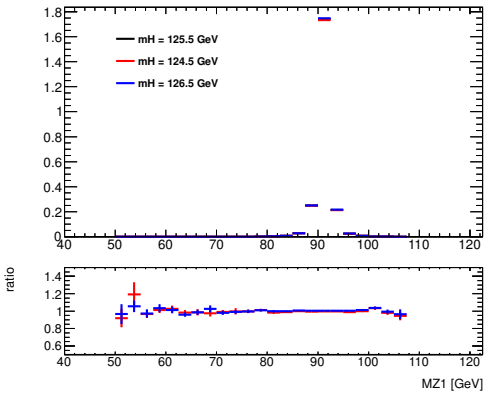

(c)

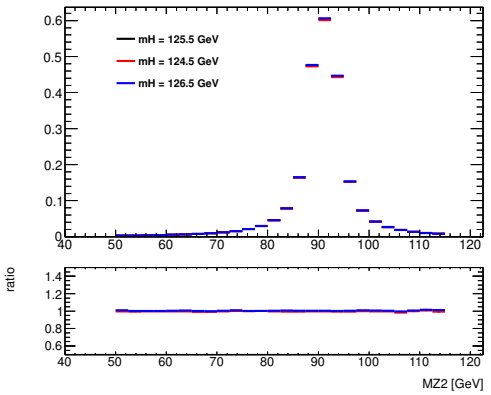

(d)

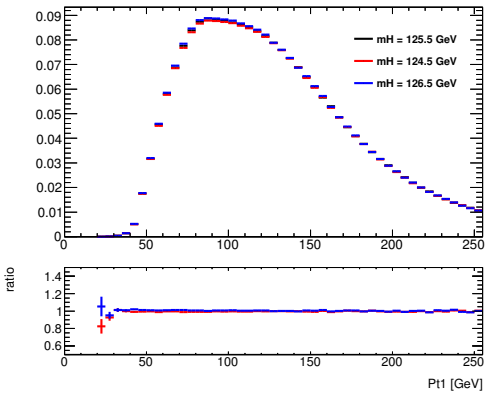

(e)

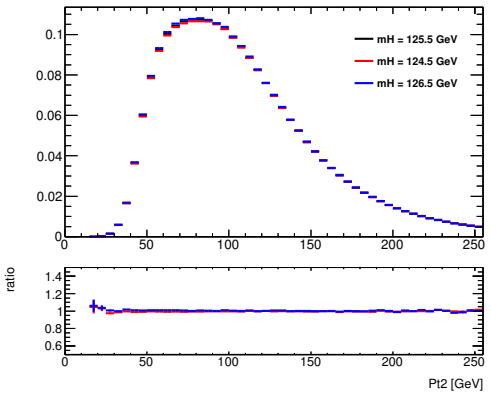

(f)

Figure A.1 *Kinematic distributions for the $gg \to H \to ZZ \to 4\ell$ in the off-peak region with different Higgs mass.*

Appendix B

Dependence of the off-shell signal and background interference on the signal strength

B.1 Dependence of the $gg \to (H^* \to)ZZ$ off-shell cross-sections on the signal strength

An event sample $\sigma_{gg\to(H^*\to)ZZ}(\mu_{\text{off-shell}})$ for the $gg \to (H^* \to)ZZ$ process with an arbitrary value of the off-shell Higgs boson signal strength $\mu_{\text{off-shell}}$ can be constructed from the MC sample for the SM Higgs boson signal $gg \to H^* \to ZZ$ ($\sigma^{\text{SM}}_{gg\to H^*\to ZZ}$), the $gg \to ZZ$ continuum background MC sample ($\sigma_{gg\to ZZ,\,\text{cont}}$) and a full SM Higgs boson signal plus background $gg \to (H^* \to)ZZ$ MC sample ($\sigma^{\text{SM}}_{gg\to(H^*\to)ZZ}$) using the following weighting function:

$$\begin{aligned}
\sigma_{gg\to(H^*\to)ZZ}(\mu_{\text{off-shell}}) &= \mathrm{K}^{H^*}(m_{4\ell}) \cdot \mu_{\text{off-shell}} \cdot \sigma^{\text{SM}}_{gg\to H^*\to ZZ} \qquad \text{(B.1)}\\
&+ \sqrt{\mathrm{K}^{H^*}_{gg}(m_{4\ell}) \cdot \mathrm{K}^{\mathrm{B}}(m_{4\ell}) \cdot \mu_{\text{off-shell}}} \cdot \sigma^{\text{SM}}_{gg\to ZZ,\,\text{Interference}}\\
&+ \mathrm{K}^{\mathrm{B}}(m_{4\ell}) \cdot \sigma_{gg\to ZZ,\,\text{cont}}\,,\\
\sigma^{\text{SM}}_{gg\to ZZ,\ \text{Interference}} &= \sigma^{\text{SM}}_{gg\to(H^*\to)ZZ} - \sigma^{\text{SM}}_{gg\to H^*\to ZZ} - \sigma_{gg\to ZZ,\,\text{cont}}\,, \qquad \text{(B.2)}
\end{aligned}$$

where the K-factors are calculated inclusively without any selections.

As a direct simulation of an interference MC sample is not possible, Eq. (B.2)

and $\mathrm{R}^{B}_{H^*}$ are used to obtain:

$$\begin{aligned}
\sigma_{gg\to(H^*\to)ZZ}(\mu_{\text{off-shell}}) &= \left(\mathrm{K}^{H^*}(m_{4\ell})\cdot\mu_{\text{off-shell}} - \mathrm{K}^{H^*}_{gg}(m_{4\ell})\cdot\sqrt{\mathrm{R}^{B}_{H^*}\cdot\mu_{\text{off-shell}}}\right)\cdot\sigma^{\text{SM}}_{gg\to H^*\to ZZ} \\
&+ \mathrm{K}^{H^*}_{gg}(m_{4\ell})\cdot\sqrt{\mathrm{R}^{B}_{H^*}\cdot\mu_{\text{off-shell}}}\cdot\sigma^{\text{SM}}_{gg\to(H^*\to)ZZ} \\
&+ \mathrm{K}^{H^*}_{gg}(m_{4\ell})\cdot\left(\mathrm{R}^{B}_{H^*} - \sqrt{\mathrm{R}^{B}_{H^*}\cdot\mu_{\text{off-shell}}}\right)\cdot\sigma_{gg\to ZZ,\,\text{cont}}.
\end{aligned} \tag{B.3}$$

Bibliography

[1] Georges Aad et al. Constraints on the off-shell Higgs boson signal strength in the high-mass ZZ and WW final states with the ATLAS detector. *Eur. Phys. J.*, C75(7):335, 2015. doi: 10.1140/epjc/s10052-015-3542-2.

[2] S. L. Glashow. Partial Symmetries of Weak Interactions. *Nucl. Phys.*, 22: 579–588, 1961. doi: 10.1016/0029-5582(61)90469-2.

[3] Steven Weinberg. A Model of Leptons. *Phys. Rev. Lett.*, 19:1264–1266, 1967. doi: 10.1103/PhysRevLett.19.1264.

[4] F. Englert and R. Brout. Broken Symmetry and the Mass of Gauge Vector Mesons. *Phys. Rev. Lett.*, 13:321–323, 1964. doi: 10.1103/PhysRevLett.13.321.

[5] G. S. Guralnik, C. R. Hagen, and T. W. B. Kibble. Global Conservation Laws and Massless Particles. *Phys. Rev. Lett.*, 13:585–587, 1964. doi: 10.1103/PhysRevLett.13.585.

[6] Peter W. Higgs. Broken Symmetries and the Masses of Gauge Bosons. *Phys. Rev. Lett.*, 13:508–509, 1964. doi: 10.1103/PhysRevLett.13.508.

[7] Georges Aad et al. Observation of a new particle in the search for the Standard Model Higgs boson with the ATLAS detector at the LHC. *Phys. Lett.*, B716:1–29, 2012. doi: 10.1016/j.physletb.2012.08.020.

[8] Serguei Chatrchyan et al. Observation of a new boson at a mass of 125 GeV with the CMS experiment at the LHC. *Phys. Lett.*, B716:30–61, 2012. doi: 10.1016/j.physletb.2012.08.021.

[9] Georges Aad et al. Combined Measurement of the Higgs Boson Mass in pp Collisions at $\sqrt{s} = 7$ and 8 TeV with the ATLAS and CMS Experiments. *Phys. Rev. Lett.*, 114:191803, 2015. doi: 10.1103/PhysRevLett.114.191803.

[10] CMS Collaboration. Constraints on the spin-parity and anomalous HVV couplings of the Higgs boson in proton collisions at 7 and 8 TeV. 2014.

[11] ATLAS Collaboration. Measurement of the Higgs boson mass from the $H \to \gamma\gamma$ and $H \to ZZ^* \to 4\ell$ channels with the ATLAS detector using

25 fb^{-1} of pp collision data. *Phys. Rev.*, D 90:052004, 2014. doi: 10.1103/PhysRevD.90.052004.

[12] Georges Aad et al. Measurements of the Higgs boson production and decay rates and constraints on its couplings from a combined ATLAS and CMS analysis of the LHC pp collision data at $\sqrt{s} = 7$ and 8 TeV. *JHEP*, 08:045, 2016. doi: 10.1007/JHEP08(2016)045.

[13] G Apollinari, I Bjar Alonso, O Brning, M Lamont, and L Rossi. High-Luminosity Large Hadron Collider (HL-LHC) : Preliminary Design Report. 2015. doi: 10.5170/CERN-2015-005.

[14] Nicola Cabibbo. Unitary Symmetry and Leptonic Decays. *Phys. Rev. Lett.*, 10:531–533, 1963. doi: 10.1103/PhysRevLett.10.531. [,648(1963)].

[15] Makoto Kobayashi and Toshihide Maskawa. CP Violation in the Renormalizable Theory of Weak Interaction. *Prog. Theor. Phys.*, 49:652–657, 1973. doi: 10.1143/PTP.49.652.

[16] David Galbraith. Standard Model. `http://davidgalbraith.org/portfolio/ux-standard-model-of-the-standard-model/`.

[17] T. D. Lee and C. N. Yang. Question of parity conservation in weak interactions. *Phys. Rev.*, 104:254–258, Oct 1956. doi: 10.1103/PhysRev.104.254. URL `http://link.aps.org/doi/10.1103/PhysRev.104.254`.

[18] J. H. Christenson, J. W. Cronin, V. L. Fitch, and R. Turlay. Evidence for the 2π decay of the k_2^0 meson. *Phys. Rev. Lett.*, 13:138–140, Jul 1964. doi: 10.1103/PhysRevLett.13.138. URL `http://link.aps.org/doi/10.1103/PhysRevLett.13.138`.

[19] M. Gell-Mann and Yuval Ne'eman. Current-generated algebras. *Annals Phys.*, 30:360–369, 1964. doi: 10.1016/0003-4916(64)90122-8.

[20] R. H. Dalitz. Book review on The Eightfold Way by M. Gell-Mann and Yuval Ne'eman. *Endeavour*, 24:168, 1965.

[21] R. P. Feynman, Murray Gell-Mann, and G. Zweig. Group U(6) x U(6) generated by current components. *Phys. Rev. Lett.*, 13:678–680, 1964. doi: 10.1103/PhysRevLett.13.678.

[22] M. Y. Han and Yoichiro Nambu. Three Triplet Model with Double SU(3) Symmetry. *Phys. Rev.*, 139:B1006–B1010, 1965. doi: 10.1103/PhysRev.139.B1006.

[23] H. Fritzsch, Murray Gell-Mann, and H. Leutwyler. Advantages of the Color Octet Gluon Picture. *Phys. Lett.*, B47:365–368, 1973. doi: 10.1016/0370-2693(73)90625-4.

[24] D. J. Gross and Frank Wilczek. Asymptotically Free Gauge Theories. 1. *Phys. Rev.*, D8:3633–3652, 1973. doi: 10.1103/PhysRevD.8.3633.

[25] J. D. Bjorken. Asymptotic Sum Rules at Infinite Momentum. *Phys. Rev.*, 179:1547–1553, 1969. doi: 10.1103/PhysRev.179.1547.

[26] A. D. Martin, W. J. Stirling, R. S. Thorne, and G. Watt. Parton distributions for the LHC. *Eur. Phys. J.*, C63:189–285, 2009. doi: 10.1140/epjc/s10052-009-1072-5.

[27] R. P. Feynman and Murray Gell-Mann. Theory of Fermi interaction. *Phys. Rev.*, 109:193–198, 1958. doi: 10.1103/PhysRev.109.193.

[28] E. C. G. Sudarshan and R. e. Marshak. Chirality invariance and the universal Fermi interaction. *Phys. Rev.*, 109:1860–1860, 1958. doi: 10.1103/PhysRev.109.1860.2.

[29] J. Schwinger. A theory of the fundamental interactions. *Annals of Physics*, 2:407–434, 1957. doi: 10.1016/0003-4916(57)90015-5.

[30] Chen-Ning Yang and Robert L. Mills. Conservation of Isotopic Spin and Isotopic Gauge Invariance. *Phys. Rev.*, 96:191–195, 1954. doi: 10.1103/PhysRev.96.191.

[31] Yoichiro Nambu and G. Jona-Lasinio. Dynamical Model of Elementary Particles Based on an Analogy with Superconductivity. 1. *Phys. Rev.*, 122: 345–358, 1961. doi: 10.1103/PhysRev.122.345.

[32] Yoichiro Nambu and G. Jona-Lasinio. Dynamical Model of Elementary Particles Based on an Analogy with Superconductivity. 2. *Phys. Rev.*, 124: 246–254, 1961. doi: 10.1103/PhysRev.124.246.

[33] J. Goldstone. Field Theories with Superconductor Solutions. *Nuovo Cim.*, 19:154–164, 1961. doi: 10.1007/BF02812722.

[34] Gauge Fields. `https://web2.ph.utexas.edu/~coker2/index.files/gaugef.htm`.

[35] Jeffrey Goldstone, Abdus Salam, and Steven Weinberg. Broken Symmetries. *Phys. Rev.*, 127:965–970, 1962. doi: 10.1103/PhysRev.127.965.

[36] Steven Weinberg. Physical Processes in a Convergent Theory of the Weak and Electromagnetic Interactions. *Phys. Rev. Lett.*, 27:1688–1691, 1971. doi: 10.1103/PhysRevLett.27.1688.

[37] Steven Weinberg. General Theory of Broken Local Symmetries. *Phys. Rev.*, D7:1068–1082, 1973. doi: 10.1103/PhysRevD.7.1068.

[38] Georges Aad et al. Study of the spin and parity of the Higgs boson in diboson decays with the ATLAS detector. *Eur. Phys. J.*, C75(10):476, 2015. doi: 10.1140/epjc/s10052-015-3685-1,10.1140/epjc/s10052-016-3934-y. [Erratum: Eur. Phys. J.C76,no.3,152(2016)].

[39] Georges Aad et al. Measurements of the Higgs boson production and decay rates and coupling strengths using pp collision data at $\sqrt{s} = 7$ and 8 TeV in the ATLAS experiment. *Eur. Phys. J.*, C76(1):6, 2016. doi: 10.1140/epjc/s10052-015-3769-y.

[40] LHC Higgs Cross Section Working Group, S. Heinemeyer, C. Mariotti, G. Passarino, and R. Tanaka (Eds.). Handbook of LHC Higgs Cross Sections: 3. Higgs Properties. *CERN-2013-004*, CERN, Geneva, 2013. doi: 10.5170/CERN-2013-004.

[41] Georges Aad et al. Observation and measurement of Higgs boson decays to WW* with the ATLAS detector. *Phys. Rev.*, D92(1):012006, 2015. doi: 10.1103/PhysRevD.92.012006.

[42] Vardan Khachatryan et al. Precise determination of the mass of the Higgs boson and tests of compatibility of its couplings with the standard model predictions using proton collisions at 7 and 8 TeV. *Eur. Phys. J.*, C75(5): 212, 2015. doi: 10.1140/epjc/s10052-015-3351-7.

[43] Georges Aad et al. Evidence for the Higgs-boson Yukawa coupling to tau leptons with the ATLAS detector. *JHEP*, 04:117, 2015. doi: 10.1007/JHEP04(2015)117.

[44] Pushpalatha C. Bhat. Multivariate Analysis Methods in Particle Physics. *Ann. Rev. Nucl. Part. Sci.*, 61:281–309, 2011. doi: 10.1146/annurev.nucl.012809.104427.

[45] G. Aad et al. The ATLAS Experiment at the CERN Large Hadron Collider. *JINST*, 3:S08003, 2008. doi: 10.1088/1748-0221/3/08/S08003.

[46] S. Chatrchyan et al. The CMS experiment at the CERN LHC. *JINST*, 3: S08004, 2008. doi: 10.1088/1748-0221/3/08/S08004.

[47] A. Augusto Alves, Jr. et al. The LHCb Detector at the LHC. *JINST*, 3: S08005, 2008. doi: 10.1088/1748-0221/3/08/S08005.

[48] K. Aamodt et al. The ALICE experiment at the CERN LHC. *JINST*, 3: S08002, 2008. doi: 10.1088/1748-0221/3/08/S08002.

[49] O. Adriani et al. The LHCf detector at the CERN Large Hadron Collider. *JINST*, 3:S08006, 2008. doi: 10.1088/1748-0221/3/08/S08006.

[50] G. Anelli et al. The TOTEM experiment at the CERN Large Hadron Collider. *JINST*, 3:S08007, 2008. doi: 10.1088/1748-0221/3/08/S08007.

[51] James Pinfold et al. Technical Design Report of the MoEDAL Experiment. (CERN-LHCC-2009-006. MoEDAL-TDR-001), Jun 2009. URL `https://cds.cern.ch/record/1181486`.

[52] Lyndon Evans and Philip Bryant. LHC Machine. *JINST*, 3:S08001, 2008. doi: 10.1088/1748-0221/3/08/S08001.

[53] 203828. LEP Design Report: Vol.2. The LEP Main Ring. 1984. URL https://cds.cern.ch/record/102083. Copies shelved as reports in LEP, PS and SPS libraries.

[54] LHC-Accelerator-Complex. http://te-dep-epc-oms.web.cern.ch/te-dep-epc-oms/general-fr/pagesources/Cern-Accelerator-Complex.jpg.

[55] M Capeans, G Darbo, K Einsweiller, M Elsing, T Flick, M Garcia-Sciveres, C Gemme, H Pernegger, O Rohne, and R Vuillermet. ATLAS Insertable B-Layer Technical Design Report. Technical Report CERN-LHCC-2010-013. ATLAS-TDR-19, Sep 2010. URL https://cds.cern.ch/record/1291633.

[56] Detector and Technology, ATLAS Experiment at CERN. http://atlas.cern/resources/multimedia/detector.

[57] R. L. Gluckstern. Uncertainties in track momentum and direction, due to multiple scattering and measurement errors. *Nucl. Instrum. Meth.*, 24: 381–389, 1963. doi: 10.1016/0029-554X(63)90347-1.

[58] Gabriele Chiodini. ATLAS RPC time-of-flight performance. *PoS*, RPC2012:007, 2012.

[59] A Nisati. An Integrated RPC and TGC Detector for the ATLAS Muon Trigger. Technical Report ATL-MUON-94-042. ATL-M-PN-42, CERN, Geneva, Jun 1994. URL http://cds.cern.ch/record/685822.

[60] The ATLAS Data Acquisition and High Level Trigger system. *JINST*, 11 (06):P06008, 2016. doi: 10.1088/1748-0221/11/06/P06008.

[61] Georges Aad et al. Performance of the ATLAS Trigger System in 2010. *Eur. Phys. J.*, C72:1849, 2012. doi: 10.1140/epjc/s10052-011-1849-1.

[62] The ATLAS three levels trigger system. - Scientific Figure on ResearchGate. https://www.researchgate.net/figure/4291333_fig1_Fig-1-The-ATLAS-three-levels-trigger-system.

[63] Morad Aaboud et al. Luminosity determination in pp collisions at $\sqrt{s} =$ 8 TeV using the ATLAS detector at the LHC. (arXiv:1608.03953. CERN-EP-2016-117), Aug 2016. URL http://cds.cern.ch/record/2208146.

[64] Peter Vankov. ATLAS Upgrade for the HL-LHC: Meeting the challenges of a five-fold increase in collision rate. *EPJ Web Conf.*, 28:12069, 2012. doi: 10.1051/epjconf/20122812069.

[65] G. Aad et al. Expected Performance of the ATLAS Experiment - Detector, Trigger and Physics. 2009. URL https://cds.cern.ch/record/1125884.

[66] Improved electron reconstruction in ATLAS using the Gaussian Sum Filter-based model for bremsstrahlung. (ATLAS-CONF-2012-047), May 2012. URL https://cds.cern.ch/record/1449796.

[67] Georges Aad et al. Electron performance measurements with the ATLAS detector using the 2010 LHC proton-proton collision data. *Eur. Phys. J.*, C72:1909, 2012. doi: 10.1140/epjc/s10052-012-1909-1.

[68] B. Lenzi and R. Turra. Monte Carlo calibration update for electrons and photons using multivariate techniques. Technical Report ATL-COM-PHYS-2013-1426, CERN, Geneva, Oct 2013. URL `https://cds.cern.ch/record/1609589`.

[69] Georges Aad et al. Electron and photon energy calibration with the ATLAS detector using LHC Run 1 data. *Eur. Phys. J.*, C74(10):3071, 2014. doi: 10.1140/epjc/s10052-014-3071-4.

[70] Georges Aad et al. Measurement of the muon reconstruction performance of the ATLAS detector using 2011 and 2012 LHC protonproton collision data. *Eur. Phys. J.*, C74(11):3130, 2014. doi: 10.1140/epjc/s10052-014-3130-x.

[71] Georges Aad et al. Jet energy measurement and its systematic uncertainty in proton-proton collisions at $\sqrt{s} = 7$ TeV with the ATLAS detector. *Eur. Phys. J.*, C75:17, 2015. doi: 10.1140/epjc/s10052-014-3190-y.

[72] Matteo Cacciari, Gavin P. Salam, and Gregory Soyez. The Anti-k(t) jet clustering algorithm. *JHEP*, 04:063, 2008. doi: 10.1088/1126-6708/2008/04/063.

[73] T. Barillari et al. Local Hadronic Calibration. Technical Report ATL-LARG-PUB-2009-001-2. ATL-COM-LARG-2008-006. ATL-LARG-PUB-2009-001, CERN, Geneva, Jun 2008. URL `https://cds.cern.ch/record/1112035`.

[74] Matteo Cacciari, Gavin P. Salam, and Gregory Soyez. FastJet User Manual. *Eur. Phys. J.*, C72:1896, 2012. doi: 10.1140/epjc/s10052-012-1896-2.

[75] The ATLAS collaboration. Pile-up subtraction and suppression for jets in ATLAS. (ATLAS-CONF-2013-083), Aug 2013. URL `https://cds.cern.ch/record/1570994`.

[76] The ATLAS collaboration. Performance of Missing Transverse Momentum Reconstruction in ATLAS studied in Proton-Proton Collisions recorded in 2012 at 8 TeV. (ATLAS-CONF-2013-082), Aug 2013. URL `https://cds.cern.ch/record/1570993`.

[77] Recent progress of the HiLumi project. `http://acceleratingnews.web.cern.ch/content/recent-progress-hilumi-project-0`.

[78] Letter of Intent for the Phase-I Upgrade of the ATLAS Experiment. Technical Report CERN-LHCC-2011-012. LHCC-I-020, CERN, Geneva, Nov 2011. URL `https://cds.cern.ch/record/1402470`.

[79] ATLAS muon spectrometer: Technical design report. 1997. URL `https://cds.cern.ch/record/331068`.

[80] Performance of the ATLAS Inner Detector Track and Vertex Reconstruction in the High Pile-Up LHC Environment. (ATLAS-CONF-2012-042), Mar 2012. URL https://cds.cern.ch/record/1435196.

[81] A. Annovi et al. Design of a hardware track finder (Fast TracKer) for the ATLAS trigger. *JINST*, 9(01):C01045, 2014. doi: 10.1088/1748-0221/9/01/C01045.

[82] A. Annovi et al. Development of FTK architecture: a fast hardware track trigger for the ATLAS detector. 2009. URL https://arxiv.org/pdf/0910.1126v1.

[83] A. Clark et al. Final Report: ATLAS Phase-2 Tracker Upgrade Layout Task Force. (ATL-UPGRADE-PUB-2012-004), Oct 2012. URL https://cds.cern.ch/record/1482960.

[84] A. Clark, M. Elsing, and P. Wells. Performance Specifications of the Tracker Phase II Upgrade. (ATL-UPGRADE-PUB-2012-003), Sep 2012. URL https://cds.cern.ch/record/1478374.

[85] D. Wardrope. Instrumentation of the upgraded ATLAS tracker with a double buffer front-end architecture for track triggering. *JINST*, 7:C08010, 2012. doi: 10.1088/1748-0221/7/08/C08010.

[86] Jorg Dubbert, Sandra Horvat, Oliver Kortner, Hubert Kroha, and Robert Richter. Upgrade of the ATLAS Muon Trigger for the SLHC. *JINST*, 5:C12016, 2010. doi: 10.1088/1748-0221/5/12/C12016.

[87] Alessandro Cerri. L1Track: A fast Level 1 track trigger for the ATLAS high luminosity upgrade. *Nucl. Instrum. Meth.*, A824:263–264, 2016. doi: 10.1016/j.nima.2015.09.099.

[88] M. R. Sutton. Tracking for the ATLAS Level 1 Trigger for the high luminosity LHC. In *Proceedings, 14th ICATPP Conference on Astroparticle, Particle, Space Physics and Detectors for Physics Applications (ICATPP 2013): Como, Italy, September 23-27, 2013*, pages 416–421, 2014. doi: 10.1142/9789814603164_0064.

[89] Georges Aad et al. Performance of the ATLAS muon trigger in pp collisions at $\sqrt{s} = 8$ TeV. *Eur. Phys. J.*, C75:120, 2015. doi: 10.1140/epjc/s10052-015-3325-9.

[90] Paolo Nason and Carlo Oleari. NLO Higgs boson production via vector-boson fusion matched with shower in POWHEG. *JHEP*, 02:037, 2010. doi: 10.1007/JHEP02(2010)037.

[91] Torbjorn Sjostrand, Stephen Mrenna, and Peter Z. Skands. A Brief Introduction to PYTHIA 8.1. *Comput.Phys.Commun.*, 178:852–867, 2008. doi: 10.1016/j.cpc.2008.01.036.

[92] Jun Gao et al. CT10 next-to-next-to-leading order global analysis of QCD. *Phys. Rev.*, D89(3):033009, 2014. doi: 10.1103/PhysRevD.89.033009.

[93] Summary of ATLAS Pythia 8 tunes. (ATL-PHYS-PUB-2012-003), Aug 2012. URL `http://cds.cern.ch/record/1474107`.

[94] S. Agostinelli et al. GEANT4, a simulation toolkit. *Nucl. Instrum. Meth.*, A 506:250, 2003. doi: 10.1016/S0168-9002(03)01368-8.

[95] The atlas simulation infrastructure. *Eur. Phys. J.*, C 70:823, 2010. ISSN 1434-6044. doi: epjc/s10052-010-1429-9.

[96] Georges Aad et al. A particle consistent with the Higgs Boson observed with the ATLAS Detector at the Large Hadron Collider. *Science*, 338: 1576–1582, 2012. doi: 10.1126/science.1232005.

[97] Georges Aad et al. Measurements of the Higgs boson production and decay rates and coupling strengths using pp collision data at $\sqrt{s} = 7$ and 8 TeV in the ATLAS experiment. *Eur. Phys. J.*, C76(1):6, 2016. doi: 10.1140/epjc/s10052-015-3769-y.

[98] Sara Bolognesi, Yanyan Gao, Andrei V. Gritsan, Kirill Melnikov, Markus Schulze, Nhan V. Tran, and Andrew Whitbeck. On the spin and parity of a single-produced resonance at the LHC. *Phys. Rev.*, D86:095031, 2012. doi: 10.1103/PhysRevD.86.095031.

[99] Nikolas Kauer and Giampiero Passarino. Inadequacy of zero-width approximation for a light Higgs boson signal. *JHEP*, 08:116, 2012. doi: 10.1007/JHEP08(2012)116.

[100] Fabrizio Caola and Kirill Melnikov. Constraining the Higgs boson width with ZZ production at the LHC. *Phys. Rev.*, D 88:054024, 2013. doi: 10.1103/PhysRevD.88.054024.

[101] H.M. Pilkuhn. *The interactions of hadrons*. North-Holland Pub. Co., 1967. URL `https://books.google.co.uk/books?id=n2FeAAAAIAAJ`.

[102] Christoph Englert and Michael Spannowsky. Limitations and Opportunities of Off-Shell Coupling Measurements. *Phys. Rev.*, D 90:053003, 2014. doi: 10.1103/PhysRevD.90.053003.

[103] Giacomo Cacciapaglia, Aldo Deandrea, Guillaume Drieu La Rochelle, and Jean-Baptiste Flament. Higgs couplings: disentangling New Physics with off-shell measurements. *Phys. Rev. Lett.*, 113:201802, 2014. doi: 10.1103/PhysRevLett.113.201802.

[104] Aleksandr Azatov, Christophe Grojean, Ayan Paul, and Ennio Salvioni. Taming the off-shell Higgs boson. *JETP*, 147 (3), 2015.

[105] Margherita Ghezzi, Giampiero Passarino, and Sandro Uccirati. Bounding the Higgs Width Using Effective Field Theory. *PoS LL2014*, 072, 2014.

[106] Malte Buschmann, Dorival Goncalves, Silvan Kuttimalai, Marek Schonherr, Frank Krauss, and Tilman Plehn. Mass Effects in the Higgs-Gluon Coupling: Boosted vs Off-Shell Production. *JHEP*, 02:038, 2015. doi: 10.1007/JHEP02(2015)038.

[107] Christoph Englert, Yotam Soreq, and Michael Spannowsky. Off-Shell Higgs Coupling Measurements in BSM scenarios. *JHEP*, 05:145, 2015. doi: 10.1007/JHEP05(2015)145.

[108] Heather E. Logan. Hiding a Higgs width enhancement from off-shell gg($\rightarrow$ h*) $\rightarrow$measurements. *Phys. Rev.*, D92(7):075038, 2015. doi: 10.1103/PhysRevD.92.075038.

[109] Giampiero Passarino. Higgs CAT. *Eur. Phys. J.*, C 74:2866, 2014. doi: 10.1140/epjc/s10052-014-2866-7.

[110] Nikolas Kauer. Interference effects for H $\rightarrow$ WW/ZZ $\rightarrow \ell\bar{\nu}_\ell\bar{\ell}\nu_\ell$ searches in gluon fusion at the LHC. *JHEP*, 12:082, 2013. doi: 10.1007/JHEP12(2013)082.

[111] John M. Campbell, R. Keith Ellis, and Ciaran Williams. Bounding the Higgs width at the LHC using full analytic results for $gg \rightarrow e^-e^+\mu^-\mu^+$. *JHEP*, 04:060, 2014. doi: 10.1007/JHEP04(2014)060.

[112] John M. Campbell, R. Keith Ellis, and Ciaran Williams. Bounding the Higgs width at the LHC: complementary results from $H \rightarrow WW$. *Phys. Rev.*, D 89:053011, 2014. doi: 10.1103/PhysRevD.89.053011.

[113] F. Cascioli et al. Precise Higgs-background predictions: merging NLO QCD and squared quark-loop corrections to four-lepton + 0,1 jet production. *JHEP*, 01:046, 2014. doi: 10.1007/JHEP01(2014)046.

[114] T. Gleisberg et al. Event generation with SHERPA 1.1. *JHEP*, 02:007, 2009. doi: 10.1088/1126-6708/2009/02/007.

[115] Fabio Cascioli, Philipp Maierhöfer, and Stefano Pozzorini. Scattering Amplitudes with Open Loops. *Phys. Rev. Lett.*, 108:111601, 2012. doi: 10.1103/PhysRevLett.108.111601.

[116] Ansgar Denner, Stefan Dittmaier, and Lars Hofer. COLLIER - A fortran-library for one-loop integrals. *PoS*, LL2014:071, 2014.

[117] Marco Bonvini, Fabrizio Caola, Stefano Forte, Kirill Melnikov, and Giovanni Ridolfi. Signal-background interference effects for $gg \rightarrow H \rightarrow W^+W^-$ beyond leading order. *Phys. Rev.*, D 88:034032, 2013. doi: 10.1103/PhysRevD.88.034032.

[118] J. Alwall et al. The automated computation of tree-level and next-to-leading order differential cross sections, and their matching to parton shower simulations. *JHEP*, 07:079, 2014. doi: 10.1007/JHEP07(2014)079. optimised by the authors for the production of VBF ($H^* \rightarrow$)VV.

[119] Alessandro Ballestrero, Aissa Belhouari, Giuseppe Bevilacqua, Vladimir Kashkan, and Ezio Maina. PHANTOM: A Monte Carlo event generator for six parton final states at high energy colliders. *Comput. Phys. Commun.*, 180:401–417, 2009. doi: 10.1016/j.cpc.2008.10.005. Extended by the authors to include the production of the VBF $H^* \to VV$ signal process.

[120] LHC Higgs Cross Section Working Group, S. Dittmaier, C. Mariotti, G. Passarino, and R. Tanaka (Eds.). Handbook of LHC Higgs Cross Sections: 2. Differential distributions. *CERN-2012-002*, CERN, Geneva, 2012.

[121] J. Pumplin et al. New generation of parton distributions with uncertainties from global QCD analysis. *JHEP*, 07:012, 2002. doi: 10.1088/1126-6708/2002/07/012.

[122] Torbjorn Sjostrand et al. PYTHIA 6.4 physics and manual. *JHEP*, 05:026, 2006. doi: doi:10.1088/1126-6708/2006/05/026.

[123] Tom Melia, Paolo Nason, Raoul Röntsch, and Giulia Zanderighi. W^+W^-, WZ and ZZ production in the POWHEG BOX. *JHEP*, 11:078, 2011. doi: 10.1007/JHEP11(2011)078.

[124] F. Cascioli et al. ZZ production at hadron colliders in NNLO QCD. *Phys. Lett.*, B 735:311, 2014. doi: 10.1016/j.physletb.2014.06.056. Extended by the authors to provide NNLO/NLO K-factors as a function of m_{ZZ}.

[125] Anastasiya Bierweiler, Tobias Kasprzik, and Johann H. Kühn. Vector-boson pair production at the LHC to $\mathcal{O}(\alpha^3)$ accuracy. *JHEP*, 12:071, 2013. doi: 10.1007/JHEP12(2013)071.

[126] Julien Baglio, Le Duc Ninh, and Marcus M. Weber. Massive gauge boson pair production at the LHC: a next-to-leading order story. *Phys. Rev.*, D 88:113005, 2013. doi: 10.1103/PhysRevD.88.113005.

[127] Stefan Gieseke, Tobias Kasprzik, and Johann H. Kühn. Vector-boson pair production and electroweak corrections in HERWIG++. *Eur. Phys. J.*, C 74:2988, 2014. doi: 10.1140/epjc/s10052-014-2988-y.

[128] Meyer, Jochen and Kasprzik, Tobias. Reweighting method to incorporate higher order electroweak corrections into resonant heavy gauge boson pair production predictions. *ATL-COM-PHYS-2014-152*, Feb 2014.

[129] ATLAS Collaboration. Observation of a new particle in the search for the Standard Model Higgs boson with the ATLAS detector at the LHC. *Phys. Lett.*, B 716:1, 2012. doi: 10.1016/j.physletb.2012.08.020.

[130] CMS Collaboration. Observation of a new boson at a mass of 125 GeV with the CMS experiment at the LHC. *Phys. Lett.*, B 716:30, 2012. doi: 10.1016/j.physletb.2012.08.021.

[131] Georges Aad et al. Measurements of Higgs boson production and couplings in diboson final states with the ATLAS detector at the LHC. *Phys. Lett.*, B726:88–119, 2013. doi: 10.1016/j.physletb.2014.05.011,10.1016/j.physletb.2013.08.010. [Erratum: Phys. Lett.B734,406(2014)].

[132] James S. Gainer, Joseph Lykken, Konstantin T. Matchev, Stephen Mrenna, and Myeonghun Park. Beyond Geolocating: Constraining Higher Dimensional Operators in $H \to 4\ell$ with Off-Shell Production and More. *Phys. Rev.*, D91(3):035011, 2015. doi: 10.1103/PhysRevD.91.035011.

[133] Vardan Khachatryan et al. Constraints on the Higgs boson width from off-shell production and decay to Z-boson pairs. *Phys. Lett.*, B736:64–85, 2014. doi: 10.1016/j.physletb.2014.06.077.

[134] ATLAS Collaboration. Search for Invisible Decays of a Higgs Boson Produced in Association with a Z Boson in ATLAS. *Phys. Rev. Lett.*, 112:201802, 2014. doi: 10.1103/PhysRevLett.112.201802.

[135] CMS collaboration. Search for invisible decays of Higgs bosons in the vector boson fusion and associated ZH production modes. *Eur. Phys. J.*, C74:2980, 2014. doi: 10.1140/epjc/s10052-014-2980-6.

[136] Georges Aad et al. Measurements of Higgs boson production and couplings in the four-lepton channel in pp collisions at center-of-mass energies of 7 and 8 TeV with the ATLAS detector. *Phys. Rev.*, D91(1):012006, 2015. doi: 10.1103/PhysRevD.91.012006.

[137] Reconstruction of collinear final-state-radiation photons in Z decays to muons in sqrts=7 TeV proton-proton collisions. (ATLAS-CONF-2012-143), Nov 2012. URL `https://cds.cern.ch/record/1491697`.

[138] ATLAS Collaboration. Evidence for the spin-0 nature of the Higgs boson using ATLAS data. *Phys. Lett.*, B 726:120, 2013. doi: 10.1016/j.physletb.2013.08.026.

[139] G. Corcella et al. HERWIG 6: An Event generator for hadron emission reactions with interfering gluons (including supersymmetric processes). *JHEP*, 01:010, 2001. doi: 10.1088/1126-6708/2001/01/010.

[140] G. Cowan, K. Cranmer, E. Gross, and O. Vitells. Asymptotic formulae for likelihood-based tests of new physics. *Eur. Phys. J.*, C 71:1554, 2011. doi: 10.1140/epjc/s10052-011-1554-0.

[141] Glen Cowan, Kyle Cranmer, Eilam Gross, and Ofer Vitells. Asymptotic formulae for likelihood-based tests of new physics. *Eur. Phys. J.*, C71:1554, 2011. doi: 10.1140/epjc/s10052-011-1554-0,10.1140/epjc/s10052-013-2501-z. [Erratum: Eur. Phys. J.C73,2501(2013)].

[142] S. S. Wilks. The Large-Sample Distribution of the Likelihood Ratio for Testing Composite Hypotheses. *Annals Math. Statist.*, 9(1):60–62, 1938. doi: 10.1214/aoms/1177732360.

[143] A. Wald. Tests of statistical hypotheses concerning several parameters when the numbers of Hypotheses observations is large. *Trans. Amer. Math. Soc.*, 54(1):426–482, 1943. doi: http://dx.doi.org/10.1090/S0002-9947-1943-0012401-3.

[144] Alexander L. Read. Presentation of search results: The CL_s technique. *J. Phys.*, G28:2693, 2002. doi: 10.1088/0954-3899/28/10/313.

[145] Combined search for the Standard Model Higgs boson in pp collisions at $\sqrt{s}$=7 TeV with the ATLAS detector. *Phys. Rev.*, D 86:032003, 2012. doi: 10.1103/PhysRevD.86.032003.

[146] Michelangelo L. Mangano and Juan Rojo. Cross Section Ratios between different CM energies at the LHC: opportunities for precision measurements and BSM sensitivity. *JHEP*, 08:010, 2012. doi: 10.1007/JHEP08(2012)010.